ABSTRACT

Title of Dissertation: CFD Based Unsteady Aerodynamic

Modeling for Rotor Aeroelastic Analysis

Jayanarayanan Sitaraman, Doctor of Philosophy, 2003

Dissertation directed by: Associate Professor James D. Baeder

Department of Aerospace Engineering

A Computational Fluid Dynamics (CFD) analysis is developed for 3-D rotor unsteady aerodynamic load prediction. It is then coupled to a rotor structural analysis for predicting aeroelastic blade response, airloads and vibration. The CFD analysis accounts for the elastic deformations using a dynamically deforming mesh system. All the rotor blades are assumed to be identical, therefore to reduce the computational complexity the CFD calculations are performed for a single blade. This accounts for the near wake flow field. But the far wake effects because of the trailed tip vortices from all the blades have to be included separately. This is achieved by the use of the field velocity approach, which is a method for modeling unsteady flows via apparent grid movement. In this method, the induced velocity field caused by the trailed vortex wake is included by modifying the grid time metrics.

The CFD method developed is systematically validated for a range of problems starting from simple 2-D model problems to full scale forward flight cases.

The CFD analysis shows significant improvements in airloads prediction compared to a table lookup based lifting-line analysis. The CFD analysis is then used to investigate the fundamental mechanisms of rotor vibration. It is found that both the normal forces and pitching moments are dominated by three dimensional aerodynamic effects. The curvature introduced by the blade elasticity appears to play a key role in the generation of the vibratory harmonics in airloads. The pitching moments near the blade tip (85% outboard) are significantly affected by transonic tip relief effects. The fundamental understanding of rotor vibrations gained from this study is then used to develop generic corrections for improving the accuracy of a lifting line analysis.

Finally the CFD analysis developed is coupled with an advanced comprehensive rotor aeroelastic analysis. The coupling procedure is formulated in a way such that there is an exchange of information between the structural model and CFD model every rotor revolution. The coupled CFD/structure scheme is found to considerably improve the prediction of rotor vibratory airloads compared to the baseline rotor aeroelastic analysis which uses a lifting line based aerodynamic model.

CFD Based Unsteady Aerodynamic Modeling for Rotor Aeroelastic Analysis

by

Jayanarayanan Sitaraman

Dissertation submitted to the Faculty of the Graduate School of the
University of Maryland, College Park in partial fulfillment
of the requirements for the degree of
Doctor of Philosophy
2003

Advisory Committee:

Associate Professor James D. Baeder, Chairman/Advisor
Professor J. Gordon Leishman
Professor Inderjit Chopra
Professor Roberto Celi
Professor Benjamin Shapiro
Professor J. G. Liu

DEDICATION

To my dear friend Swami, I wish I hadn't lost him

ACKNOWLEDGEMENTS

I would like to express my deepest gratitude to my thesis advisor, Dr. James Baeder, who with his unique dedication, infinite patience and remarkable kindness saw me through every aspect of this work. I would also like to thank him for the freedom he allowed in the course of this investigation and for the ways he showed me to approach scientific problems. It is a pleasure and honor being his student.

I would also like to thank Dr. Inderjit Chopra for co-advising this work and giving some of the most insightful comments. Also he has been a great mentor for me in both academic and personal life. I have been greatly influenced by his leadership, hard work and passion for research. I wish to thank all the members of my examining committe, Dr. Gordon Leishman in particular, for taking active interest in my work and providing very useful suggestions.

Among the several contributions made to this thesis and the author himself; both personal and scientific, I wish to distinguish those made by Anubhav Datta. The present work has benefited tremendously by his pathbreaking investigations and I would always remain indebted him. His unparalleled meticulousness and infinite patience always filled me with awe. He has been my inspiring role model and an invaluble friend throughout these years.

This work would not have taken shape without the significant interactions I had with both the government labs and helicopter industry. I wish to thank Dr. Robert Ormiston, Dr. Wayne Johnson and Dr. Mark Potsdam at NASA Ames for the extensive discussions and exchange of key information. I am very grateful to Mr. Thomas Alan Egolf, Dr. Jim Duh and Dr. Chip Berezin at

No words are sufficient to describe their tender care and deep love. My journey has been their journey and this little success fills us all with joy.

TABLE OF CONTENTS

LIST OF TABLES

LIST OF FIGURES

xix

LIST OF SYMBOLS

a	lift curve slope	
A	rotor disk area$=\pi R^2$	m^2
c	rotor blade chord	
C_d	sectional drag coefficient $(dD/(1/2\rho V_\infty^2 c))$	
C_l	sectional lift coefficient $(dL/(1/2\rho V_\infty^2 c))$	
C_n	sectional normal force coefficient $(dN/(1/2\rho V_\infty^2 c))$	
C_m	sectional pitching Moment coefficient $(dM/(1/2\rho V_\infty^2 c^2))$	
C_T	rotor thrust coefficient $(T/\rho A(\Omega R)^2)$	
C_P	rotor power coeffcient $(P/\rho A(\Omega R)^3)$	
C_{PL}	pitch link load coefficient $(PL/\rho A(\Omega R)^2)$	
E	total Energy	Nm
H	total Enthalpy	Nm
I_b	blade flap moment of inertia	kgm^2
J	Jacobian of transformation	
M	free stream Mach number	
M_{tip}	tip Mach number	
N_b	number of blades	
Pr	Prandtl Number	
p	pressure	Nm^{-2}
q	flux vector	
R	rotor radius	m
Re	Reynolds Number	
r_c	vortex core radius	m
s	non dimensional time $(2V_\infty t/c)$	

t	time	s
U	resultant airvelocity at blade section	ms^{-1}
U_P	air velocity at blade section, normal to the disk	ms^{-1}
U_R	air velocity at blade section, radial component	ms^{-1}
U_T	air velocity at blade section, chordwise component	ms^{-1}
V_∞	free stream velocity	ms^{-1}
V_i	rotor induced velocity	ms^{-1}
w_{tip}	flap deflection at the tip	rad
x, y, z	cartesian coordinates	
α	angle of attack	
α_s	longitudinal rotor shaft tilt angle	rad
ϕ_s	lateral rotor shaft tilt angle	rad
ϕ_{tip}	elastic torsional deformation at the tip	rad
β	rotor flap angle	rad
β_p	precone angle	rad
β_0	coning blade flap angle	rad
β_{1c}	longitudinal blade flap angle	rad
$\beta1s$	lateral blade flap angle	rad
η_r	distance of 3/4 chord from feather axis	
γ	lock number $(\rho a c R^4 / I_b)$	
Γ	vortex circulation strength	m^2s^{-1}
λ	rotor inflow ratio, $= (V_i / \Omega R)$	
μ	advance Ratio $(V_\infty / \Omega R)$	
ψ	azimuthal coordinate	deg
ϕ	elastic torsional deformation	rad
σ	Solidity $(Nbc/(\pi R)$	

τ	time in transformed cooridnates	s
θ	total rigid pitch angle	rad
θ_1	total pitch angle at any section, including elastic torsion	rad
θ_0	collective blade pitch angle	rad
θ_{1c}	lateral blade pitch angle	rad
θ_{1s}	longitudinal blade pitch angle	rad
Ω	rotor frequency	rads^{-1}
ξ, η, ζ	curvilinear coordinates	

Abbreviations

AVI   Airfoil Vortex Interaction

BVI   Blade Vortex Interaction

Chapter 1

Introduction

Helicopters are the most versatile flying machines in existence today. They have unmatched operational capabilities compared to fixed wing aircraft, such as performing hover and vertical take off and landing on unprepared sites. However, helicopters suffer from excessive noise and high levels of perceived vibration. Their rotors are also susceptible to several aeromechanical instabilities. Therefore, designing the new generation helicopters for reduced noise and vibration levels requires an in depth understanding of the fundamental physical phenomenon causing them.

Figure 1.1 shows the different physical phenomena occurring during a steady flight operation of a helicopter, all of which contribute to rotor vibration. The rotor blades and hub form a dynamic system, which is harmonically excited by motion dependent forces and unsteady aerodynamic loads. The rotor blades respond to this periodic excitation by motions in axial, chordwise bending (lag), flapwise bending (flap) and torsional directions. The torsional motions of the blade consist of a rigid motion caused by pilot applied controls in addition to the elastic deformations caused by the unsteady aerodynamic forcing.
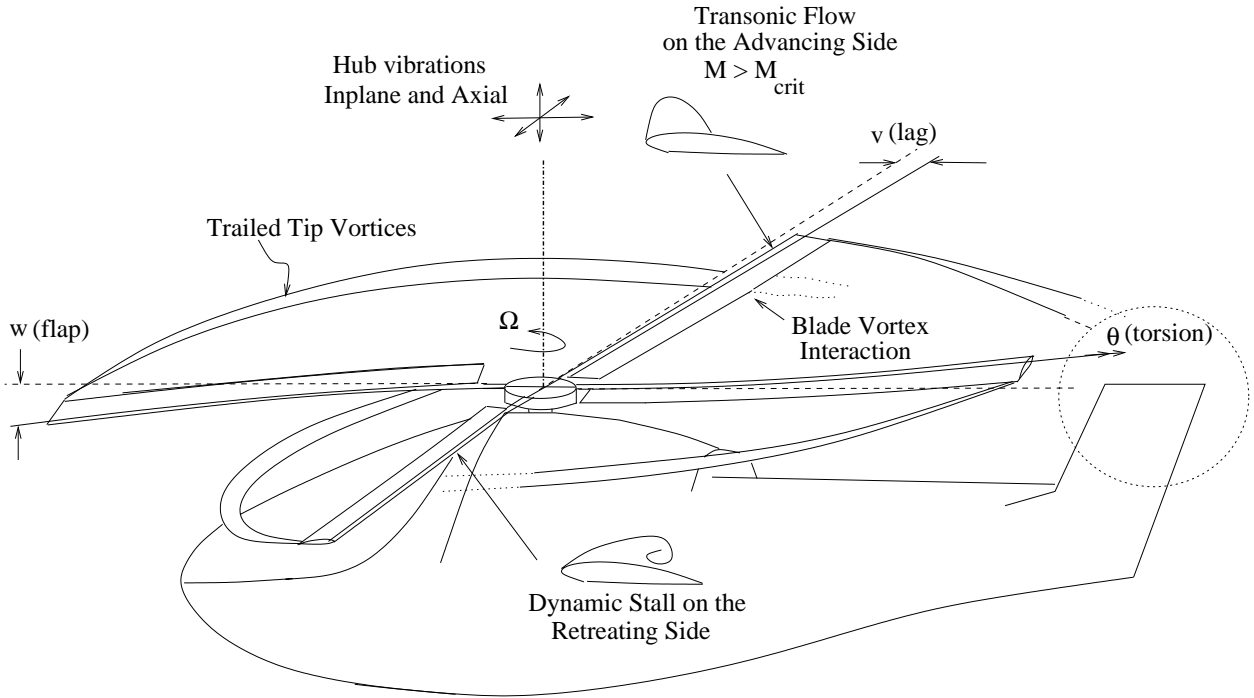
Figure 1.1: Sources of rotor vibration

The dynamic response of the rotor in the flap direction is used to vector the thrust of the rotor so as to generate the necessary control moments that transition the helicopter in to different flight regimes (forward flight, maneuver, descent etc.). This is accomplished by 1/rev pitch control inputs by the pilot such that the necessary orientation of the tip path plane (plane traced by the 1/rev motion of the blade tip) is achieved.

The rotor blade undergoes other higher harmonic excitations in addition to the low frequency (1 to 3/rev) aerodynamic forcing caused by the pitch control. The interaction of the blades with the trailed tip vortices is one of the major sources of aerodynamic excitation. At some flight conditions (especially descent and low speed forward flight), the rotor blades pass very close to the tip vortices shed from the other blades causing a phenomenon termed Blade Vortex Interac-

tion (BVI). The BVI is a major source of noise and perceived levels of vibration at these flight conditions. Also, at high speed forward flight conditions with large thrust levels, a significant portion of the rotor blade (inboard) has large incidence of reversed flow conditions during the retreating blade phase. This combined with the high angle of attacks owing to pitch control at the retreating side may lead to a phenomenon called dynamic stall. During dynamic stall the sectional aerodynamic loads, especially pitching moments, show large excursions from their normal behavior. There can be a 180 degree phase difference between the pitch rate of the airfoil and the associated pitching moment leading to a negative pitch damping. A negative pitch damping would excite larger torsional vibration levels which in turn would influence the overall vibration level to a large extent.

1.1   The Problem of Rotorcraft Aeroelastic Analysis

The highly unsteady forcing because of the periodic blade motion and various aerodynamic interactions combined with the complex structural coupling makes the rotorcraft aeroelastic analysis one of the most difficult problems to be modeled. Researchers in rotorcraft aeroelastic analysis are posed with a myriad of modeling choices for both structural and aerodynamic analysis. Also, varied levels of refinement can be used in each of these models. Figure 1.2 summarizes the various structural and aerodynamic modeling choices and their progressive refinements. One has to often derive a compromise between performance and accuracy to determine an efficient analysis methodology. The choice of the high-

est level of refinement in the most sophisticated analysis approach might provide one with a refined solution at an impractical computational cost. The lowest order approach, although attractive as a routine design tool, might be inaccurate for analyzing advanced rotor systems.

1.1.1   Choices for structural modeling

The fundamental problem of the structural analysis is to estimate the rotor blade motions as a function of space and time because of an unsteady aerodynamic forcing. One way of solving the governing partial differential equations of structural dynamics is to decouple the spatial and temporal variations such that the equations reduce to a set of ordinary differential equations (ODE's) that can be integrated in time.

The structural dynamic analysis can be progressively refined from a simple modal analysis to a complex multibody based approach. In the modal analysis, one assumes the blade response to be a linear superposition of a set of structural modes at any instant. These structural modes are chosen such that they satisfy the geometric boundary conditions. The governing equations are first linearized about a steady state periodic solution. Using the modal approach in space they are then reduced to a set of periodic coefficient ordinary differential equation system, which can be integrated in time to obtain the total rotor response.

The Finite Element (FEM) approach spatially discretizes the rotor blade in to a set of elements. The spatial variation of displacements in an element can be described in terms of the generalized nodal displacements and interpolating shape functions. The elements are formulated to preserve continuity and differentiability of displacements at the inter element junctions. The FEM approach
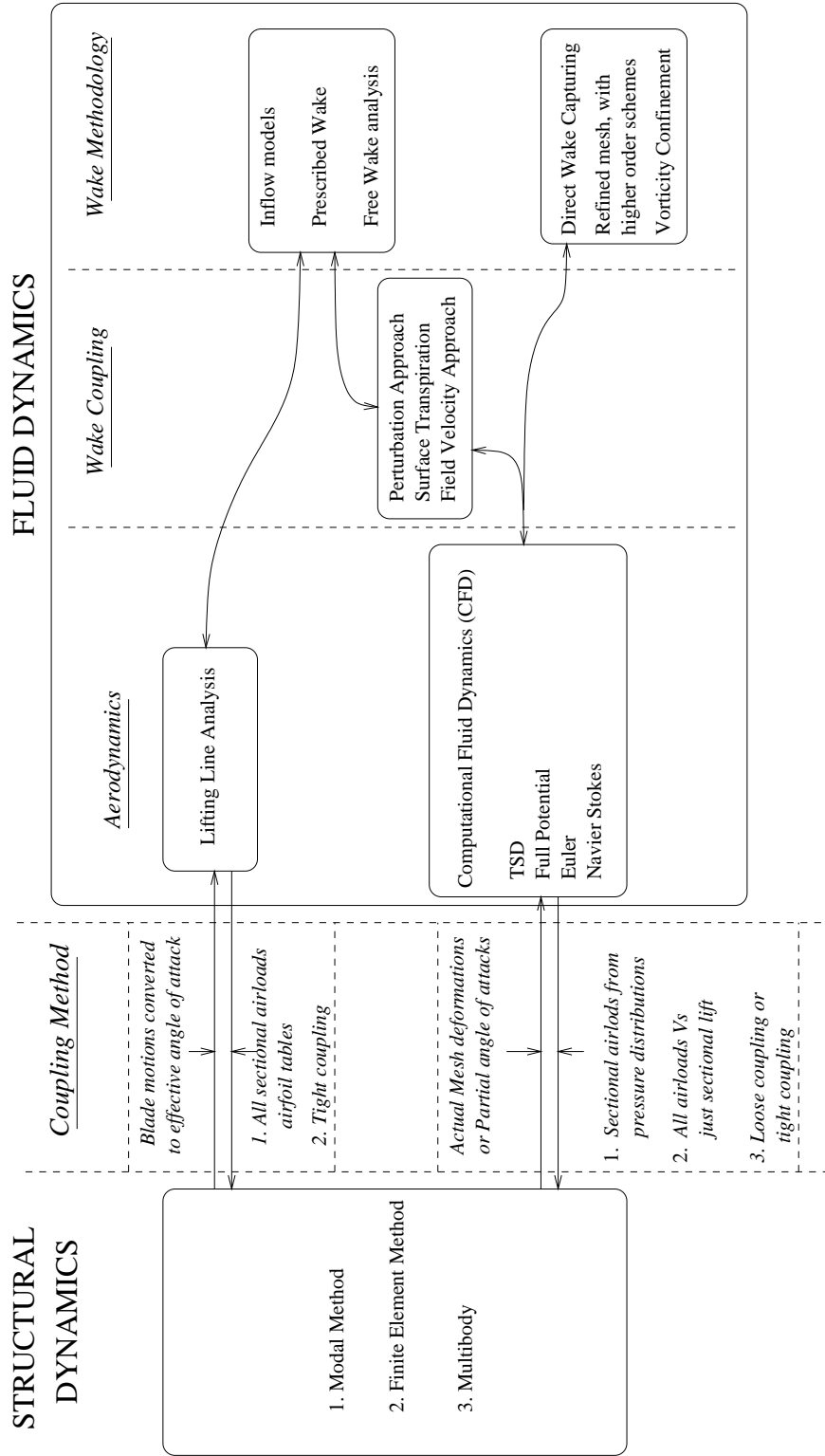
Figure 1.2: Overall methodology and analysis choices for rotorcraft aeroelastic analysis

reduces the governing equations to a time dependent ODE system. It provides flexibility compared to a modal approach in that the normal modes are extracted automatically as a combination of generalized interpolating functions. Both the FEM and modal approaches begin with non-linear governing equations which are derived based on a small strain and moderate slope assumptions.

A multibody approach provides a method for handling large frame deflections. It may provide a versatile way of handling kinematics of complex boundary conditions (e.g., a detailed control system model by explicitly describing the details of joints, linkages, contacts etc.). In this case, the governing equations are reduced to a non-linear time dependent ODE system.

1.1.2 Choices of aerodynamic modeling

The aerodynamic analysis can be incrementally refined from a lifting line analysis to a full Computational Fluid Dynamics (CFD) simulation of the entire flow field. The first step in a lifting line analysis is to determine the effective angle of attack at the individual blade elements. The effective angle of attack is composed of contributions from the pitch control, blade elastic motions and the induced inflow caused by the trailed vortex wake. The aerodynamic loading at the blade element can be then determined by using the known airfoil characteristics. Linearized unsteady aerodynamic modeling based on a indicial response formulation is often used to account for the unsteady effects. An extended lifting line theory (Weissinger-L [1]) based formulation is used to account for the 3-D finite-wing effects.

A CFD based approach calculates the aerodynamic loads by integrating the pressure distributions achieved on the rotor blade. The levels of refinement can

vary from a potential flow model (e.g. transonic small distrubance, full potential) to a complete Navier-Stokes simulation. In all the approaches, the governing equations, which are the fluid conservation laws, are numerically discretized and solved to achieve time accurate solutions of the flow variables.

The blade motions obtained from the structural analysis have to be incorporated in the CFD scheme. Most potential flow approaches do not actually deform the blade, but prescribe the effect of the deformations as so called 'partial angle of attack' distributions. The partial angles of attacks are calculated in the same fashion as the effective angles of attack in the lifting line analysis. But the effect of induced inflow contributed by the near wake (i.e., the downwash induced by the blade itself) is removed from the effective angle of attack. Hence, the approach is to use a better definition of the near wake flow field as computed by the CFD solver. The most sophisticated approach is to actually deform the CFD mesh such that it conforms to the rotor blade geometry at any time. This method requires modification of the numerical algorithm to strictly satisfy volume conservation in the moving meshes.

The interaction of the blade with the trailing vortex wake is an important aspect of the rotor aerodynamics. Hence, embedded in any aerodynamic analysis is an approach for determining the vortex wake definition. The simplest way is to use empirical induced inflow models. A more refined approach chooses a prescribed wake model whose geometry is known empirically. Alternatively, the wake can be computed using a Lagrangian vortex lattice method, which is often referred as a "Free Wake" analysis. The lifting line analysis is coupled then with a free wake solver to model the induced inflow effects. A full-fledged CFD analysis with a fine spatial discretization in regions of concentrated vorticity

can be used to directly capture the full vortex wake. But, such an approach is computationally intensive and still very impractical for routine analysis. Therefore, even the CFD solvers are often coupled with free wake analysis to include the trailed wake induced inflow. There are various methods that can be used to include the effect of the trailed vortex wake in to the CFD solver. Some of the commonly used ones are the perturbation method, surface transpiration and the field velocity approach. The perturbation method obtains the potential field solution because of the vortex wake and superposes it on the flow solution. The surface transpiration approach modifies the boundary conditions at the wall surface to include the effect of the wake, while the field velocity approach includes the induced velocities from the wake via apparent grid movement.

1.1.3   Integrating structural and aerodynamic analysis

The aerodynamic analysis and structural dynamic analysis have to be coupled to achieve a full aeroelastic solution. A tight coupling approach simultaneously integrates the structural and aerodynamic governing equations in time. The extended lifting line analysis, owing to its analytical simplicity, can be often integrated easily into such an analysis frame work. But it is quite involved to include CFD based aerodynamic modeling in the same fashion. Hence, CFD based analysis are often coupled externally to the structural dynamic model. The exchange of information (blade motions from structure and loads from aerodynamics) is often performed every rotor revolution. Another aspect of a rotor aeroelastic analysis is to obtain a trim solution for the whole aircraft. The trim solution ensures the force and moment balance about the center of gravity of the aircraft for steady flight conditions. Mathematically, the force and moment

balance equillibrium can be posed as a set of non-linear equations, which can be solved by Newton's method. Alternately, one can pose the whole system as an optimization problem and minimize the force and moment residuals.

1.2   Motivation

A comprehensive rotor aeroelastic analysis model which consistently gives accurate predictions of helicopter vibration still eludes researchers in the rotorcraft field. For example, in Fig 1.3 the predicted 4-per-revolution hub vibration for the Lynx helicopter from several state-of-the-art comprehensive rotor analysis codes are shown (from Ref [2]). Clearly, there is a large deviation in blade load predictions from different comprehensive codes. Also, all the predictions differ from the flight test measurement with over 50%. Bousman in his detailed review [3] of the state-of-the-art in rotorcraft vibration prediction identifies two key issues to be resolved for articulated rotors before one can perform comprehensive predictions for all flight conditions. They are: (1) inaccuracy of negative lift phase in high-speed forward flight, and (2) underprediction of blade pitching moments and hence the pitch link loads (Figure 1.4).

Various modeling refinements in both aerodynamics and structural dynamics were tested by numerous researchers in the past decade to resolve these problems (See Section 1.3.4). It appears from these research efforts that the accurate prediction of the blade torsional response is important for the accurate prediction of the lift phase. The underprediction of pitch link loads seem to be because of the inability of classical lifting line based analyses to predict section pitching moments accurately. Pitching moments are very sensitive to flow non-linearities
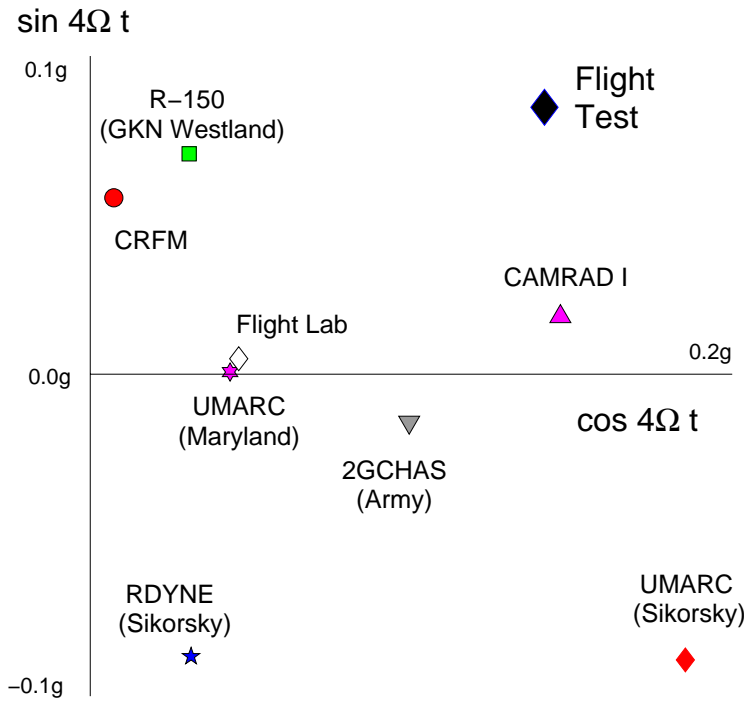
Figure 1.3: Predicted 4/rev hub vibration for the Lynx (airspeed=158 knots)

in the highly unsteady rotor environment. Also the inability to predict section pitching moments produces an inaccurate torsional response solution. It follows from these approaches that one might be able to get acceptable vibration prediction if the aerodynamic modeling was improved using a computational fluid dynamics (CFD) based model, which may provide much more refined results for both sectional lift and pitching moments.

There were a few research efforts in the past two decades (See Section 1.3.3) that replaced classical lifting line analysis with the CFD based modeling in the comprehensive analysis framework. Most of the research efforts used a "loose" coupling methodology (i.e., exchange of information between CFD and structural analysis only once every rotor revolution). However these approaches were limited in the extent that:
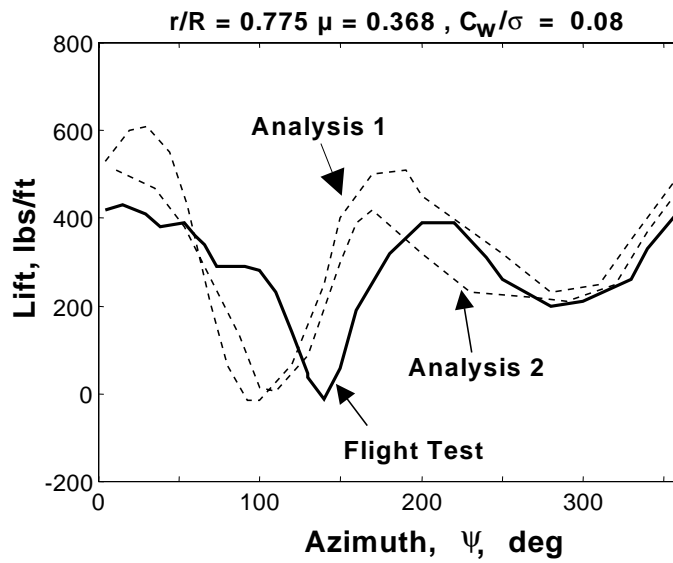
(a) Normal Force prediction for high speed flight
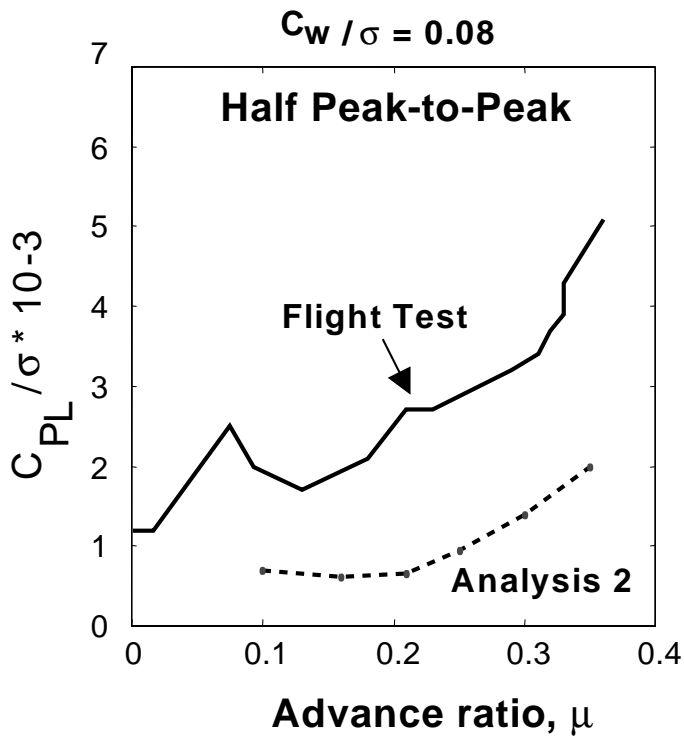
(b) Prediction of pitch link loads

Figure 1.4: Two major problems in rotorcraft aeroelastic analysis methods (Ref. [3])

1. They were able to couple only lift distributions obtained from CFD model in to the structural dynamic modeling. Torsional response divergence was noted when pitching moments were included.

2. In cases where pitching moments from CFD were used, they had to be included as an average of those predicted by lifting line theory and CFD model to aid convergence.

3. The blade motions were included in the CFD computations as "partial angle of attacks" rather than including the actual deformed blade surface geometry. For moderately large deformations, this approach would induce errors in the analysis.

4. The CFD models were limited by the use of potential flow based methods rather than Euler/Navier-Stokes solvers. In the highly unsteady rotor flow field with transonic Mach numbers, a potential flow assumption may lead to inaccuracies in load prediction.

Recently, there have been research efforts which replaced the loosely coupled approach with the so called "tight" coupling approach. In the tight coupling approach, equations representing the fluid conservation laws and structural dynamic response are integrated simultaneously. But the approach presents severe numerical challenges for ensuring trim states and periodic response solutions. Also, a comprehensive validation and identification of fundamental physical mechanisms have been limited in these efforts.

The motivation of this research work stems from the aforementioned problems in rotorcraft vibration prediction. The primary objective of this research effort is to develop and validate a time and grid independent CFD computation that can

give acceptable prediction of aerodynamic loads, so that it can be included in to a rotor aeroelastic analysis (overcoming limitations (3) and (4)). This will be followed by the reexamination of the loosely-coupled iteration scheme for coupling CFD and comprehensive rotor analyses (overcoming limitations (1) and (2)). Efforts will also be focussed on identifying the key physical phenomenon that causes the rotor vibrations. The strengths and limitations of CFD based aerodynamic model compared to the classical lifting line based analysis will also be evaluated.

1.3   Previous Work

The focus of this research work is in developing a CFD methodology for rotor problems that includes aeroelastic blade deformations. Historically, CFD methods were first used to replace lifting line theory in fixed wing aeroelasticity research. Therefore, a brief review of the use of CFD modeling for fixed wing aeroelastic problems is presented first. This is followed by a survey of different wake modeling techniques, which are an essential modeling difference between fixed wing and rotary wing problems. The various research efforts which coupled CFD codes with computational structural dynamics (CSD) analyses for rotary wing problems are reviewed next, followed by efforts that are focused more on validation and isolation of the potential modeling deficiencies.

1.3.1   Fixed wing aeroelasticity

The use of computational fluid dynamics for modeling transonic unsteady airfoil problems was initiated in the early 1970s. Among the most promising efforts

was the one by Magnus and Yosihara [4] who computed transonic flow over a NACA 64A410 airfoil by solving the Euler equations. They performed unsteady calculations for a step change in angle of attack, a step change in a pitching angular velocity and for harmonic oscillation about the airfoil mid chord for a range of reduced frequencies. They used the perturbation approach [5] to model the boundary conditions for unsteady motions. Thus, the mesh was unchanged with time, and the boundary condition for motion of the airfoil surface was modeled by modifying the velocity along the surface normal appropriately.

Ballhaus and Goorjian [6] constructed a scheme for unsteady transonic small disturbance equations in the place of Euler equations to model a similar problem of low frequency unsteady transonic flow around airfoils. They reported results consistent with those predicted by Magnus and Yosihara. Ballhaus and Goorjian [7] are also credited with, perhaps, the first CFD effort for solving an aeroelastic problem by simultaneous time-integration of the structural and flowfield equations. They compared predictions obtained from classical indicial methods and time-integration computations for oscillating airfoils and hence defined limits of applicability of the indicial methods. Also, they demonstrated that equations governing non-linear aerodynamics and structural motions can be integrated simultaneously to provide solutions to aerodynamic problems. This work formed the basis of further development of computational aeroelastic models to analyze wing flutter problems.

Guruswamy [8] pioneered the application of the simultaneous integration approach suggested by Ballahaus and Goorjian. The approach was first comprehensively validated for two dimensional problems with thin airfoils and later extended to three dimensional flutter problems for finite wings [9, 10]. These

CFD BASED MODELING

	time line →		
	1970	*1980*	*1990 - present*
Magnus and Yosihara *Ballhaus and Goorjian*	*Transonic flow* *over airfoils undergoing unsteady motion*		
Guruswamy et al.	*2-D transonic aeroelasticity, 3-D wing flutter analysis, 3-D full aircraft aeroelastic calculations* *Development of ENSAERO, general purpose aeroelasticity simulation package*		
Robinson, Batina and Yang *Cunningham, Batina and Bennet* *Lee-Rauch and Batina*		*3-D Euler/ Navier Stokes, with deforming meshes* *for analysis of wing flutter*	

REDUCED ORDER MODELING

Ballhaus and Goorjian	*2-D transonic flows using indicial method*		
Crouse and Leishman		*2-D transonic aeroelasticity using* *state-space approach*	
Dowell *Hall* *Wilcox et al.*		*Proper Orthogonal Decomposition Techniques (POD)* *Applied for 2-D airfoil, 3-D wing and turbomachinery problems*	

Figure 1.5: Pioneering works in fixed wing aeroelasticity

research efforts led to the development of an efficient general purpose aeroelastic code for aircraft problems called ENSAERO [11], which is widely used and has become an accepted standard for fixed wing aeroelasticity. Robinson, Batina and Yang [12, 13] modified a three-dimensional unsteady Euler/Navier-Stokes solver (CFL3D) to include a deforming mesh capability that makes the mesh continuously conform to the instantaneous shape of aeroelastically deforming wing surface. They followed the simultaneous time integration scheme to perform aeroelastic analysis of a 45 degree swept back wing with NACA 0012 cross section. A unique grid deformation scheme which models the computational mesh as a spring network was proposed. They also recognized the conservation problems which arise because of changing cell sizes in a deforming mesh and applied the necessary correction term in the flow solution algorithm. The aeroe-

lastic time marching scheme thus developed was later used to comprehensively perform linear stability analysis and hence the flutter boundaries of swept back wings [14].

The modern day trend in fixed-wing aeroelasticity looks in to developing reduced order models for non-linear aerodynamics to replace the computationally expensive CFD calculations. A time marching aeroelastic analysis with CFD based aerodynamics has the limitation that it is often difficult to extract the aerodynamic damping in the system directly. Hence, the determination of the stability boundaries often require a large amount of computations. An alternative simplified representation of the unsteady aerodynamic behavior that provides intuitive physical sense and hence a direct estimate of aerodynamic damping is very useful from a practical design point of view. Ballhaus and Goorjian in their initial work did use indicial response functions instead of direct CFD calculations. Crouse and Leishman [15] refined this approach and performed aeroelastic analysis for an airfoil with flapping and torsion degree of freedom using a generalized state-space approach. The unsteady aerodynamics was modeled using indicial response functions. The indicial response function was a combination of non-circulatory response and circulatory response. The non-circulatory or impulsive response were obtained from piston theory [16], while circulatory load response were obtained from CFD predictions in the frequency domain. The Proper Orthogonal Decomposition technique (POD) is the state-of-the-art now for extracting reduced order models. The basic idea behind this technique is to extract basis vectors which span the solution space from frequency domain solutions obtained using a higher order (often direct CFD) model. These basis vectors obtained are used to develop a model in the time domain, usually rep-

resented in a state-space form. Dowell [19, 20] and Hall [21, 22] in their several works developed mathematical formulations for extracting the basis vectors using eigen analysis from the higher order methods. Wilcox et al. [23, 24] recently applied these formulations to develop lower order aerodynamic models for aeroelastic control of turbomachinary. The technique developed is demonstrated for pitching and plunging motion of a single stage rotor under inviscid flow conditions. Applications of these methods for viscous three dimensional problems have not been reported yet and are much awaited.

The pioneering works in fixed wing aeroelasticity are summarized in Figure 1.5.

1.3.2 Fixed wing vs rotary wing

The main difference in a CFD analysis model for fixed wing and rotary wing is the wake modeling. Unlike the fixed wing case a rotor blade is always operating in the wake generated by vortices trailed by other blade/blades as well as from itself (Figure 1.6). This additional effect has to be carefully modeled to get a good estimate of sectional aerodynamic loads for a rotor blade. Finite volume and finite difference numerical schemes commonly employed in CFD models have inherent numerical dissipation present in them. This numerical dissipation causes the vortices in the flow field to diffuse at a faster rate than their physical diffusion rate. The numerical dissipation could be decreased by decreasing the cell sizes (i.e, using a finer mesh). However, the extent of mesh refinement is limited in practice as the computational complexity increases with the number of grid points. So, often one has to resort to alternative methods for including the vortex wake into the CFD calculations. Currently, there are three approaches

FIXED WING

Tip vortices

ROTARY WING

Relative wind

Tip vortices
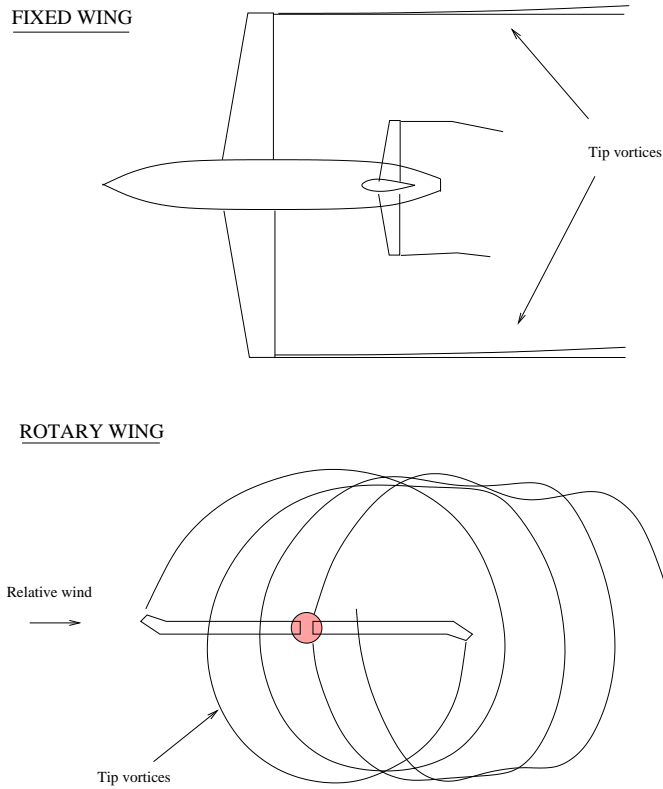
Figure 1.6: Trailed wake structures for fixed wing and rotary wing

mainly used for predicting the flowfield of a rotor using CFD methods. They
are:

Direct wake capturing: In this approach Euler/Navier Stokes equations are
solved with sufficient mesh resolution and clustering to minimize the dissipation
of the wake and hence maintain its integrity. This approach was initiated in
the 1980's for hovering rotors by Roberts and Murman [25] and investigated in
detail by Kramer et al. [26] and Chen and McCroskey [27].

Srinivasan et al. [28] proposed a novel approach using periodic boundary
conditions on a cylindrical mesh around a single blade for wake capturing. The
method was shown to be applicable even in cases were strong viscous effects

18
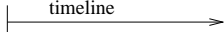
DIRECT WAKE CAPTURING	timeline →	
	1980	1990–present
Roberts and Murman Kramer et.al Chen and McCroskey	Wake capturing using grid clustering and higher order schemes	
Srinivasan et.al Wake and Baeder Tang and Baeder		Periodic boundary conditions on a cylindrical mesh using single blade geometry
Duque and Srinivasan Strawn and Duque Ahmad and Strawn		Overset mesh approach for wake capturing for multiblade simulations.

COUPLING CFD WITH FREE WAKE SOLUTIONS		
Ramachandran et. al Carradona and Tung	Surface transpiration boundary conditions for wake inclusion	
Tang and Baeder Srinivasan and McCroskey	Perturbation methods for wake inclusion	
Parameswaran and Baeder Khanna and Baeder Singh and Baeder Sitaraman and Baeder		Field velocity approach, which models the wake effects via apparent grid movement

Figure 1.7: Summary of wake inclusion techniques developed/applied in CFD

and shock separations were prevalent. They also showed good predictions for both hover performance and surface pressure distributions for the Caradonna and Tung [29] model rotor. Wake and Baeder [30] used this approach to validate hover performance of a Black Hawk model rotor blade. The solutions were found to improve with grid adaptation and higher order schemes by Tang and Baeder [39].

The present day approaches use chimera grids for wake capturing. In the chimera (overset) mesh approach, a boundary conforming mesh is used for the rotor blades and a background Cartesian mesh encompassing all the rotor blades to capture the trailed wake. Information is exchanged with the various meshes at

each time step using carefully tailored interpolation techniques. Srinivasan and Duque [32] were the first to investigate overset grid approaches to model the hovering flow field. Strawn et al. [33] further refined and applied this approach for rotor aerodynamics and aeroacoustics computations. Ahmad and Strawn [34], on a follow-up work, comprehensively investigated grid independence of solutions obtained using such multiple mesh based approaches. They found that the solution is fairly grid dependent and concluded that the grid independence of the wake capturing methodology needs to be rigorously established to ensure the accuracy and credibility of the CFD solutions. Pomin and Wagner [35] also recently used the overset mesh approach for studying hovering and non-lifting forward flight conditions. For the hover calculations they also performed an aeroelastic analysis by simultaneously integrating the rotor structural equations with the flow solutions.

Coupling free wake solutions and CFD: In these methodologies the wake geometry is obtained using a Lagrangian based free vortex wake solution. The free wake models use the principle of vorticity transport to solve for the wake geometry. The vortex filaments are allowed to convect with the self and mutually induced velocities until a force free wake state is obtained. For steady flight cases the wake geometry is periodic at the rotor frequency. Hence, solutions for such cases can be obtained using a relaxation approach. The Pseudo-Implicit Predictor-Corrector (PIPC) method by Bagai and Leishman [36] is one method to determine the wake geometry prediction for steady flight cases. Although in cases where the wake is aperiodic (i.e., for maneuvering flight and flight conditions with multiple rotors) the wake geometry has to be found by time integra-

tion. The stability, convergence and accuracy of such a numerical scheme needs to be rigorously investigated before it can be routinely applied. Bhagwat and Leishman [37] have recently developed numerical schemes for time accurate free wake calculations. They applied the methodology developed for maneuvering flight conditions and reported good correlation of the predicted wake geometry with flight test observations. This methodology has been incorporated in to numerous comprehensive rotor aeroelastic analyses.

Coupling the flow solvers with an externally generated wake geometry is achieved commonly using three approaches, namely: (1) the perturbation approach, (2) the surface transpiration approach, and (3) the field velocity approach. In the perturbation approach, the flowfield is decomposed into two parts despite nonlinearity. The first is a prescribed vortical disturbance known to satisfy the governing equations in the absence of solid surfaces, and the second is obtained from the solution of the governing equations [5, 38]. As a result, the vortex structure is free of numerical diffusion. For a simple 2-D vortex or an infinite line vortex the induced pressure and density fields can be determined by solving a simple 2-D normal momentum equation analytically. This approach has been used extensively in studying airfoil vortex interaction (AVI) problems [39]. However, it is unclear how to extend this approach for the curved vortex filaments that represent the actual helicopter wake, because exact analytical solutions cannot be determined for the vortex induced pressure and density fields.

The second approach, which is the surface transpiration approach, is the most commonly used approach for coupling the free wake solutions. The effect of the vortex wake is included in to the CFD computations through a surface

transpiration boundary condition at the blade surfaces. The Biot-Savart law is used to obtain the wake induced velocities at the blade surface grid points. The boundary conditions at the wall are subsequently modified to include the effect of these induced velocities. For an Euler or full potential calculation (when no boundary layer needs to be modeled) the velocity at the blade surface can be non-zero. For such inviscid calculations, the normal flux boundary conditions at the blade surface is modified. The velocity normal to the surface is then calculated such that it exactly cancels the effect of the wake induced velocity normal to the surface. This method is equivalent to modeling the effect of the wake using an equivalent angle of attack. This methodology cannot be directly extended for viscous (i.e., Navier-Stokes) based simulations as a no-slip boundary condition has to be imposed at the wall. The wake effect is mostly included in such computations by explicitly modifying the blade section angle of attack using the wake induced velocities. References [40] to [41] use this approach for prediction of unsteady rotor aerodynamic loads.

The third method used is called the field velocity or the grid velocity approach. The wake induced effects are modeled by an apparent grid movement. The vortex wake generates a non-uniform induced velocity distribution over the entire flow field. Therefore, the vortex wake effect can be thought of as modifying the velocities along all three coordinate axis directions instantaneously. This is similar to the indicial response problem [42].

For instance, the indicial response to a step change in angle of attack can be modeled by incorporating a step change in vertical grid velocity (i.e. create an apparent movement for the grid in the vertical direction by modifying the grid time metrics). Using the same idea, the vortex wake induced effects can be mod-

eled by modifying the time metrics at each grid point using the wake induced velocities. This does require the additional computational expense of calculating the induced velocities at all the mesh points at every time step. The field velocity approach lies between the perturbation and surface transpiration methods in terms of complexity. However, it is far superior in robustness and range of applicability compared to the other two approaches. The field velocity approach for indicial calculations was proposed by Parameswaran and Baeder [42], and comprehensively applied to study indicial responses of finite wings by Singh and Baeder [43]. This method was introduced for coupled free wake-CFD computations by Khanna and Baeder [44], who performed coupled hover computations. Recent works by Sitaraman [45] and Boisard [46] extended this approach to study more complex BVI problems in low speed forward flight. This approach is chosen for wake inclusion in this dissertation because it was found to be the most reliable and sufficiently accurate method for the inclusion of the vortex wake induced effects.

Vorticity confinement/embedding methods: The vorticity confinement technique proposed by Steinhoff et al. [47] is a novel approach born out of the motivation to mitigate the effects of the inherent diffusion in numerical schemes for the Euler and Navier-Stokes equations. In essence, the method can be looked upon as a way to add an anti-diffusive term to the discretized form of conservation equations without affecting stability. It is normally incorporated into a solver as source terms on the right hand side of the momentum and energy equations.

The vorticity embedding technique is another way of including additional

vorticity into the numerical scheme. This model does not formulate the solution at the vortical regions using partial differential equations. The locations of the vortical regions are determined by tracing irrotational stream lines on the mean flow, and assuming the vortical regions lie in between them. The vortical strength is determined by solving difference equations. The actual variation of the velocity in the vortical region could be prescribed using known empirical models. This method differs from the direct wake capturing schemes in the sense that the latter uses solution of hyperbolic conservation laws formulated in the strong (PDE) form for solving the vortex structure. Also, compared to the prescribed wake methods, the wake system is solved for directly in this methodology rather than being specified from an external calculation. However, the internal structure of the vortical regions also needs to be modeled in this case.

The vorticity confinement/embedding approach has gained interest in the recent past among rotorcraft researchers and has been used as a wake capturing methodology. Steinhoff and Ramachandran [48, 49] applied this methodology for predicting free wake structures for two bladed and four bladed rotors and real helicopter geometries with rotor and fuselage. Unfortunately, the validations of the aerodynamic loads obtained have been limited in these approaches. Bridgeman et al. [50] modified the FPR code [51] to include vorticity embedding into its modified version, the FPX code. The FPX code was used as the aerodynamic model for rotorcraft aeroelastic analysis by Lee et al. [52]. Recently, Bridgeman and Dietz [53] used the vorticity confinement approach to perform an aeroelastic analysis of an airfoil undergoing dynamic stall. They used the simultaneous time integration approach of a two degree of freedom structural dynamic system along with the flow conservation equations.

The various wake modeling/inclusion techniques discussed in this section are summarized in Fig 1.7.

1.3.3 CFD coupling into comprehensive rotorcraft analysis

Historically, there have been two ways researchers have tried to couple CFD based aerodynamics into rotor structural analysis. The first method, often referred to as *loose coupling*, involves transfer of information between the structural dynamic analysis and CFD analysis every rotor revolution. The second method, which is the *tight coupling* approach, uses the simultaneous time integration of both structural dynamic and fluid dynamic equations. In essence, there is transfer of information between both analyses at every time step. The loose coupling method has the inherent advantage that a trim solution can be also achieved along with the convergence of structural dynamic response. But, because some of the frequencies of interest in the rotor system are much larger than the rotor rotational frequency (which is the same as the frequency of information exchange), often the credibility of the vibration predictions by this approach is suspect. The tight coupling is a more rigorous aeroelastic analysis from a fundamental point of view, however, the practicality of the approach is limited because of the inherent numerical challenges of ensuring both trim state and a periodic response solution.

One of the earliest successful efforts which used the loose coupling approach was by Tung and Caradonna [54] who coupled the comprehensive rotor analysis code CAMRAD [55] to FDR [51], a transonic small disturbance finite difference code. The procedure used CAMRAD aerodynamic formulation of lifting line

Loose Coupling (transfer of data between CFD and structure every rotor revolution)

Tung & Caradonna (1986)	FDR & CAMRAD	1/7 OLS, DNW	C_l, partial α
Strawn & Tung (1986, 1987)	FPR & CAMRAD	Gazelle	C_l, partial α
Yamauchi & Heffernan (1988)	FPR & CAMRAD	Gazelle	C_l, partial α
Strawn et al.(1989)	FPR & CAMRAD	PUMA	C_l, partial α
Strawn and Bridgeman (1991)	FPR & CAMRAD	PUMA	C_l, C_m, α_p
Kim, Desopper & Chopra (1991)	TSD & UMARC	Gazelle	C_l, C_m, α_p

Limitations: Use of partial angle of attacks, divergence when lift and pitching
moments are simultaneously coupled

Tight Coupling (transfer of data between CFD and structure every time step)

Bauchau and Ahmad (1996)	OVERFLOW & DYMORE	UH-60A	Wake
Lee, Saberi and Ormiston(1997)	FPX & 2GCHAS	UH-60A, PUMA	capturing and
Altmikus & Wagner (2000)	INROT & DYNROT	Hughes 500	deforming
Pomin & Wagner (2001, 2002)	INROT & DYNROT	ONERA, 7A	mesh

Limitations: Numerical challenges in obtaining simultaneous trim and response
convergence solutions

Figure 1.8: Summary of research efforts which coupled CFD to comprehensive
analsysis

theory, discrete vortex wake, and tabulated airfoil data to calculate airloads
except for substitution of FDR calculated blade lift (not pitching moment) within
a specified region on the advancing blade side of the rotor disc. The blade
motion information and far wake information from CAMRAD was provided to
FDR using the so called "partial angle of attack" method. The partial angle
of attacks were calculated from CAMRAD by modifying the effective angle of
attack at the blade sections excluding all the inflow contributions caused by the
near wake (i.e., the part of the free wake geometry contained inside the CFD
mesh boundaries). The Full Potential Rotor code (FPR) was the successor to
the FDR code. Strawn and Tung [56, 57] used the FPR code and improved the
coupling approach by extending the computational region to the full 360 degrees
of azimuth rather than just at advancing blade azimuths. Also, the coupling

between the codes was automated to run on a single machine.

The loose-coupled iteration FPR/CAMRAD iteration scheme was further applied to predict airloads on the AS-330 PUMA helicopter configuration by Strawn et al. [58]. The correlation between predicted and measured aerodynamic loads did not show significant improvement, even with the FPR based advanced aerodynamic modeling. Strawn and Bridgeman later extended this analysis by adding contributions of the pitch rate and lead-lag blade motions in the boundary conditions of FPR. They also for the first time tried to couple both FPR calculated lift and pitching moment into the comprehensive analysis. But they noted significant convergence problems when lift and pitching moments were simultaneously coupled into the comprehensive analysis, and suggested that the loose coupling procedure might be inadequate when pitching moments/torsional dynamics were included. There were other investigations contemporary to these efforts which also followed the similar methodology. Yamauchi et al. [60] used a similar approach (i.e., FPR/CAMRAD) to predict structural bending and aerodynamic loads on an advanced geometry rotor blade of a SA349/2 Gazelle helicopter and showed good correlation with flight test data. Kim et al. [61] improved the iteration scheme by coupling both the lift and pitching moment obtained from the CFD computations. They coupled a transonic small distrubance (TSD) code with UMARC. However, they also noted convergence issues when both lift and pitching moment were simultaneously coupled. Therefore, the approach was modified by including the pitching moments only at a later stage of the iteration scheme to ensure convergence.

The research efforts on developing a tightly coupled approach was initiated by Bauchau and Ahmad [62] who coupled an overset mesh based CFD solver

(OVERFLOW [63]) and a multibody dynamics code (DYMORE [64]). Results were obtained for a four-bladed UH-60A rotor in forward flight and compared with flight test measurements. At each time step the coupling procedure used the CFD aerodynamic forcing as input excitation for the structural dynamic analysis and then used the blade dynamics computed as input for predicting the aerodynamic forcing. The CFD analysis using OVERFLOW includes direct wake capturing and hence no external inputs of the wake geometry were needed. A trim analysis could not be performed in such a coupling frame work. Hence, using experimentally measured rotor trim control inputs, the blade lift and moment results were compared with flight test data. The results showed similar trends to test data, although there were significant differences in the mean values and even the higher frequency components.

Recently there were additional research efforts focussed on a tightly coupled scheme, where the structural dynamics and fluid dynamics governing equations are integrated simultaneously rather than per revolution. Lee et al. [52] have conducted one of the most comprehensive research effort of tightly coupling CFD and CSD methodologies. They coupled the FPX [50] code with 2GCHAS [65], and analyzed the UH-60A and PUMA helicopter rotor configurations. The boundary conditions for FPX used a combination of actual grid motions and surface transpiration to represent the aeroelastic response calculated by 2GCHAS. Initial solutions were unstable because of inaccurate calculation of the pitching moments, which lead to the presence of negative aerodynamic damping from the CFD moments. Ultimately a finer temporal resolution was used, and convergence of the response was obtained for the PUMA case. Unfortunately, substantial computational resources were found to be required, even for the full-potential

formulations in this case.

Buchtala et al. [66] investigated a staggered time marching scheme for fluid structure coupling for an ONERA 7A model rotor. They indicated good correlation of the chordwise pressure data with the experimental results. Beumier [67] studied helicopter rotor performance in hover using a Reynolds Averaged Navier-Stokes based aerodynamic modeling. The aero-elastic effects were coupled by prescribing the deformations to the grid. Because this was a hover case, the blade deformation was assumed to remain unchanged with azimuth. This work primarily focussed on the accuracy of the flow solvers themselves rather than the coupling scheme. Altmikus and Wagner [68] provided a comprehensive report on the accuracy of tightly coupled schemes for aeroelastic simulations. Pomin and Wagner [35] used these coupling schemes to analyze helicopter rotor performance in hover and forward flight using chimera grids for wake capturing. Overall, the tightly coupled approaches showed considerable success, but they were performed for prescribed control angles and so did not ensure the simultaneous convergence of trim and blade response solutions. A trim solution could be achieved by changing the control angles (collective and cyclic) to produce enough rotor aerodynamic loading (averaged per revolution) that would ensure both force and moment balance in all three directions. A tightly coupled approach poses severe numerical challenges in ensuring such a trim solution as part of the analysis.

Berkman et al. [69] developed the hybrid Navier-Stokes/Full potential methodology for predicting three dimensional unsteady flows over multibladed rotors in hover and forward flight. The flow solution was divided in to three zones in this analysis consisting of an inner zone where Navier-Stokes equations were solved,

a potential flow region which carries the acoustic and pressure waves generated by the rotor to far field, and a Lagrangean scheme for capturing the vorticity that leaves the viscous region and convecting it away to the far field. Yang et al. [70] coupled this hybrid Navier-Stokes/full potential methodology to a structural analysis model for predicting rotor unsteady airloads. The coupling methodology followed an open loop approach (i.e., the predicted aerodynamic loads from CFD were not passed back to the structural analysis) in which the measured elastic deformation and control angles based on a wind tunnel trim was supplied to the CFD analysis. Dynamically deforming meshes were used to prescribe the elastic deformation to the CFD analysis. Fair agreement with flight test data for the case of a four blade rotor in forward flight was reported in this effort.

The summary of all the key CFD coupling research efforts that were discussed in this section is presented in Figure 1.8.

1.3.4 Comprehensive validation and isolation of modeling deficiencies

The coupled nature of rotorcraft aeromechanics problems makes it one of the most difficult problems for detecting modeling deficiencies. There have been some research efforts in the past which tried to isolate the modeling deficiencies in structural and aerodynamic modeling.

Bousman et al. [71] provided the most comprehensive evaluation of lifting line and CFD methods by correlating the predictions with the flight test data of the Puma helicopter. For the Puma flight test case, most of the methods produced good correlation with measured aerodynamics loads (good for normal forces,

fair for pitching moments). Yet recent validation with the full scale UH-60A flight test data performed by Lim et al. [72] showed poor to fair correlation of predicted blade aerodynamic loads with flight test data. Bousman [3] addresses this issue in his comprehensive review of problems in rotor aeromechanics. Two unsolved problems, namely, phase of negative lift on the advancing side in high speed forward flight and underprediction of pitching moments and hence the pitch link loads, were identified as the primary problems rotorcraft researchers need to address before one could resort to comprehensive validation.

Torok et al. [75] validated the structural dynamic model by using measured aerodynamic loads obtained from the UH-60A model rotor tests conducted by Lorber et al. [76] as input to the structural dynamic analysis. They were able to obtain good correlation of flap bending loads with measured data. The torsion moment correlation was found to be fair. Overall, it was concluded that the structural dynamic models are in general capable of predicting sufficiently accurate flap dynamics if accurate aerodynamic loads are provided, whereas torsion dynamics needed refinement.

Bousman [73] showed that the advancing blade negative lift character is similar for both model and full scale helicopter and therefore seems to be a fundamental phenomenon independent of specific hub configurations (e.g., for hubs with dampers, bifilar pendulum vibrations absorbers etc). Datta and Chopra [74] showed by frequency separation that the lift phase problems stems from inaccurate vibratory lift prediction in the advancing side of the rotor disk. The advancing side lift was also shown to be affected mostly by elastic torsional deformations, unlike the low speed case where it is primarily affected by the trailed vortex wake. However, an inconsistency was noted between the phase errors in

pitching moment and lift indicating that elastic torsion may not be the only contributing component of the error in the lift phase.

Torok and Berzin [77] in the follow up work evaluated different aerodynamic and wake methodologies, including CFD based (FPR) modeling. They used the measured aeroelastic deflections as input to the aerodynamic methodologies and correlated the predictions with measured aerodynamic loads. It was found that the measured torsional deformation was a significant contributor for the accurate prediction of both magnitude and phase of the aerodynamic loads. Good correlations were noted between the surface pressure measurements and the pressure coefficients evaluated by FPR models.

Lee et al. [52] performed one of the most comprehensive tight coupling approaches also identified that the inaccurate prediction of pitching moments by CFD codes was one of the primary reasons for torsional response divergence. Earlier, loose-coupling efforts with full-potential CFD codes had identified this divergence as a numerical robustness problem.

1.4 Objectives

The main objectives of this dissertation are framed in a way such that the procedures developed and knowledge gained from this work would serve as a platform for improved vibration prediction.

- *Develop grid and time independent solutions to unsteady aerodynamic loads using Navier-Stokes based CFD calculations:* An existing Navier-Stokes solver was extensively modified to consistently incorporate the aeroelastic blade motions and effects of the trailed vortex wake. The method was

formulated in a way such that it strictly satisfies the conservation laws. Grid and time step independence studies were performed for different flight conditions and differing mesh geometries. Performance enhancement techniques were incorporated to improve the practicality of conducting simulations in a routine basis.

- *Validation of the CFD model developed:* The validation of the CFD model was performed in a step-by-step manner. The 2-D predictions for airfoils were validated first for a range of Mach numbers and angle of attacks. This was followed by validation of the procedures used to include aeroelastic deformations and the trailed vortex wake. Complete validation of the unsteady aerodynamic loads (lift and pitching moment) were also performed on a flight test case with prescribed deformations and blade pitch controls.

- *Improve coupling of the CFD model with structural analysis:* The loose coupling approach between CFD and comprehensive rotor analysis was evaluated and improved using the higher fidelity CFD model. The improvements in vibration prediction from the baseline comprehensive analysis were identified and emphasized.

- *Investigate the physics of rotor vibrations:* The CFD model developed was used as a tool to identify the fundamental mechanisms of rotor vibrations. The insights gained were used to identify key modeling deficiencies of the lifting line based aerodynamic models. The feasibility of applying corrections to the lifting line models to improve their prediction capabilities are also investigated.

1.5   Organization of the Thesis

This thesis emphasizes the development of a CFD model for better rotor vibration prediction. It uses the standard organization format, which follows an introduction, methodology, validation, key results and conclusion chapters, in that order.

The methodology chapter describes the formulation of the Euler/Navier-Stokes solver, which in principle is capable of accurately and robustly incorporating aeroelastic deformations and effects of an external vortex field. The structural dynamic model used in a comprehensive rotor analysis model is also briefly described. The extended lifting line model, which is used as the baseline for evaluating the improved prediction capabilities of the CFD model developed, is also presented.

The comprehensive validation of the methodology developed is presented in the third chapter. The validation of the numerical schemes developed is conducted for a range of problems including 2-D model problems and actual helicopter flight problems. The feasibility of coupling the CFD model and structural dynamic analysis is investigated. A simplified structural dynamic analysis is used in this context to reduce the complexity of the problem.

The investigations conducted to isolate key contributors to rotor vibration are presented in Chapter 4. The CFD model is used as a tool to conduct an investigation on major effects of different physical phenomena (transonic effects, viscous effects, three dimensional effects, etc.). The knowledge gathered from this investigation will be useful for understanding the limitations and perhaps enhancing the prediction capabilities of the lifting line analysis.

Chapter 5 presents the results of the coupling process developed between

the CFD model and comprehensive rotor analysis. The convergence issues in the full coupling approach and procedures developed to maintain robustness are described. The improvements in the prediction of rotor vibratory loads compared to the baseline comprehensive analysis is also presented.

Conclusions and observations noted during the development, validation and application of the methodologies developed are summarized in the final chapter.

1.6   Scope of the Thesis

The research work conducted in this thesis forms an important stepping stone in the direction of the development of low vibration rotor systems. The analysis developed shows improved vibration prediction capabilities compared to existing comprehensive rotor aeroelastic analyses. The methodology developed could be used as a tool for analyzing advanced rotor systems. A high fidelity analytical model minimizes the requirements for scaled rotor testing, that may help reduce the associated development and production costs. Also, it encourages designers to probe more innovative configurations within the usual financial constraints of design analyses.

Specifically, the contributions of the thesis are the following:

1. Development of a methodology for incorporating deforming mesh algorithms in a CFD solver.

2. Inclusion of the external velocity field (e.g., because of the trailed vortex wake) into the unsteady flow computations.

3. Consistent coupling of a structural model with the CFD analysis.

4. Identification of the key physical contributors to rotor vibration.

It is noteworthy that although the development of the CFD scheme is mainly driven by rotor applications, the methodologies are valid for any three dimensional unsteady Navier-Stokes analysis. The procedure developed can be incorporated into any finite volume based Navier-Stokes solver, and extended to other diverse applications that require modeling of unsteady flows.

Chapter 2

Methodology

2.1 Introduction

This chapter describes the overall methodology used in this dissertation. The methodology can be broadly divided into the development of an aerodynamic prediction method, a structural dynamic analysis and the approaches used for performing fluid-structure coupling. The aerodynamic prediction analysis is further divided into a Computational Fluid Dynamics based (CFD) approach and a modified lifting line analysis.

The CFD approach involves modeling rotor blades undergoing elastic deformations and interacting with vortex wakes. The governing equations are the conservations laws of fluid motion. The resulting partial differential equations are discretized and solved using a finite volume approach. Special modification, rigorously satisfying the *Geometric Conservation Laws*, is required for modeling aeroelastically deforming rotor blades. Also, the effects of the vortex wake are included using the so called *Field Velocity Approach* which requires a modification of the grid time metrics. The inclusion of the vortex wake using this approach of-

ten increases the computational complexity of the numerical scheme by an order or magnitude. Hence, performance enhancement techniques that use hierarchical data processing need to be investigated to make the simulations practical. The detailed mathematical derivation of the performance enhancement techniques is presented in Appendix A.

The extended lifting line aerodynamic analysis is developed primarily to understand the strengths and limitations of the CFD based approach. The method uses airfoil lift, drag and pitching moment characteristics constructed using experimental data for obtaining the steady aerodynamic load coefficients. The unsteady aerodynamic loadings are accounted for, using a linear superposition of time domain based indicial response models. Indicial response models (e.g., Leishman-Beddoes [78]) and those developed for the specific airfoils of study are implemented. A Weissinger-L based extended lifting line theory, which can model the effects of blade sweep and taper, is used to account for the finiteness of the rotor blade. This aerodynamic analysis methodology is typical of those used in comrehensive rotor aeroelastic analysis codes.

The structural dynamic analysis involves the calculation of the rotor pitch controls, vehicle orientation, and blade response such that the vehicle trim equations and the blade coupled periodic non-linear response equations are simultaneously satisfied. The satisfaction of vehicle trim equations imply that the resultant forces and moments on the vehicle, averaged over one rotor revolution, becomes zero. A simplified rotor structural model which consists only of flap and torsion degree of freedom is developed initially to test the feasibility of loosely coupling CFD based aerodynamics with structural dynamics analysis. Later on, a more advanced structural analysis, which accounts for all the degrees of free-

dom and non-linear elastic couplings is used. A finite element based approach that can accurately model the kinematic and elastic behavior of a rotating blade is chosen for analyzing both articulated and hingeless rotors. In the simplified analysis, the blade is modeled as a slender beam undergoing flap bending and torsional deformations. The blade equations are transformed into normal mode space first, and then the resulting ordinary differential equations are solved using a temporal finite element method. The temporal finite element method has proven to be robust and efficient to solve blade nonlinear response.

2.2 Fluid Dynamic Modeling

The governing equations for the fluid modeling in this work are the three dimensional Navier-Stokes equations, which are numerically discretized and solved with necessary boundary conditions for the specified geometry.

2.2.1 Navier-Stokes equations

The Navier-Stokes equations are the fundamental partial differential equations which describe the flow of compressible fluids. They represent the conservation of mass, momentum and energy. The strong conservation-law form of the Navier-Stokes equations in Cartesian coordinates can be written as [79]:

$$\frac{\partial q}{\partial t} + \frac{\partial f}{\partial x} + \frac{\partial g}{\partial y} + \frac{\partial h}{\partial z} = \frac{\partial \sigma}{\partial x} + \frac{\partial \theta}{\partial y} + \frac{\partial \omega}{\partial z} + \hat{R} \tag{2.1}$$

Where the state vector q and the inviscid flux vectors f, g and h are defined as

$$q = \begin{Bmatrix} \rho \\ \rho u \\ \rho v \\ \rho w \\ \rho E \end{Bmatrix} \qquad (2.2)$$

$$f = \begin{Bmatrix} \rho u \\ \rho u^2 + p \\ \rho u v \\ \rho u w \\ \rho u H \end{Bmatrix} \qquad (2.3)$$

$$g = \begin{Bmatrix} \rho v \\ \rho v u \\ \rho v^2 + p \\ \rho v w \\ \rho v H \end{Bmatrix} \qquad (2.4)$$

$$h = \begin{Bmatrix} \rho w \\ \rho w u \\ \rho v u \\ \rho w^2 + p \\ \rho w H \end{Bmatrix} \qquad (2.5)$$

Where u, v, w are the velocity components in the coordinate directions x, y, z, ρ is the density, p is the pressure, e the specific internal energy and σ, θ, ω represent the viscous stress and work terms for each coordinate direction, respectively. The

term $\hat{R}$ represents the source terms that have to be included to account for the centrifugal and Coriolis accelerations if the equations are formulated in a non-inertial frame of reference. The total energy E and enthalpy H are given by the equations

$$E = e + \frac{u^2 + v^2 + w^2}{2} \tag{2.6}$$

$$H = e + \frac{p}{\rho} \tag{2.7}$$

Transformation to generalized curvilinear coordinates

The governing equations can be expressed in strong conservation law form in generalized body-conforming curvilinear coordinate system with the aid of the chain rule of partial derivatives. In effect, the equations after being transformed to the the computational coordinates ξ, η, ξ are as follows:

$$\frac{\partial \hat{q}}{\partial \tau} + \frac{\partial \hat{f}}{\partial \xi} + \frac{\partial \hat{g}}{\partial \eta} + \frac{\partial \hat{h}}{\partial \zeta} = \frac{1}{Re}\left(\frac{\partial \hat{\sigma}}{\partial \xi} + \frac{\partial \hat{\theta}}{\partial \eta} + \frac{\partial \omega}{\partial \zeta}\right) + \hat{R} \tag{2.8}$$

where, the normalized inviscid fluxes are given by

$$\begin{aligned}
\hat{q} &= Jq \\
\hat{f} &= \hat{\xi}_t q + \hat{\xi}_x f + \hat{\xi}_y g + \hat{\xi}_z h \\
\hat{g} &= \hat{\eta}_t q + \hat{\eta}_x f + \hat{\eta}_y g + \hat{\eta}_z h \\
\hat{h} &= \hat{\zeta}_t q + \hat{\zeta}_x f + \hat{\zeta}_y g + \hat{\zeta}_z h
\end{aligned} \tag{2.9}$$

and the normalized viscous fluxes are given by

$$\hat{\sigma} = \hat{\xi}_x \sigma + \hat{\xi}_y \theta + \hat{\xi}_z \omega$$

$$\hat{\theta} = \hat{\eta}_x \sigma + \hat{\eta}_y \theta + \hat{\eta}_z \omega \tag{2.10}$$

$$\hat{\omega} = \hat{\zeta}_x \sigma + \hat{\zeta}_y \theta + \hat{\zeta}_z \omega$$

Here terms of the form $\hat{\xi}_{x,y,z}$, $\hat{\eta}_{x,y,z}$ and $\hat{\zeta}_{x,y,z}$ are the space metrics, $\hat{\xi}_t$, $\hat{\eta}_t$ and $\hat{\zeta}_t$ are the time metrics in the computational domain, and J is the Jacobian of the inverse coordinate transformation (i.e., $J = \det(\frac{\partial(x,y,z)}{\partial(\xi,\eta,\zeta)})$).

Thin-layer approximation

The flow fields encountered in helicopter flows are often inertia dominated. The viscous effects are concentrated in the boundary layer and in the wake in such high Reynolds number flows. These regions are generally smaller compared to the complete flow field. The order-of-magnitude estimates used to derive the boundary-layer equations show that the streamwise viscous terms are negligible compared to the other terms in the Navier-Stokes equations. Thus, one can drop the streamwise viscous terms. This eliminates the cross derivatives in the normalized viscous fluxes and so simplifies the numerical discretization. There are three conditions necessary for the thin-layer approximation to be valid. These are:

1. Body surfaces are mapped onto coordinate surfaces and wakes are mapped onto parallel surfaces in the computational space. Therefore, for slender beam structures, like wings and rotor blades, a "C" type mesh is appropriate at each spanwise section with the ζ=constant surface mapped on the body surface.

2. Grid lines must be clustered to the surface and in the wake, and must be close to orthogonal to each other.

3. Viscous derivatives in streamwise (ξ,η) direction are small and therefore can be neglected. The viscous derivatives are retained only in the normal (ζ) direction.

The non-dimensionalized thin-layer Navier-Stokes equations in computational space can be written as

$$\frac{\partial \hat{q}}{\partial \tau} + \frac{\partial \hat{f}}{\partial \xi} + \frac{\partial \hat{g}}{\partial \eta} + \frac{\partial \hat{h}}{\partial \zeta} = \frac{1}{Re}\frac{\partial \hat{S}}{\partial \zeta} + \hat{R} \tag{2.11}$$

where the viscous flux vector $\hat{S}$ is given by:

$$\hat{S} = \left\{ \begin{array}{c} 0 \\ \mu m_1 u_\zeta + \frac{\mu}{3}m_2\hat{\zeta}_x \\ \mu m_1 v_\zeta + \frac{\mu}{3}m_2\hat{\zeta}_y \\ \mu m_1 w_\zeta + \frac{\mu}{3}m_2\hat{\zeta}_z \\ \mu m_1 m_3 + \frac{\mu}{3}(\hat{\zeta}_x u + \hat{\zeta}_y v + \hat{\zeta}_z w) \end{array} \right\} \tag{2.12}$$

with

$$m_1 = \hat{\zeta}_x^2 + \hat{\zeta}_y^2 + \hat{\zeta}_z^2$$
$$m_2 = \hat{\zeta}_x u_\zeta + \hat{\zeta}_y v_\zeta + \hat{\zeta}_z w_\zeta \tag{2.13}$$
$$m_3 = \tfrac{1}{2}(u^2 + v^2 + w^2)_\zeta + \tfrac{1}{Pr(\gamma-1)}(a^2)_\zeta$$

Equation 2.11 is the simplified partial differential equation form of the fluid conservation laws that is discretized and integrated in time to obtain time accurate solutions of the flow variables used for this work.

2.2.2 Numerical algorithm

The baseline flow solver is the Transonic Unsteady Rotor Navier-Stokes (TURNS) research code which has been applied to a variety of helicopter rotor problems [28, 80, 81]. The inviscid fluxes are evaluated using a finite volume upwind numerical algorithm. The upwind biased flux-difference scheme used is that proposed by Roe [82] and later extended to three-dimensional conservation laws by Vatsa et al. [83]. The use of upwinding eliminates the addition of explicit numerical dissipation, which is often required in central difference schemes. Upwind schemes have been demonstrated to produce less dissipative numerical solutions compared to their central difference counterparts [83]. First order schemes have unrealistic mesh discretization requirements. Therefore, the Van Leer [84] Monotone Upstream-Centered Scheme for Conservation Laws (MUSCL) approach is used to obtain higher order accuracy. Appropriate flux limiting is used to make the scheme total variation diminishing (TVD). The Lower-Upper-Symmetric Gauss-Seidel (LU-SGS) scheme, suggested by Jameson and Yoon [86, 87] is used as the implicit operator.

The space discretized form of the differential in Eq 2.11 at any computational node (j, k, l) is

$$\partial_\tau \hat{q} = -\frac{\hat{f}_{j+\frac{1}{2}} - \hat{f}_{j-\frac{1}{2}}}{\Delta \xi} - \frac{\hat{g}_{k+\frac{1}{2}} - \hat{g}_{k-\frac{1}{2}}}{\Delta \eta} - \frac{\hat{h}_{l+\frac{1}{2}} - \hat{h}_{l-\frac{1}{2}}}{\Delta \zeta} + \frac{1}{Re} \frac{\hat{s}_{l+\frac{1}{2}} - \hat{s}_{l-\frac{1}{2}}}{\Delta \zeta} \quad (2.14)$$

Here j, k and l correspond to the coordinate directions ξ, η and ζ. Roe's [82] upwinding is performed in a locally one-dimensional manner along the coordinate directions. The fluxes at the half points can be written (e.g., in the ξ direction), as

$$\hat{f}\left[q_L, q_R, \left(\tfrac{\Delta\xi}{J}\right)_{j+\frac{1}{2}}\right] = \tfrac{1}{2}(\hat{E}\left[q_R, \left(\tfrac{\Delta\xi}{J}\right)_{j+\frac{1}{2}}\right] + \hat{f}\left[q_L, \left(\tfrac{\Delta\xi}{J}\right)_{j+\frac{1}{2}}\right]$$
$$-|A\left[q_L, q_R, \left(\tfrac{\Delta\xi}{J}\right)_{j+\frac{1}{2}}\right]|(q_R - q_L))$$

(2.15)

where A is the Roe-averaged Jacobian matrix and q_L and q_R are the left and right state variables, respectively. Higher order schemes can be constructed by using higher order monotone interpolation schemes (Suresh and Huynh [88]) for the primitive variables ρ, u, v, w and p at the $j+\frac{1}{2}$ and $j-\frac{1}{2}$ points. This work uses the third order accurate method proposed by Koren [85].

The integration in time is performed implicitly using the Lower Upper-Symmetric Gauss Seidel (LU-SGS) method [86]. Briefly, the LU-SGS method is a direct modification of the approximate lower-diagonal-upper (LDU) factorization to the unfactored implicit matrix. The resulting factorization can be regarded as the symmetric Gauss-Seidel relaxation method. The diagonal elements in the LDU factorization have the absolute values of the Jacobian matrices making it more stable than a LU factorization.

The final form of this algorithm can be written for a first-order time-accurate scheme as

$$LDU\Delta\hat{q}^n = -\Delta t RHS^n$$
$$\hat{q}^{n+1} = \hat{q}^n + \Delta q^n$$

(2.16)

where

$$L = I - \Delta t \hat{A}^-|_{j,k,l} + \Delta t \nabla_\xi \hat{A}^+ - \Delta t \hat{B}^-|_{j,k,l} + \Delta t \nabla_\eta \hat{B}^+$$
$$- \Delta t \hat{C}^-|_{j,k,l} + \Delta t \nabla_\zeta \hat{C}^+$$
$$D = \left[I + \Delta t (\hat{A}^+ - \hat{A}^- + \hat{B}^+ - \hat{B}^- + \hat{C}^+ - \hat{C}^-)|_{j,k,l} \right]^{-1} \quad (2.17)$$
$$U = I + \Delta t \hat{A}^+|_{j,k,l} + \Delta t \Delta_\xi \hat{A}^- + \Delta t \hat{B}^+|_{j,k,l} + \Delta t \Delta_\eta \hat{B}^- + \Delta t$$
$$\hat{C}^+|_{j,k,l} + \Delta t \hat{C}^+|_{j,k,l} + \Delta t \Delta_\zeta \hat{C}^-$$

where Δt is the time step, RHS represents the discretized flux terms and n refers to the current time level. Here Δ_ξ represents a forward difference and ∇_ξ represents a backward difference. Also, the split flux Jacobians (e.g., $\hat{A}^+$ and $\hat{A}^-$) may be given by a spectral radius approximation as $A^+ = \frac{1}{2}(A + \sigma_\xi)$, $A^- = \frac{1}{2}(A - \sigma_\zeta)$, $\sigma_\xi = (|U| + ar_\xi) * (1 + \epsilon)$, $\epsilon = 0.01$ typically, and $r_\xi = \sqrt{\xi_x^2 + \xi_y^2 + \xi_z^2}$. As a result of the simplified form of the Jacobian terms (e.g., $\hat{A}^+$), all of the diagonal elements in L, D and U reduce to scalar elements. Thus, this method requires only two (one forward and one backward) sweeps with scalar inversions and leads to a reduced factorization error. This work uses a similar second order backwards difference scheme along with Newton subiterations to remove the factorization error and maintain conservation at each time step.

2.2.3   Calculation of space and time metrics

In Equation 2.9, the terms of form $\hat{\xi}_{x,y,z}$, $\hat{\eta}_{x,y,z}$ and $\hat{\zeta}_{x,y,z}$ are the space metrics, $\hat{\xi}_t$, $\hat{\eta}_t$ and $\hat{\zeta}_t$ are the time metrics in the computational domain, and J is the Jacobian of the inverse coordinate transformation (i.e $J = \det(\frac{\partial(x,y,z)}{\partial(\xi,\eta,\zeta)})$).
A modified finite volume method is developed as part of this dissertation to calculate fourth order accurate space metrics. A methodology to calculate time metrics in a way that preserves geometric conservation is also improvised. The

field velocity approach is used to include the effects of an external field (e.g., the velocities induced by a vortex wake).

Field Velocity Approach

Mathematically, the field velocity approach can be explained by considering the velocity field, V, in the physical Cartesian domain. It can be written as

$$V = (u - x_\tau)i + (v - y_\tau)j + (w - z_\tau)k \tag{2.18}$$

where u, v and w are components of the velocity along the coordinate directions and x_τ, y_τ and z_τ are the corresponding grid time velocity components. For the flow over a stationary wing, these components are zero. For a rotor blade rotating about the z-axis, both x_τ and y_τ have non-zero values owing to the rotation of the mesh. Let the velocity induced by the external potential be represented by a velocity field (u', v', w'). Thus, the velocity field becomes

$$V = (u - x_\tau + u')i + (v - y_\tau + v')j + (w - z_\tau + w')k \tag{2.19}$$

The field velocity approach models this changed velocity field by changing the grid velocities. The modified grid velocities are defined as

$$\tilde{x}_\tau i + \tilde{y}_\tau j + \tilde{z}_\tau k = (x_\tau - u')i + (y_\tau - v')j + (z_\tau - w')k \tag{2.20}$$

After the modified grid velocities are obtained, the grid time metrics in the computational domain $(\hat{\xi}_t, \hat{\eta}_t \ \hat{\zeta}_t)$ are computed as:

$$
\begin{aligned}
\hat{\xi}_t &= -(\hat{\xi}_x \tilde{x}_\tau + \hat{\xi}_y \tilde{y}_\tau + \hat{\xi}_z \tilde{z}_\tau) \\
\hat{\eta}_t &= -(\hat{\eta}_x \tilde{x}_\tau + \hat{\eta}_y \tilde{y}_\tau + \hat{\eta}_z \tilde{z}_\tau) \\
\hat{\zeta}_t &= -(\hat{\zeta}_x \tilde{x}_\tau + \hat{\zeta}_y \tilde{y}_\tau + \hat{\zeta}_z \tilde{z}_\tau)
\end{aligned}
\tag{2.21}
$$

Geometric Conservation Law

The geometric conservation law (GCL) has the same form as the mass conserva-
tion law (first component of the vector in Eq. 2.8) as it essentially represents the
conservation of cell volumes. The differential form of the GCL can be obtained
from the mass conservation equation by setting $\rho=1$ and $V = (u, v, w) = 0$:

$$J_\tau + (\hat{\xi}_t)_\xi + (\hat{\eta}_t)_\eta + (\hat{\zeta}_t)_\zeta = 0 \tag{2.22}$$

The integral form of the GCL can be obtained in a similar manner and can be
stated as:

$$\nu(t_2) - \nu(t_1) = \int\limits_{t_1}^{t_2} \oint\limits_{S(t)} \vec{V}_s.\vec{dS}dt \tag{2.23}$$

where $\nu(t_2)$ and $\nu(t_1)$ are the initial and final volumes and $\vec{V}_s$ is the moving
velocity of the cell surface. Equation 2.22 or 2.23 needs to be satisfied in order
to make the numerical discretization strictly conservative. Otherwise, artificial
sources and sinks can be generated as a result of the numerical discretization.
Thomas and Lombard [90] proposed the solution of Eq. 2.22 with the same
differencing scheme as that used for solving the flow conservation equations to
maintain the GCL. But this adds to the computational overhead of the calcula-
tion.

A more practical approach is to compute the Jacobian, J, by its geometric def-
inition and calculate the time metrics according to the GCL [91]. For example,
for a first order accurate time metric calculation one could find the time metrics
in the computational domain as:

$$\hat{\xi}_t = -\frac{V_{S\xi}}{\Delta t}$$

$$\hat{\zeta}_t = -\frac{V_{S\zeta}}{\Delta t} \tag{2.24}$$

$$\hat{\eta}_t = -\frac{V_{S\eta}}{\Delta t}$$

Where $V_{S\xi}$, $V_{S\eta}$ and $V_{S\zeta}$ are the volumes swept by the faces of the cell volume in the computational coordinate directions. This approach provides a methodology for implicitly satisfying the GCL without solving any additional equations. But, in a purely finite difference approach one is posed with the problem of identifying cell volumes. In other words, a strategy needs to be identified to define bounded volumes around mesh points which can be used for the computations of the Jacobian, space metrics and time metrics in a consistent manner.

Defining Cell Volumes

To preserve the overall order of accuracy of the computations, the space and time metrics need to be calculated to at least the same order of accuracy as that of the underlying spatial and temporal numerical discretization. Using a classical finite difference approach, one calculates the transformation matrix $\frac{\partial(x,y,z)}{\partial(\xi,\eta,\zeta)}$ and inverts it to find the space metrics. The Jacobian of transformation is the determinant of this transformation matrix. The order of accuracy of the space metrics can be improved by using a larger finite difference stencil for evaluating individual terms of the above matrix. But, for surface conforming mesh geometries, it is possible to create overshoots and undershoots (e.g. at the trailing edge of an airfoil) when arbitrarily increasing the finite difference stencil, which causes divergence of the flow solution at times. Hence, a modified strategy, often referred to as the dual refined mesh approach, which computes the space metrics and Jacobian in a finite-volume like way, is proposed.

Figures 2.1(a) and 2.1(b) show the volumes around a mesh point for a 2-D mesh and 3-D mesh respectively. The open symbols represent the mesh points of the original mesh in which the computations of flow variables are performed. The closed symbols show the refined mesh generated by one dimensional interpolation in the direction of each of the computational coordinates. For this work, the refined mesh points are generated using a quadratic monotone interpolation scheme proposed by Suresh and Hyunh [89]. The monotonicity of the interpolation scheme prevents the generation of overshoots and undershoots in the refined mesh geometry. Also, the fourth order interpolation makes the calculation of the Jacobians and space metrics spatially 4th order accurate, even though the computations of these are made in a finite-volume like way.

After the refined mesh is obtained, a volume which is bounded by 24 faces (8 edges in 2-D) can be defined around the mesh point. The Jacobian of the transformation to the computational coordinates at every mesh point can be evaluated by consistently evaluating the volumes of these bounded cells. The Jacobian(J) in Eq. 2.8 is that of the inverse transformation and can be found by taking the inverse of the volumes calculated. The algorithms used for calculating cell volumes preserving the consistency at the interface between neighboring cells is given in detail in Appendix B.

Evaluation of Space metrics

The space metrics are gradients to ξ = const, η = const and ζ = const surfaces scaled by the Jacobian of inverse transformation. The definition of these surfaces are known from the refined mesh which was computed while defining the volumes. The gradients of these surfaces can be evaluated at every mesh point to find the

space metrics.

For the computation of the right hand side of the flow conservation equations in the discretized form, one often needs the space metrics at the interface points ($\xi = i \pm \frac{1}{2}, \eta = j \pm \frac{1}{2}, \zeta = k \pm \frac{1}{2}$). These are actually surface normals to the bounded cell defined around the mesh point (graphically described in Fig 2.1) which can be evaluated by computing the gradient vector to the appropriate surface.

Evaluation of time metrics

The evaluation of the time metrics require computation of volumes swept by the faces of the bounded volume. The time metrics should have components of both the actual deformation of the mesh and the external velocity field, which is included using the field velocity approach. Figure 2.2 illustrates the methodology of computation. The time metric in a particular computational coordinate direction is calculated by accumulating the volume swept by the face because of actual deformation and the apparent volume swept because of the field velocity components.

The temporal order of accuracy can be improved by using the volumes swept at previous time steps and devising an appropriate backward difference stencil (similar to the flow equations). To make the scheme strictly conservative, the Jacobian is recalculated by including the change in volume because of the apparent contribution from the field velocity components. The space metrics are still evaluated as surface normals to the actual deformed mesh, although they are rescaled by the modified Jacobian. Thus, this approach presents a unique way of satisfying the GCL together with the use of the field velocity approach.
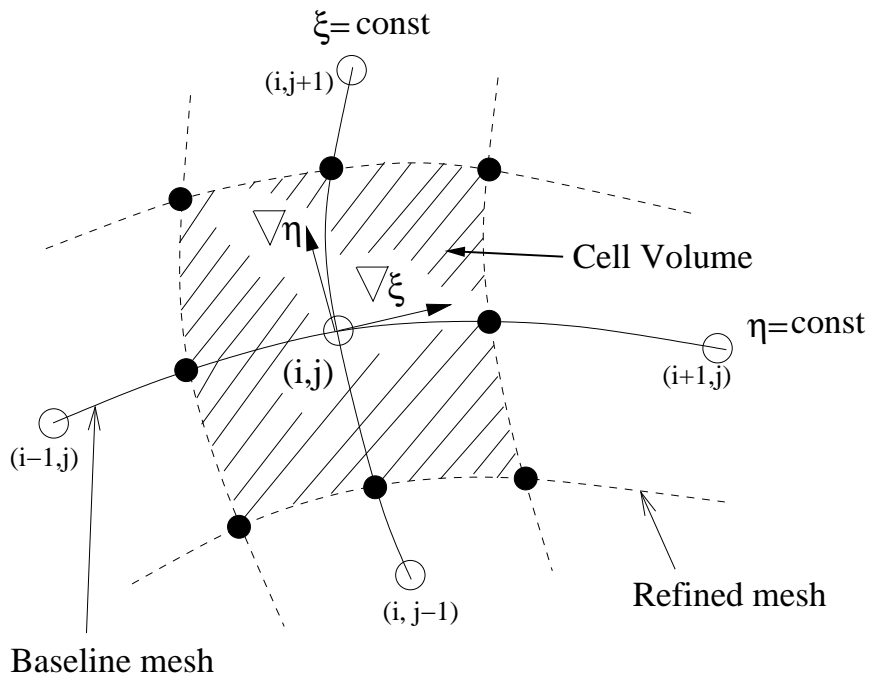
(a) two dimensionsional
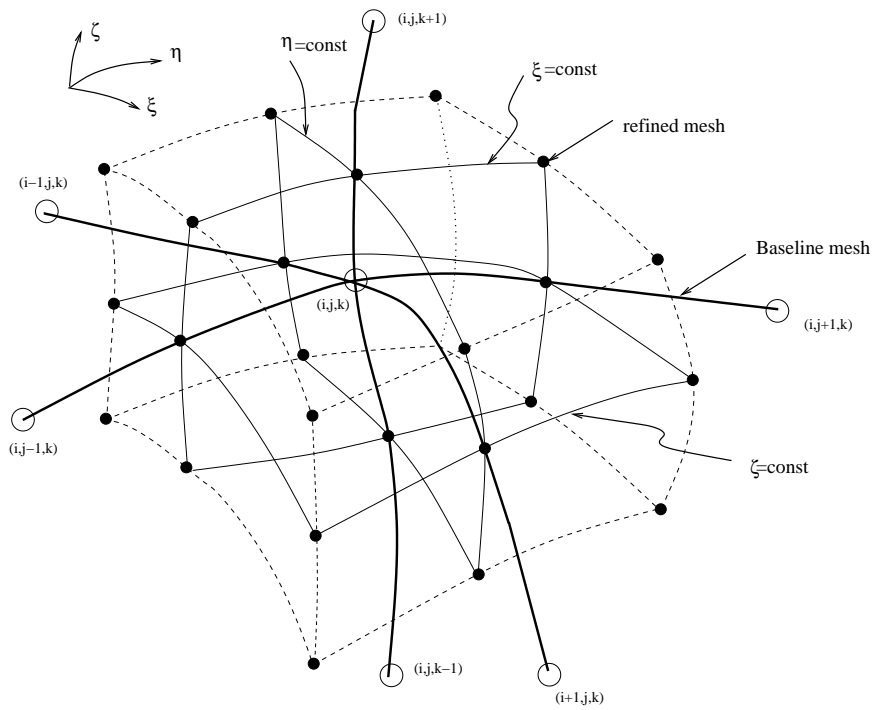
(b) three dimensions

Figure 2.1: Cell volume representation in the finite volume scheme

Cell face because of
Apparent movement due to
field velocity components

V1

V2

Cell face at time=t+Δt

Volume swept = V1 + V2

Cell face at time=t
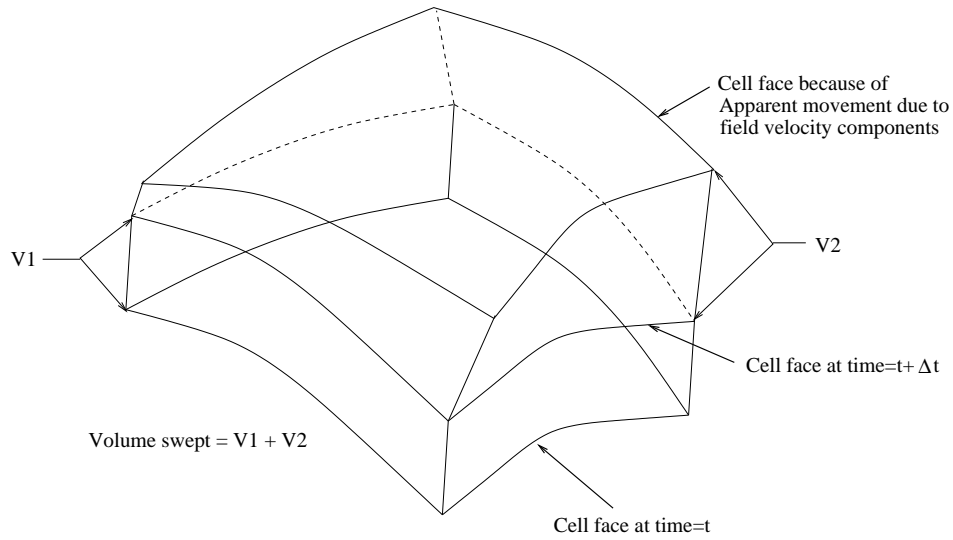
Figure 2.2: Evaluation of volumes swept by cell faces

2.2.4 Mesh generation

Rotor blade geometries (e.g., the UH-60A) often have swept tips and non-linear twist and chord distributions defined as a function of span. A hyperbolic mesh generation technique [92] is used to generate 2-D C-type meshes around the airfoil sections at the various spanwise loacations. The C-type meshes are free of the geometrical singularity at the trailing edge, which is a major disadvantage of O-type meshes. Also, the grid clustering at the trailing edge provides good resolution for capturing the shed wake. The C-meshes obtained are stacked in the spanwise direction to produce a single block three dimensional C-H mesh. The wrap around C direction is in the chordwise direction and H type is in the spanwise direction. A schematic of typical C-H mesh topology is shown in Fig 2.3. One of the major disadvantages of C-H meshes are their inability to
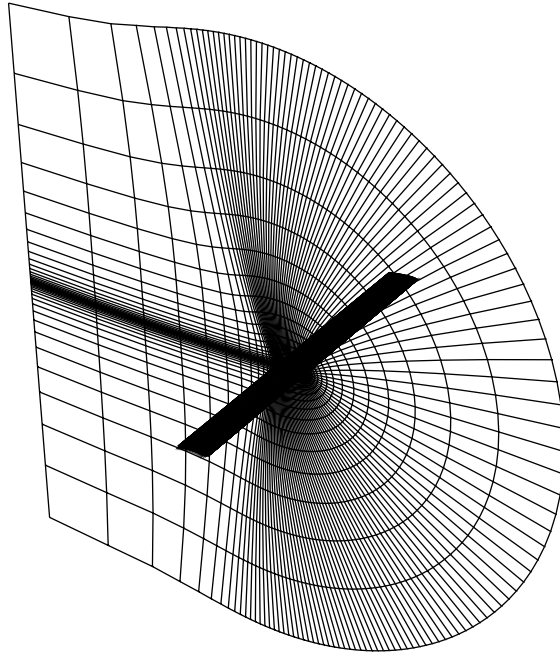
(a) C-mesh at each section
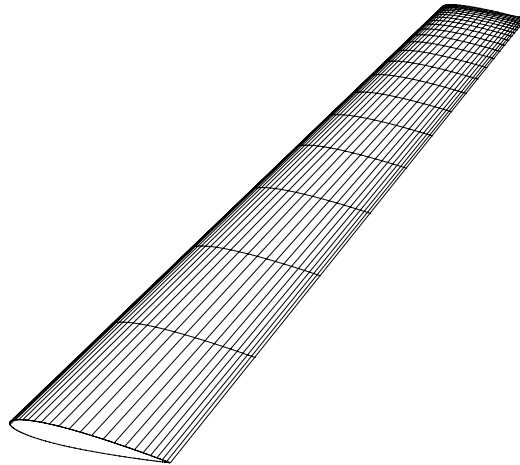
(b) Stacking in spanwise direction

Figure 2.3: Hyperbolic C-H mesh used for CFD computations (Every other point on the mesh is shown).

accurately model the tip geometry shapes. The tip geometry is approximated as a bevel shape because of the H topology in the spanwise direction. An alternate approach known as the C-O mesh approach can be used to provide better tip definition. Thus, the mesh generation algorithm is modified to generate C-O meshes as well. Representative C-H and C-O mesh topologies that emphasize the salient differences in tip definition are shown in Fig 2.4. A detailed description of the C-O mesh generation technique is provided in Appendix C.

2.2.5 Vortex wake modeling

The vortex wake is found using the principles of vorticity transport in a Lagrangian frame. The Maryland Free Wake [94] analysis was used for computing the wake geometry. The analysis uses a Pseudo Implicit Predictor Corrector (PIPC) [36], which finds the solution to the vorticity transport through a relaxation approach. For the steady flight conditions studied the rotor wake can be considered to be periodic. Wake periodicity is assumed when performing the relaxation solution. The trailed wake is discretized into vortex filaments which are allowed to convect under the self and mutually induced velocities caused by all the vortex filaments in the wake. A converged wake geometry is obtained when the system becomes force-free, i.e. when the vortex filaments reach such a location in space where the net forces from all of the self and mutually induced velocities approach zero.

The free wake analysis needs inputs of the vortex release points and the circulation strengths of the individual wake filaments. The tip vortex release points and bound vortex locations are calculated using the exact structural deformation of the rotor blade. The circulation strengths are computed using the sectional
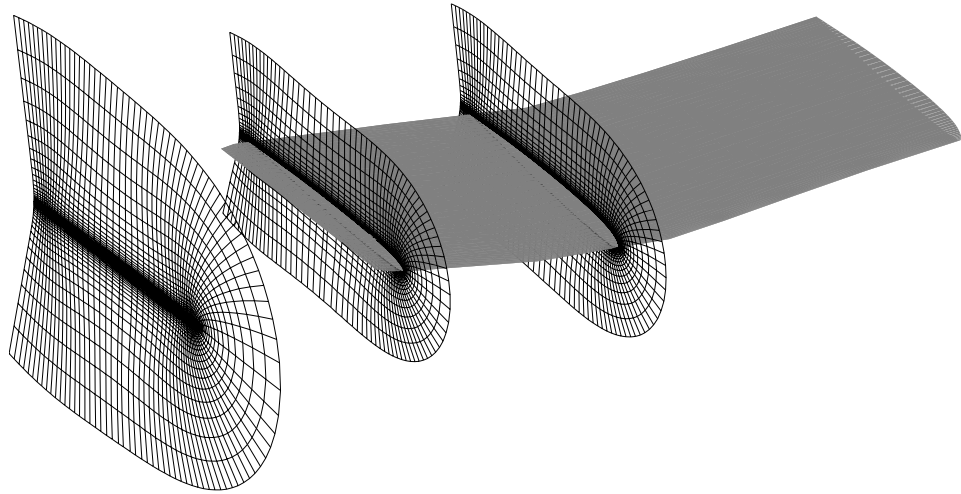
(a) C-H mesh
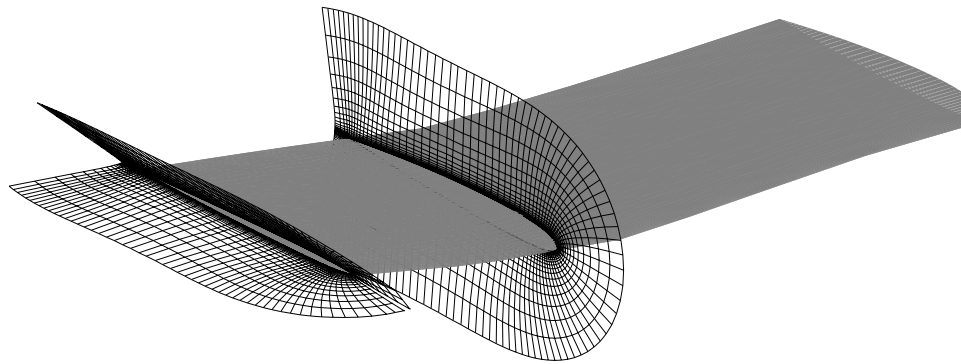
(b) C-O mesh

Figure 2.4: Near body C-H and C-O meshes at the blade tip

lift coefficient integrated from the pressure distributions obtained from the CFD solution of the flow around the deformed blade geometry. The bound vortex strengths as given by

$$\Gamma = \frac{1}{2}UcC_l \tag{2.25}$$

where c, U, C_l are the chord, local free stream velocity and sectional lift coefficient respectively. The bound circulation outboard of the maximum circulation point along the radius is assumed to roll up in to a single tip vortex. Therefore, the maximum bound vortex strength along span is used as the tip vortex strength. A desingularized vortex-core model is used to avoid singularity at the center of the vortex. The model is described for an infinite vortex filament as

$$V_\theta = \frac{\bar{\Gamma}r}{2\pi(r_c^2 + r^2)} \tag{2.26}$$

where V_θ is the tangential velocity, r is the radial distance from the center, and r_c is the core radius and $\bar{\Gamma}$ is the circulation strength. An empirical viscous diffusion model [37] is used to account for the core radius growth with wake age. An example of the typical vortex wake geometry predicted is shown in Fig 2.5.

2.2.6 Inclusion of the vortex wake in to the CFD calculations

The field velocity approach(Section 2.2.3) is used to incorporate the necessary conditions for simulating interaction of the blade with the rotor wake. The effect of the wake is simulated by superposing a velocity field equivalent to that induced by the wake over the free stream conditions. The velocity field (u', v', w') in Eq 2.19 at each grid point is evaluated by aggregating the velocities induced by all the individual vortex filaments in the discretized vortex wake structure.
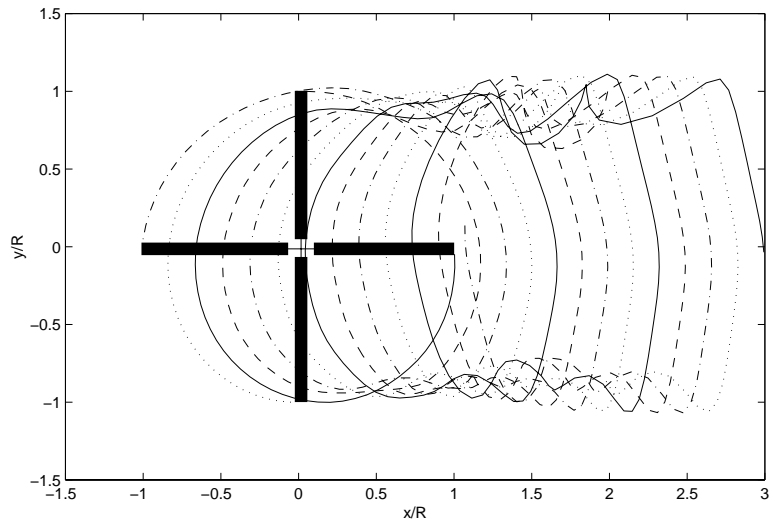
(a) Top View
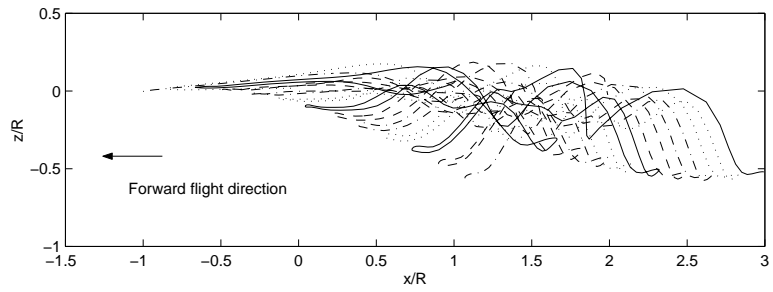
(b) Side View
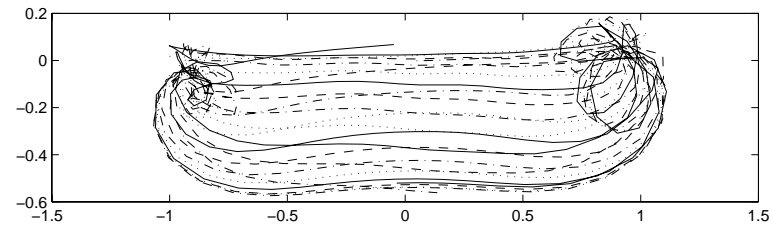
(c) Back View

Figure 2.5: Representative wake geometry computed by the Free Wake Analysis
: Present case is for UH-60A rotor at advance ratio of μ=0.110, C_T/σ=0.0783

Wake interpolation and calculation of induced velocities

The time steps used in CFD computations are often one order of magnitude smaller than that used in the free wake computations. This necessitates the interpolation of the wake geometry for in between azimuthal locations. The periodicity of the wake geometry (for each rotor) with azimuth facilitates the use of a spectral interpolation. A one dimensional fast Fourier transform is performed on the coordinate location of the wake filaments with the same wake age at all azimuth angles. The wake interpolation is conducted by extending the Fourier series to the higher time resolution used in the CFD computations. The use of the FFT technique improves the accuracy and speed of the interpolation process.

As mentioned previously, the wake induced velocities at all the grid points need to be recalculated every time (azimuthal) step to consistently incorporate the vortex wake geometry using the field velocity approach. The near wake sheet is computed as part of the CFD solution. The near wake is assumed to roll up in to a tip vortex in 30 degrees of azimuth. Therefore, the first 30 degrees of the free wake geometry are excluded in the induced velocity calculations. The induced velocities at any point in space caused by a single wake filament can be directly evaluated by the Biot-Savart law given by:

$$\vec{V_{ind}} = \frac{1}{4\pi} \int\limits_0^l \frac{\Gamma(y) \times \vec{r}}{|\vec{r}|^3} dy \qquad (2.27)$$

where l is the length of the vortex filament, Γ is the circulation strength and r is the vectorial displacement of the evaluation point with respect to the vortex filament. The Biot-savart kernal is mollified to avoid singulaties using the core

function described in Eq 2.26.

The induced velocity calculation is a computationally intensive process as there are as many Biot-Savart operations per grid point as there are free vortex filaments. This is an $O(M * N)$ operation, where M is the number of grid points and N is the number of vortex filaments. Typically the effects of about 1000 vortex filaments need to be found at all of the 1 million mesh points per time step. Hence, fast evaluation algorithms need to be developed to make the simulation practical.

A fast hierarchical algorithm that uses a divide and conquer methodology is developed to minimize the Biot-Savart computations. The mesh is enclosed in a rectangular bounding box (Fig 2.6), which is recursively subdivided in to smaller boxes. The induced velocity contributed by all the free vortices are evaluated at the vertices of the smallest boxes. Vortices are indexed and the indices of vortices in each box is found hierarchically. For any given grid point the Biot-Savart law is evaluated directly for all the vortex filaments contained in the smallest box, which contains the grid point and also for all the vortex filaments that are in its immediately neighboring boxes. The velocity induced by all the near field vortex filaments so found are also found at the vertices of the box containing the grid point. The influence of the far field is found at the vertices of the box by subtracting the effect of the near field vortices from the induced velocity caused by the whole wake, which was precomputed. The far field contribution at the grid point is then evaluated by interpolating the values at the vertices consistently. This approach was found to give good performance gain with little loss in accuracy and is used to calculate field velocities used in the present work. However, it is not possible to obtain strict bounds for the approximation errors

in this approach.
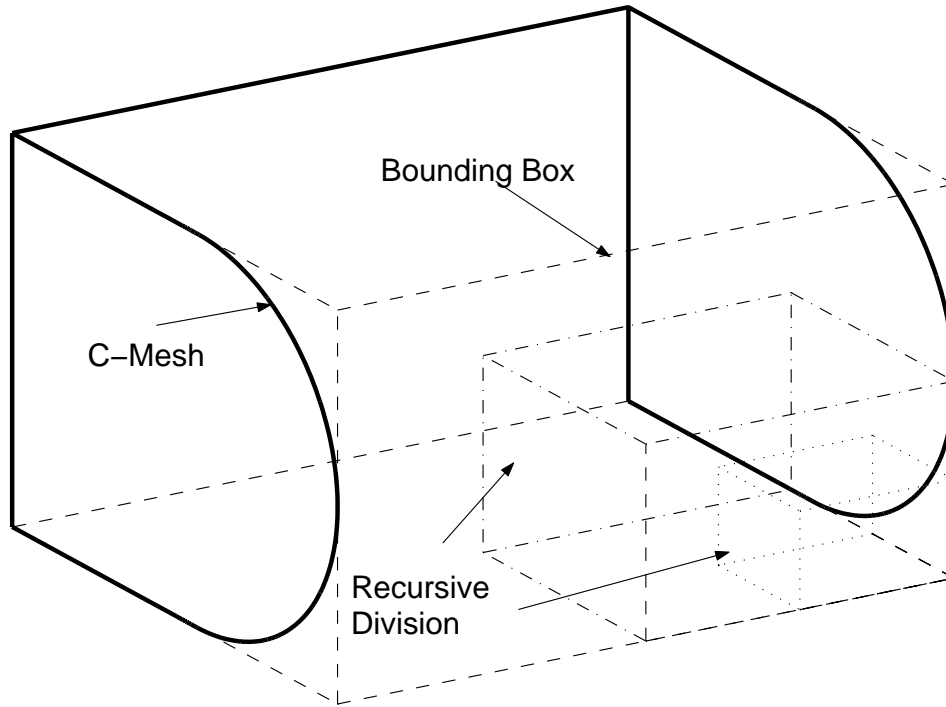
Figure 2.6: Bounding box and its recursive division

The fast multipole method (FMM) [93] provides yet another powerful method for fast evaluation of potential fields. Analytical models have been developed by researchers in the past for fast evaluation of scalar potential fields. But, the present problem involves a vector field, which requires derivation of the underlying analytical models. The multipole expansion of the Biot-Savart integral, the re-expansion and translation operators and the octree based multi level hierarchical algorithm are described in detail in Appendix A.

2.2.7 Inclusion of aeroelastic deformations into the CFD computations

A blade dynamic response distribution that includes elastic and rigid flap, lag and torsional deformations is calculated from the structural dynamic analysis. The given rotor geometry is dynamically deformed in accordance with these blade motions. There are different ways of expressing aeroelastic deformations. One popular way is using Euler parameters $[e_1, e_2, e_3, e_4, e_5, e_6]^T$, which represent linear motions and rotations. These parameters are obtained as a function of both radius and azimuth from the structural dynamic analysis. The Euler parameters e_1, e_2 and e_3 are linear deflections while e_4, e_5 and e_6 define rotations. The rotation matrix is found from e_4, e_5 and e_6 as follows:

$$e_0 = \sqrt{1 - e_4^2 - e_5^2 - e_6^2} \tag{2.28}$$

$$T_{DU} = \begin{bmatrix} 1 - 2e_5^2 - 2e_6^2 & 2(e_4e_5 + e_0e_6) & 2(e_4e_6 - e_0e_5) \\ 2(e_4e_5 - e_0e_6) & 1 - 2e_4^2 - 2e_6^2 & 2(e_5e_6 + e_0e_4) \\ 2(e_4e_6 + e_0e_5) & 2(e_5e_6 - e_0e_4) & 1 - 2e_4^2 - 2e_5^2 \end{bmatrix} \tag{2.29}$$

Structural dynamic analysis can also provide deformations in the form $[u, v, w, v', w', \phi]^T$, where u, v and w are the linear deformations in axial, lag and flap directions, v', w' are the radial derivatives for lag and flap degrees and ϕ is the elastic torsional deformation. The rotation matrix is found from these parameters as follows:

$$
T_{DU} =
\begin{bmatrix}
1 - \frac{v'^2}{2} - \frac{w'^2}{2} & v' & w' \\
-v' \cos\theta_1 - w' \sin\theta_1 & (1 - \frac{v'^2}{2}) \cos\theta_1 - v'w' \sin\theta_1 & (1 - \frac{w'^2}{2}) \sin\theta_1 \\
v' \sin\theta_1 - w' \cos\theta_1 & -(1 - \frac{v'}{2}) \sin\theta_1 - v'w' \cos\theta_1 & (1 - \frac{w'^2}{2}) \cos\theta_1
\end{bmatrix}
\tag{2.30}
$$

The variable θ_1 represents the total pitch of the blade which is given by $\theta_1 = \theta_c + \phi$, where θ_c are the control deflections and ϕ is the elastic torsional deflection.

Mesh deformation

The deformed mesh coordinates in the blade fixed frame are given by the following equation:

$$
\begin{bmatrix} x' \\ y' \\ z' \end{bmatrix} = (T_{DU})^T \begin{bmatrix} x \\ y \\ z \end{bmatrix} + \vec{x_{lin}}
\tag{2.31}
$$

The vector $\vec{x_{lin}}$ is $\{e_1, e_2, e_3\}$ for the former deflection convention and $\{u, v, w\}^T$ for the latter convention. A decay is applied to both the rotations and linear deflections such that the outer boundary of the mesh remains stationary (See Fig 2.7). Several algorithms including "the spring analogy" (Ref [13]) were investigated for the problem. For the present structured mesh the simple decay with cosine smoothing was found to be both robust and optimal. The procedure for the cosine decay is as follows (Eq 2.32):

$$e_i = e_i \times C \qquad (i = 1, 6)$$

$$C = 1 \qquad (r < RMIN)$$

$$C = 1 + \cos(pi * (r - RMIN)/RMAX) \qquad (RMIN \geq r < RMAX) \tag{2.32}$$

$$C = 0 \qquad (r \geq RMAX)$$

where r is the distance of any point (x, y, z) to quarter chord location of the section. Once, the deformed mesh is obtained in the blade fixed frame, it is rotated about the axis of rotation (z-axis in this case) to the appropriate azimuthal location. Typical choices of RMIN and RMAX are 4 chords and 10 chords respectively.

2.3 Structural Dynamic Modeling

The rotor system can be modeled as a 2nd order system (mass-spring-damper) which is harmonically excited by an unsteady forcing (aerodynamic loading). The blade motions (both rigid and elastic) need to be calculated such that they simultaneously satisfy the vehicle trim equations and blade periodic response equations.

Finite element based methods are known to accurately model kinematic and elastic behavior in bending and torsion of slender beams. A single rotor blade, because of its large aspect ratio, can be considered as a slender beam. The rotor blade has all the 6 degrees of freedom and undergoes simultaneous flap, lag and torsion deformations. The detailed mathematical equations for such a system is complex because of the non-linear coupling between the various degrees of freedom and hence not included here to preserve the brevity of the thesis (details
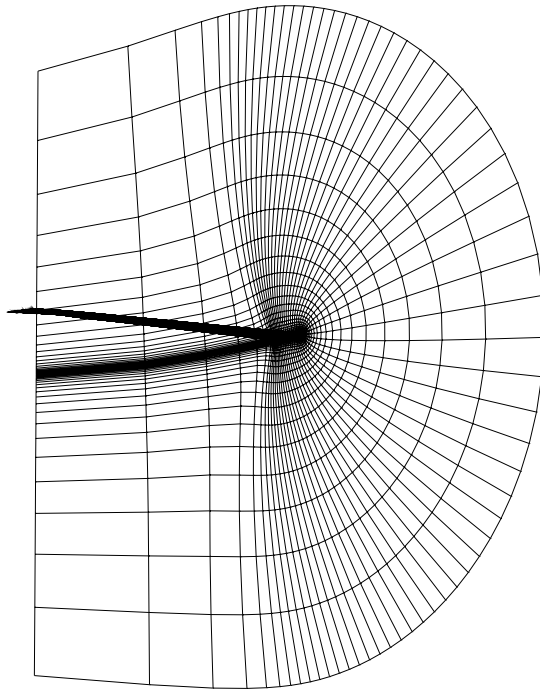
(a) Undeformed mesh
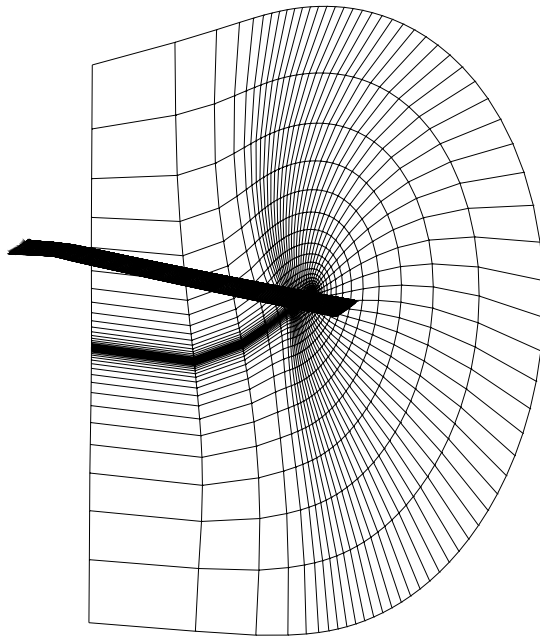
(b) Deformed mesh

Figure 2.7: Deformed and undeformed mesh : The amount of deformation di-
minishes as one moves outward

in UMARC manual [95]). The overall methodology can however be explained by considering the rotor blade as a slender beam undergoing flap bending only. The inclusion of the other degrees of freedom produces additional cross-coupling terms in the mass, stiffness and damping matrices.

2.3.1 Comprehensive rotor analysis methodology

The comprehensive rotor analysis methodology can be divided in to four major parts. The first part concerns the structural modeling of the rotor blade involving finite element discretization of the blade and subsequent analysis of the natural frequencies and mode shapes. The second part involves the calculation of the unsteady forcing and aerodynamic mass, stiffness and damping matrices. The third part involves reduction of the blade equations to the modal form and solving them by a temporal finite element method. The last part deals with calculation of the control parameters producing a rotor response that gives a set of average rotor forces and moments which satisfy the vehicle trim equations.

2.3.2 Finite element discretization of the rotor blade

For the simplified case (i.e., with only the flap bending), the blade is discretized into two noded beam elements with two degrees of freedom per node. The degrees of freedom are displacement and slope (w and w'). The distribution of displacement w in an element can be considered of the form

$$w(x,t) = \alpha_1 + \alpha_2 x + \alpha_3 x^2 + \alpha_4 x^3 \tag{2.33}$$

Applying the end conditions one can formulate the displacement in terms of the end displacements and slopes. For a displacement vector $[q_1, q_2, q_3, q_4]^T$ with

$q_1 = w_1$, $q_2 = w_1'$, $q_3 = w_2$ and $q_4 = w_2'$ respectively, the displacement is given by:

$$w(x,t) = \sum_{i=1}^{4} H_i q_i \tag{2.34}$$

where H_i are shape functions which are Hermite polynomials of the form:

$$H_1 = 2\frac{x^3}{l} - 3\frac{x^2}{l} + 1 \tag{2.35}$$

$$H_2 = \left\{ \frac{x^3}{l} - 2\frac{x^2}{l} + \frac{x}{l} \right\} l \tag{2.36}$$

$$H_3 = -2\frac{x^3}{l} + 3\frac{x^2}{l} \tag{2.37}$$

$$H_4 = \left\{ \frac{x^3}{l} - \frac{x^2}{l} \right\} l \tag{2.38}$$

Hamilton's variational principle is used to derive the system equations of motion. For a conservative system, Hamilton's principle states that the true motion of a system between presicribed initial conditions is that particular motion of which the time integral of the difference between the potential and kinetic energies is a minimum. The generalized Hamilton's principle is given by:

$$\delta\Pi = \int_{t_1}^{t_2} (\delta U - \delta T - \delta W)dt = 0 \tag{2.39}$$

where δU is the virtual variation of strain energy and δT is the virtual variation of kinetic energy. The δW is the work done by external forces. The element mass and stiffness matrices are derived based on this principle and are given as:

$$[m_{ij}] = \int_0^1 m H_i H_j ds \tag{2.40}$$

$$[k_{ij}] = \int_0^1 (F_A H_i' H_j' + (EI_z sin^2(\theta_0) + [EI_y cos^2(\theta_0)) H_i'' H_j'')) ds \tag{2.41}$$

where EI_y and EI_z are flexural rigidities in the longitudinal and transverse directions and $F_A = \int_x^1 mxdx$. All the variables are non-dimensionalized, hence w actually implies the non-dimensionalized displacement w/R. All the integrations are conducted using a six point Gauss quadrature formula.

The element mass and stiffness matrices are assembled appropriately to form the global mass and stiffness matrices. An eigen analysis is conducted on these matrices to determine the generalized eigen values and eigen vectors. The eigen values are the square of the natural frequencies of this system, while the eigen vectors represent the natural vibration mode shapes.

2.3.3   Unsteady aerodynamic forcing

The blade response is directly dependent on the aerodynamic forcing on the individual blades. Quasi-steady aerodynamic modeling is chosen for explaining the methodology. This can be replaced by a table-lookup based linear unsteady aerodynamic modeling (Section 2.4) or direct CFD based aerodynamic modeling (Section 2.2). In the quasi-steady approach, the normal (U_P), tangential (U_T) and radial (U_R) components of the free stream velocity are calculated at each section of the rotor blade. The motion and deformation of the blades are accounted for appropriately in the calculation of these components. The final non-dimensionalized form of the aerodynamic forces in the deformed frame of reference is given by (detailed description in section Section 2.4.1 Eq 2.82):

$$(L_w)_c = \tfrac{\gamma}{6a}(c_0 U_T^2 - (c_1 + d_0)U_T U_P + d_1|U_P|U_P)$$
$$(L_v)_c = \tfrac{\gamma}{6a}(-d_0 U_T^2 - (c_0 U_P - d_1|U_P|)U_T + (c_1 - d_2)U_P^2) \qquad (2.42)$$
$$(L_u)_c = \tfrac{\gamma}{6a}(-d_0 U_R U_T)$$

Here, c_0, c_1 are used represent linear variation of C_l with angle of attack, d_0, d_1, d_2 represent quardratic variation of C_d with angle of attack and f_0, f_1 represent linear variation of pitching moment with angle of attack. The quantity γ is the lock number (ratio of aerodynamic forces to inertial forces) and a is the lift-curve-slope.

The aerodynamic forces in the undeformed frame are obtained by using the orthogonal co-ordinate transformation

$$
\left\{
\begin{array}{c}
(L_u^A)_C \\
(L_v^A)_C \\
(L_w^A)_C
\end{array}
\right\} = (T_{DU})^T
\left\{
\begin{array}{c}
(L_u)_C \\
(L_v)_C \\
(L_w)_C
\end{array}
\right\}
\tag{2.43}
$$

As only the flapping degree of freedom is included for this presentation, the quantity $(L_w^A)_C$ is the only one required. $(L_w^A)_C$ can be expanded as follows:

$$
(L_w^A)_C = (L^A)_0 + (L^A)_L + (L^A)_{NL}
\tag{2.44}
$$

where L_0^A is the deformation independent aerodynamic forcing, L_L^A depends linearly on the blade motions and L_{NL}^A is the non-linear contribution to aerodynamic forcing by the blade elastic deformation. One could linearize Eq. 2.44 with respect to the degrees of freedom (w and w') to give :

$$
\begin{aligned}
(L_w^A)_C = (L^A)_0 + (L^A)_{NL}|_0 + (A_w + A_{wNL})w + \\
(A_{w'} + A_{w'NL})w' + (A_{\dot{w}} + A_{\dot{w}NL})\dot{w} + A_{\ddot{w}}\ddot{w}
\end{aligned}
\tag{2.45}
$$

Equation 2.45 is the forcing function (RHS) for the global mass and stiffness matrices (LHS) obtained from the finite element modeling of the rotor blade. The damping in the rotor system for the first flap mode is primarily produced by the aerodynamic loading. Hence, for the numerical stability of the aeroelastic

analysis the motion dependent terms of the linearized expression (e.g., A_w, $A_{\dot{w}}$ etc), are taken to the LHS. This produces additional entries in the global mass, stiffness and damping matrices. One could determine these entries by finding the aerodynamic mass, damping and stiffness matrices for any element given by (for this simplified analysis):

$$(M_b^A)^i = -\frac{\gamma}{6}l_i \int_0^1 H_s^T A_{\ddot{w}} H_s ds \qquad (2.46)$$

$$(K_b^A)^i = -\frac{\gamma}{6}l_i \int_0^1 (H_s^T((A_w + A_{wNL})H_s + (A_{w'} \\ + A_{w'NL})H_s'))ds \qquad (2.47)$$

$$(C_b^A)^i = -\frac{\gamma}{6}l_i \int_0^1 H_s^T(A_{\dot{w}} + A_{\dot{w}NL})H_s ds \qquad (2.48)$$

Also, the forcing vector is given by

$$(Q_b^A) = \frac{\gamma}{6}l_i \int_0^1 H_s^T \left((L^A)_0 + (L^A)_{NL}|_0\right) ds \qquad (2.49)$$

where l_i is the length of the element under consideration and H_s are the shape functions described in the previous section. The element matrices are assembled appropriately to determine the global aerodynamic mass, stiffness and damping matrices and the load vector which forms the right hand side. The full blade equations of motion are obtained by accumulating the structural and aerodynamic matrices.

2.3.4 Finite element in time

The finite element equation for the rotor blade after the spatial finite element discretization is of the form:

$$M(\psi)\ddot{w} + C(\psi)\dot{w} + K(\psi) = F(w, w', \psi) \tag{2.50}$$

This equation involves many degrees of freedom. To reduce the computational time, the blade finite element equations are transformed in to the normal mode space. This significantly reduces the degrees of freedom. The blade natural vibration modes determined from the finite element analysis are used for the modal transformation. The blade displacement is assumed to be decoupled in space and time and is hence expressed as:

$$w = \phi(x)p_b(t) \tag{2.51}$$

where ϕ is a matrix whose columns consist of the natural vibration mode shapes and p_b is the vector of normal mode coordinates. The ODE representing the motion of the blade can be now transformed to the normal mode co-ordinates as

$$\bar{M}\ddot{p}_b + \bar{C}\dot{p}_b + \bar{K}p_b = \bar{F} \tag{2.52}$$

where

$$\bar{M} = \phi^T M \phi \tag{2.53}$$

$$\bar{C} = \phi^T C \phi \tag{2.54}$$

$$\bar{K} = \phi^T K \phi \tag{2.55}$$

$$\bar{F} = \phi^T F \phi \tag{2.56}$$

are the modal mass, damping and stiffness matrices and the load vector respectively. Using the Hamilton principle the blade equation can be rewritten as

$$\int_0^{2\pi} \delta p_b (\bar{M}\ddot{p}_b + \bar{C}\dot{p}_b + \bar{K}p_b - \bar{F})d\psi = 0 \tag{2.57}$$

Integrating by parts and applying periodic boundary conditions $(\bar{M}(\psi) = \bar{M}(\psi + 2\pi))$ one gets

$$\int_0^{2\pi} (-\delta\dot{p}_b{}^T \bar{M}\delta\dot{p}_b + \delta\dot{p}_b{}^T \bar{C}\delta p_b + \delta p_b^T \bar{K}\delta p_b - \delta p_b^T \bar{F}) = 0 \tag{2.58}$$

The time from 0 to 2π is discretized in to Lagrangian time elements each having 6 degrees of freedom. The temporal node coordinates are denoted by ξ and the normal mode coordinate in any element is assumed to vary as $p_b = H_t\xi$ where H_t are appropriately chosen Lagrange polynomial based shape functions which satisfy the end conditions. Continuity of the generalized displacements is assumed between the time elements. The equations can be now rewritten of the form:

$$K_t^G \Delta\xi^G = Q^G \tag{2.59}$$

where

$$K_t^G = \sum_{i=1}^{N_t} \int_{\psi_i}^{\psi_{i+1}} (-\dot{H}_t{}^T \bar{M}\dot{H}_t + H_t^T \bar{C}\dot{H}_t + H_t^T \bar{K}H_t) \tag{2.60}$$

and

$$Q^G = \sum_{i=1}^{N_t} H_t^T \bar{F} \tag{2.61}$$

These are a system of non-linear algebraic equations, which are solved using Newton's method to calculate the blade response.

2.3.5 Vehicle trim equations

There are many forms of trim solutions. Broadly they can be classified into two categories: free flight and wind tunnel trim.

For free flight or propulsive trim, it is assumed that the engine can supply the necessary power required to maintain the flight condition. For a steady flight, the comprehensive propulsive trim solution can be obtained by satisfying the three force (vertical, longitudinal and lateral) and three moment (pitch, roll and yaw) vehicle equilibrium equations. For example, for a specified gross weight and level flight speed, the trim solution gives the rotor pitch controls (collective θ_0, cyclic θ_{1c} and θ_{1s}), vehicle orientation (longitudinal shaft tilt α_s and lateral shaft tilt ϕ_s) and tail rotor pitch (collective θ_{tr}). In general, the expressions for the vehicle equilibrium can be expressed as (See Figure 2.8):

$$F = 0 \tag{2.62}$$

where exact form $F^T = [F_1, ..F_n]$ depends on the trim condition considered.

The following equations are derived from the force equilibrium of a helicopter in steady flight

$$F_1 = D_F \cos \theta_{FP} + H \cos \alpha_s - T \sin \alpha_s \tag{2.63}$$

$$F_2 = Y_F + Y \cos \phi_s + T \sin \phi_s + T_{tr} \tag{2.64}$$

$$F_3 = T \cos \alpha_s \cos \phi_s - D_F \sin \theta_{FP} + H \sin \alpha_s - Y \sin \phi_s - W - L_{ht} \tag{2.65}$$

$$F_4 = M_{xR} + M_{xF} + Y_F(\bar{h}\cos\phi_s + y_{cg}\sin\phi_s) \tag{2.66}$$

$$+W(\bar{h}\sin\phi_s - y_{cg}\cos\phi_s) + T_{tr}(\bar{h} - z_{tr}) \tag{2.67}$$

$$\begin{aligned}F_5 &= M_{yR} + M_{yF} + W(\bar{h}\sin\alpha_s - x_{cg}\cos\alpha_s)\\ &- D_F(\bar{h}cos(\alpha_s + \theta_{FP}) + x_{cg}sin(\alpha_s + \theta_{FP})) + L_{ht}(x_{ht} - x_{cg})\end{aligned} \tag{2.68}$$

$$F_6 = M_{zR} + M_{zF} + T_{tr}(x_{tr} - x_{cg}) - D_F y_{cg}\cos\alpha_s - Y x_{cg}\cos\phi_s \tag{2.69}$$

where F_1, F_2 and F_3 are, respectively, the vehicle force equilibrium residuals in X, Y and Z directions in the fuselage axes, and F_4, F_5 and F_6 are the vehicle rolling, pitching and yawing moment equilibrium residuals about the vehicle cg, respectively.

The H, Y and T are respectively rotor drag, side force and thrust; and the D_F, Y_F and W are respectively fuselage drag, side force and gross weight. The terms, T_{tr}, x_{tr} and z_{tr}, denote the tail rotor thrust, the distance of the tail rotor hub behind the vehicle cg and the distance of tail rotor hub above the vehicle cg. The horizontal tail is located at a distance x_{ht} behind the vehicle cg. The terms in the three moment equations, e.g. M_{xR} and M_{xF}, denote the rotor and fuselage moments, respectively. The forces act on the rotor hub and the moments act about the rotor hub. In addition, x_{cg} and y_{cg} and $\bar{h}$ are, respectively, the relative location of the rotor hub center with respect to the vehicle center of gravity in the X_F, Y_F and Z_F directions; α_s (positive for forward flight) and ϕ_s (positive advancing side down) are the longitudinal and lateral shaft tilts,
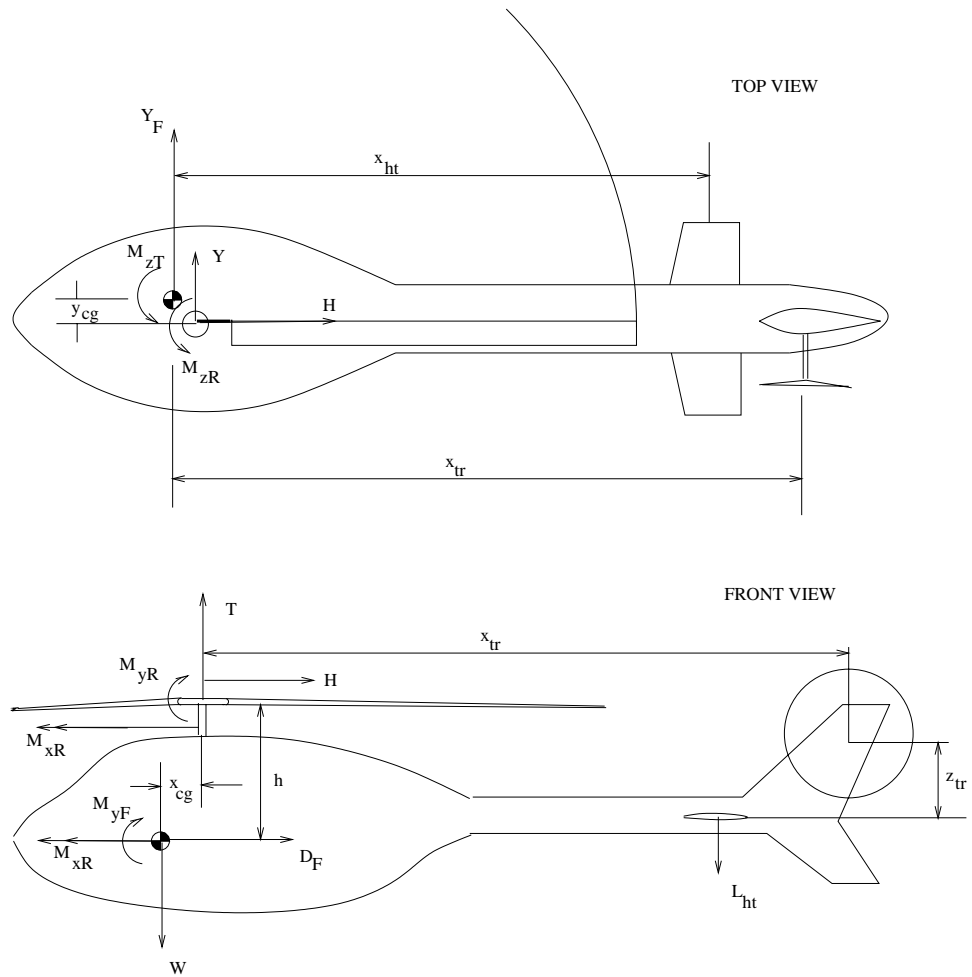
Figure 2.8: Rotor and vehicle forces and moments used for vehicle equillibrium

75

respectively, and θ_{FP} is the flight path angle relative to an axis perpendicular to the gravity vector.

2.3.6   Uncoupled and coupled trim

The convergence of the steady response for a fixed control setting is called an uncoupled trim. In a coupled trim procedure this method is coupled with the solution of the vehicle trim equations to solve to the final converged trim-response solution. As the trim analysis is non-linear in nature a reasonably accurate initial guess is a necessity. A trim analysis of a rigid rotor blade is conducted to find the initial control estimate. The vehicle force and moment equations and the blade flapping equations are solved using an appropriate non-linear equation solver. The response of the rotor to the initial control estimate is found by solving the rotor equations using the temporal finite element method. A force summation is conducted on the basis of the blade response obtained to yield the aerodynamic forces and moments produced by the deformed blade. The time averaged values (over one rotor revolution) of rotor forces and moments are substituted in the appropriate vehicle trim equations to obtain the residuals of these equations. The final aim of the coupled trim procedure is to find the control estimate which drives these residuals towards zero. Newton's method, based on the evaluation of a trim Jacobian matrix, is used to find the final control estimate.

A finite difference approximation is used to calculate the control Jacobian. The initial controls are perturbed one at a time and the variation of the residuals are used appropriately to find individual terms of the control Jacobian. The control settings are updated using the control Jacobian and the value of the residual vector. The whole process is conducted in a loop until the residues to

the vehicle trim equations are below a specified error bound.

2.4   Extended lifting line analysis

The aerodynamic analysis formulation can be divided into the following parts: two dimensional strip theory, attached linear unsteady aerodynamics and the Weissinger-L model to account for the finiteness of the rotor blade.

2.4.1   2-D strip theory

The 2-D strip theory assumes that the blade airloads are solely a function of the instantaneous blade section angle of attack. Furthermore, the lift, drag, and pitching moment data, for a specified airfoil section, is strictly based on static characteristics.

The effective angle of attack at any section can be determined by finding the normal and tangential components of the air velocity in the deformed frame. The general expression for the resultant blade velocity at a radial station x in the rotating undeformed frame is given by:

$$\vec{V} = -\vec{V_w} + \vec{V_b} + \vec{V_f} \tag{2.70}$$

where $\vec{V_w}$ is the wind velocity with contributions from the vehicle forward flight speed and the rotor inflow, $\vec{V_b}$ is the blade velocity relative to the hub fixed frame resulting from blade rotation and blade motions and $\vec{V_f}$ is the blade velocity caused by fuselage motion.

The wind velocity has components in the backward and downward direction w.r.t. to the non-rotating hub fixed coordinate system (See Fig 2.9). The com-
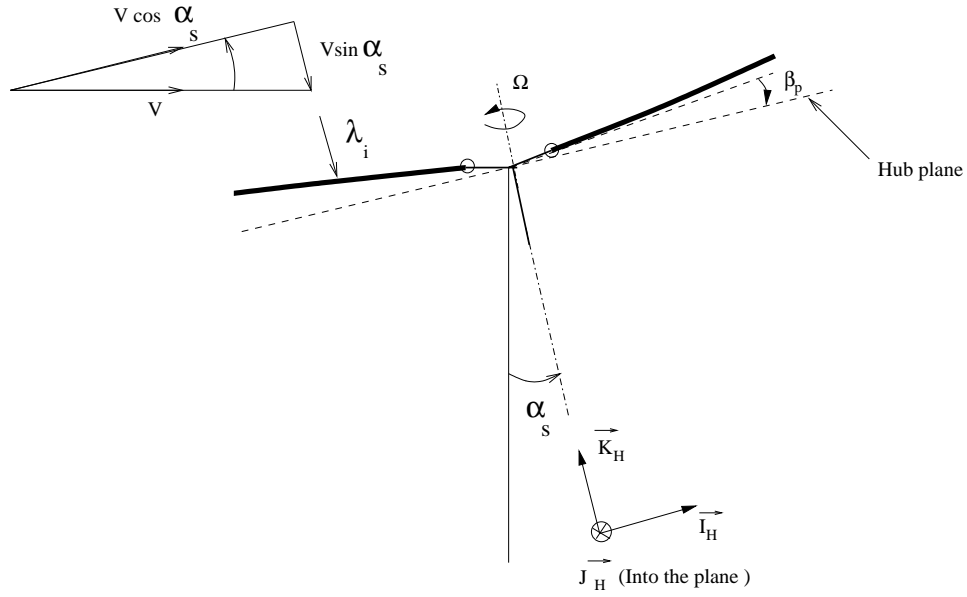
Figure 2.9: Hub fixed non-rotating coordinate system

ponent in the backward direction is because of forward motion of the helicopter at the desired advance ratio $\mu = V \cos \alpha_s / \Omega R$ (V is the vehicle forward speed; α_s the forward shaft tilt and ΩR is the rotor tip speed). The downward component is because of the total inflow through the rotor, which is in turn composed of a free stream component and an induced inflow component. Let us define $(\hat{I}_H, \hat{J}_H, \hat{K}_H)$ as the orthonormal basis vectors in the hub fixed non-rotating coordinate system. Then the wind velocity can be expressed as

$$\vec{V_w} = (\mu \Omega R) \hat{I}_H - (\lambda \Omega R) \hat{K}_H \tag{2.71}$$

The rotor inflow can be expressed as :

$$\lambda = \mu \tan \alpha_s + \lambda_i \tag{2.72}$$

As mentioned earlier, $\mu tan\alpha_s$ is the component of free stream velocity perpen-

78

dicular to the hub plane and λ_i is the non-dimensional rotor induced inflow associated with the lift on the rotor. For the quasi-steady aerodynamic modeling the wind velocity needs to be expressed in a rotating undeformed coordinate system (blade fixed). Two transformations need to be performed for this, first from non-rotating to rotating frame and second from no precone angle to a precone angle β_p. Rotor hubs are often designed with a small precone angle β_p to relieve the bending stresses in the cruise conditions and hence improve fatigue life. The wind velocity can be expressed in the rotating undeformed frame after performing these transformations and using a small angle assumption for β_p as :

$$\vec{V_w} = V_{wx}\hat{i} + V_{wy}\hat{j} + V_{wz}\hat{k} \tag{2.73}$$

where

$$
\begin{aligned}
V_{wx} &= \mu\Omega R \cos\psi - \lambda\Omega R\beta_p \\
V_{wy} &= -\mu\Omega R \sin\psi \\
V_{wz} &= -\mu\Omega R \cos\psi\beta_p - \lambda\Omega R
\end{aligned}
\tag{2.74}
$$

The blade velocity in the rotating undeformed frame can be written as:

$$\vec{V_b} = \dot{\vec{r}} + \vec{\Omega} \times \vec{r} \tag{2.75}$$

where $\vec{r} = (x_1, y_1, z_1)$ is the position vector from the center of the hub to a point on the deformed blade in the rotating undeformed coordinate system. After applying the transformation for the finite precone angle β_p one obtains:

$$\vec{V_b} = V_{bx}\hat{i} + V_{by}\hat{j} + V_{bz}\hat{k} \tag{2.76}$$

where

$$V_{bx} = \dot{x}_1 - \Omega y_1 \cos \beta_p$$

$$V_{by} = \dot{y}_1 + \Omega x_1 \cos \beta_p - \Omega z_1 \sin \beta_p \qquad (2.77)$$

$$V_{bz} = \dot{z}_1 + \Omega y_1 \sin \beta_p$$

For the quasi-steady aerodynamic modeling, we require the effective velocity at the 3/4 chord location. Substituting for $\dot{x}_1$, $\dot{y}_1$ and $\dot{z}_1$, calculated using the section wise blade deformations ($[u, v, w, v', w', \theta_1]$) one obtains:

$$V_{bx} = \dot{u} - (\dot{v}' + w'\dot{\theta}_1)\eta_r \cos \theta_1 - (\dot{w}' - v'\dot{\theta}_1)\eta_r \sin \theta_1 - \Omega(v + \eta_r \cos \theta_1)$$

$$V_{by} = \dot{v} - \dot{\theta}_1 \eta_r \sin \theta_1 + \Omega[x + u - v'\eta_r \cos \theta_1 - w'\eta_r \sin \theta_1 - (w + \eta_r \sin \theta_1)\beta_p]$$

$$V_{bz} = \dot{w} + \dot{\theta}_1 \eta_r \cos \theta_1 + \Omega \beta_p(v + \eta_r \cos \theta_1)$$

$$(2.78)$$

Here η_r is the non-dimensional distance (non-dimensionalized by the blade radius) between the feathering axis location and the three quarter chord point. For simplifying the analysis one can neglect the term $\vec{V}_f$ in Eq 2.70, assuming limited fuselage motions at steady level flight conditions and small angle assumption for the precone angle β_p.

The resultant velocity at any radial station can then be expressed in the rotating undeformed coordinate system as:

$$\vec{V} = U_x \hat{i} + U_y \hat{j} + U_z \hat{k} = (V_{bx} - V_{wx})\hat{i} + (V_{by} - V_{wy})\hat{j} + (V_{bz} - V_{wz})\hat{k} \qquad (2.79)$$

where (V_{bx}, V_{by}, V_{bz}) and (V_{wx}, V_{wy}, V_{wz}) are known from Equations 2.78 and 2.74 respectively. These velocity components could be transformed to the deformed rotating frame using the transformation:

$$\left\{ \begin{array}{c} U_R \\ U_T \\ U_P \end{array} \right\} = T_{DU} \left\{ \begin{array}{c} U_x \\ U_y \\ U_z \end{array} \right\} \tag{2.80}$$

where the transformation matrix T_{DU} is given by Eq 2.30. The variable θ_1 represents the total pitch of the blade which is given by $\theta_1 = \theta_c + \hat{\phi}$, where θ_c are the control deflections and $\hat{\phi}$ is the elastic torsional deflection. The resultant velocity at any section expressed in the deformed rotating frame ($[U_T, U_P, U_R]$) where (U_T=tangential, U_P=perpendicular and U_R=radial or out of plane) is sufficient to define an effective angle of attack (See Figure 2.10) given by:

$$\alpha = \tan^{-1} \left(\frac{-U_P}{U_T} \right) \tag{2.81}$$

For a purely strip theory based aerodynamic modeling one could lookup the C_l, C_m and C_d (aerodynamic lift, pitching moment and drag coefficients) from C81 type airfoil tables. These tables are usually compiled using available experimental data for the specific airfoil at that section. In Eq. 2.42 a simplified approximation for the aerodynamic coefficients is used, namely

$$\begin{aligned} C_l &= c_0 + c_1 \alpha \\ C_d &= d_0 + d_1 |\alpha| + d_2 \alpha^2 \\ C_m &= f_0 + f_1 \alpha \\ \text{where } \alpha &\approx \tfrac{-U_P}{U_T} \end{aligned} \tag{2.82}$$

2.4.2 Unsteady aerodynamic modeling

The 2-D strip theory accounts for only the circulatory component of the lift. This lift would be that produced in a steady state, i.e., when the airfoil is at rest

81
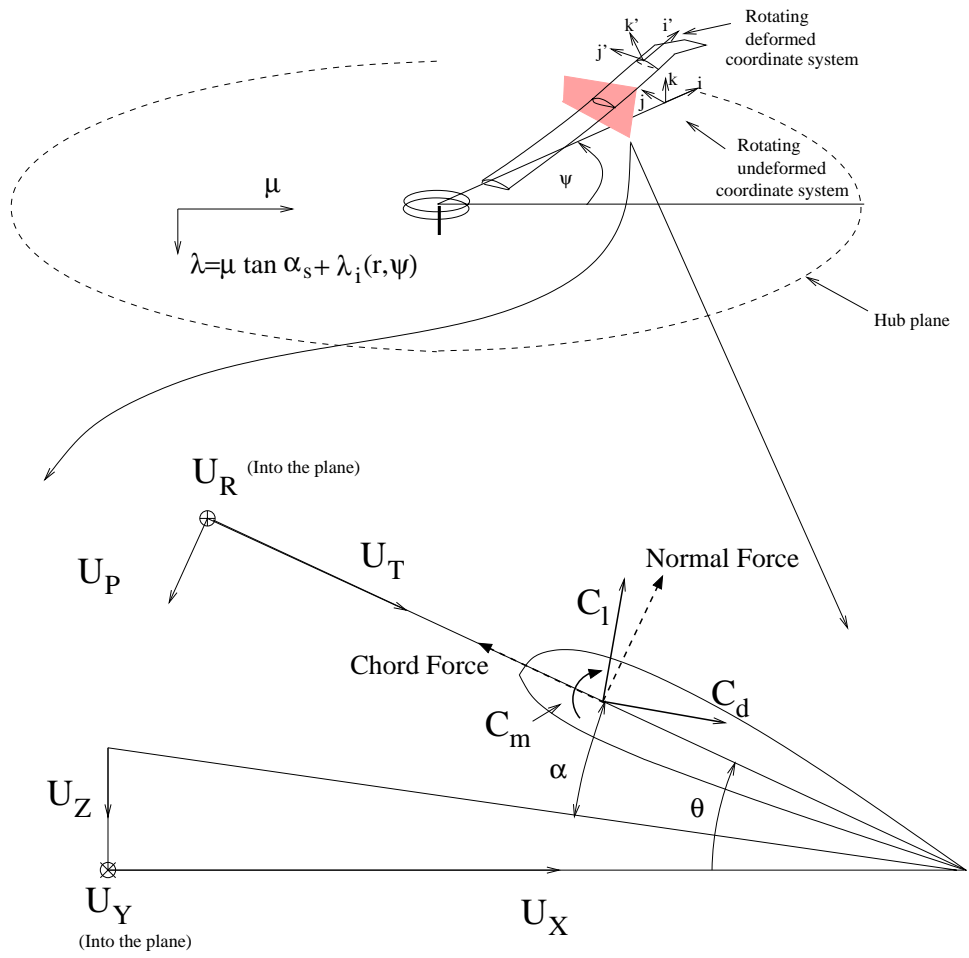
Figure 2.10: Rotating deformed and undeformed coordinate systems

and maintains a constant angle of attack. The effects of compressibility causes circulatory lift to have a deficiency, or in other words a finite time to develop in to its final asymptotic value. Furthermore in a compressible flow regime, the unsteady motions of the blade produce non-circulatory components lift components also. The non-circulatory lift can be explained using Newton's third law. The unsteady motions (plunge for example) are similar to the motion of a piston. Therefore the airfoil imparts a change in momentum to the surrounding fluid by its piston like motion. The reactive force because of this effect is termed non-circulatory lift. The non-circulatory lift is felt instantaneously and then decays with time. Overall, the flow physics in a unsteady flow environment can be modeled by developing approximations for the rate of growth of the circulatory lift and the rate of decay of the non-circulatory lift.

The effective angle of attack (Equation 2.81) is composed of unsteady terms arising from mainly three different unsteady phenomena. They are changes in pitch (plunge can be considered to be effective change in pitch) of the airfoil, change in pitch rate about the feathering axis and penetration in to a vertical velocity field caused by the induced inflow. An attached flow unsteady aerodynamic model uses the assumption that the flow field behaves linearly for small unsteady changes. Hence the angle of attack variation can be discretized and considered as small step inputs at each instant of time. The responses to these step inputs are linearly superposed to find the overall load response. Separate indicial response models are used to represent responses caused by pitch, pitch rate and gust penetration.

Indicial aerodynamic models which represent responses to step changes in pitch angle, pitch rate and penetration into a gust field can be linearly superposed to

extract the total response because of the composite unsteady motion. As described earlier the indicial response consists of two distinct regions, each having different flow physics, with an intermediate overlapping region. The initial loading (non-circulatory) decays rapidly from the initial value within a few chord lengths of distance traveled through the flow. This loading can be computed directly for two dimensional subsonic and supersonic flow quite accurately using linear piston theory. For example, the initial value of the lift magnitude for a step change in angle of attack as given by Bispilinghoff et al [101] from linear piston theory is:

$$C_l(t = 0) = \frac{4}{M}\Delta\alpha \tag{2.83}$$

where M is the free stream Mach number and $\Delta\alpha$ is the step change in angle of attack. The second part of the response is related to the steady-state response to the effective change in boundary condition caused by the impulsive input. This part is called the circulatory response; it is asymptotically reached after the perturbation caused by the step input and is a result of the change in bound circulation. This part can be accurately determined using quasi-steady theory. In the case of a step change in angle of attack for a flat plate the final value of lift is given by quasi steady theory as

$$C_l(t \rightarrow \infty) = \frac{2\pi}{\sqrt{1 - M^2}}\Delta\alpha \tag{2.84}$$

For cambered airfoils, the circulatory lift can be obtained using the steady lift data represented as airfoil tables.

Approximate functional representations of 2-D indicial responses are in general represented as a summation of exponential functions which decay with non-dimensional time (s). Non-dimensional time s is defined as the distance traveled

84

in semi-chords by the airfoil from the instant of the indicial change ($s = \frac{2U_\infty t}{c}$).

The functional forms of lift and pitching moment response for step change in angle of attack and pitch rate given by Leishman [96] are as follows

$$\frac{C_{n_\alpha}}{\alpha} = \frac{4}{M}\phi_\alpha^{nc}(s, M) + \frac{2\pi}{\beta}\phi_\alpha^c(s, M) \tag{2.85}$$

$$\frac{C_{m_\alpha}}{\alpha} = -\frac{1}{M}\phi_{\alpha_m}^{nc}(s, M) + \frac{2\pi}{\beta}\phi_\alpha^c(s, M)(0.25 - x_{ac}) \tag{2.86}$$

$$\frac{C_{n_q}}{q} = \frac{1}{M}\phi_q^{nc}(s, M) + \frac{\pi}{\beta}\phi_q^c(s, M) \tag{2.87}$$

$$\frac{C_{m_q}}{q} = -\frac{7}{12M}\phi_{q_m}^{nc}(s, M) - \frac{\pi}{8\beta}\phi_{q_m}^c(s, M) \tag{2.88}$$

where C_n and C_m respectively represent the lift and pitching moment coefficients induced by a step change in angle of angle of attack or pitch rate. The factor $\frac{2\pi}{\beta}$ in these equations is the lift-curve-slope and can be replaced by the exact value from the airfoil tables.

The functional forms and coefficients of the circulatory and non-circulatory indicial response functions (ϕ) were obtained by Leishman [100] and are given below. The circulatory lift function $\phi_\alpha^c(s, M)$ takes the form

$$\phi_\alpha^c(s, M) = 1 - \sum_{i=1}^{N} A_i e^{-b_i s} \tag{2.89}$$

and the non-circulatory lift function ϕ_α^{nc} takes the form

$$\phi_\alpha^{nc}(s, M) = e^{-s/T_\alpha} \tag{2.90}$$

where T_α is a time constant of decay of the non-circulatory loading. The coefficients A_i and b_i can be determined by an optimization process which minimizes

the least square error between a computed/measured response in frequency domain and the analytical function. The optimization is subject to constraints of initial value and initial slope which are known exactly [102]. Leishman [96] used a two term exponential function to represent the indicial response. The response to a step change was extracted from experimental measurement of responses to a sinusoidal motion using a Laplace transform approach.

Direct CFD calculations of indicial responses are feasible using the field velocity approach. Research efforts [103, 104] used these CFD calculated load time histories to estimate the indicial coefficients. The indicial coefficients can be generalized and expressed in terms of Mach number and mean angle of attack to account for the non-linearity.

2.4.3   Weissinger-L model

The indicial response model accounts only for the shed wake effects. In the 3-D flow environment the trailed vortex effects also need to be accounted for. The trailed vortex flow physics is as follows: the changes in bound circulation along the span causes near wake trailers of varying strengths to be shed along the span. These near wake trailers roll up in to a tip vortex within a few chords of distance. The CFD model gives accurate description for the near wake and its roll up. But in a linearized aerodynamic model a lifting line or lifting surface model needs to be used to account for the near wake effects. The lifting line model is computationally inexpensive, but not accurate enough to model blades with swept tips. The lifting surface (vortex lattice) methods are more computationally expensive, but considered more accurate compared to the lifting line representation. The Weissinger-L model has an intermediate

complexity compared to the lifting line and lifting surface models.

Weissinger theory or extended lifting line theory differs from lifting line theory in several respects [36, 96]. It is really a simple panel method (a vortex lattice method with only one chordwise panel), not a corrected strip theory method as is lifting line theory. This model works for wings or rotors with sweep and converges to the correct solution in both the high and low aspect ratio limits. The basic concept is to compute the strengths of each of the bound vortices required to make the flow tangent to the blade surface at a set of control points. The blade is represented as a set of horseshoe vortices. Each horseshoe vortex consists of a bound vortex leg and two trailing vortices. This arrangement automatically satisfies the Helmholtz requirement that no vortex line ends in the flow. The rotor model used is illustrated in Fig 2.11. A curved near wake trajectory that is approximated by finite length vortex segments is used . The control points are positioned at the three quarter chord location and the zero normal flow conditions at these control points are used to formulate the simultaneous equations for solving bound vortex strengths.

2.4.4   Solution procedure for the blade bound vorticity

Figure 2.11 shows the relative locations of the bound vorticity and the near wake trailed vortex sheet. The bound vortices and control points are located such that they conform to the twist and taper of the rotor blade geometry under study. The trailed vortex geometry, as mentioned previously is appoximated by straight line vortex filaments. The first filament in all cases is parallel to the chord line of the blade at all radial stations. The subsequent filements are found by sweeping the trailing edge of the rotor blade by constant angular displacements. The

boundary condition to be satisfied is the no flux boundary conditions at the blade control points. For the ith control point, this can be expressed as

$$(\vec{V_{i_b}} + \vec{V_{i_t}}).\hat{n} + V_\infty \alpha_{2D} = 0 \tag{2.91}$$

where $\vec{V_{i_b}}$ is the velocity induced by all the bound vortex filaments, $\vec{V_{i_t}}$ is the velocity induced by the trailed vortex sheet, $\hat{n}$ is the surface normal and α_{2D} is the angle of attack as obtained by 2-D strip theory with the unsteady aerodynamic modeling for the shed wake effects. Now, $\vec{V_{i_b}}$ and $\vec{V_{i_t}}$ can be expressed in terms of bound vortex and trailed vortex circulation strengths as

$$\vec{V_{i_b}} = \sum_{j=1}^{N} \Gamma_j \int_0^{l_j} \frac{\vec{dl} \times \vec{r_{ij}}}{|r_{ij}|^3} \tag{2.92}$$

$$\vec{V_{i_b}} = \sum_{j=1}^{N+1} \Gamma_{jt} \sum_{k=1}^{ND} \int_0^{l_k} \frac{\vec{dl} \times \vec{r_{ik}}}{|r_{ik}|^3} \tag{2.93}$$

where Γ_j and Γ_{jt} represent circulation strengths of the jth bound vortex filament and jth trailed vortex vilament respectively. The quantity l_j represents the length of the jth vortex filament and the r_{ij} is the vectorial displacement of the ith control point with respect to the jth vortex filament. The quantities l_k and r_{ik} have similar definition. The integral in the equation represents the Biot-Savart law, and can be evaluated analytically for a straight line vortex filament. The trailed vortex circulation strengths $Gamma_{jt}$ is given by

$$\Gamma_{jt} = -\Gamma_1 \quad j = 1$$
$$\Gamma_{jt} = \Gamma_{j-1} - \Gamma_j \quad 1 < j < N+1 \tag{2.94}$$
$$\Gamma_{jt} = \Gamma_N \quad j = N+1$$

Using Eq 2.94 in Eq 2.93 and expressing the equation Eq 2.91 for all the control points (i.e, i=1,N), a linear system can be obtained of form

$$[a_{ij}][\Gamma_j] = -V_\infty \alpha_{2D} \tag{2.95}$$

These are solved using a Gauss-Jordan elimination technique to obtain the bound vortex strenghs, Γ_j.

2.4.5 Compressibility correction

The Weissinger-L model is only strictly valid for incompressible flows, therefore Prandtl-Glaeurt corrections have to be applied to the geometry for computing compressible flows. The chordwise compressibility effects are inherent from the indicial response model. Equivalent wing planform in zero-Mach-number flow for the same wing sectional shape, angle of attack and twist can be found using Prandtl-Glauert correction of aspect ratio. For a wing, the planform can be transformed simply by contracting the span by a factor of $\sqrt{1 - M^2}$ where M is the free stream Mach number.

For a rotor in hover, the section Mach number varies linearly with distance from the blade root. Thus the blade element at distance r from the root transform to element dr_0 according to the integral

$$\int_0^r \frac{dy}{\sqrt{1 - M(y)^2}} \tag{2.96}$$

where $M(y)$ is the local Mach number of the blade section. Evaluating the integral for $M(y) = M_{tip} y$ gives the equivalent blade in compressible flow as:

$$r_0 = sin^{-1}(M_{tip}r)/M_{tip} \qquad (2.97)$$

2.4.6 Iteration process

The airloads for the prescribed aeroelastic deformations are calculated using the following iterative procedure. In the first step, the prescribed blade motions, measured control angles, and a uniform inflow obtained from the measured thrust are used to calculate the sectional angle of attack. The sectional angle of attack and the incident normal Mach number are used to calculate sectional lift using the airfoil tables and the attached flow unsteady aerodynamic model.

From the lift, the bound circulation strengths are calculated using Kutta-Joukowski (K-J) theory. In the second step, the bound circulation strengths are used to calculate the rotor free wake using a single rolled up tip vortex model. All the circulation beyond the point of maximum circulation is assumed to roll up in to the tip vortex. This approach is chosen based on that used by Bagai [36].

With the new free wake generated inflow, the sectional angle of attack distribution is recalculated. Note that the first 30 degrees of the free wake geometry for the rotor blade under study is not used when the free wake generated inflow is computed. This is to prevent doubly accounting for the tip vortex, because the near wake sheet is modeled in the Weissinger-L model and assumed to roll up within 30 degrees of azimuth.

In the third step, the new angle of attack distribution is used as input to the Weissinger-L model to recalculate the bound circulation strengths. Steps two and three are performed iteratively until the bound circulation converges. Three iterations are usually enough for this purpose.
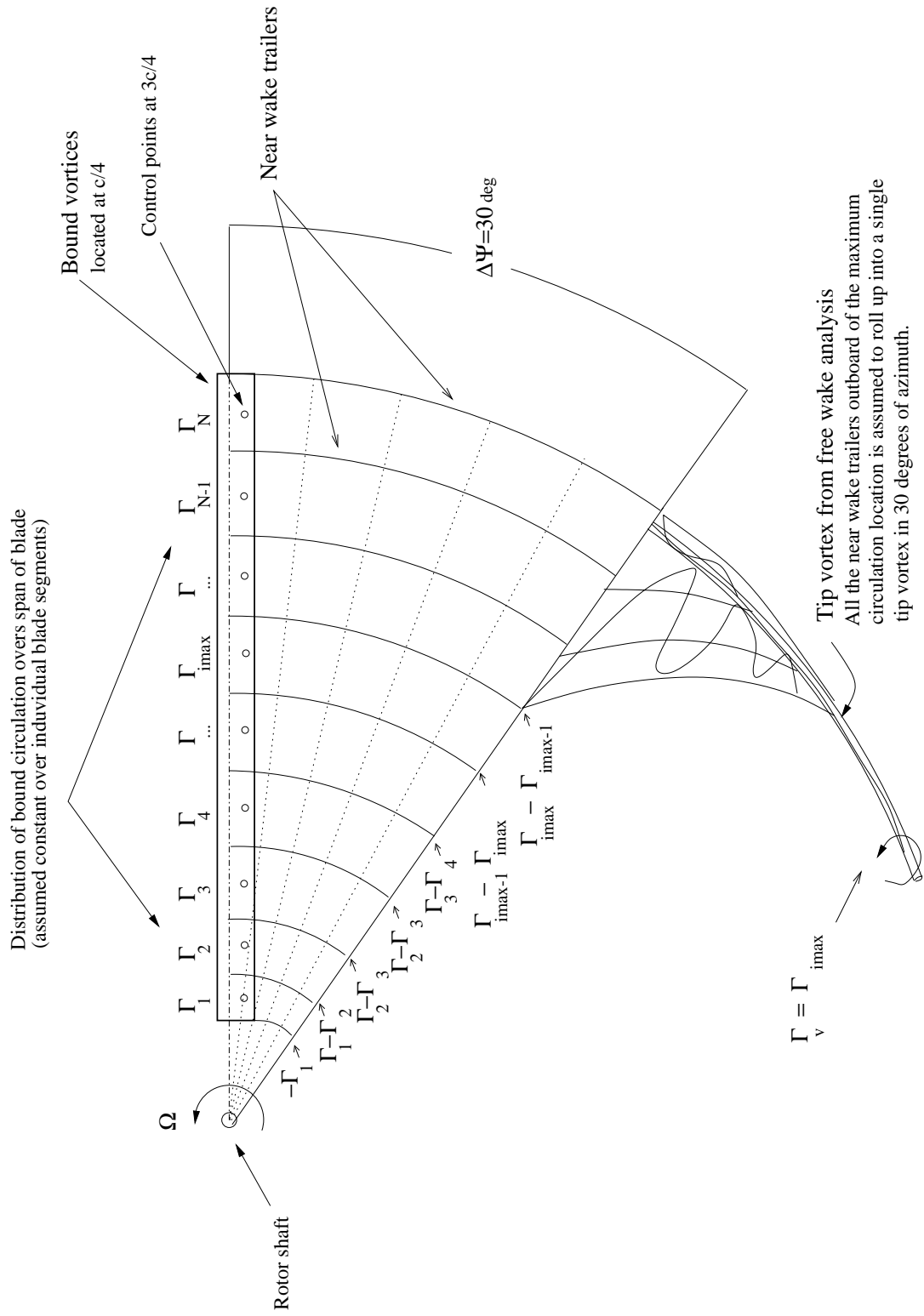
Figure 2.11: Adapted Weissinger-L for trailed wake modeling

Within the above general framework the airfoil tables can be included using two different methods. In the first method the effective angle of attack obtained in step two is scaled to an equivalent flat plate angle of attack. This equivalent angle of attack is used in step three. The resultant bound circulation strength is then used directly to compute lift using the K-J theorem. The angle of attack is reverse looked up using the airfoil tables to obtain the drag and pitching moment. In the second method, the angle of attack in step two is not scaled but provided directly as input to step three. Bound circulation strength obtained in step three is not used to calculate lift using K-J theorem. Instead, they are used to calculated the circulation strengths of near wake trailers. These near wake trailers are used to estimate the induced angle of attack at quarter chord points. This induced angle of attack is subtracted from the angle of attack in step two and the resulting effective angle is used to obtain lift, drag and pitching moment from the airfoil tables.

2.5 Coupling Fluid Dynamics and Structural Dynamics

The *loose coupling* approach, which involves transfer of information between structural dynamic analysis and CFD analysis at every rotor revolution is used for coupling. This technique has the inherent advantage that the trim solution can be obtained simultaneously with the aeroelastic blade response.

The major problems faced by researchers in the loose coupling approach was the divergence of torsional response. Earlier efforts used full potential CFD analysis which overpredicted the pitching moment magnitudes and led to divergence

of torsional response. The present approach, using the Navier-Stokes based CFD analysis, was found to give good prediction of the pitching moments and hence did not show divergence of pitch response.

The sectional aerodynamic coefficients for normal force, chord force and pitching moment are obtained as a function of radius and azimuth from the CFD computations (i.e., $C_n(r, \psi)$ $C_c(r, \psi)$ and $C_m(r, \psi)$). These aerodynamic forces are obtained in the deformed blade frame. The structural analysis reqiures aerodynamic loads in the undeformed frame which can be obtained by expressing the (RHS) of Eq 2.43 as:

$$
\left\{ \begin{array}{c} (L_u)_C \\ (L_v)_C \\ (L_w)_C \end{array} \right\} = \left\{ \begin{array}{c} 0 \\ \frac{\gamma}{6a} C_c U_T^2 \\ \frac{\gamma}{6a} C_n U_T^2 \end{array} \right\} \tag{2.98}
$$

The pitching moment changes are assumed to be negligible with the transformation from the deformed to the undeformed frame. Therefore, C_m obtained from CFD, is directly used as the right hand side of the torsional response equations in the structural analysis.

Briefly the general algorithm for loose coupling is as follows:

1. Obtain an initial guess for control angles and blade motions using UMARC comprehensive analysis solution. The sensitivity of the control angles to the vehicle trim residues (trim Jacobian) are evaluated. The free wake geometry is also obtained as part of the comrehensive rotor analysis solution.

2. Calculate CFD airloads using the control angles, the prescribed blade motions and free wake geometry as inputs.

3. Calculate blade response by using the CFD airloads (normal force, pitching

moment and chord force) as the forcing function in the structural model. The free wake geometry is also recomputed using the CFD based sectional aerodynamic loads.

4. Correct the control angles according to the rotor trim residues using the trim Jacobian evaluated in step 1.

5. Check for blade response and trim convergence. If the convergence condition is not satisfied return to step 2.

This algorithm was used with slight modifications to achieve converged solution in actual practice. The specific details of the modified algorithm used is explained in more detail in the Chapters 3 and 5.

2.6 Summary

This chapter described the fluid dynamic and structural analysis methodology used in this dissertation. The modifications of the CFD analysis to incorporate aeroelastic blade motions and induced velocities caused by a trailed vortex wake were discussed in detail. The structural and aerodynamic methodologies used in a typical comprehensive rotor analysis were also detailed. A brief description of the *loose coupling methodology* which is used to achieve coupling of CFD based three dimensional aerodynamic modeling was also presented.

Chapter 3

Validation and Feasibility Study

The eventual goal of this work is to obtain a coupled CFD based aeroelastic analysis for helicopter rotor systems. However, this requires a careful systematic validation of the 3-D unsteady CFD based aerodynamic model, as well as a feasibility study of the loose coupling approach to tie together the CFD based aerodynamic model with a structural analysis.

The systematic validation of the CFD based modeling starts with the comparison of 2-D static airfoil characteristics of typical rotor airfoils with data tables compiled using experimental data available from various sources. It continues with looking at validating 2-D unsteady model problems (step change in angle of attack and traveling vertical gust) by comparing CFD based results with those from exact analytical solutions obtained from linearized aerodynamics.

Next, the suitability of the field velocity approach for modeling the rotor wake is validated for a 2-D airfoil vortex interaction. The results are validated against those obtained with other CFD based approaches used for incorporating the unsteady velocity field. The requirement of rigorously satisfying the Geometric Conservation Law (GCL) is also elucidated. The accuracy and relative

performance measure of the algorithm developed for the fast evaluation of induced velocities caused by the trailed vortex wake is also examined. Finally, the unsteady airloads measured for a UH-60A helicopter rotor in high speed forward flight are used to validate the 3-D unsteady CFD based aerodynamics model using a prescribed aeroelastic response obtained by forcing the structural dynamics model with the measured airloads. In Chapter 4, this validated approach forms the basis for the method used for identifying the key aerodynamic mechanisms involved in the generation of vibratory airloads.

After the validation of the CFD based model is obtained for prescribed aeroelastic blade response, it is necessary to study the feasibility of the loose coupling approach. This is first performed with a simplified structural analysis, since the success of performing the loose coupling with a simplified structural analysis is at least necessary, though not sufficient, before resorting to a full coupling with a comprehensive rotor structural analysis. The complete loose coupling with a comprehensive rotor structural analysis is examined in more detail in Chapter 5.

3.1   2-D Airfoil Validation

The UH-60A rotor blade is constituted by SC1095 and SC1095R8 sections (Figure 3.1). Typically, comprehensive rotor analyses use airfoil characteristics in C81 table format. These C81 tables are compiled using experimental data available from different sources. A critical assessment of the wind tunnel data for SC1095 and SC1095R8 is documented by Totah [97]. The assessment method followed the same approach as that by McCroskey [98], who examined and eval-
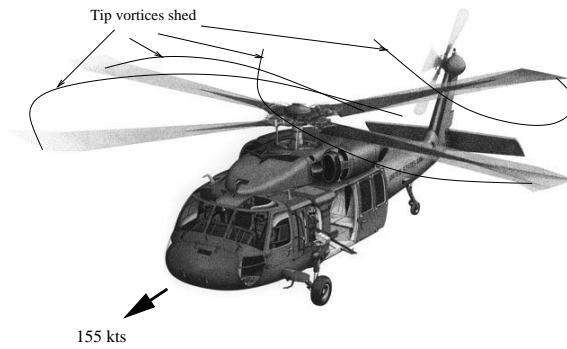
(a) Black Hawk schematic
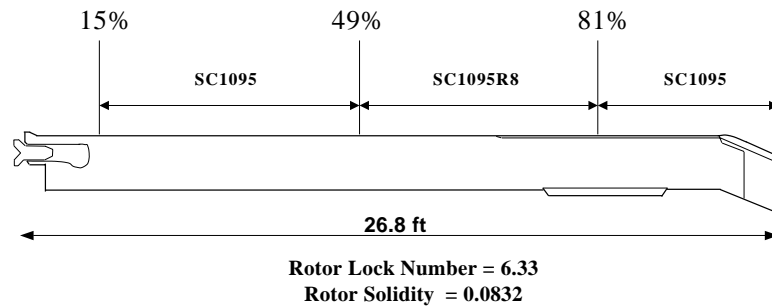
(b) Rotor blade geometry
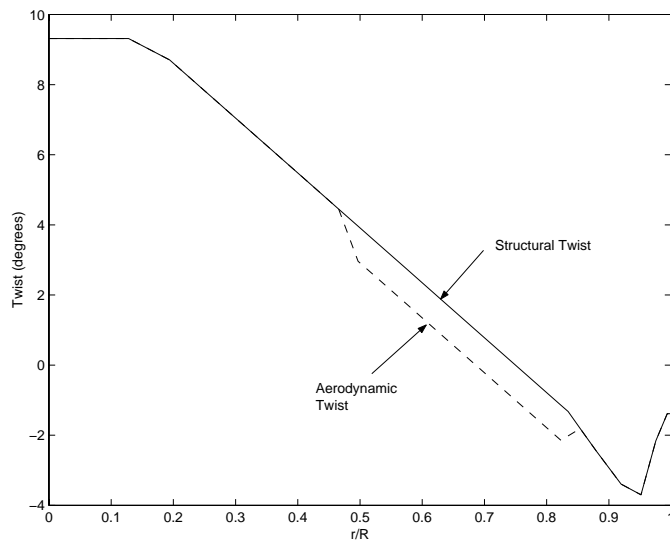
(c) Twist definition

Figure 3.1: UH-60A Black Hawk geometry

1	UTRC Large Subsonic Wind Tunnel
2	Ohio State University Transonic Wind Tunnel
3	National Research Council (NRC) icing tunnel
4	Naval Ship Research and Development Center (NSRDC) 7 by 10 feet Wind Tunnel
5	NASA Langley 6 by 2 inch Transonic Wind Tunnel
6	NASA Ames 2 by 2 feet Transonic Wind Tunnel
7	NASA Ames 11 feet Transonic Wind Tunnel
8	NASA Ames 7 by 10 feet subsonic wind tunnel
9	Glenn L Martin 8 by 11 feet subsonic wind tunnel

Table 3.1: Wind tunnel tests for SC1095

uated the quality of data from 40 wind tunnel tests. The parameters examined include lift-curve slope, minimum drag, maximum lift-to-drag ratio, maximum lift versus Mach and Reynolds number, pitching moment and moment coefficient slope. The major sources for the C81 tables used in this dissertation are listed in Table 3.1 and 3.1. Yeo [99] assessed the quality of this data and generated C81 tables for comparison with CFD calculations. Because of the large number of sources, the reliability and accuracy of these airfoil tables was a concern. Therefore, the CFD analysis is conducted for the SC1095 and SC1095R8 sections to semi-validate both the CFD methodology and the C81 tables. Additionally, effects of using different turbulence models on the predicted aerodynamic characteristics were also investigated.

1	Ohio State Transonic Wind Tunnel
2	National Research Council (NRC) icing tunnel
3	NASA Langley 6 by 28 inch Transonic Wind Tunnel
4	NASA Ames 11ft Transonic Wind Tunnel
5	Glenn L Martin 8 by 11 feet Subsonic Wind Tunnel

Table 3.2: Wind tunnel tests for SC1095R8

3.1.1 RAE2822 airfoil

It is customary to present a case with pressure coefficient validation before one embarks upon a detailed validation of force coefficient variations with angle of attack. The test case chosen was that of the RAE 2822 airfoil as a SC1095 airfoil measured pressure distribution was unavailable to the authors. The data from pressure measurement for this case is from the AGARD test data base [105]. This test case is the accepted standard for CFD research code validation. Figure 3.2 shows the plot of $-C_p$ vs chord location on the airfoil. The salient features of the pressure field including the shock location are well captured. The lower surface pressure coefficient prediction shows excellent correlation with the experimental data. The leading edge suction peak magnitude and location is well captured by both the turbulence models. The shock is predicted to occur closer to the leading edge than that observed from measurements by the Baldwin-Lomax (BL) turbulence model. However, the one equation Spalart-Allmaras (SA) turbulence model shows very good prediction of the shock location. The C-H mesh used in this case was locally refined near the shock location to improve the accuracy of the computations.
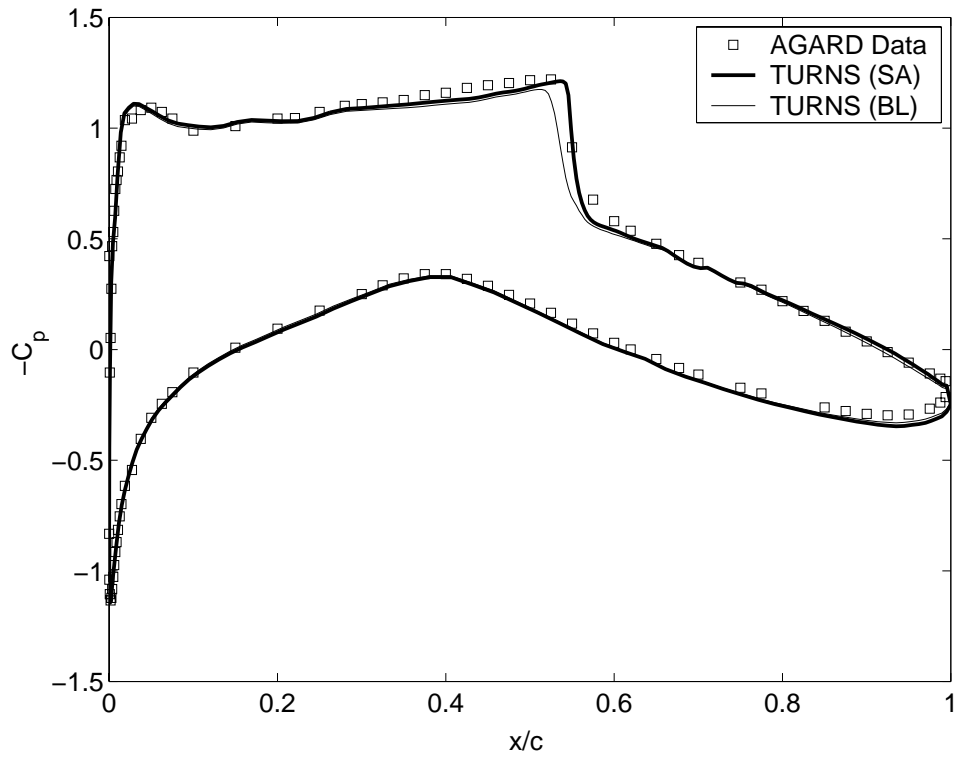
Figure 3.2: $-C_p$ vs $\frac{x}{c}$ for RAE2822 airfoil (M=0.729, α=2.31, Re=6.5 million)

Mach Number	AoA range(deg)
0.3	-10 to 22
0.4	-10 to 22
0.5	-8 to 20
0.6	-8 to 16
0.7	-6 to 12
0.8	-6 to 10
0.9	-4 to 8
1.0	-4 to 6

Table 3.3: Computation Matrix

3.1.2 SC1095 and SC1095R8 airfoil validation

Comprehensive rotorcraft codes often incorporate aerodynamic models that look up force coefficients from airfoil tables (C81 format) generated from experimental data. One of the goals of this investigation is to establish correlation of this 2-D data with CFD computations.

The computational grid used to study this problem is of a C-type topology (Fig 3.3). It has 217 points in the wrap around direction of which 145 are on the airfoil surface. The number of points in the normal direction is 91. The spacing at the airfoil surface is set as 5×10^{-5} chords for the viscous simulations that were performed.

The experimental data base for the SC1095 airfoil consists of force coefficient (C_l, C_m, C_d) data over a range of angle of attacks and Mach numbers. The cases for which the computations are conducted are shown in Table 3.3.

40 chords
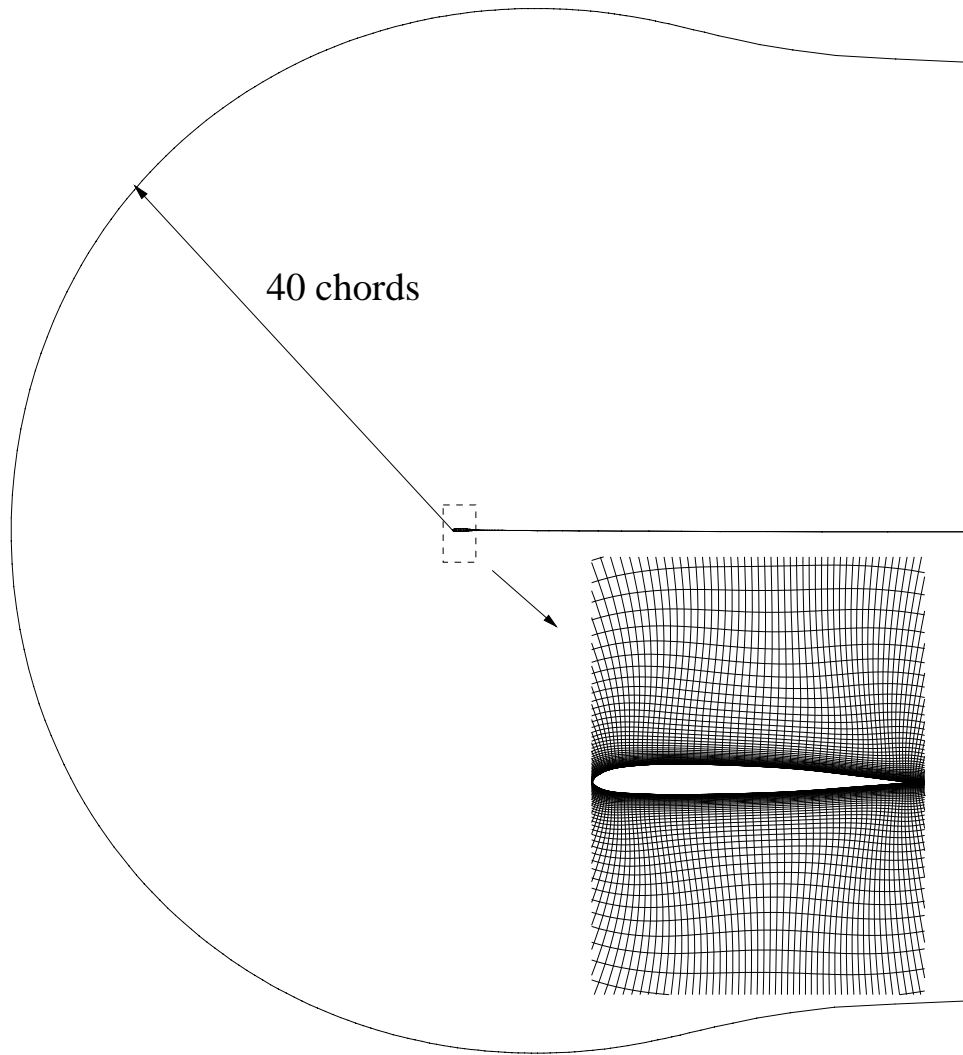
Figure 3.3: C type mesh used (217 X 91)
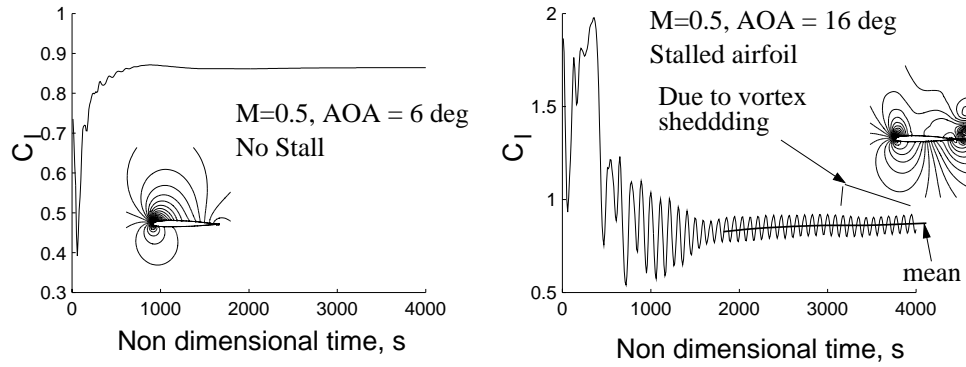
Figure 3.4: Flow fields and lift time history for stalled and unstalled SC1095 airfoil

All the 2-D test cases are conducted at a Reynolds number of 6.5 million which is typical for rotorcraft environments. For cases that do not indicate presence of static stall, the computations are conducted until a steady state is achieved and the final force coefficients are found by integrating the pressure and viscous stresses at the airfoil surface. But for cases in which the airfoil stalls, the flow field no longer reaches a steady state. There is periodic shedding of vortices that results in periodic oscillations in the force coefficients. Hence, in these cases force coefficients are averaged over a period of time. Figure 3.4 indicates salient features of non-stalled and stalled airfoil pressure fields and the lift coefficient time history. In the stalled case, the periodic oscillation in the lift is caused by periodic vortex shedding.

The lift, drag and pitching moment coefficients obtained at each data point in Table 3.3 is plotted against the experimental data in Figures 3.5, 3.6 and 3.7 respectively. The figures consist of a series of 8 subplots each representing a different Mach number. The experimental data is plotted against results obtained using both the Spalart-Allmaras and Baldwin-Lomax turbulence mod-

els. The dark closed symbols represent the cases in which stall was noticed, the aerodynamic coefficient values were found by time averaging in these cases.

The results of all, lift, drag and pitching moment show good agreement with experimental data in the stall free regime at the lower Mach numbers. For the high transonic Mach numbers (M=0.8 and M=0.9), the CFD predictions show a larger lift curve slope compared to the experimental data. The positive static stall angle at all the Mach numbers obtained using both the turbulence models compares well with the experimental data. The abrupt decrease of pitching moment and sudden increase of drag coefficient at the onset of stall is very well represented by both the turbulence models. The closed symbols are given to the data points, which represent cases that showed presence of stall (i.e., force coefficients were time averaged).

The correlation with the test data deteriorates for the SC1095R8 airfoil section (Figures 3.8, 3.9, 3.10). The SC1095R8 airfoil section is more cambered and hence has a smaller zero lift angle of attack compared to the SC1095 airfoil section. The pitching moment magnitudes are also larger for the SC1095R8 airfoil section owing to the larger camber. Although these trends are well predicted by the CFD analysis, there seems to be more differences in the quantitative prediction of the airloads for the SC1095R8 airfoil.

The aerodynamic coefficient values show considerable differences from experimental data in the post stall regime especially at high Mach numbers. In the stall free region both turbulence models predict very similar force and pitching moment coefficient values. But once the airfoil stalls they behave very differently. This is particularly evident in the pitching moment plots. Spalart-Allmaras turbulence model evidently shows better correlation with pitching moment data at

all Mach numbers.

At the low Mach number regime, the Baldwin-Lomax turbulence model is unable to capture the onset of negative stall. However, the Spalart-Allmaras turbulence model shows encouraging results even for these cases. It should be noted though that, further mesh refinement showed deterioration in agreement between the experimental data and predicted lift coefficients even when using the SA turbulence model.

On the whole, the correlation with experimental data could be considered good except at highly stalled conditions. The CFD predictions are found to follow most of the specific trends in variation of aerodynamic characteristics with Mach number and angle of attack.

3.2   Validation of the Field Velocity Approach

The field velocity approach (Section 3.13) is used for including the effects of the trailed vortex wake in the full 3-D rotor computations. The accuracy of the approach is validated for 2-D model problems. The predictions obtained for the 2-D model problems are validated against exact analytical solutions, where available. In cases where closed form solutions are unavailable the predictions are correlated with results obtained using different analysis methods.

The 2-D model problems studied are

1. Step change in angle of attack (indicial problem)

2. Interaction with a sharp edged traveling vertical gust (indicial problem)

3. Airfoil vortex interaction
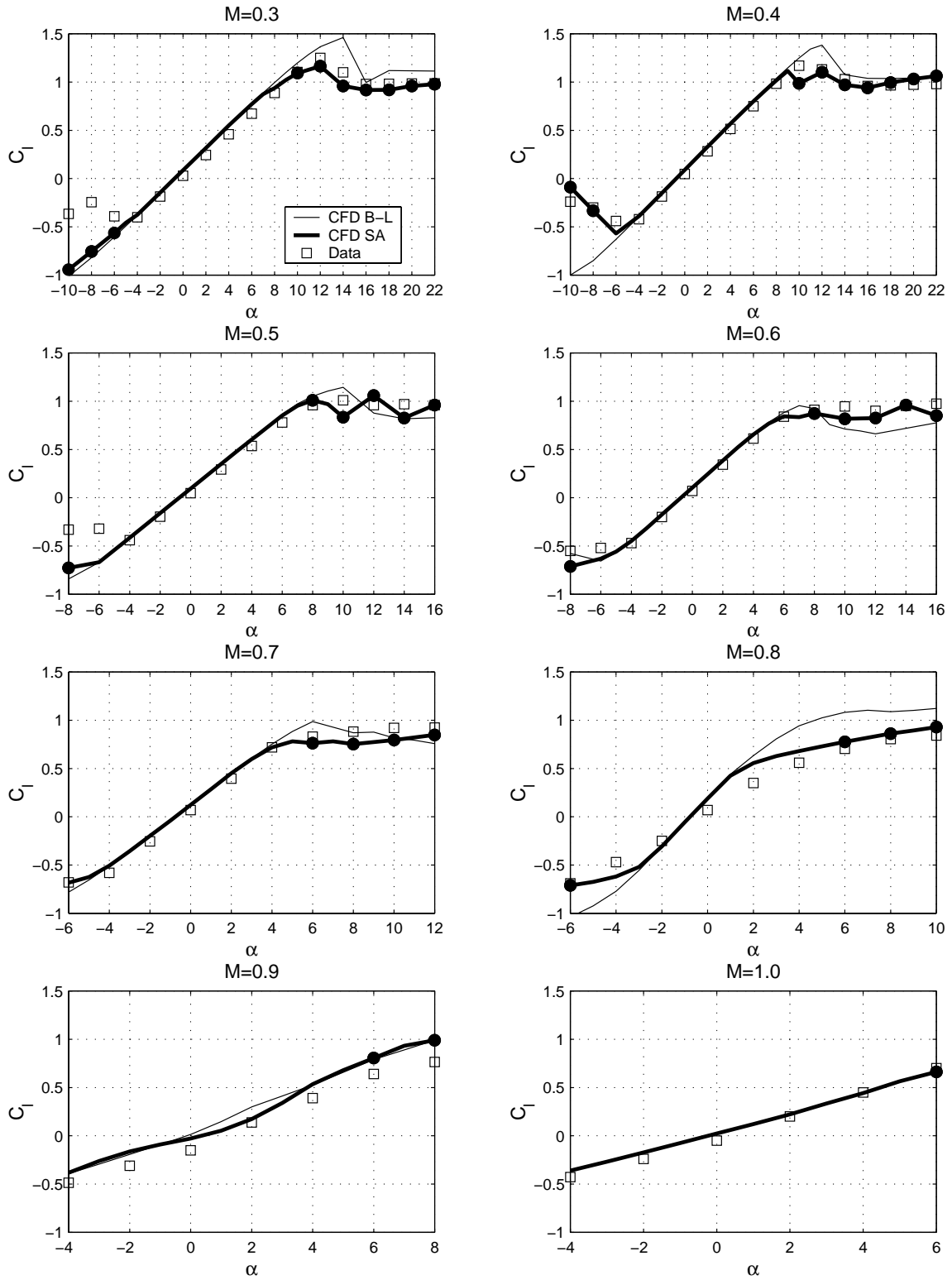
Figure 3.5: C_l Vs α for various Mach numbers for SC1095 airfoil
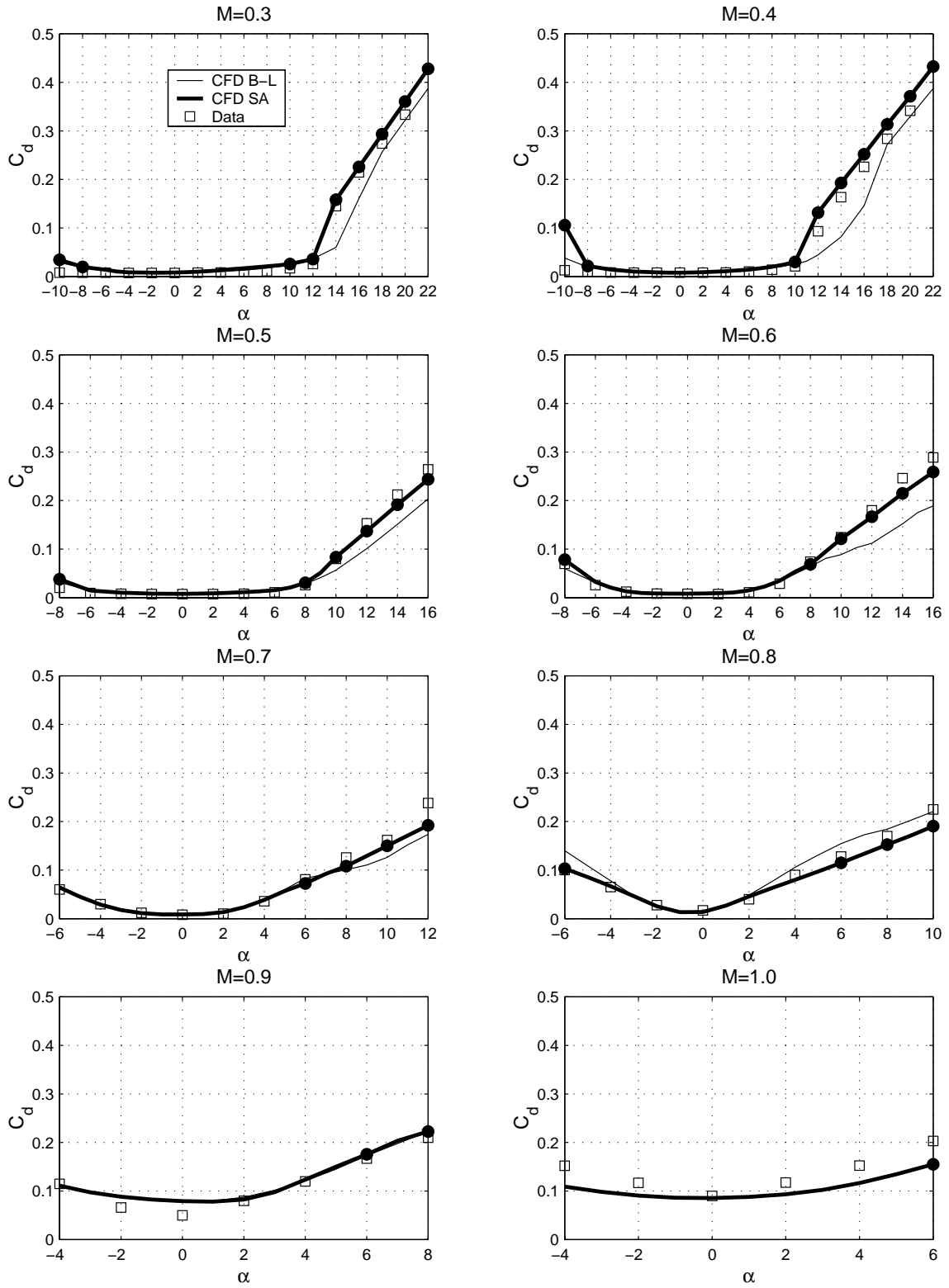
Figure 3.6: C_d Vs α for various Mach numbers for SC1095 airfoil

107
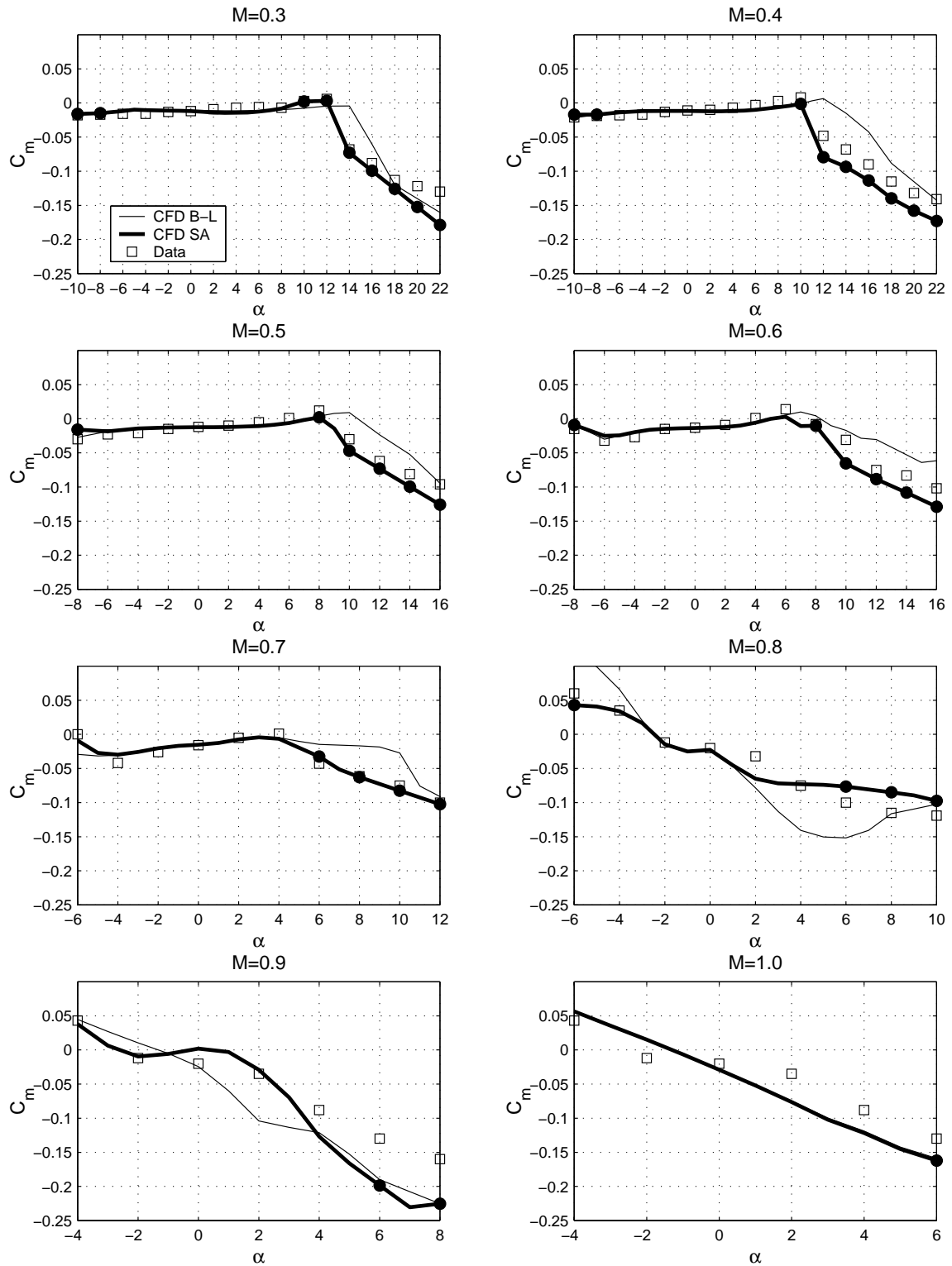
Figure 3.7: C_m Vs α for various Mach numbers for SC1095 airfoil
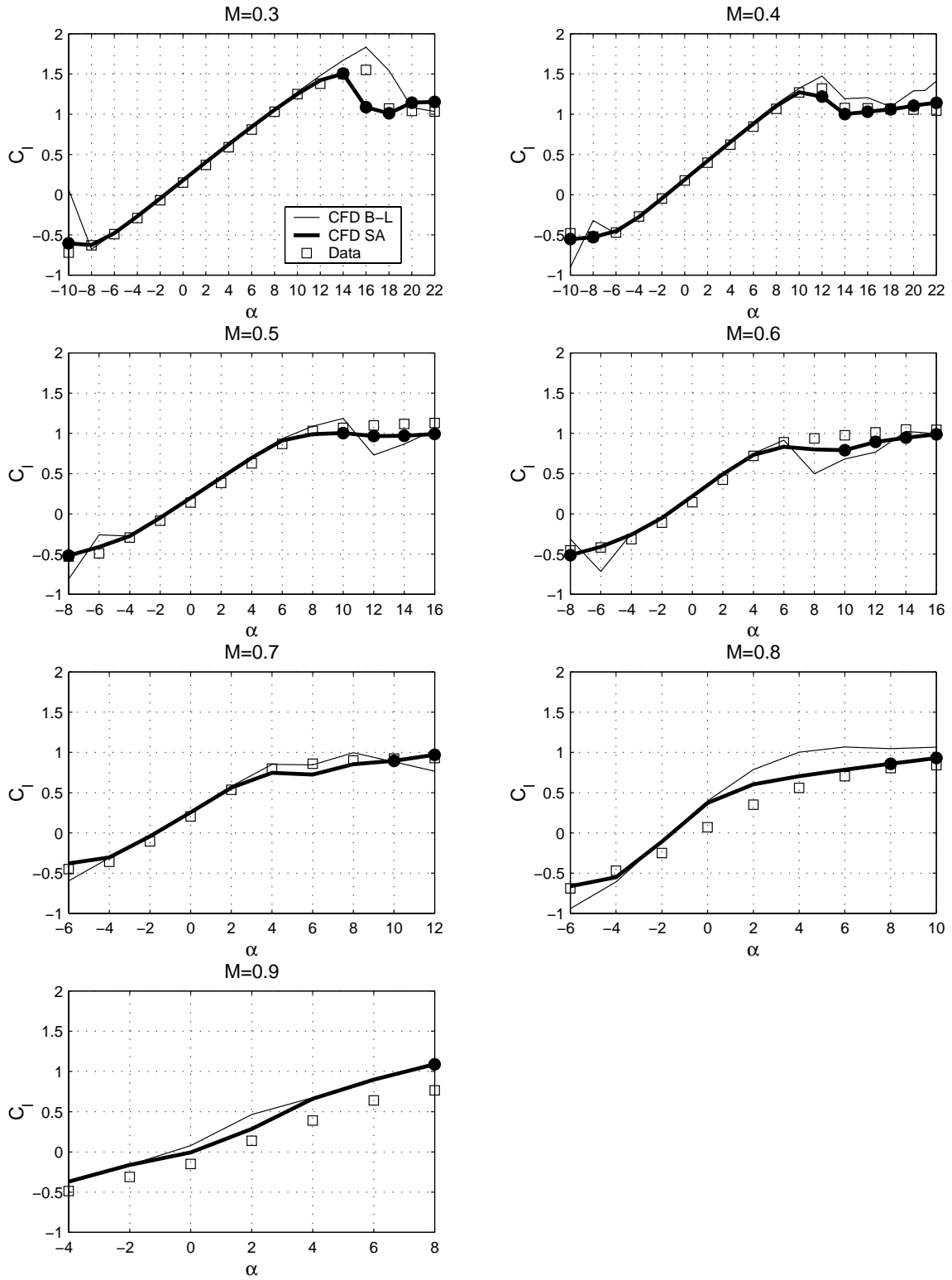
Figure 3.8: C_l Vs α for various Mach numbers for SC1095R8 airfoil
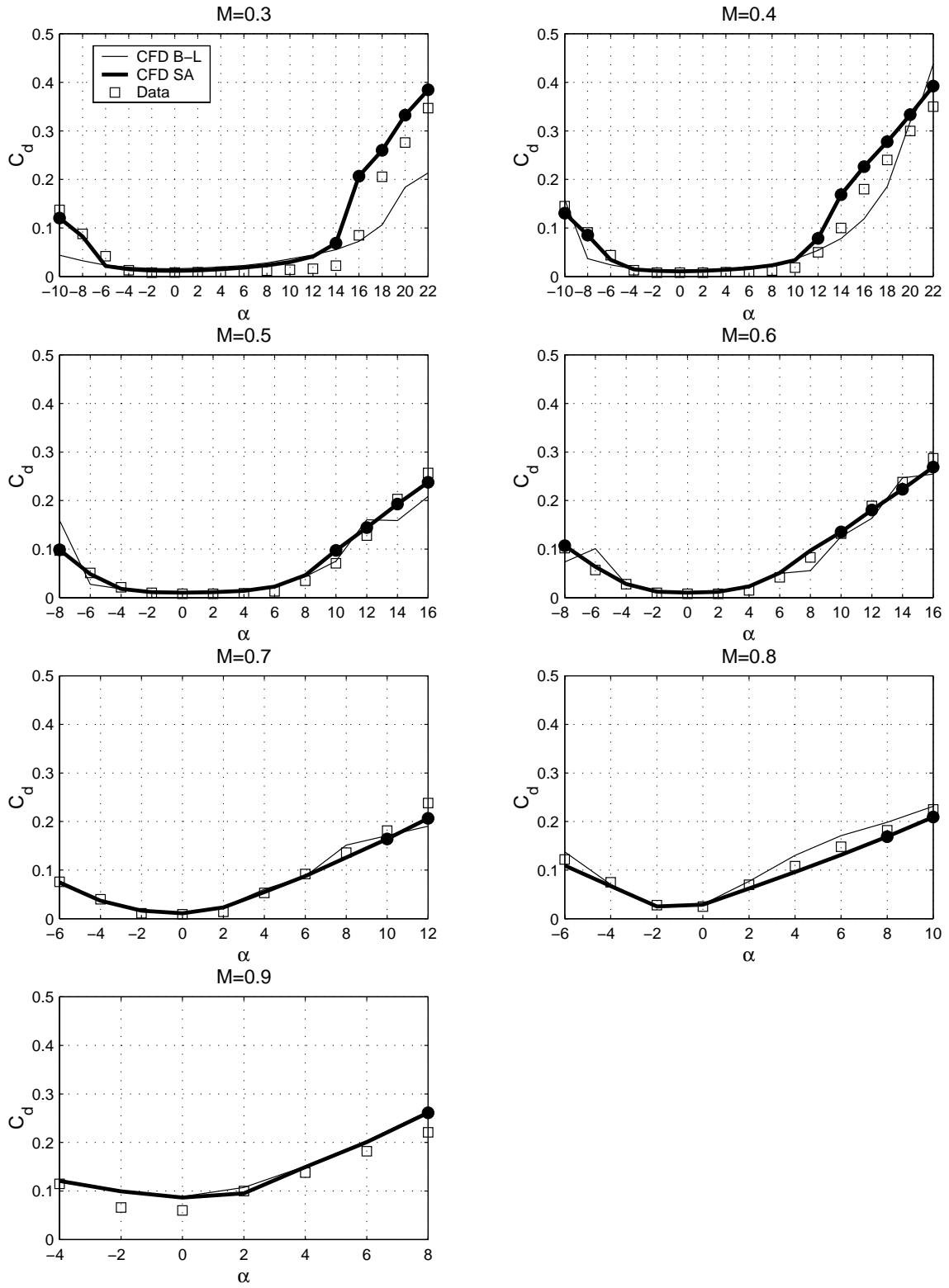
Figure 3.9: C_d Vs α for various Mach numbers for SC1095R8 airfoil
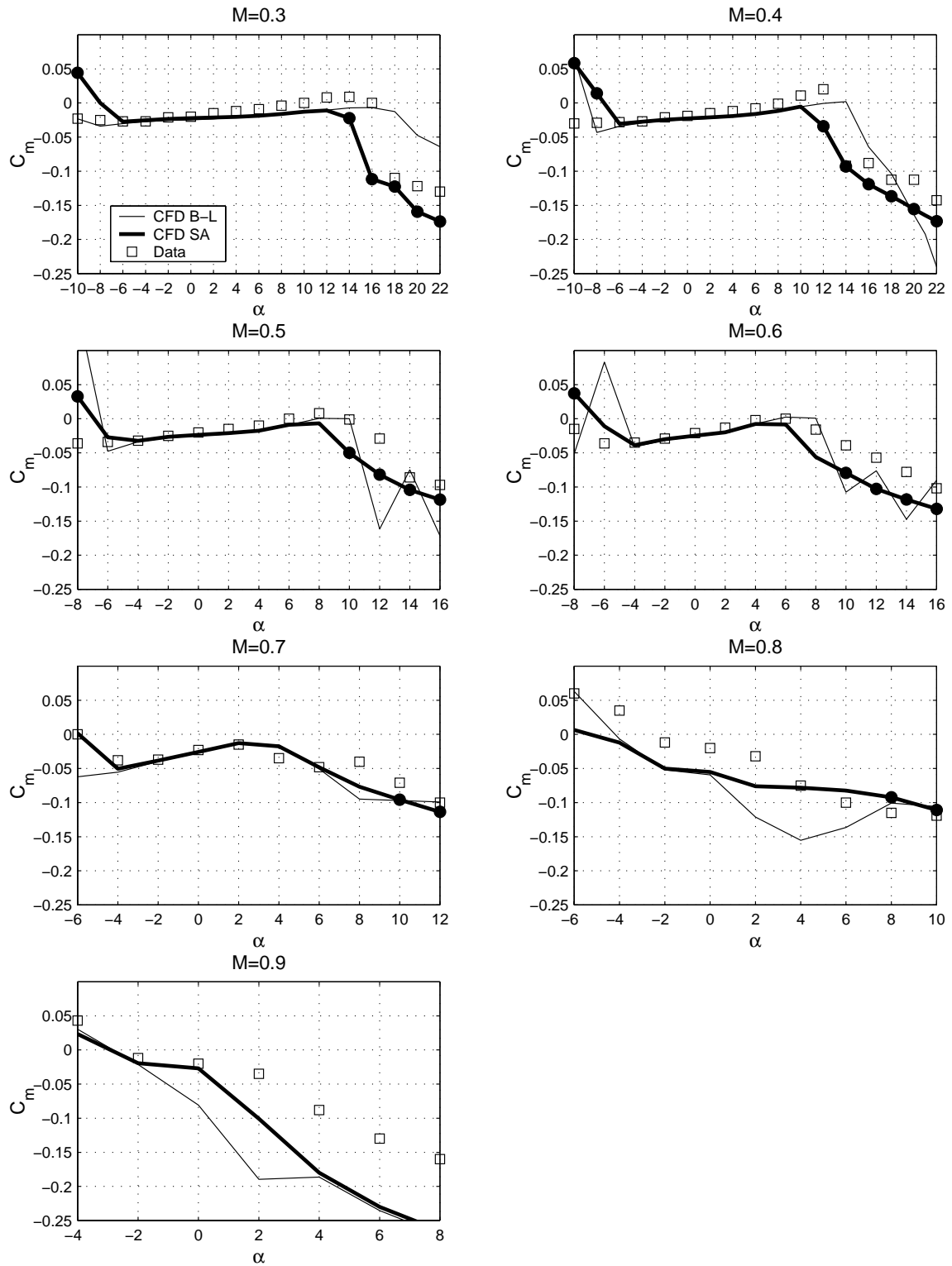
Figure 3.10: C_m Vs α for various Mach numbers for SC1095R8 airfoil

The investigations conducted for the first two model problems are presented in detail in Appendix D. The problem of 2-D airfoil vortex interaction is discussed in detail in this section.

3.2.1 Airfoil vortex interaction

Airfoil vortex interaction is an unsteady two dimensional problem in which a vortex convects perpendicular to the vorticity vector and influences the flow around an airfoil (Figure 3.11). It is the 2-dimensional equivalent of the parallel blade vortex interaction phenomenon observed in helicopter flight. Blade Vortex Interaction (BVI) is one of the dominant source of the low frequency rotor noise. The BVI noise propagates out of plane, usually forward and down making it the most audible noise to an observer on the ground, especially during the landing approach of the helicopter.

The aerodynamic generating mechanism of BVI noise can be explained briefly as follows. When the vortex is upstream of the blade it induces a downwash, and after the vortex passes by the blade an upwash is induced. The time varying vertical velocity change produced during the passage of the vortex changes the effective local angle of attack and causes a corresponding fluctuation in the blade loading. Thus, a sharp impulsive noise signature is created by the large rate of change of loading with time.

There are various ways of simulating the airfoil vortex interaction. One of the popular methodologies is called the perturbation approach [38], in which a flow field is decomposed into two parts despite nonlinearity: one is a prescribed vortical disturbance known to satisfy the governing equations, and the other obtained from the solution of the governing equations. As a result, the vortex structure

is free of numerical diffusion. The second methodology is to use an accurate vortex-preserving Euler/Navier-Stokes solver [39], in which the vortex solution is computed directly from the numerical solution of the governing partial differential equations. This methodology requires a high resolution grid to prevent excessive numerical dissipation. The field velocity approach discussed earlier provides yet another methodology for simulating this problem. The grid time metrics are modified to include the velocity field induced by the vortex.

The results of the aerodynamic loads obtained from all three methodologies are presented in Figure 3.12. The correlation of the results from all three approaches are excellent. The field velocity approach presents a computationally efficient way of simulating the problem, as it does not require a high resolution grid and is computationally less complex compared to the perturbation approach.

The vortex preserving approach requires solution adaptive grid generation to prevent numerical dissipation. An adaptive grid generation causes changes in the volumes of grid cells with each time step. The results presented are from the work of Tang [39], which clearly illustrate the necessity of satisfying the GCL in such computations.

Figure 3.2.1 shows the unadapted and adapted mesh for the vortex preserving approach. If the geometric conservation law is not satisfied, an artificial source term is created which leads to the radiation of pressure waves from the leading edge of the airfoil. Figure 3.14, which shows the pressure contours when the vortex is about 5 chords upstream of the airfoil, clearly illustrates this phenomenon. Satisfying the GCL eliminates these spurious source terms and produces a smoother and more accurate solution as shown in Figure 3.15.
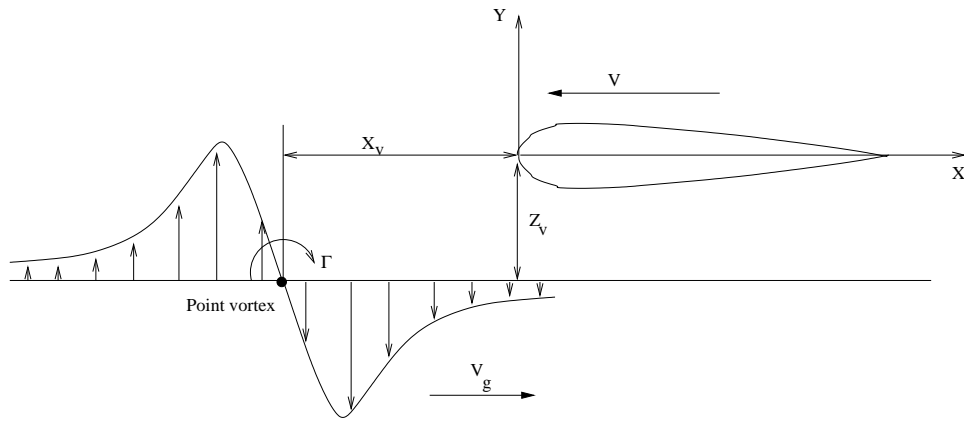
Figure 3.11: Schematic of Airfoil Vortex Interaction
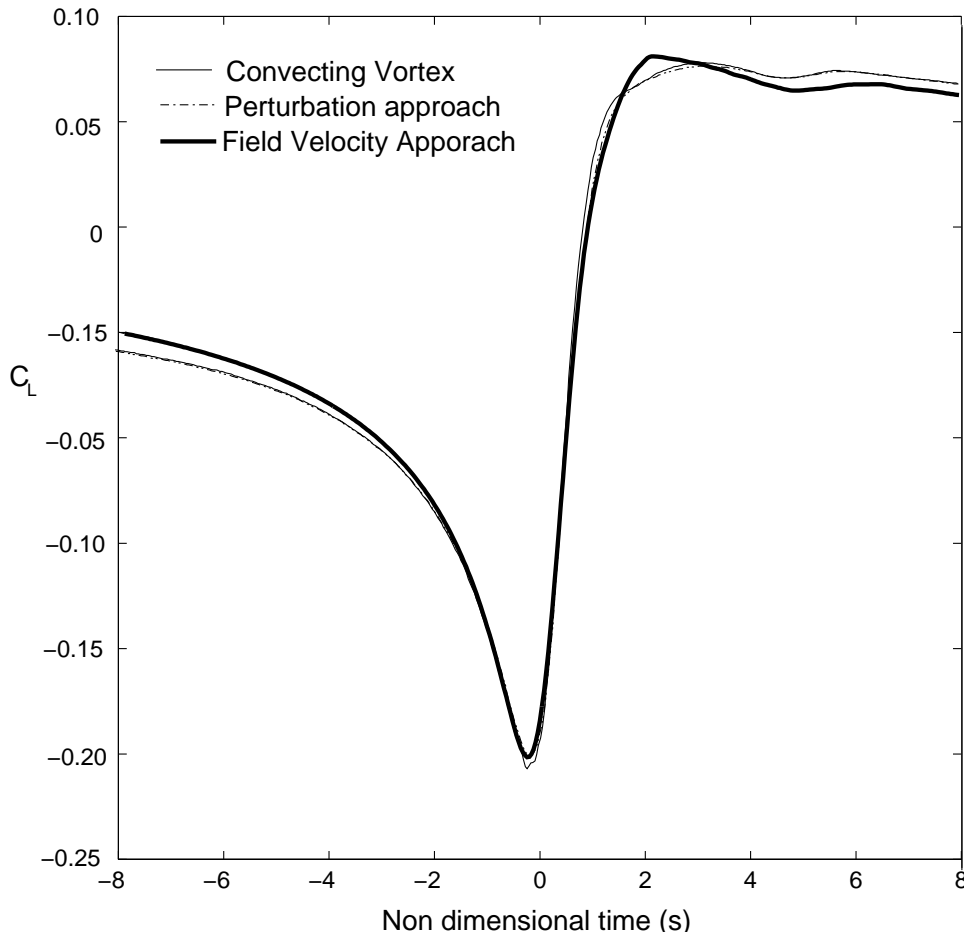
Figure 3.12: Blade Loading time history (M=0.6, miss distance(Z_v=-0.25c))

(a) unadapted   (b) adapted
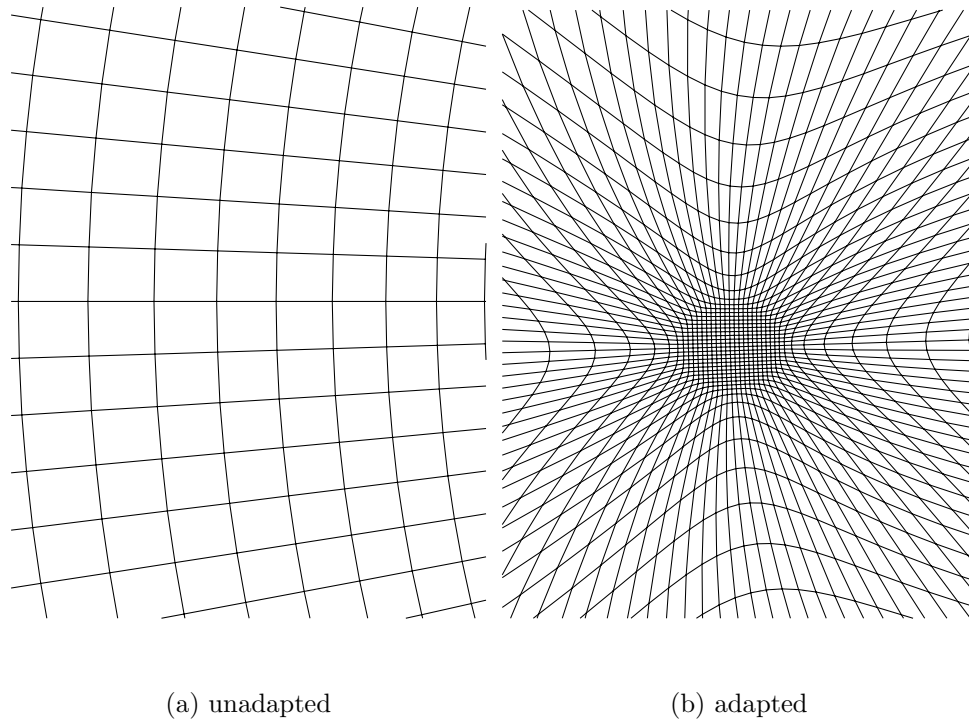
Figure 3.13: Grids in Vortex region
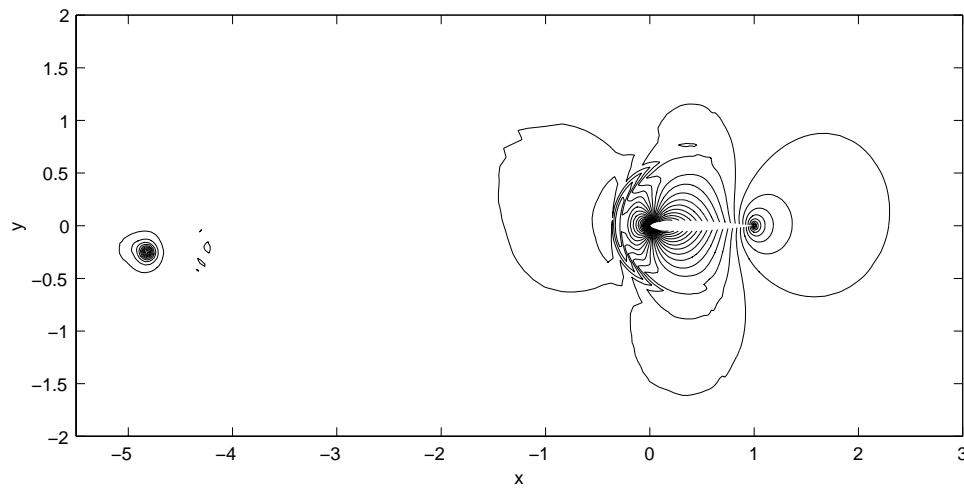
Figure 3.14: Non dimensionalized pressure contours without satisfying the GCL
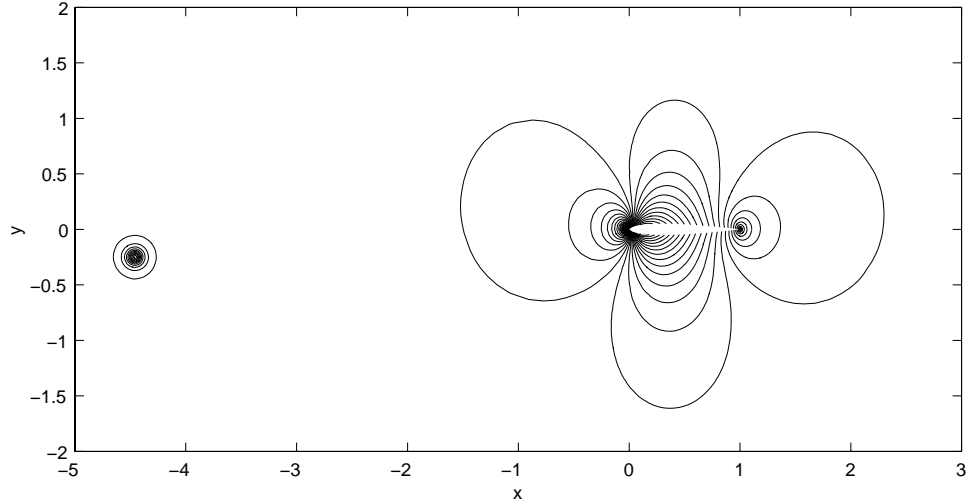
Figure 3.15: Non dimensionalized pressure contours with the time metrics satisfying the GCL

3.2.2 Accuracy of the algorithms for fast evaluation of induced velocities

Simulation of a real helicopter rotor blade in forward flight, as mentioned earlier, requires the use of the field velocity approach to prescribe the effects of the self generated trailed wake as well as the trailed wake from the other rotor blades. The rotor blade motions which consists of pitch, flap and lag also needs to be included.

The trailed vortex wake geometry can be obtained using a prescribed empirical formulae [111] or can be predicted using a free wake analysis using a Lagrangian vortex lattice method [94] as described in the previous chapter. The vortex wake geometry obtained consists of a description of the locus of the vortex filaments in space at discrete azimuthal positions of the rotor blade. Often, the azimuthal discretization of the wake geometry is much coarser ($\Delta\psi = 5^o$) than the az-

116

imuthal discretization used for the flow computations ($\Delta\psi = 0.25^o$). This necessitates the use of an appropriate interpolation technique to obtain the vortex wake geometries at the finer discretization level. In this case, the interpolation is performed spectrally, taking in to advantage the periodicity of the wake with azimuthal angle.

The field velocity approach requires the evaluation of induced velocities caused by the vortex wake system at every grid point in the computational domain. Therefore, a performance enhancement technique which maintains the necessary accuracy is required to perform routine computations using this methodology.

The performance enhancement is obtained using fast hierarchical algorithms [93, 112]. Briefly, these algorithms use the recursive subdivision of the computational domain and a delineation of the near-field and far-field regions. The algorithm is explained in more detail in Chapter 2. Hence, for any grid point, the influence because of all the vortex filaments in its near field is evaluated exactly, while the effects of vortex filaments in the far-field are evaluated using an appropriate interpolation or multipole expansion of the far field potential. Typical run-times are reduced by an order of magnitude (i.e. from 4 days to 10 hours) using the performance enhancement with very little loss of accuracy.

A detailed mathematical description of the fast hierarchical algorithm and quantitative estimates of the performance measure for a blade vortex interaction (BVI) problem is presented in Appendix A.

3.3 Validation of Unsteady Aerodynamic Load Prediction

The flight condition chosen is that of the UH-60A helicopter in high speed forward flight with V=158kts and a blade loading C_T/σ=0.0783. This particular test case was chosen because of the noted modeling issues that occur for such a condition, such as the phase error in the negative lift and the error in the peak to peak magnitudes of predicted pitching moments (Bousman [3]). Also, a plethora of aerodynamic flight test data (Kufeld et al. [116]) is available for this case to validate the numerical solutions computed.

A first principle based airload prediction scheme required coupling of both aerodynamic and structural methodologies. The aerodynamic and structural models have to be validated independently before resorting to full coupling. The aerodynamic model can be validated by prescribing measured elastic deformations and validating the airloads predicted with measured airloads. But there are no measured aeroelastic deformations available. Hence, the following strategy is adopted:

1. Measured aerodynamic and structural dynamic loads are available. Therefore, measured aerodynamic loads were prescibed as the forcing in to the structural model and the aeroelastic blade response were extracted. The structural loads obtained were correlated with the measured structural dynamic loads to ascertain the fidelity of the structural model.

2. The blade motions obtained from the validated structural model was be treated as the best blade motion set available. These were prescribed in to the CFD model and sectional aerodynamic loads were extracted.

3. The CFD predicted aerodynamic loads were then compared with the flight test measurements.

The aeroelastic deformations are obtained from two separate structural analysis codes, namely UMARC [95] and DYMORE [64].

The computations are conducted using the blade motions obtained from the structural model, when it was forced with measured aerodynamic loads. The measurements of the collective and cyclic angles (θ_0=13.21 deg, θ_{1c}=6.56 deg, θ_{1s}=-9.07 deg) is also prescribed together with the elastic torsional deformations obtained from the structural model. A trim procedure was not conducted by the structural model in this analysis. Hence, prescribing the measured control angles without the appropriate trim procedure causes large steady and 1/rev errors in the normal forces. These can be removed by adjusting the collective and cyclics to maintain trim. The primary interest of the excercise is to validate the vibratory airload prediction. Therefore, a low frequency filter is applied on the normal forces (2/rev and higher will be shown). Also, the pitching moments show large steady errors which are present at some radial stations and absent in other ones. This was determined to be because of the offsets in surface pressure measurements towards the trailing edge [117]. Therefore, the pitching moments variations shown will be with the steady values removed (i.e 1/rev and higher).

3.3.1 Accuracy of the flight test data

The flight test data used in this dissertation is from the UH-60A flight test data base generated at the NASA Ames. Comprehensive flight testing was conducted using a research aircraft with pressure intrumented rotor blades for a period of 10 years staring from 1984 (Bousman [118]). The present test cases are among

the few that have been widely published. There are two data sets used in this dissertation, one for the high speed case (μ=0.368) and one for the low speed case (μ=0.110). Both the cases are from flight 85 (C_T/σ=0.0783) and have code numbers C8534 and C8515 respectively.

The UH-60A rotor blade was instrumented at 9 radial staions. The maximum number of transducers at any radial station was 30. The pressure transducers had a gaussian distribution in the chordwise direction. The pressure measurements from the chordwise transducers are integrated to obtain section normal force, section chord force and section pitching moments. There are many sources of errors possible in this approach. The major sources of errors can be categorized as pressure transducer errors and integration algorithm errors. The quantitative estimates of pressure transducer errors are unavailable. However, Bousman [119] showed that there is negligible variation in sectional aerodynamic loads between cycles in the same counter (e.g., C8534). Therefore, it can be inferred that there is a low probability of pressure transducer induced errors.

The integration algorithm would also contribute large errors when a sparse number of chordwise transducers are used. An investigation is conducted to quantify the errors in the pressure integration scheme. The methodology is as follows:

A 2-D CFD computation was conducted for the SC1095R8 geometry. The mesh topology used 150 points on the airfoil surface. The flow computations are conducted at M=0.4 and α=8°. Given the lower and upper pressure distributions (C_{p_l} and C_{p_u}) the sectional normal force (C_n), chord force (C_c) and pitching

moment (C_m) are known as

$$\Delta C_p = C_{p_l} - C_{p_u}$$
$$C_n = \int_0^1 \Delta C_p d(x/c)$$
$$C_c = \int_0^1 (\frac{dy_l}{dx} C_{p_l} - \frac{dy_u}{dx} C_{p_u}) d(x/c) \tag{3.1}$$
$$C_{m_{le}} = \int_0^1 \Delta C_p (x/c) d(x/c)$$

The accuracy of the integration can be improved by performing the transformation as:

$$x^*/c = \sqrt{(x/c)}$$
$$C_p^* = 2C_p x^*/c \tag{3.2}$$

The integration is performed using a parabolic quadrature (modified Simpson's rule for unequal spacing). The sectional aerodynamic coefficients obtained for 150 points is treated as the most accurate solution. The accuracy of the integration approach is then assessed by using smaller number of points (15 to 50) and quantifying the relative error with the most accurate solution. The results of this analysis is shown in Fig 3.16. It is evident that at the UH-60A transducer spacing with 30 chordwise transducers, there is about 0.15% error in the normal force, 1.1% error in the chord force and 2% error in the pitching moment. However, this is the best possible case. All the radial stations did not have the same number of transducers, the stations with lesser number of transducers will evidently have larger pressure integration errors. Also, in the flight test case considered (Flight 85) it is known that 19 transducers performed unsatisfactorily. Therefore, the analysis performed was extended to the exact UH-60A transducer spacing accounting for the unreliable transducers. The results from this analysis are quantified in Table 3.4. The table presents the expected relative error(%) because of pressure integration algorithm in sectional normal force, sectional chord force and pitching moment at each radial station.
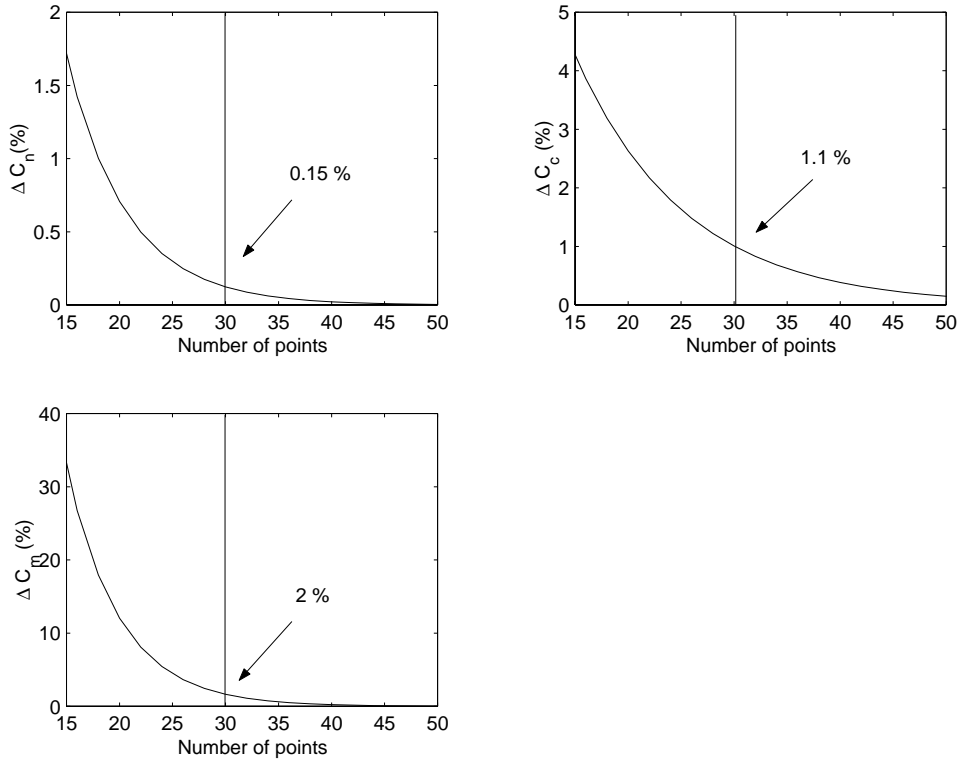
Figure 3.16: Variation of relative error in pressure integration with number of points on the airfoil

r/R	No. of working transducers	$\Delta NF(\%)$	$\Delta CF(\%)$	$\Delta PM(\%)$
0.225	18	1	3.2	18.3
0.400	19	0.7	2.6	12.1
0.550	18	0.8	3	14.4
0.675	17	1	3.4	19.1
0.775	23	0.35	1.8	5.4
0.865	25	0.25	1.5	3.5
0.920	26	0.18	1.3	2.5
0.965	29	0.15	1	2.1
0.990	26	0.17	1.3	2.6

Table 3.4: Expected errors at each radial station because of pressure integration (Flight 85)

3.3.2 Grid dependence study

A study of the grid and time step dependence of the CFD solution is conducted to establish the fidelity of the prediction. The same set of deformation data was prescribed on three sets of meshes. The aeroelastic deformations used were those obtained from DYMORE. The meshes used were a coarse C-H mesh ($133 \times 43 \times 43$) and fine C-O mesh ($217 \times 71 \times 61$) and a fine C-H mesh ($217 \times 71 \times 61$). The azimuthal time step for the coarse mesh computations were 0.25 degrees, while the azimuthal time step for the fine mesh computations were 0.125 degrees. Figure 3.17 shows the oscillatory normal force (2/rev and higher) and pitching moment (1/rev and higher) obtained from the computations using the aforementioned meshes at the two radial stations. The control angles used are the same as those given by the flight test measurements. Again, the steady and 1/rev

harmonics of normal force are removed as the rotor is out of trim because of uncertainities in the measured control angles. The aerodynamic load responses show some grid dependence, especially in the pitching moment response at the outboard radial station. The coarse and refined C-H meshes predict almost the same response, while the C-O) mesh (which has a better tip definition) seems to resolve the higher harmonics better. Overall, the solution could be considered fairly grid independent and acceptable to be used for further prediction. Thus, all of the remaining CFD results use the fine C-H mesh.

A comparison of the aerodynamic loads obtained using deformations obtained from UMARC and those obtained from DYMORE are presented in Fig 3.18. The normal force (2/rev and higher) and pitching moments (1/rev and higher) show good correlation with flight test data for both set of deformations. The computations using the deformations from UMARC better captures the phase of the negative lift, while those using the deformations from DYMORE show better correlation in the pitching moment magnitudes towards the tip. Most of the remaining CFD results use the aeroelastic deformations obtained from UMARC.

3.3.3 Airloads prediction

The aerodynamic loads obtained for the forward flight case of 155 knots (μ=0.368) are shown in Figures 3.19 and 3.20 respectively. CFD results are for the fine mesh using the Baldwin-Lomax turbulence model. The validations, as mentioned earlier, are performed for 2/rev and higher normal force and 1/rev and higher pitching moment because of uncertainities in rotor trim.

From Figure 3.19 it can be inferred that the normal force distributions pre-
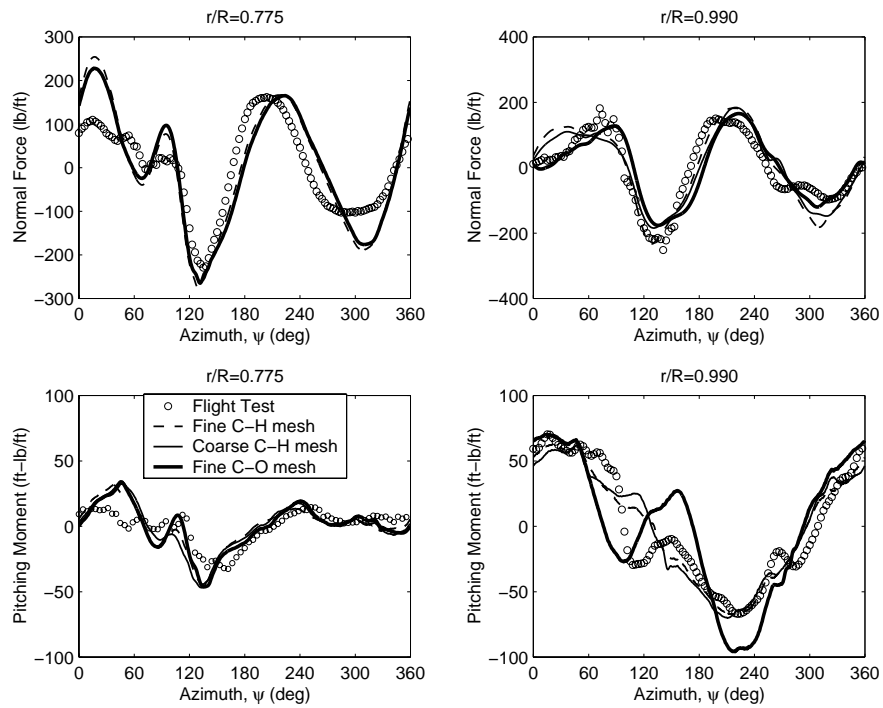
Figure 3.17: Aerodynamic loads, normal force (2/rev and higher) and pitching moment (1/rev and higher) obtained for three different meshes
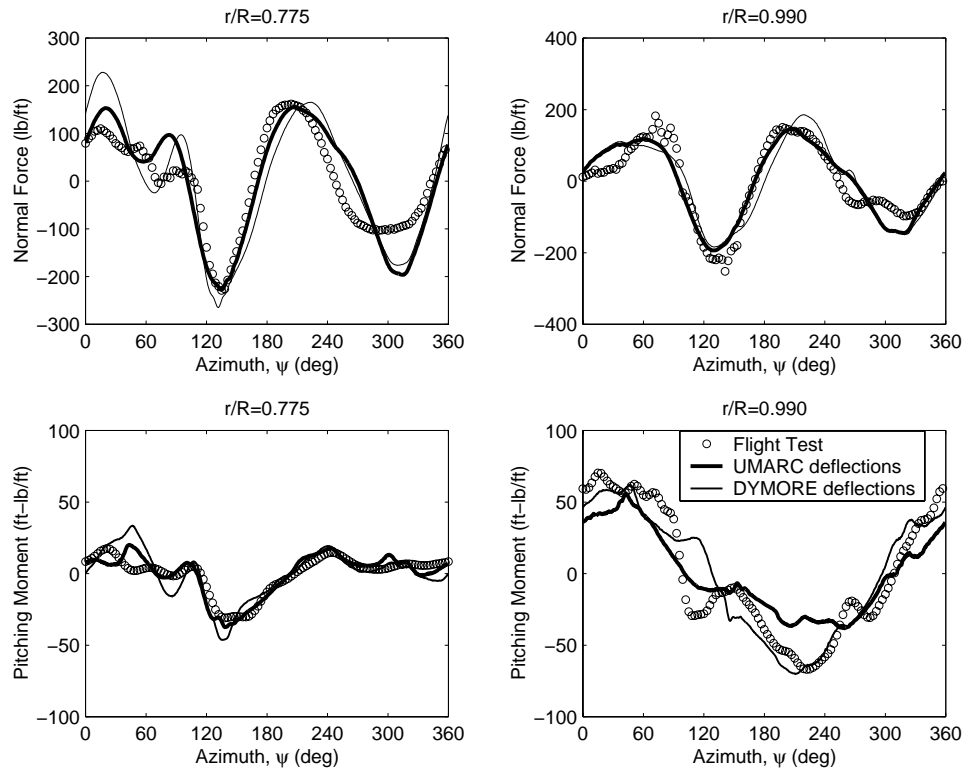
Figure 3.18: Aerodynamic loads, normal force (2/rev and higher) and pitching moment (1/rev and higher) obtained from CFD, prescribed elastic deformations from UMARC and DYMORE, (μ=0.368)

dicted from the CFD calculations show good phase correlation with the test data at all the four radial stations. The lifting line analysis (table lookup, linear unsteady aero, Weissinger-L) was provided the same set of prescribed blade motions. The results obtained from the lifting line analysis are also compared with those obtained from the CFD analysis and test data. The normal force variations show an absence of the updown impulse and a larger phase error with the flight test data compared to the CFD computations at the inboard stations. However, it should be noted that this phase error is less than that noted in a full comprehensive analysis solution, because the "correct" blade deformations are prescribed.

The advancing blade lift impulse is a major source of all higher harmonics which are transfered to the hub. The rotor acts as a filter for harmonics in airloads. For example, a N blade rotor would only let frequencies which are multiples of N (N, 2N, 3N.. etc) be transfered to the fuselage. For this particular case ($N=4$) the major hub vibrations will be of frequency 4/rev. The frequencies of 3/rev and 5/rev in the rotating frame contribute to 4/rev frequencies in the fixed frame. Therefore, for accurate prediction of hub vibrations, accurate predictions of 3, 4 and 5/rev aerodynamic loads are a necessity.

The pitching moments predicted from the CFD computations show good correlations with the test data at all four span stations shown in Fig 3.20. Both the phase and magnitude of the pitcing moments are resolved accurately. Accurate prediction of pitching moments is a necessity for accurate prediction of torsional elastic response which in turn would play a key role in determining the normal force variation in a coupled simulation. The pitching moments predicted by the lifting line analysis; on contrast show poor correlation with the

127

test data. The pitching moment magnitudes are underpredicted inboard and overpredicted outboard. The phase of the negative pitching moments are also predicted inaccurately.

The chord force predicted from CFD (Fig 3.21) shows significant difference from the flight test data. The CFD computations contain both the viscous and induced drag contributions in the chord force. The flight test chord force is constructed by integrating the pressure measurements from the transducers located on the blade. Hence, the flight test data would have only the induced drag contribution to the chord force. This is the primary reason of the over prediction of the chordforce magnitude by the CFD computations. The lifting line analysis also includes the viscous drag terms because the table-lookup drag coefficients do include the parasite drag component. Therefore, the lifting ling analysis also shows larger chord force magnitude compared to the flight test measurements.

Acoustic pressure and hence noise is dependent on the time rate of change of the normal force. Figure 3.22 shows the time derivative of the normal force obtained from the CFD computations plotted against the flight test data. The peak-to-peak magnitudes of the lift derivatives predicted also show good correlation with the flight test data. But, the prediction does not capture some of the higher harmonic oscillations present in the flight test data.

Figures 3.19 and 3.20 also demonstrate the superior aerodynamic predication capability of the present approach compared to the table-lookup based linearized aerodynamic prediction schemes used in routine comprehensive rotorcraft aeroelastic analysis.

As described earlier, the CFD computations do show differences in the steady

and 1/rev components of the normal force. The changes in control angles and inflow distributions primarily affect the steady and 1/rev components. So, it is possible that the error in the steady and 1/rev components are because the rotor is untrimmed. The control angles (θ_0, θ_{1c} and θ_{1s}) of the rotor were iteratively adjusted to retrim the rotor preserving the elastic deformations. The desired trim target (balance of forces in all three directions) was obtained in about 5 iterations. The changes in control angles obtained were $\Delta\theta_0=1.84^o$, $\Delta\theta_{1c}=-3.64^o$ and $\Delta\theta_{1s}=-1.11^o$ respectively. The changes in inflow because of the presence of fuselage is not modeled in the CFD computations. This might be one of the reason for the changes in control angles from the flight test values when the rotor is retrimmed. A comparison of the total aerodynamic loads at four radial stations with and without retrimming are presented in Fig 3.23. The predicted pitching moments are not greatly affected by retrimming (as expected) and therefore are not shown. The aerodynamic loads obtained with the trimmed rotor show good correlation with the flight test data in both phase and magnitude. It is also clear that the vibratory load phase changes are relatively small for the small changes in control angles. Hence, one could decipher that the vibratory load phase is primarily determined by the elastic motion rather than the rigid motion of the blade. But one should view these results with caution as they do not represent a completely independent approach for trim. The blade response does change with changes in aerodynamic loads. This effect is not modeled here as the structural dynamic analysis is not included in the trim loop. Therefore, these results are presented more to emphasize the relative insensitivity of vibratory aerodynamic loads to control angles rather than good correlation of the overall airloads with the test data.

Figure 3.19: Sectional vibratory normal force (2/rev and higher) for high speed forward flight (μ=0.368, C_T/σ=0.0783) at four radial stations

Figure 3.20: Sectional vibratory pitching moment (1/rev and higher) for high speed forward flight (μ=0.368, C_T/σ=0.0783) at four radial stations
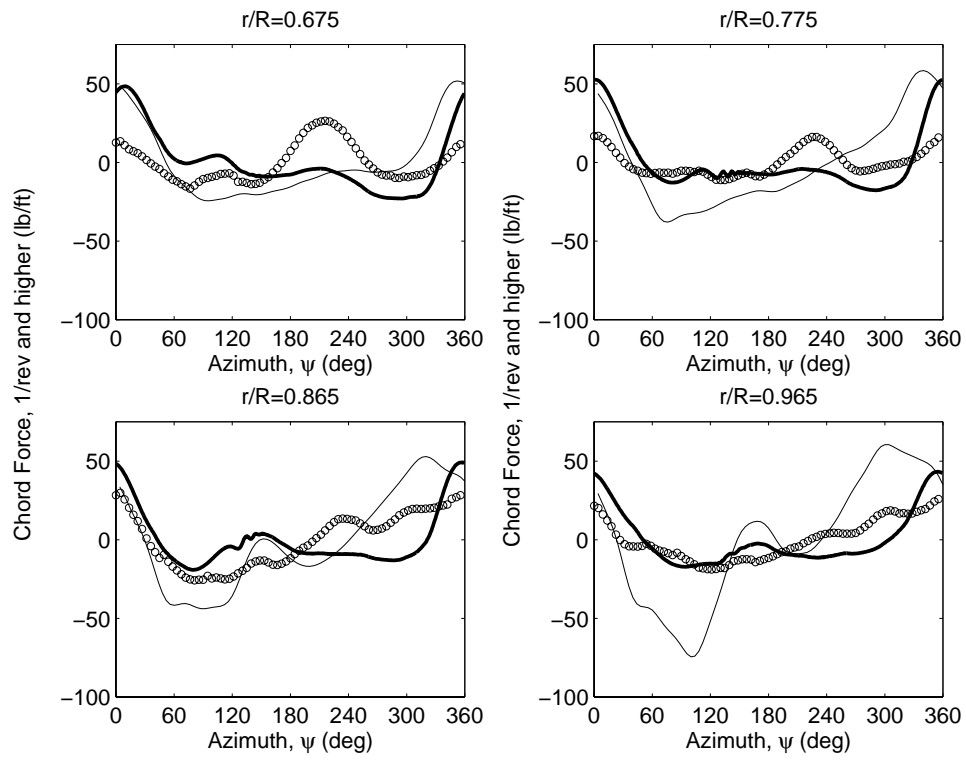
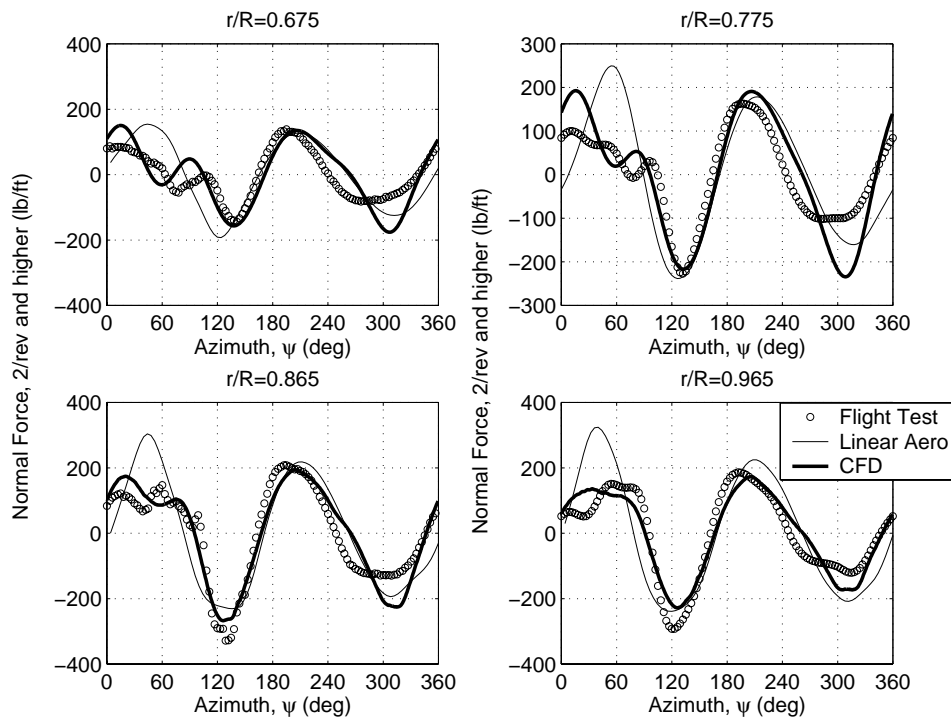Figure 3.21: Sectional vibratory chord force (1/rev and higher) for high speed forward flight (μ=0.368, C_T/σ=0.0783) at four radial stations

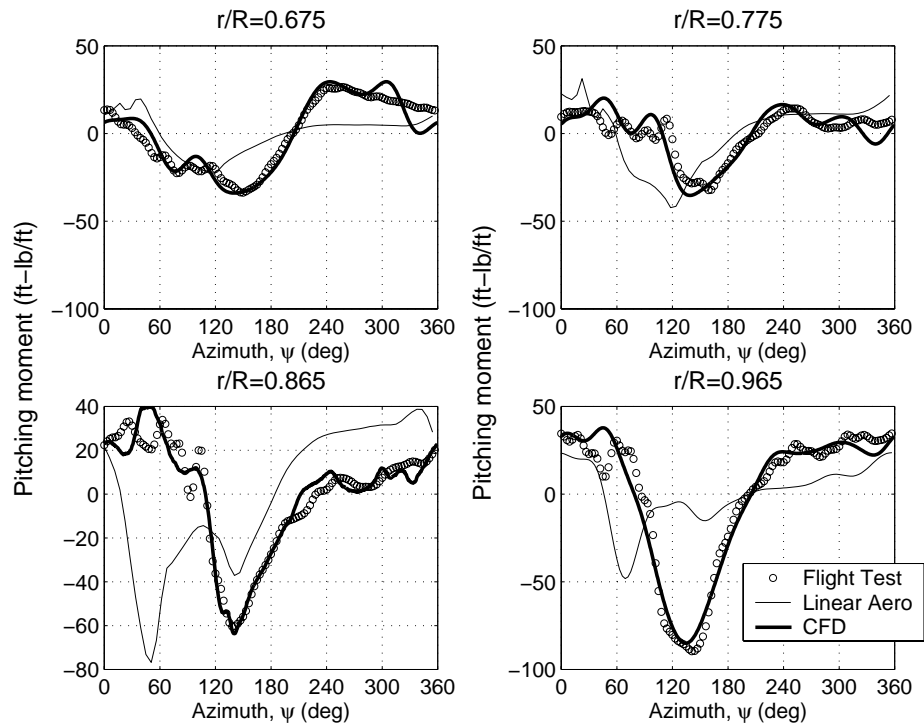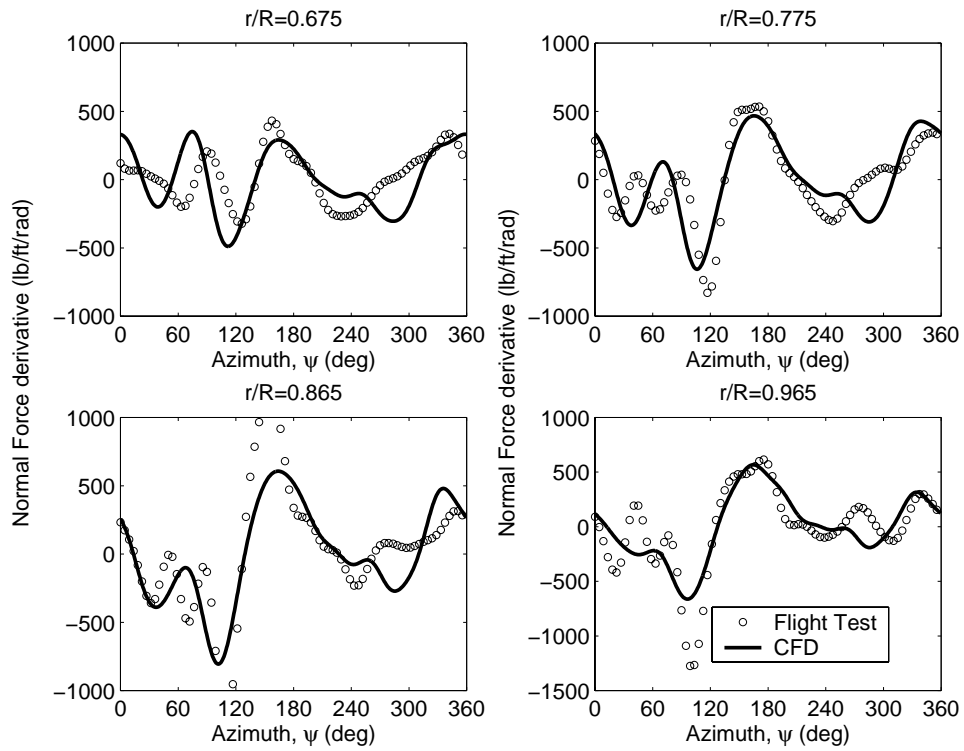Figure 3.22: Time derivative of normal force for high speed forward flight (μ=0.368, C_T/σ=0.0783) at four radial stations
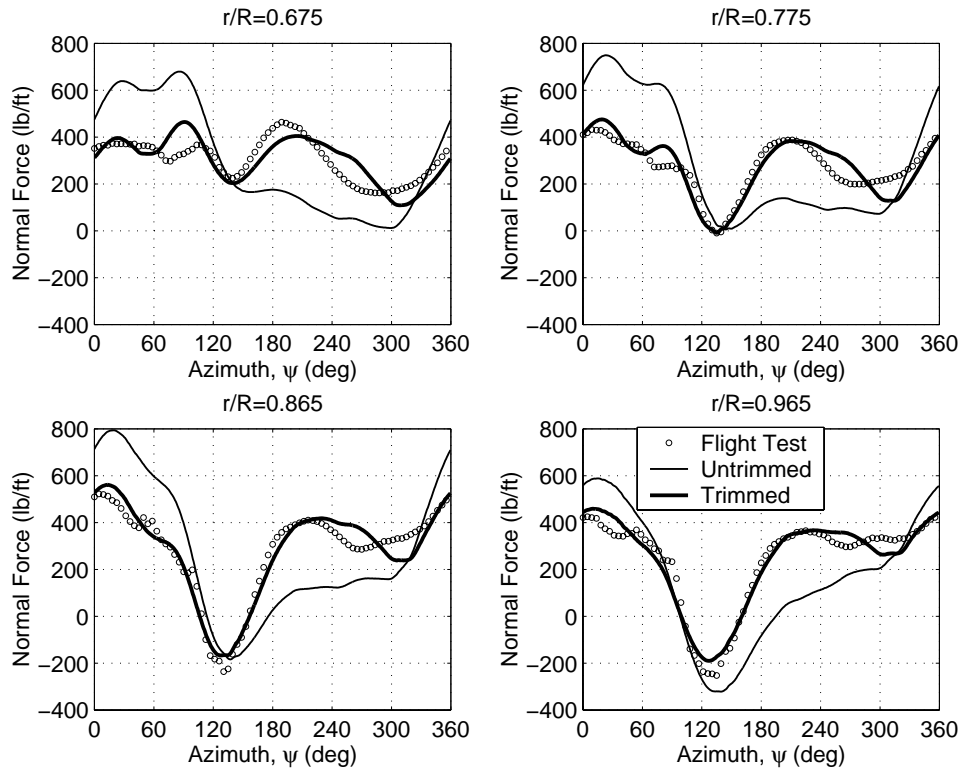
Figure 3.23: Sectional aerodynamic loads for high speed forward flight (μ=0.368, C_T/σ=0.0783) with the rotor retrimmed

3.3.4 Necessity for satisfying the geometric conservation law

For a high speed forward flight case, the elastic deformations are more important than the influence of the vortex wake. The wake becomes relatively unimportant as the trailed wake is swept farther away from the rotor plane because of the higher free stream velocity. Therefore, the elastic deformation of the rotor blade needs to be incorporated accurately.

The satisfaction of the GCL is a necessity to prevent spurious oscillations in a solution which has relatively large grid deformations as shown earlier for AVI with the deforming mesh (Section 3.2.1, Figures 3.14 and 3.15).

Figures 3.24 and 3.25 show the sectional oscillatory aerodynamic loads computed with and without satisfying the GCL correlated against the flight test data. The sectional normal force does not show large differences when the GCL is not satisfied. But the effects of spurious source terms are prominent in the sectional pitching moments, which are more sensitive to the variation of the surface pressure distributions. The sectional pitching moment computed without satisfying the GCL shows both a change in peak to peak magnitude and the presence of high frequency oscillations, compared to the smoother solution predicted with the GCL being satisfied. The test data, as expected, correlates better with the solution which satisfies the GCL.

3.4 Feasibility Study of Loose Coupling Approach

A simplified structural model which models the rotor blade as a one dimensional Euler-Bernoulli beam is used to study the feasibility of the loose coupling. Each
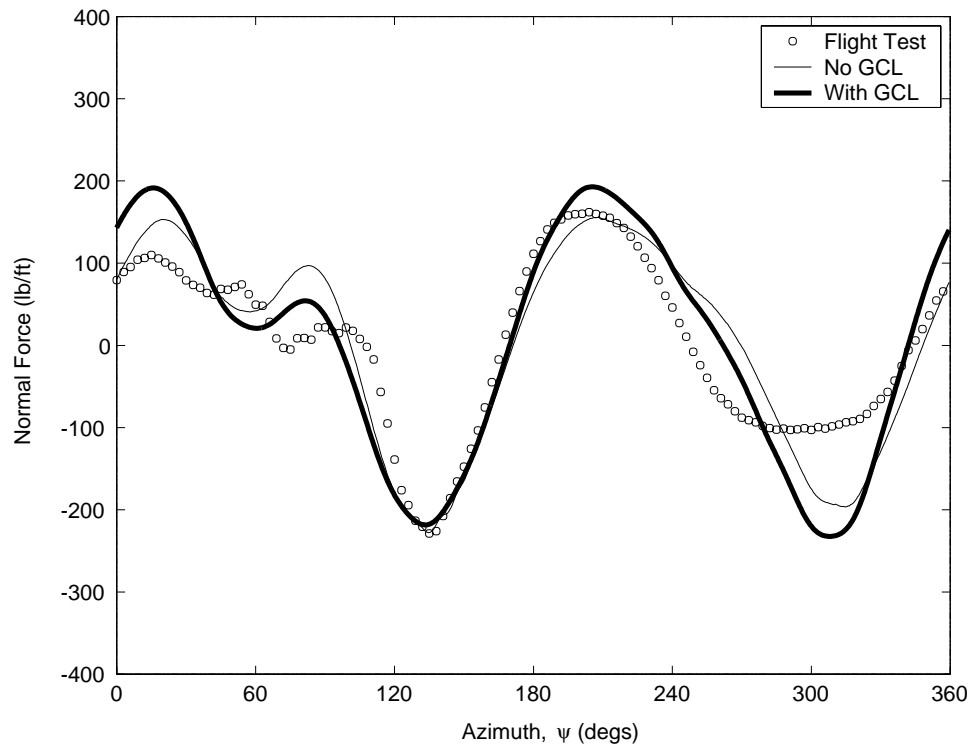
Figure 3.24: Sectional lift (2/rev and higher) at r/R=0.775 for the UH-60A rotor (μ=0.368, C_T/σ=0.0783)
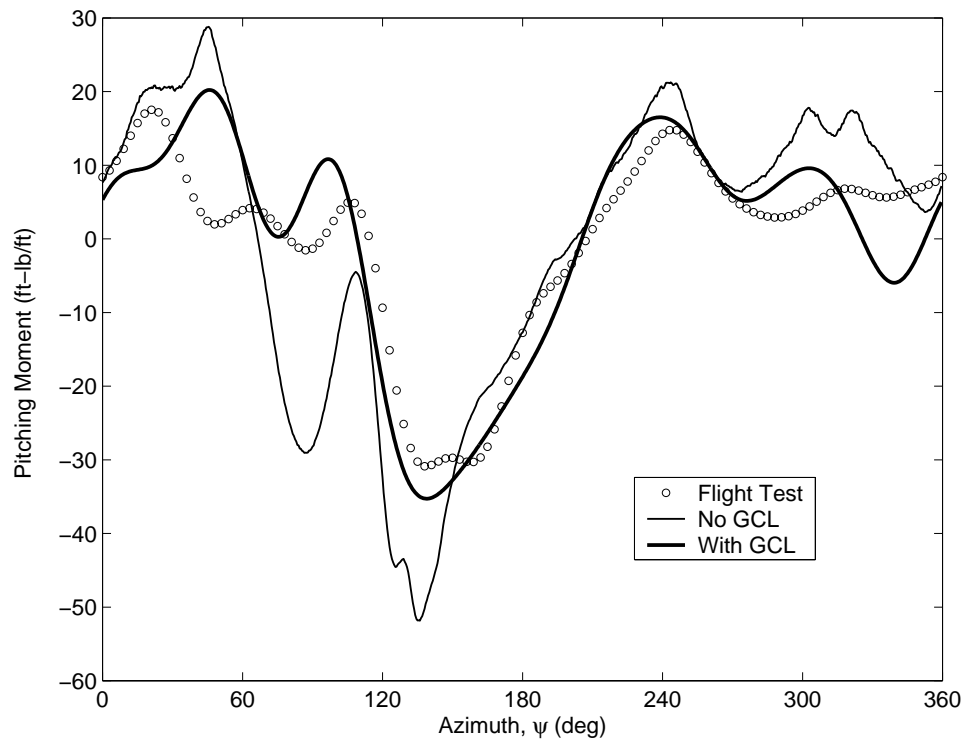
Figure 3.25: Sectional pitching moment (1/rev and higher) at r/R=0.775 for the UH-60A rotor (μ=0.368, C_T/σ=0.0783

blade is assumed to be an elastic beam undergoing flap bending and elastic twist. The three dimensional aerodynamic loading is expected to have larger effects on flap and torsional response compared to lag and axial motion. The blade is discretized into beam elements with 7 degrees of freedom distributed for 3 element nodes (2 boundary nodes and 1 interior node). Between elements, there is continuity of displacement and slope for flap deflection and continuity of displacement for torsional deflection. A normal mode reduction is performed to reduce the number of equations solved. The first four flap modes and first two torsional modes are chosen for the normal mode analysis. The final equations of motions of the blade system can be expressed as a system of nonlinear, periodic, ordinary differential equations of the form

$$M(\psi)\ddot{q} + C(\psi)\dot{q} + K(\psi)q = F_{rhs}(\psi, q) \qquad (3.3)$$

where q is the generalized displacement vector and M, C and K are the generalized mass, damping and stiffness matrices. The right hand side is the time varying forcing vector which is a function of q. As the response is known to be periodic, a temporal finite element method is used to integrate the governing equations in time. The temporal response is approximated using Lagrange polynomials as shape functions in a time element. Continuity of generalized displacements are ensured between the time elements. The finite element in time approach reduces the governing equations to a set of nonlinear algebraic equations which are solved using a modified Newton method. A more detailed description of the structural model is presented in Chapter 2.

The boundary conditions in the assembled finite element equations are modified appropriately to analyze various rotor configurations, including articulated

and hingeless rotors. The right hand side, or the forcing term, is evaluated from the detailed pressure distributions on the blade (spanwise and chordwise) obtained from the time accurate CFD solutions at each azimuthal location.

The CFD computations are performed in the Euler mode (inviscid) using the modifed TURNS code. The aeroelastic flap and torsion motions obtained from the structural analysis is used to deform the mesh in space. The wake geometry is computed using the Lagrangian vortex lattice method. The induced velocities caused by the wake is included using the *field velocity approach*. The transfer of information between the CFD and structural analysis happens every rotor revolution. The wake computations are also performed as part of the coupled solution scheme. The exact tip locations are found from the blade motions, while the circulation strengths of the tip vortex trailed is calculated from the CFD solution.

3.4.1 Coupling methodology

The goal is to achieve solution to the blade motions such that the vehicle trim equations and blade response equations are simultaneously satisfied. The blade loading (C_T/σ) and advance ratio (μ) are specified and trim solutions calculates the shaft tilt angles (α_s, ϕ_s) and the blade pitch control settings $(\theta_0, \theta_{1c}, \theta_{1s})$. The initial conditions for starting the calculations are conducted by performing the elastic blade response and the trim calculations using quasi-steady aerodynamics. The trim jacobian for predicting the control settings based on the trim residues is also computed. The rotor response solution, consisting of the periodic blade response and vehicle trim, are calculated as one coupled solution using a Newton-Raphson scheme. The methodology of the coupled analysis scheme is

summarized in Fig 3.26.
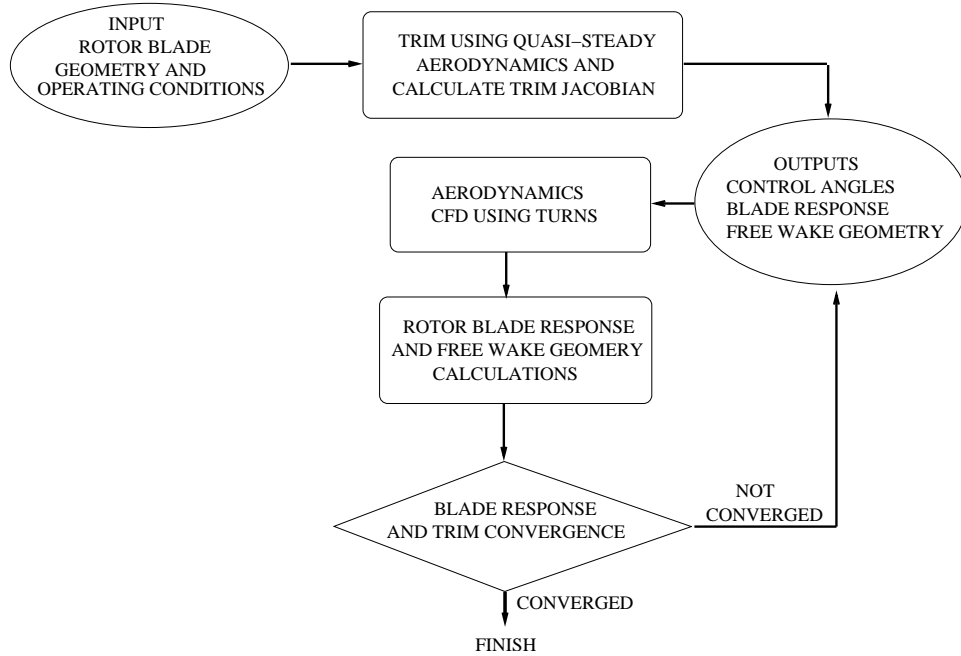
Figure 3.26: Coupling scheme

3.4.2 Aerodynamic damping

Aerodynamic loading contributes primarily to the damping in the first flap and torsion modes. Quasi-steady aerodynamic modeling provides the ease for linearizing the aerodynamic forcing on the right hand side as:

$$F_{rhs}(\psi, q) = F_0(\psi) + F_{\dot{q}}(\psi)\dot{q} + F_q(\psi)q + ...\text{non-linear terms} \qquad (3.4)$$

Therefore one could take the velocity dependent terms $(F_{\dot{q}})$ to the left hand side and construct an aerodynamic damping matrix, $C_A(\psi)$, such that the total damping matrix is $C(\psi) = C_S(\psi) + C_A(\psi)$, where $C_S(\psi)$ is the structural damping that is present in the system. The aerodynamic forcing has a frequency

140

very close to the natural frequency of the first flap mode. Hence the presence of aerodynamic damping is numerically helpful to prevent divergence of the 1st mode response solution.

The aerodynamic forcing vector, $F(\psi, q)$, obtained from the CFD computations cannot be linearized with ease unlike the quasi-steady aerodynamic loads. Hence, one needs to identify a way for introducing damping in the system to ensure convergence of the blade response. Artificial structural damping can be introduced (i.e. in $C_S(\psi)$), which is progressively removed to obtain a stable solution. This approach is used in the full coupling with UMARC (Chapter 4). Another approach is to continue using linearized damping terms derived from quasi-steady aerodynamic modeling in the left hand side. This requires subtraction of these terms from the right hand side. The response found in the previous iterative step is used to find the terms to be subtracted from the right hand side. For instance, at the nth coupling iteration step, where q_{n+1} denotes the blade response to be solved at this step, the equations are formulated as:

$$M(\psi)\ddot{q}_{n+1} + (C_S(\psi) + C_A(\psi))\dot{q}_{n+1} + K(\psi)q_{n+1} = F_{rhs}(\psi, q_n) - C_A(\psi, q_n)\dot{q}_n \quad (3.5)$$

3.4.3 Computation specifics

The computational grid used in the CFD computations follows a C-H topology. The periodic response of the blade is obtained from the structural model every iteration. The response can be used to reconstruct the exact blade geometry at any azimuthal location. A typical variation of periodic blade flap response as a function of azimuth and radius is shown in Fig 3.27. The mesh is dynamically deformed such that it conforms with the geometry of the blade surface at any
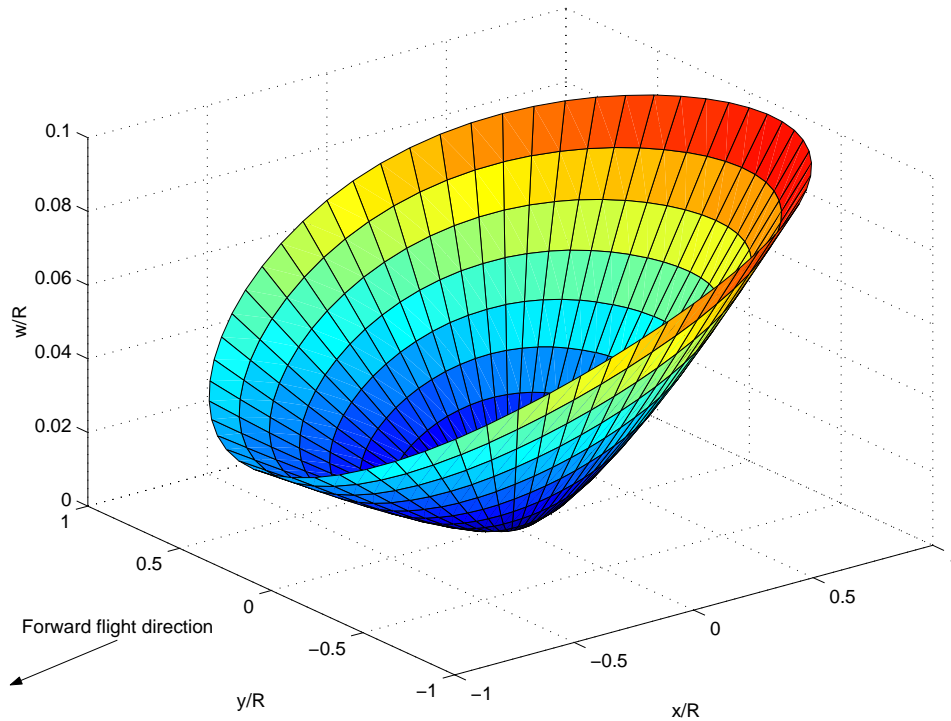
Figure 3.27: Steady state response as a function of radius and azimuth (BO-105, μ=0.3, C_T/σ=0.08)

azimuthal location. A coarse mesh, which has 133 points in the wrap around direction, 43 points in the spanwise direction and 43 points in the normal direction, and a refined mesh (217 x 71 x 61) are used for the grid and time step independence studies. The blade response convergence studies and trim calculations are conducted for a B0-105 hingeless rotor and a UH-60 articulated rotor.

3.4.4 Grid dependence study

A grid and time step dependence study for the CFD computations are performed to verify the fidelity of the analysis and implementation. Figure 3.28 shows the non-dimensional lift and pitching moment at r/R=0.965 for the UH-60 rotor

for two meshes and three azimuthal steps. The lift time history indicates good grid and time step independence. The pitching moment time history, although it shows some time step dependence, has even greater grid dependence present in it. The pitching moment is extremely sensitive to the chordwise pressure distribution, especially at the trailing edge. This is probably the reason for the grid dependence present in the pitching moment time history even when the lift time history is fairly grid independent. The coarse mesh with an azimuthal resolution of 0.25^o was deemed sufficient for this initial coupling feasibility study.

3.4.5   Blade response convergence studies

An investigation is conducted on the blade response convergence for a prescribed control setting. Two configurations, a BO-105 hingeless rotor and a UH-60 articulated rotor are investigated. The computations for the B0-105 rotor are conducted for an advance ratio of $\mu = 0.3$ while those for the UH-60 rotor are conducted for an advance ratio of $\mu = 0.368$. Figures 3.29 and 3.30 show the convergence characteristics for the B0-105 rotor. The flap and torsional responses converged in about 4 coupling iterations when both the lift and pitching moment coefficients computed using the CFD are coupled in to the aeroelastic code. Figure 3.29 shows the case in which only the lift coefficient was coupled from the CFD while Fig 3.30 shows the case in which both the lift and pitching moment coefficients were coupled. Significant differences can be observed between the responses obtained in both these cases, especially in the torsional response. The differences between the responses obtained indicate the necessity of coupling both the lift and pitching moment from CFD computations simultaneously into the aeroelastic analysis.
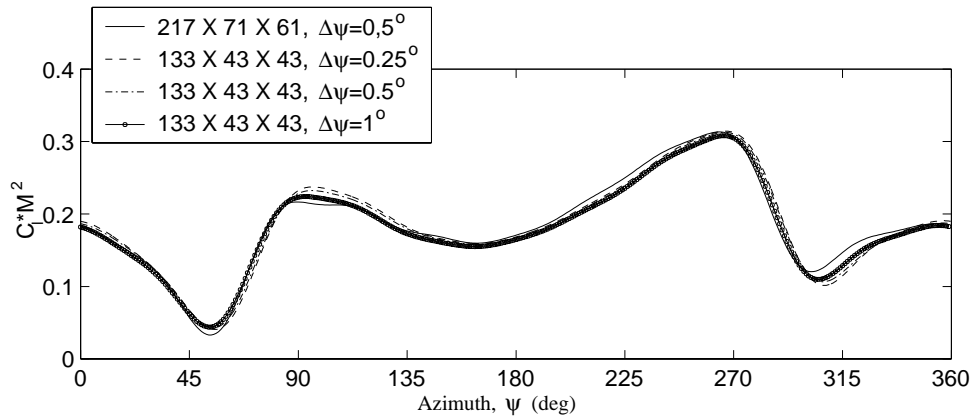
(a) Lift time history
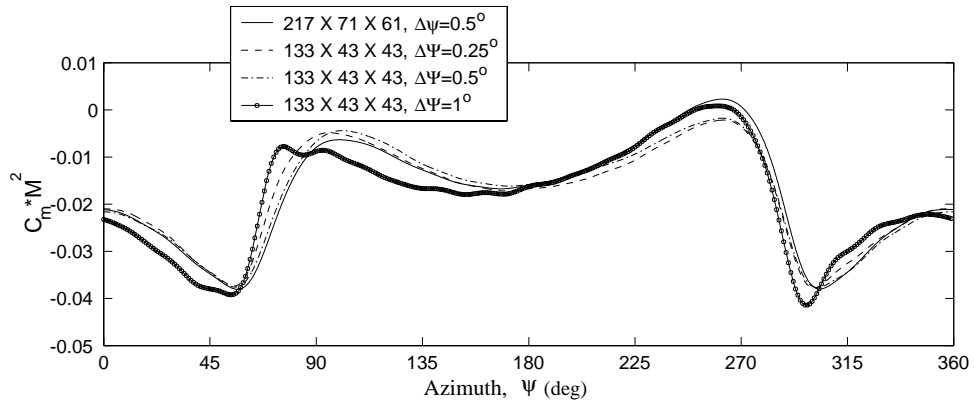
(b) Pitching moment time history

Figure 3.28: Lift and pitching moment time history at r/R=0.965 for UH-60 (μ=0.105, C_T/σ=0.0783)

144

The convergence of the lift and pitching moment time histories are presented in Fig 3.31. The results indicate the convergence of the aerodynamic loading to a periodic steady state also, in addition to the convergence of the blade response itself.

Figure 3.32 shows the blade response convergence history for the UH-60 rotor. Unlike the B0-105 case, the blade response computed using CFD based aerodynamics shows significant departure from that calculated from quasi-steady aerodynamics. But it is evident that the blade response converges even for the articulated rotor case when both lift and pitching moment from CFD computations are included in the response calculations.

3.4.6 Trim convergence studies

The simultaneous convergence of blade response and the trim are investigated for two advance ratios (μ=0.105 and μ=0.368) for the UH-60A, for which test data are available. The response convergence metric is defined as

$$\epsilon_1 = \frac{\sqrt{\sum_{i=1}^{N_\psi}(w_1 - w_0)^2}}{\sqrt{\sum_{i=1}^{N_\psi}(w_1)^2}} \tag{3.6}$$

while the trim convergence metric is defined as

$$\epsilon_2 = \sqrt{\sum_{i=1}^{6} F_i^2} \tag{3.7}$$

where w_0 is the blade response at the tip for the previous iteration and w_1 is the blade response at the tip for the current iteration and F_i are the residuals of the vehicle forces and moments. The blade response and trim convergence histories are shown in Fig 3.33. Both blade response and trim residue time

145
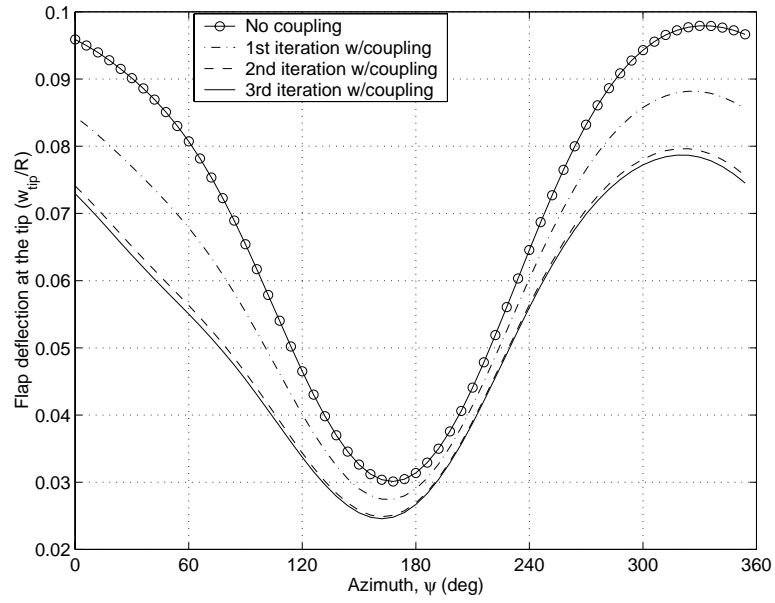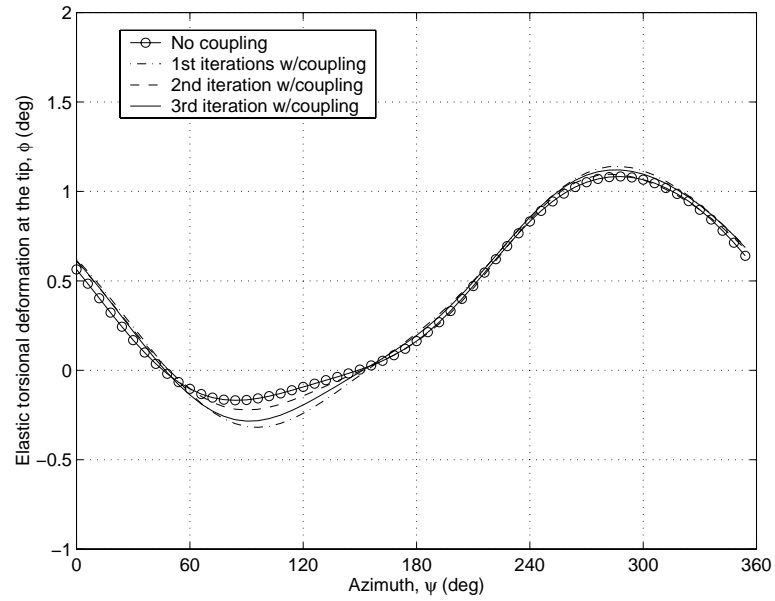
(a) Flap deflection

(b) Torsional deflection

Figure 3.29: Deflections at the tip of the blade (Only CFD C_l included) (BO-105, μ=0.3,C_T/σ=0.08
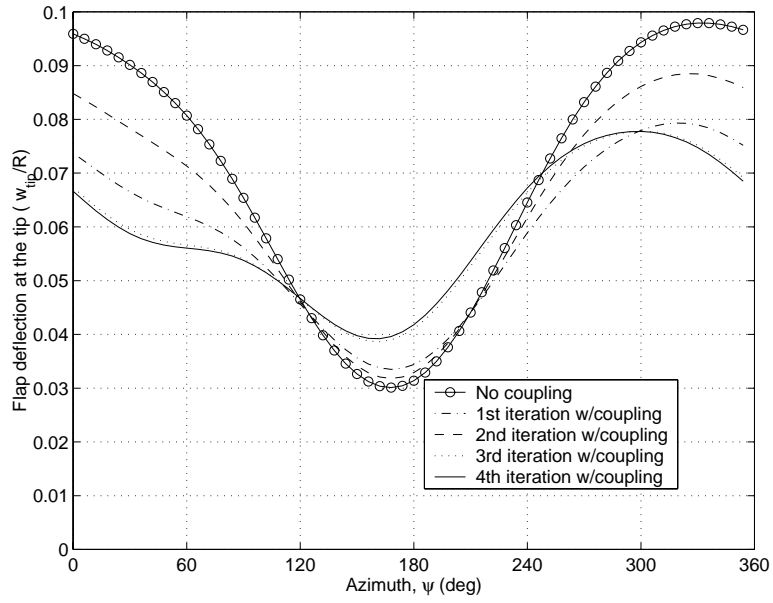
(a) Flap deflection
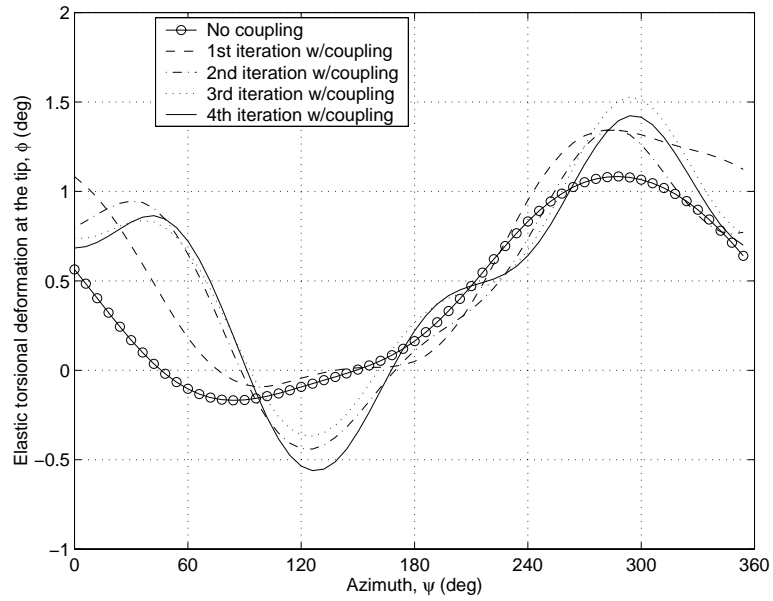
(b) Torsional deflection

Figure 3.30: Deflections at the tip of the blade (Both CFD C_l and C_m included), BO-105, μ=0.3, C_T/σ=0.08

147
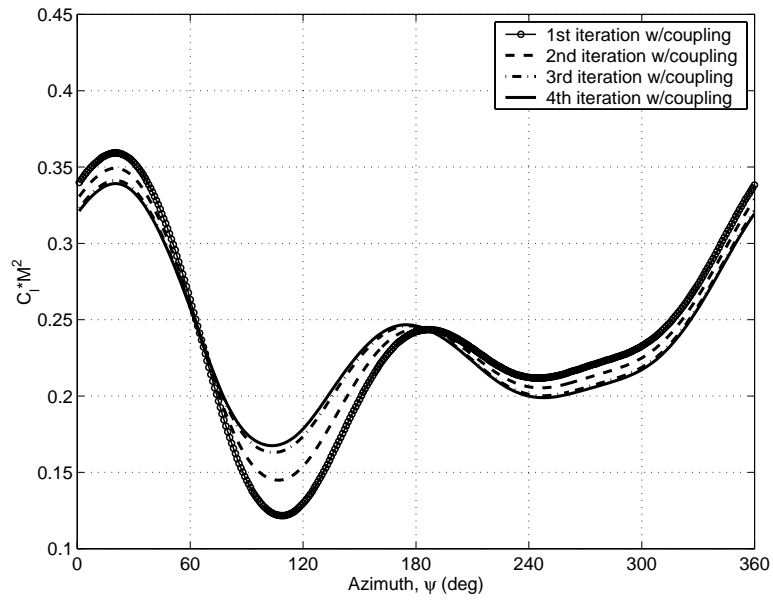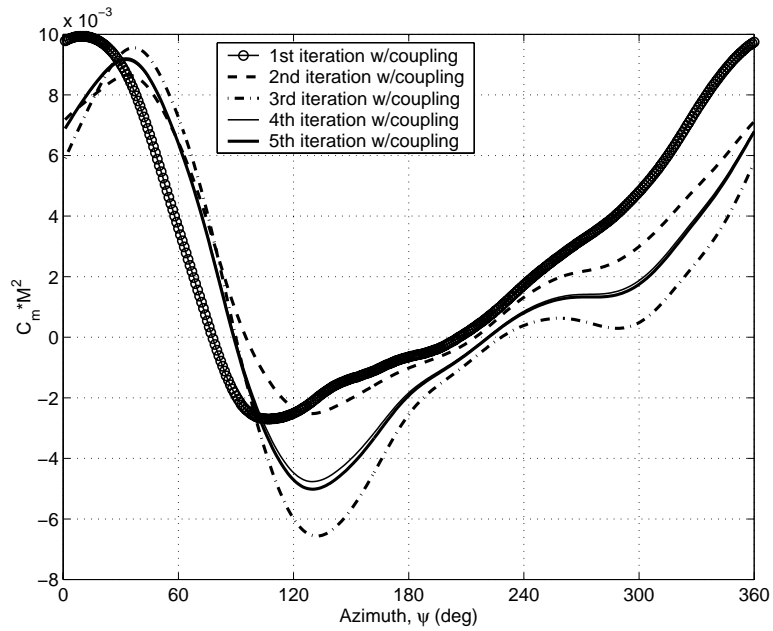
(a) Lift response

(b) Pitching moment response

Figure 3.31: Lift and pitching moment responses at r/R=0.8, (BO-105, μ=0.3)
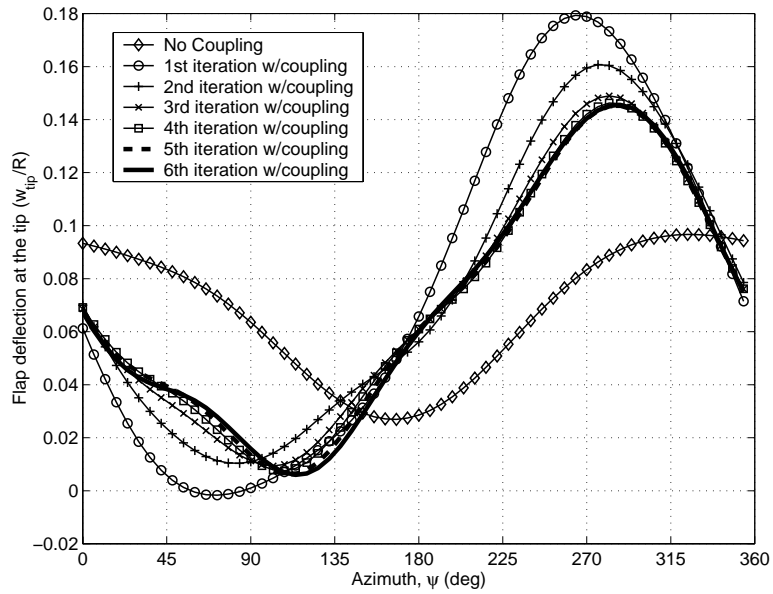
(a) Flap deflection
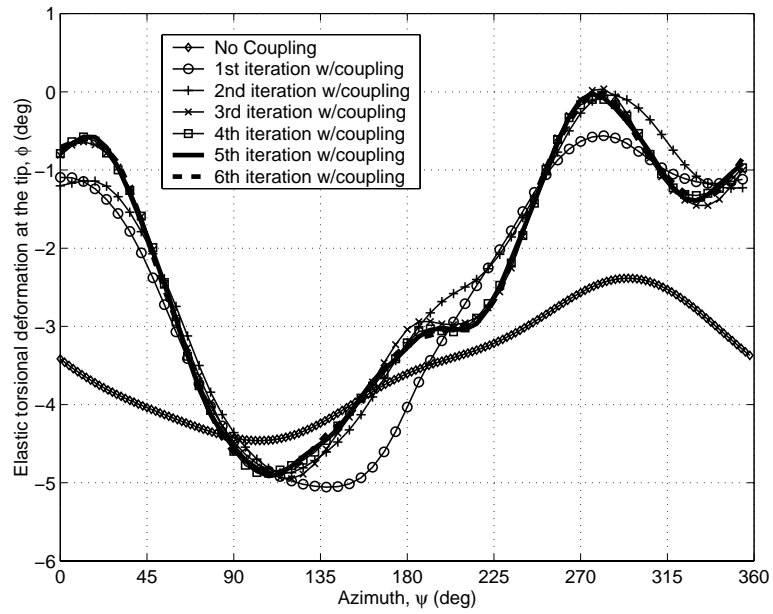
(b) Torsional deflection

Figure 3.32: Deflections at the tip of the blade (Both CFD C_l and C_m included) , UH-60, μ=0.368

149

histories show monotonic convergence for μ=0.105. But in the case of μ=0.368, there is significant departure from monotonic convergence. The trim residue shows oscillations and does not decrease to the same extent that it does for the lower advance ratio case. The oscillatory nature of the trim control settings deteriorates the blade response convergence.

All the predicted trim control angles, except the lateral cyclic obtained from the analysis, show good correlation with the test data (Figure 3.34). The lateral offset of the center of gravity and the level of tail rotor modeling have a large influence on the lateral cyclic. The reason for the discrepency is probably because of the differences in these parameters between the actual test conditions and the vehicle data used for analysis.

3.5 Conclusions and observations

The validation of the CFD model developed was discussed in this chapter. The predictions for rotor airfoil charactersistics were compared with experimental data (available as C81 tables) for a range of Mach numbers and angle of attacks. The aerodynamic coefficients predicted showed good correlation with the experimental data in the pre-stall regime. The use of Spalart-Allmaras turbulence model showed better prediction capabilities in the post-stall regime compared to the Baldwin-Lomax turbulence model. The agreement with experimental data was found to deteriorate at higher Mach numbers (M >0.7).

The accuracy of field velocity approach was evaluated for 2-D unsteady model problems (Appendix D). The results showed good agreement with exact analytical solutions. Investigation was also conducted for an airfoil vortex interaction
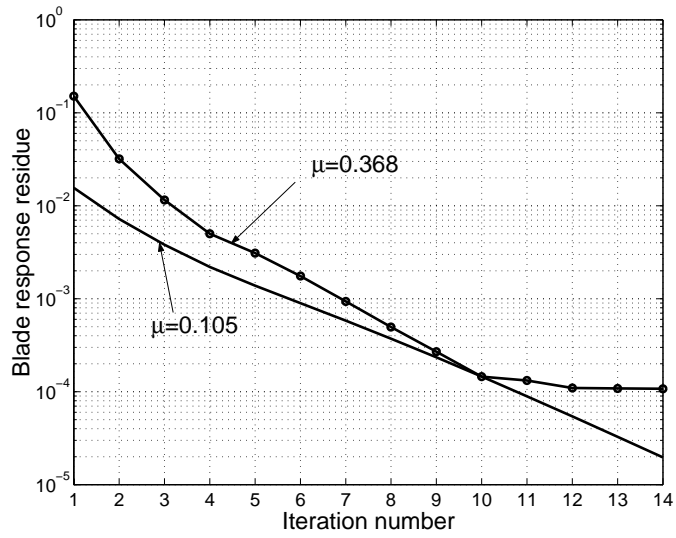
(a) Blade response residue
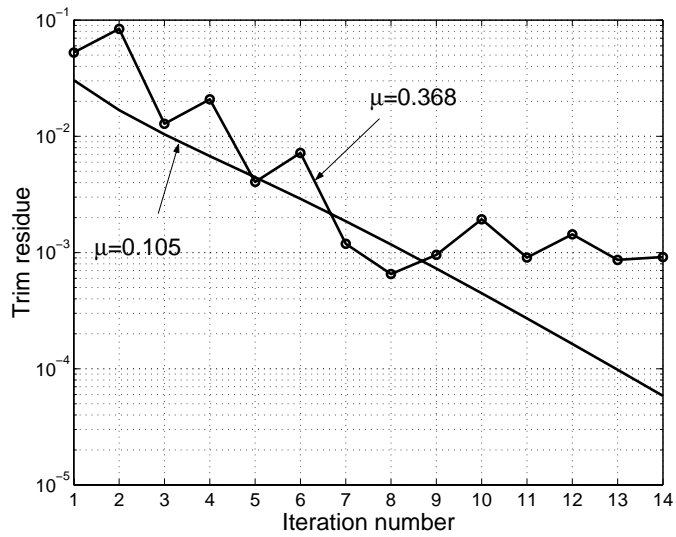
(b) Trim residue

Figure 3.33: Convergence histories for UH-60 rotor at μ=0.105 and μ=0.368

(a) μ=0.105
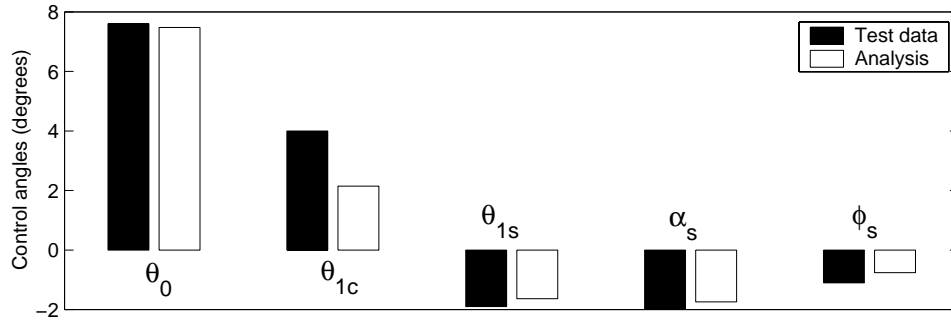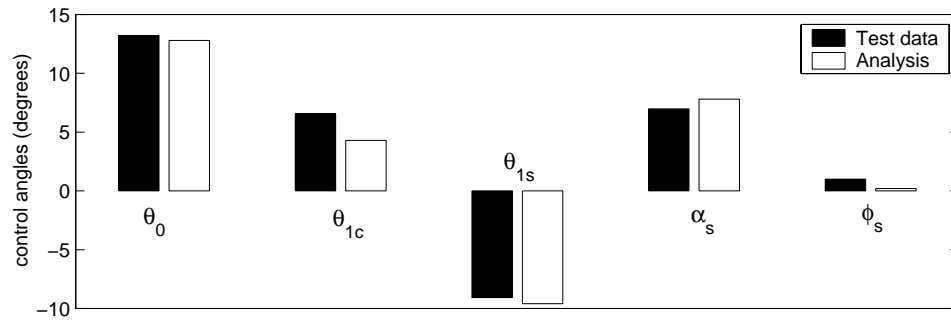
(b) μ=0.368

Figure 3.34: Comparison of control angles obtained from analysis with test data

problem. The predictions obtained showed good correlation with predictions which used alternate CFD approaches (i.e, convecting vortex and perturbation method).

The hierarchical algorithm developed for fast evaluation of induced velocities was found to give accurate results (within 0.5 % of the baseline approach) with large gain in the run time performance (described in detail in Appendix A).

The predictions of rotor vibratory loads were obtained from the CFD model using prescribed aeroelastic deformations. These aeroelastic deformations were obtained by using the measured aerodynamic loads as the forcing in the structural dynamic model. The phase and magnitude of the predicted vibratory normal forces show good correlation with the test data. The predictions from the Weissinger-L analysis shows only fair agreement for the identical set of aeroelastic deformations. The phase of the advancing blade negative lift and the up-down impulse in the first quadrant was also captured accurately by the CFD predictions. The pitching moment predictions obtained from CFD also showed good correlation with the flight test data, the Weissinger-L analysis showed poor correlation for the identical set of aeroelastic deformations.

A feasibility study for the loose coupling approach was conducted by coupling the CFD model with a simplified structural model (i.e., with only flap and torsion degrees of freedom). It was possible to attain blade response convergence even when both the lift and pitching moment obtained from the CFD based aerodynamics are included in to the rotor aeroelastic analysis. It was also found that blade response convergence can be obtained for both articulated and hingeless rotors. For the lower advance ratio case, trim and blade response monotonically converged in about 12 iterations. But, for the higher advance ratio, the trim

convergence was not as fast. This study served as a "proof-of-concept" test for the loose coupling approach. The insights gained from this study will be used in the coupling the CFD model developed with an advanced structural model (UMARC).

Chapter 4

Understanding of Rotor Unsteady Aerodynamic Loads

In the previous chapter the CFD model was validated against flight test data for a high speed forward flight test case. The blade motions used for the study were obtained by forcing the structural dynamic model with the measured aerodynamic loads. It was found that the predicted vibratory aerodynamic loads showed good agreement with the measured airloads (in both the phase and magnitude). However, the extended lifting line based analysis (Weissinger-L) showed inaccurate prediction for the vibratory airloads for identical set of blade motions. Following are the discrepancies noted in the predictions from the Weissinger-L analysis (illustrated in Fig 4.1).

1. Phase error of the advancing blade negative lift (although less than for fully comprehensive analysis)

2. Poor resolution of the "advancing blade lift impulse" (up-down variation of the normal force at 60 to 80 degrees of azimuth).

77.5 % R

96.5 % R
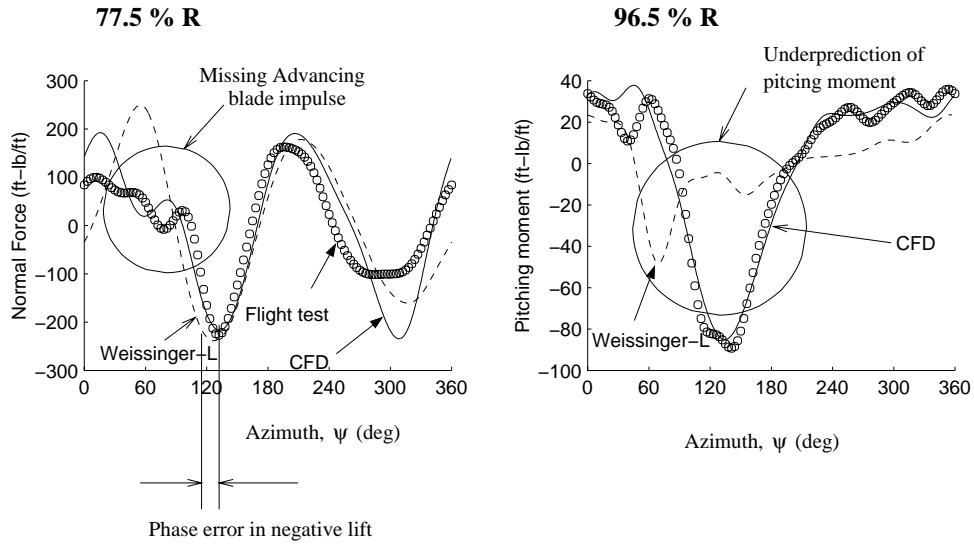
Figure 4.1: CFD vs Lifting line analysis (μ=0.368, C_T/σ=0.078)

3. Poor correlation in pitching moment magnitude and phase towards the tip of the rotor blade.

The advancing blade lift impulse is the source of much of the 3/rev and higher harmonics which transfer to the fuselage. Hence, the accurate prediction of this impulse is required for high fidelity vibration prediction. The prediction of pitching moments towards the tip is absolutely important for the correct prediction of the torsional response, which in turn is the deciding factor for the phase of the negative advancing blade lift. Also, the accurate prediction of pitch link loads is directly related to the accurate prediction of section pitching moments.

The superior prediction capability of the CFD model is because of its ability to capture certain elements of flow physics which is not captured by the Weissinger-L model. This chapter attempts to isolate these physical phenomena that are modeled by CFD computations but are not resolved accurately by the

156

Weissinger-L based analysis. The CFD method developed is used as a diagnostic tool to investigate the various aerodynamic mechanisms and identify the key players. The knowledge gained in this study will be used to determine the feasibility of applying corrections to improve the prediction capabilities of the conventional lifting line model.

Following are the major aerodynamic mechanisms investigated

1. Radial flow effects

2. Inflow effects

3. Transonic effects

4. Viscous effects

5. Role of blade motions

6. Three dimensional effects

All the simulations are performed for the high speed forward flight with the prescribed set of blade motions. The predictions are compared where possible with corresponding predictions from the Weissinger-L analysis to identify the key contributors to the accurate vibratory airload prediction.

4.1 Radial Flow Effects

The rotor blade in forward flight encounters significant amount of radial flow. The lifting line analysis assumes the validity of the independence principle and hence discards the radial component of the flow field. Figure 4.2 shows the azimuthal variation of yaw angle at a few chosen radial stations. It can be
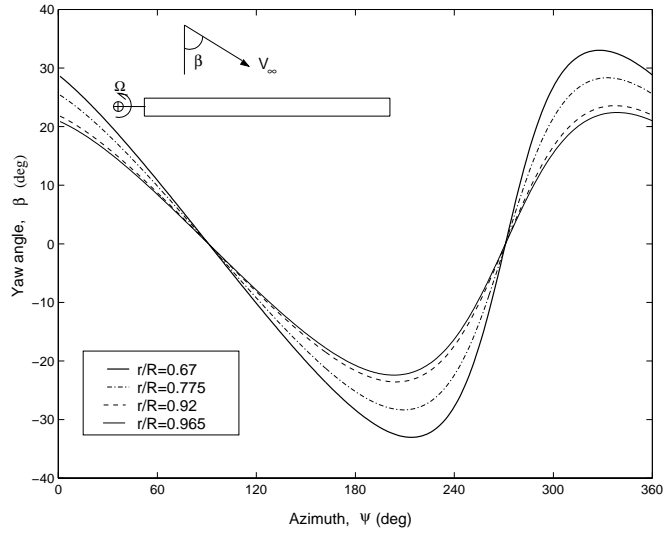
Figure 4.2: Yaw angle variation encountered by a rotor blade at μ=0.368

observed that the inboard radial stations can have yawed flow angles as large as 35 degrees.

The first comprehensive experimental study for yawed flow effects on finite wings were conducted by Purser et al. [120]. The independence principle was found to be valid from the analysis of the experimental data. Also linear aerodynamic theory of wings at an angle of side-slip using the small disturbance approach (Jones [122]) shows that the pressure distributions on an infinite aspect ratio wing is determined solely by the component of velocity in a direction normal to the leading edge.

Harris [121] analyzed the Purser data comprehensively and determined that the radial flow has little effect on rotor performance in the pre-stall regime. However, in the post stall regime it was observed that the radial flow stabilizes the boundary layer and causes it to stay attached leading to the phenomenon called stall delay.

158

The effects of compressibility are negligible in the Purser experiment because of low Mach number. At higher Mach numbers there are larger non-linearities in the flowfield that violate the validity of the small disturbance theory which forms the basis of linearized aerodynamics. The investigations conducted in this work are to assert the extent of validity of the independence principle even at the higher operating Mach numbers.

The effects of radial flow would be different for a finite wing in comparison to an infinite wing. This is because of the differences in the geometry of the near field trailed wake. The rotor blades are similar to a large aspect ratio finite wing. Therefore, studies are performed on yawed flow effects on finite wings.

4.1.1   Steady angle of attack variation

Simulations are conducted first for an infinite wing under yawed flow. This study is performed to isolate the effects of pure yaw from finiteness effects as in the case of the finite yawed wing. The boundary conditions (in the CFD solver) for the infinite wing are applied as shown in Fig 4.3. The simulation is conducted using three planes, which are sheared at the desired yaw angle. The free-stream Mach number is so specified such that the velocity normal to the leading edge is equal to the desired Mach number. The sectional aerodynamic loads are extracted at the sheared sections (i.e., in the wind axis system). These are transformed to the sections perpendicular to the leading edge (stability axis system [120]) using the transformation $C_{ls} = C_{lw}/\cos^2 \beta$.

Figure 4.4 shows the lift and pitching moment characteristics obtained for an infinite yawed wing. As expected the variations in lift and pitching moment curve slopes are negligible. The onset of supercritical flow (shock formation) causes

M/cos(β)

β

k=1

k=2

k=3
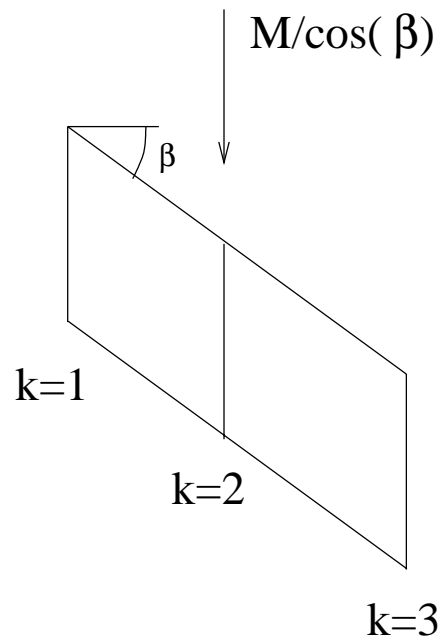
BC: q(k=1)=q(k=3)=q(k=2)

Figure 4.3: Boundary conditions used for the simulations of an infinite yawed wing

non-linearities at the higher Mach number. This is the reason for the larger differences in the aerodynamic characteristics with yaw angle at the higher Mach number. Pitching moments can be observed to be more sensitive to yaw angle than the lift. This is because the small changes in surface pressure distributions affect the pitching moments to a larger extent than the lift. Overall, the results do indicate the validity of the independence principle until the onset of supercritical flow.

The finite wing studies are conducted using a wing of rectangular planform with same aspect ratio as the UH-60A rotor blade (AR=15.30). The wing is untwisted, and has the same airfoil cross section (SC1095R8) along the whole span. The geometry of the finite wing and boundary conditions used for CFD simulation are shown in Fig 4.5. The free stream velocity is prescribed at the desired yaw angle. Parametric studies are conducted varying the Mach number normal to the leading edge and the pitch angle of the finite wing. The sectional aerodynamic coefficients (C_l and C_m) are found using the normal Mach number as the reference. Figure 4.6 shows typical spanwise variation of C_l and C_m with yaw angle. The results are plotted for two cases, a low Mach number with low angle of attack case and a moderate Mach number with high angle of attack case. The results indicate that a positive yaw angle consistently produces a larger lift and lower pitching moment at stations 60% outboard of the wing. The negative yaw angle produced the exactly opposite effect. The variations are larger at the larger Mach number, indicating that the flow non-linearities caused by the compressibility effects augment the effects of yawed flow for a finite wing. All the results from here on would be plotted at 75% span station and show the variation of lift and pitching moment with positive yaw angles and angle of
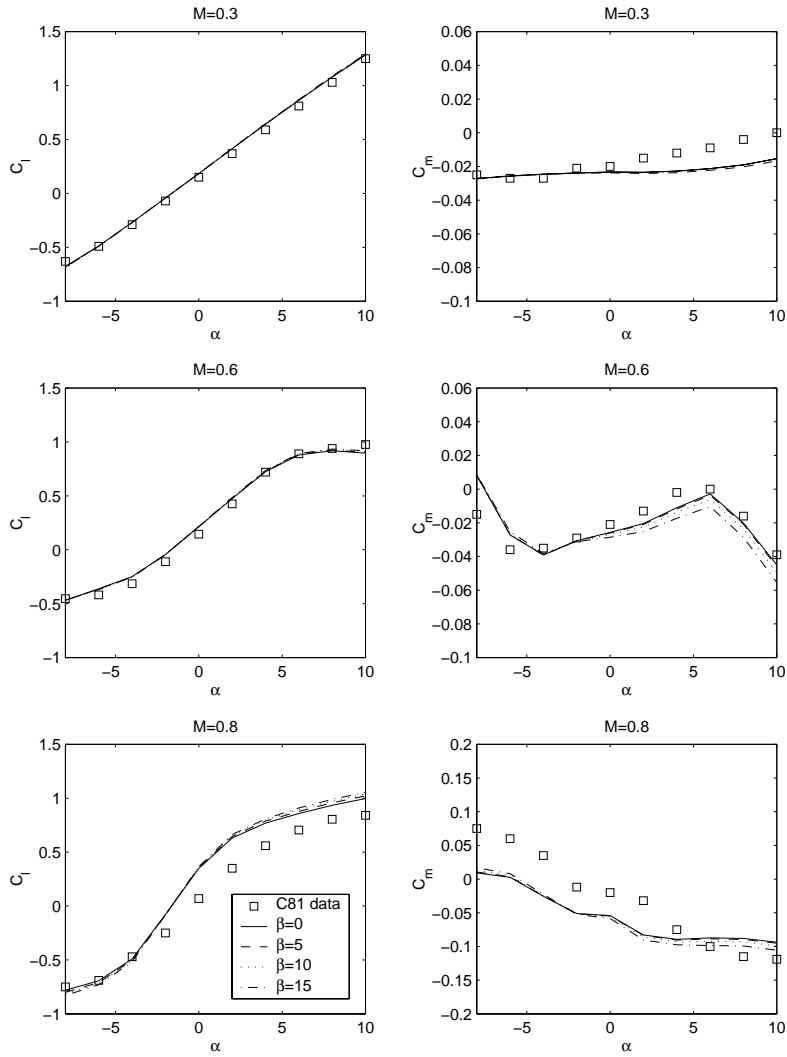
Figure 4.4: Lift and pitching moment characteristics of SC1095R8 infinite wing section for three Mach numbers

1st Order Extrapolation

β

AR = 15.30
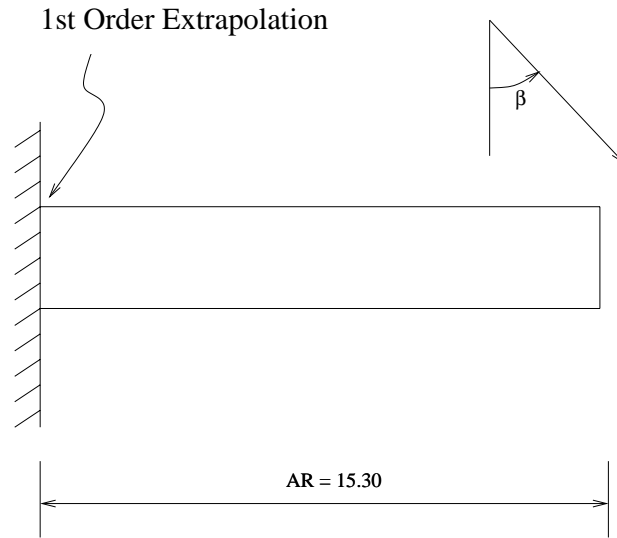
Figure 4.5: Boundary conditions used for yawed finite wing simulation

attack at different Mach numbers.

Figure 4.7 shows the lift and pitching moment characteristics for three Mach numbers at the four positive yaw angles studied. For the lower Mach numbers the effect of yaw angles is to increase the lift curve slope by a marginal amount. At the highest Mach number(M=0.8) the flow field is more non-linear because of the incidence of shock formations. Therefore, the lift and pitching moment characteristics show larger deviation than just being a gradual increase in the slope.

The comparison between finite and infinite wing results show that the effect of yaw is more prominent in the case of the finite wing. Yawed flow affects the geometry of the near wake vortex sheet behind the rotor blade (Figure 4.8). This is the primary reason for changes in lift curve slope. For positive yaw angles (i.e., similar to a backward swept wing), the near wake is more expanded and is convected away from the wing, while for negative yaw angles the near
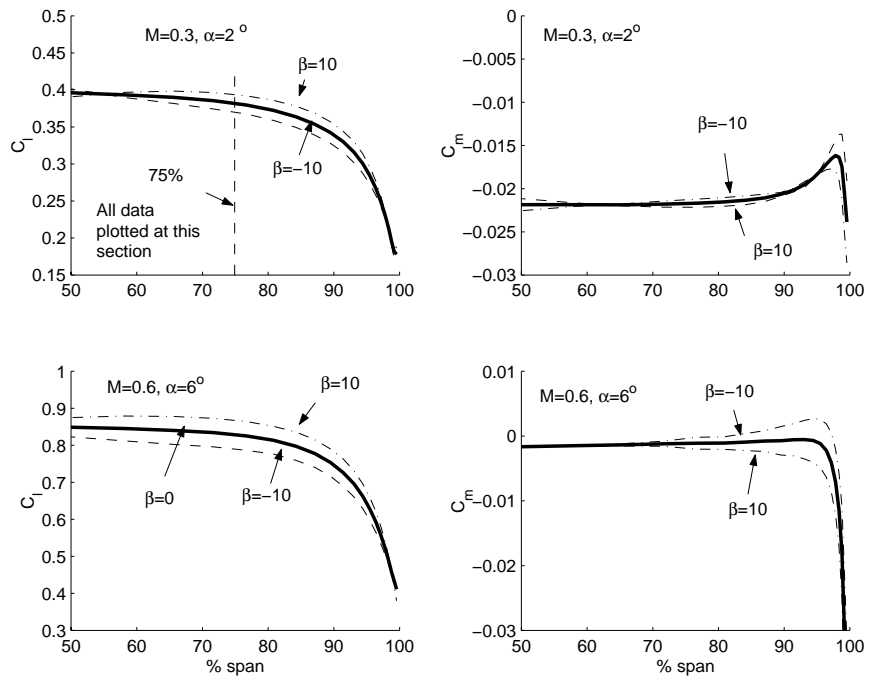
Figure 4.6: Spanwise variation of lift and pitching moment for a yawed finite wing
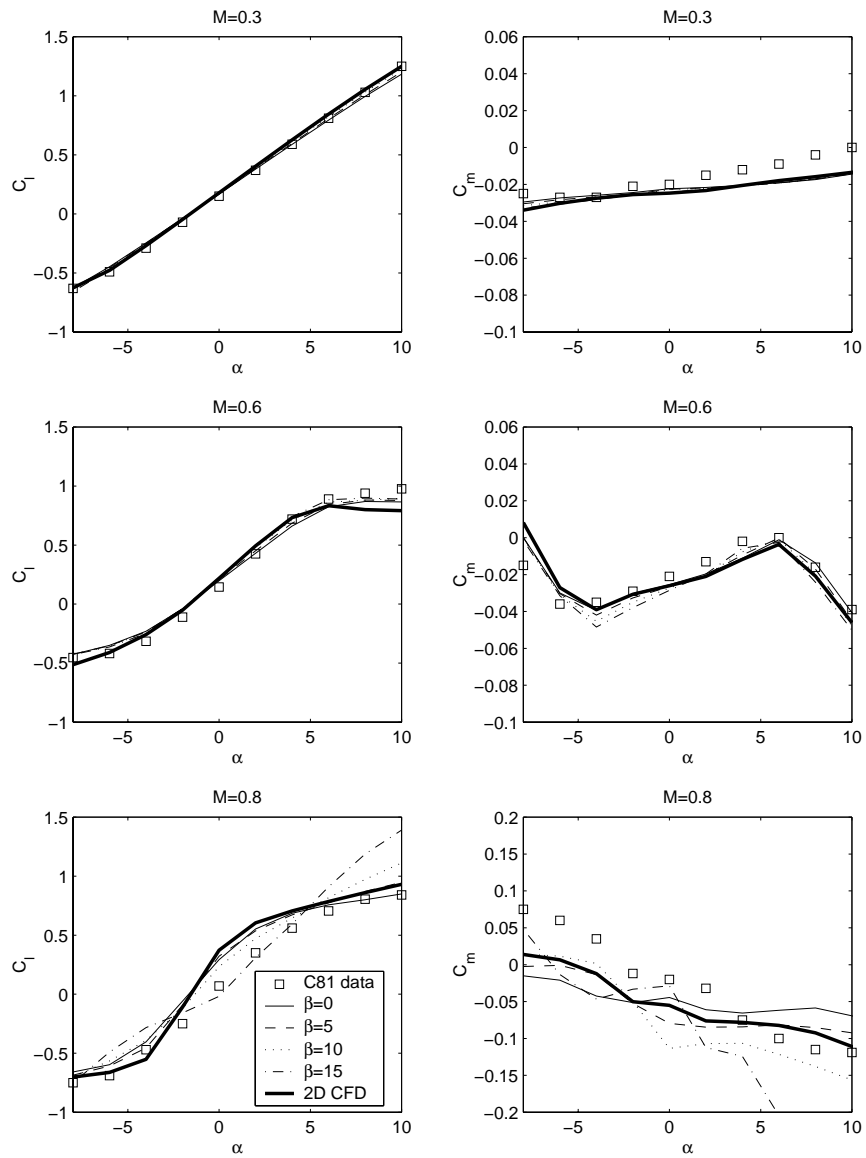
Figure 4.7: Lift and pitching moment characteristics of SC1095R8 wing at three Mach numbers (y/b=0.75)

wake is convected closer to the wing. The spanwise variation of the induced angle of attack is mostly determined by the geometry of the near wake sheet. For example, in the case of the positive yaw angle the induced angle of attack because of the near wake trailers would be smaller compared to the zero yawed flow case because the near wake sheet is at a larger distance from the wing. Therefore, the effective angle of attack would be higher along the span and so the lift produced would be consistently larger compared to the zero yawed flow case (Figure 4.6). This explains the larger lift curve slope for positive yaw angles.

It should be noted that in the case of rotor simulations in forward flight, the amount of yawed flow changes with azimuth. The CFD analysis provides accurate description of the near field vortex sheet. The Weissinger-L analysis on the other hand approximates the geometry and circulation strengths of the near wake sheet. This is the best method available within the limitations of extended lifting line theory. Hence it is possible that the near wake modeling deficiencies in Weissinger-L analysis might be the source of the inaccurate vibratory load prediction. However, the yawed flow studies performed indicate that the effect of yawed flow on steady aerodynamic loading is only predominant at high Mach numbers. Even at the high Mach numbers the effect appears to be relatively small. Therefore, the next logical step is to identify effects of yawed flow on unsteady aerodynamics.

4.1.2   Indicial response of yawed finite and infinite wings

The unsteady aerodynamic load responses are extracted for a yawed infinite wing to understand effects of yaw on unsteady blade motions. The wing was initially maintained at zero pitch angle and flow computations are iterated until

β < 0   β > 0

Near wake sheet

Near wake sheet

Rolled up tip vortex

Rolled up tip vortex
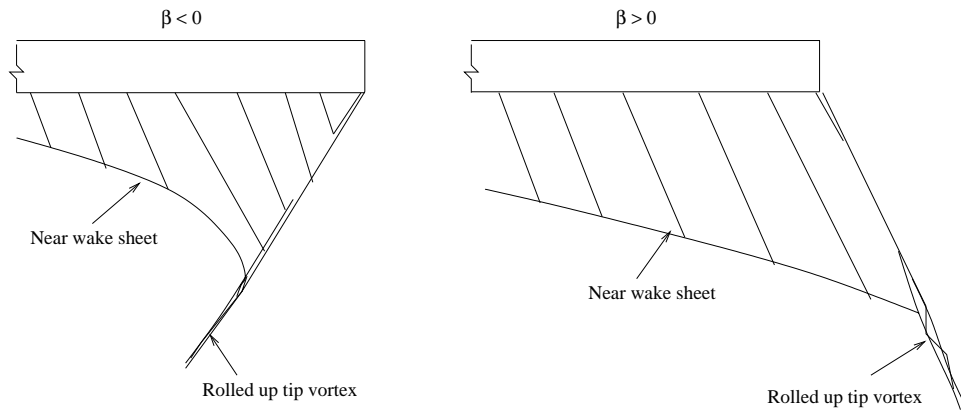
Figure 4.8: Schematic of near wake field for positive and negative yaw angles

a steady state is reached. A unit step change in pitch angle (1 degree) is applied and the flow computations were performed maintaining 2nd order time accuracy to extract the indicial response. The unit step change in the pitch angle is introduced through the field velocity approach (Chapter 2).

The results of the indicial response computations performed for the yawed infinite wing are shown in Figure 4.9. Both the lift and pitching moment response show very little sensitivity to yawed flow angle at the low Mach number. At the higher Mach number the lift response shows a gradual increase in the finally asymptotic value. The pitching moment shows a more nose-down trend for larger yawed flow angle at the steady state. The growth characteristics of the pitching moment is observed to be more sensitive to the yawed flow compared to the corresponding lift characteristics.

Figure 4.10 shows the sectional lift responses at (y/b=0.75) for a finite wing obtained for three Mach numbers at yaw angles varying from -20 degrees to +20 degrees in steps of 5 degrees. The plots on the left side show the actual CFD predicted response. Notice that the initial non-circulatory value is unchanged
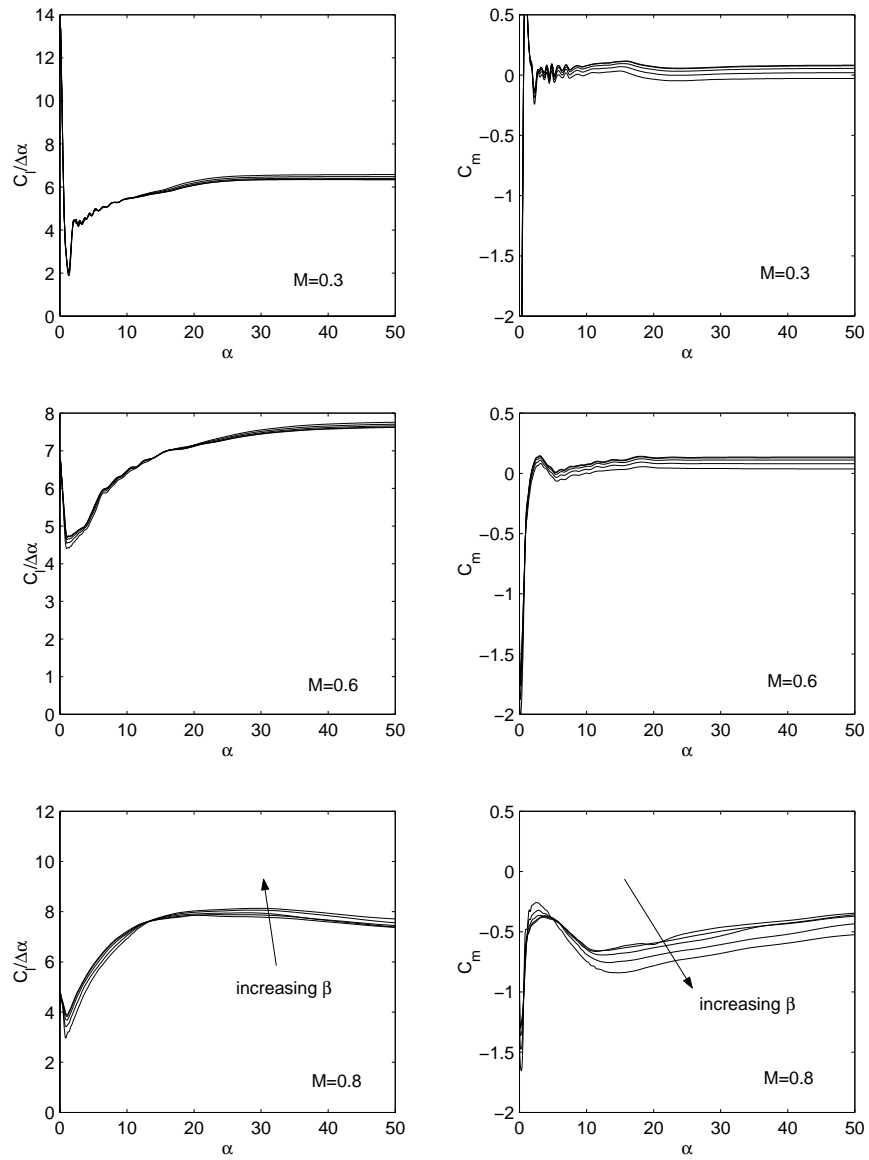
Figure 4.9: Indicial response for a yawed infinite wing
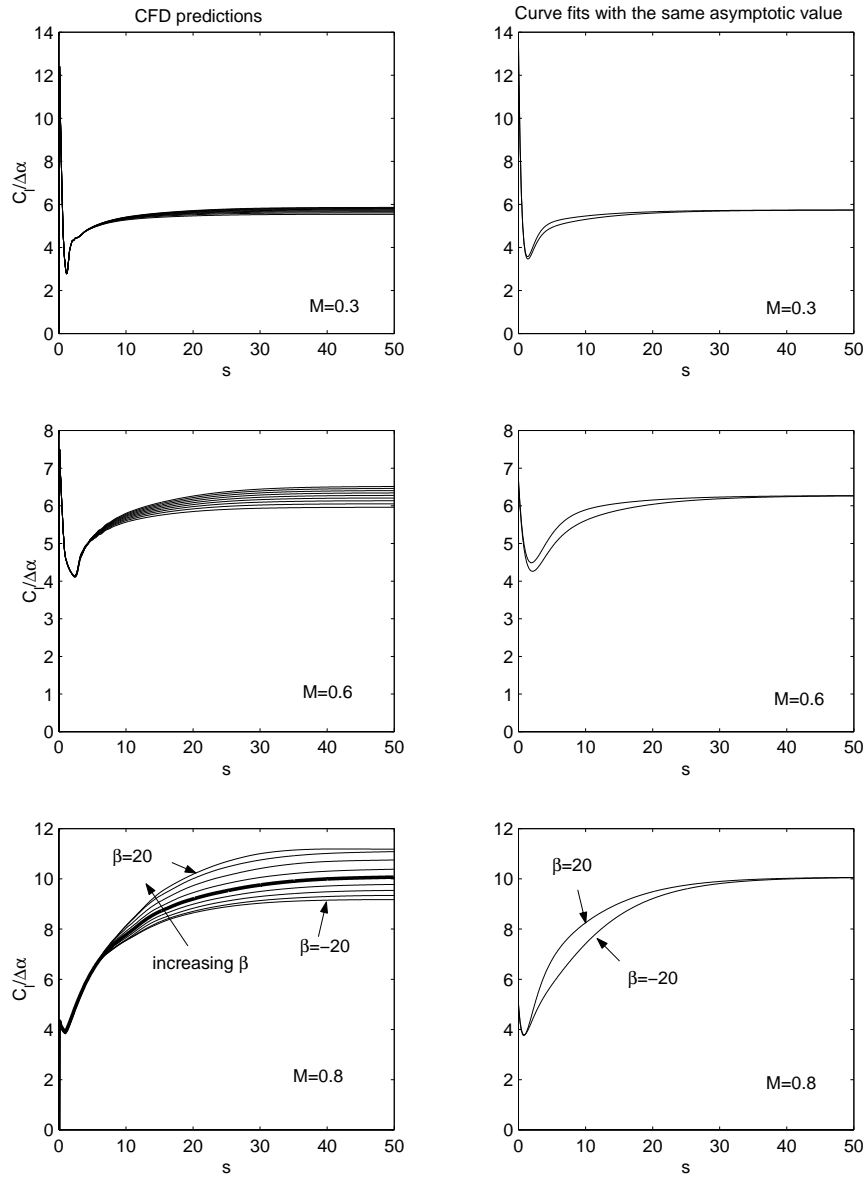
Figure 4.10: Lift characteristics of SC1095R8 finite wing section for three Mach numbers ($\frac{r}{R}$=0.75)

for all the yaw angles. The non-circulatory airload decays and the circulatory airloads grow and asymptote to the final steady state. The final steady state value increases with yaw angle because of the near wake effects. The indicial responses obtained from CFD are curve fitted using a 5 term exponential series. The equation for the indicial responses used are given by:

$$\frac{C_l(s)}{\Delta \alpha} = \frac{4}{M} e^{-s/T_\alpha} + C_{l_\alpha} * (1 - \sum_{i=1}^{5} A_i e^{-b_i s})$$ (4.1)

Here the first term represents the decay of the non-circulatory loading and the second term represents the asymptotic growth of the circulatory lift. The coefficents A_i, b_i and time constant T_α are determined using a constrained optimization process which minimizes the error between Eq. 4.1 and the indicial response obtained from CFD in a least square sense. The constraints used are the the initial value of the lift and time derivative of lift which are known from the exact solution [102]. This methodology was originally developed by Leishman [100] and further applied by Sitaraman [103] and Lee [104]. The coefficients obtained for the three Mach numbers studied (M=0.3, M=0.6 and M=0.8) for the range of yaw angles (-20< β <20) are shown in Table 4.1, 4.2 and 4.3 respectively.

The exponential approximation developed (Eq 4.1) are plotted as a function of time with the same asymptotic value. This allows one to ascertain the changes

170

β	A_1	b_1	A_2	b_2	A_3	b_3	A_4	b_4	A_5	b_5
-20	0.1623	0.1202	0.6860	1.2087	2.7849	1.2183	1.2183	1.2253	-3.8515	1.5330
-15	0.1784	0.1188	0.6608	1.2220	2.9762	1.2328	1.2328	1.2347	-4.0482	1.5268
-10	0.1893	0.1164	0.7234	1.2003	2.4493	1.2104	1.2104	1.2205	-3.5724	1.5486
-5	0.1969	0.1139	0.6791	1.2206	2.7742	1.2374	1.2374	1.2279	-3.8877	1.5346
0	0.2041	0.1124	0.6945	1.2150	2.6223	1.2311	1.2311	1.2252	-3.7520	1.5404
5	0.2109	0.1112	0.6804	1.2227	2.7231	1.2363	1.2363	1.2321	-3.8508	1.5362
10	0.2174	0.1104	0.6730	1.2270	2.7777	1.2334	1.2334	1.2439	-3.9015	1.5347
15	0.2230	0.1099	0.6642	1.2326	2.8502	1.2495	1.2495	1.2380	-3.9870	1.5325
20	0.2282	0.1096	0.6825	1.2269	2.6768	1.2426	1.2426	1.2354	-3.8302	1.5394

Table 4.1: Indicial coefficients for lift at yaw angles ranging from -20 deg to 20 deg and M=0.3

β	A_1	b_1	A_2	b_2	A_3	b_3	A_4	b_4	A_5	b_5
-20	0.1527	0.1031	0.8458	0.5676	0.9950	0.5783	0.5783	0.5789	-1.5718	0.7056
-15	0.1761	0.1031	0.8292	0.5756	1.0486	0.5827	0.5827	0.5831	-1.6366	0.7034
-10	0.1955	0.1025	0.8436	0.5787	0.9264	0.5812	0.5812	0.5809	-1.5466	0.7076
-5	0.2120	0.1017	0.8348	0.5831	0.9464	0.5858	0.5858	0.5856	-1.5790	0.7087
0	0.2264	0.1009	0.8351	0.5860	0.9189	0.5882	0.5882	0.5880	-1.5686	0.7111
5	0.2402	0.1001	0.8329	0.5899	0.9102	0.5918	0.5918	0.5916	-1.5751	0.7135
10	0.2524	0.0995	0.8305	0.5940	0.9072	0.5952	0.5952	0.5949	-1.5853	0.7154
15	0.2633	0.0991	0.8236	0.5975	0.9335	0.6001	0.6001	0.6000	-1.6205	0.7171
20	0.2728	0.0989	0.8282	0.6003	0.8949	0.6018	0.6018	0.6015	-1.5977	0.7203

Table 4.2: Indicial coefficients for lift at yaw angles ranging from -20 deg to 20 deg and M=0.6

β	A_1	b_1	A_2	b_2	A_3	b_3	A_4	b_4	A_5	b_5
-20	0.8119	0.1278	0.0682	0.5051	0.2795	0.5051	0.5051	0.5051	-0.6648	1.4281
-15	0.8156	0.1192	0.0403	0.4707	0.1900	0.4707	0.4707	0.4707	-0.5165	1.5348
-10	1.5042	0.1289	-0.7719	0.1801	0.0927	0.3888	0.3888	0.3869	-0.2137	1.7262
-5	2.3585	0.1242	-1.4989	0.1322	-1.3870	0.8221	0.8221	0.6200	0.7053	3.5851
0	1.5063	0.1233	-0.7568	0.1704	-0.2344	0.9816	0.9816	0.3731	-0.4966	3.0083
5	1.5513	0.1236	-0.8034	0.1777	-0.2239	0.8999	0.8999	0.3618	-0.4239	3.1091
10	0.9575	0.1123	-0.0057	0.8110	0.3349	0.4654	0.4654	1.5177	-0.7521	2.2030
15	1.0040	0.1146	0.0024	0.6517	0.2844	0.5491	0.5491	1.8726	-0.8398	1.8751
20	1.0329	0.1232	0.0484	0.9960	0.5074	1.0632	1.0632	1.0635	-1.6518	1.3519

Table 4.3: Indicial coefficients for lift at yaw angles ranging from -20 deg to 20 deg and M=0.8

in the growth rate of the circulatory lift. It can be observed that the circulatory lift reaches the final asymptotic state faster with increase in yaw angle.

Figure 4.11 shows the pitching moment responses for a finite wing for the desired Mach number and yaw angle range. The indicial response shows little variation for the lower Mach numbers. As observed earlier, the onset of super-critical flow causes variation in the indicial response for the higher Mach number. The response shows changes in final asymptotic value and variation in the growth characteristics of the circulatory pitching moment at this higher Mach number. As in the case of the lift response, the indicial responses obtained from CFD are curve fitted using a 5 term exponential series given by:

$$\frac{C_m(s)}{\Delta \alpha} = \frac{-1}{M} e^{-s/T_{\alpha_m}} + C_{m_\alpha} * (1 - \sum_{i=1}^{5} A_i e^{-b_i s}) \tag{4.2}$$

Again, the coefficients A_i, b_i and time constant T_{α_m} are determined using a constrained optimization process which minimizes the error between Eq. 4.2 and the indicial response obtained from CFD in a least square sense. The constraints used are the the initial value of the lift and time derivative of lift which are known from the exact solution. The coefficients obtained for the three Mach numbers studied (M=0.3, M=0.6 and M=0.8) for the range of yaw angles (-20< β <20) are shown in Table 4.4, 4.5 and 4.6 respectively.

This exponential approximation is plotted as a function of time with the same asymptotic value (Figure 4.11. As observed in the case of the lift response, the pitching moment response also reaches the final steady state value faster as the yaw angle increases.

Overall, the indicial response studies for both lift and pitching moment indicate that the effect of yaw predominantly affects the the final steady state values
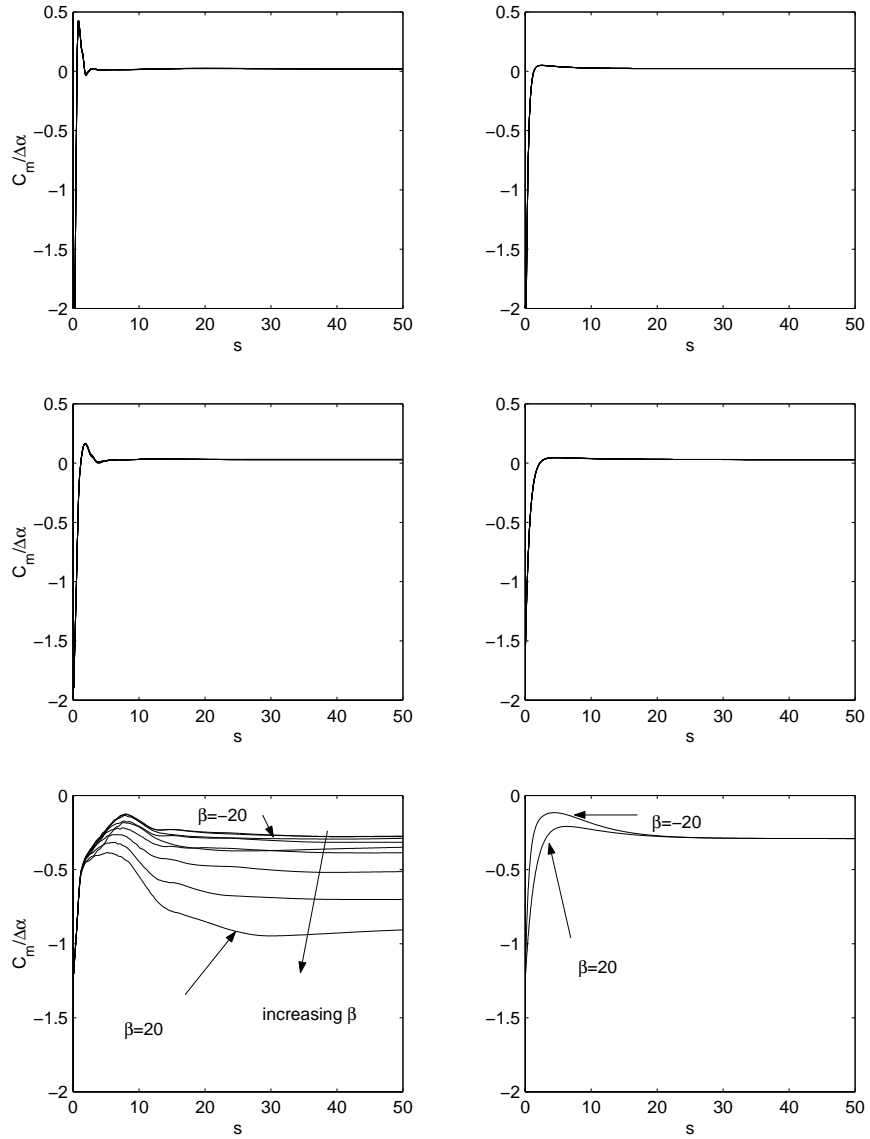
Figure 4.11: Pitching moment characteristics of SC1095R8 finite wing section for three Mach numbers

β	A_1	b_1	A_2	b_2	A_3	b_3	A_4	b_4	A_5	b_5
-20	0.2699	1.9976	1.2504	2.0451	15.9921	2.5742	16.5247	2.5750	-33.0371	0.8571
-15	0.2972	1.9981	1.2616	2.0504	16.1696	2.5456	16.7260	2.5437	-33.4544	0.8705
-10	0.3027	2.0009	1.2536	2.0519	16.2291	2.5462	17.2416	2.5426	-34.0269	0.8704
-5	0.3072	1.9992	1.2607	2.0498	16.3470	2.5533	16.8466	2.5516	-33.7616	0.8662
0	0.2810	2.0040	1.2393	2.0465	16.7922	2.5876	17.3058	2.5892	-34.6182	0.8542
5	0.2739	2.0009	1.2489	2.0475	16.5319	2.5794	17.4417	2.5811	-34.4962	0.8558
10	0.2928	1.9998	1.2652	2.0521	16.2114	2.5441	16.6847	2.5416	-33.4541	0.8665
15	0.2938	2.0014	1.2603	2.0539	16.1006	2.5440	16.6883	2.5420	-33.3430	0.8741
20	0.2797	2.0041	1.2596	2.0567	16.2926	2.5309	16.8071	2.5282	-33.6390	0.8764

Table 4.4: Indicial coefficients for pitching moment respone at yaw angles ranging from -20 deg to 20 d eg and M=0.3

β	A_1	b_1	A_2	b_2	A_3	b_3	A_4	b_4	A_5	b_5
-20	0.3249	1.1068	0.8214	1.1111	8.5680	1.2578	8.8258	1.2558	-17.5401	0.5296
-15	0.3151	1.1024	0.8320	1.1042	8.2855	1.3007	8.5213	1.3018	-16.9540	0.5127
-10	0.3171	1.1032	0.8325	1.1052	8.3036	1.3017	8.5455	1.3026	-16.9988	0.5113
-5	0.3176	1.1046	0.8308	1.1065	8.3678	1.3024	8.6091	1.3034	-17.1253	0.5130
0	0.3180	1.1056	0.8294	1.1074	8.3594	1.3029	8.6019	1.3039	-17.1088	0.5142
5	0.3178	1.1066	0.8282	1.1084	8.3180	1.3028	8.5624	1.3038	-17.0263	0.5158
10	0.3161	1.1079	0.8265	1.1096	8.2493	1.3014	8.4965	1.3025	-16.8884	0.5189
15	0.3249	1.1087	0.8172	1.1103	8.0854	1.3059	8.3037	1.3076	-16.5312	0.5205
20	0.3317	1.1131	0.8167	1.1172	8.0313	1.2681	8.2918	1.2659	-16.4715	0.5313

Table 4.5: Indicial coefficients for pitching moment response at yaw angles ranging from -20 deg to 20 deg and M=0.6

β	A_1	b_1	A_2	b_2	A_3	b_3	A_4	b_4	A_5	b_5
-20	1.7568	0.1448	0.0404	1.1175	1.5891	1.1486	1.7453	1.1484	-4.1317	1.4207
-15	1.6198	0.1631	0.4059	0.1598	0.4531	0.9600	0.6912	1.0011	-2.1699	1.6040
-10	1.4666	0.1621	0.5728	0.1631	0.7516	0.9036	0.8933	0.9058	-2.6843	1.4888
-5	1.3903	0.1726	0.6345	0.1750	0.8993	0.8575	1.0219	0.8564	-2.9460	1.3926
0	1.1867	0.1976	0.5065	0.1936	0.6243	0.1937	0.9402	0.8931	-2.2577	1.3898
5	1.1250	0.2036	0.1697	0.8865	0.9469	0.2020	0.5443	1.0000	-1.7859	1.3551
10	1.1221	0.1826	0.1691	0.9455	0.8128	0.1823	0.4687	1.0656	-1.5727	1.2493
15	1.1605	0.1638	0.1539	0.9589	0.6805	0.1642	0.5283	1.0276	-1.5233	1.0637
20	2.3351	0.1944	1.7859	0.6686	1.2966	0.1957	0.8917	0.7349	-5.3094	0.3651

Table 4.6: Indicial coefficients for pitching moment response at yaw angles ranging from -20 deg to 20 deg and M=0.8
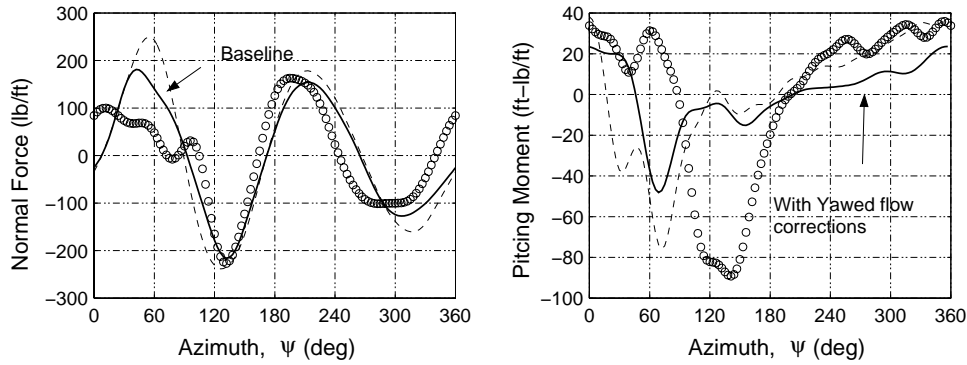
Figure 4.12: Effects of yawed flow corrections to lifting line analysis (μ=0.368, C_T/σ=0.078

more than the growth rate of the circulatory aerodynamic loads.

4.1.3 Corrections to the lifting line analysis

Corrections were applied to the lifting line analysis using a table lookup (C81 format) created from CFD computations including the yawed flow effects [123]. The aerodynamic lift, drag and pitching moment coefficients were parametrized with Mach number, angle of attack and yaw angle. Indicial aerodynamic models were also constructed from the CFD predicted responses. The indicial functions were expressed as a sum of exponential functions (Eq 4.1 and 4.2. The coefficients of these functions were also parameterized in terms of Mach number and yaw angle.

The predictions obtained from the the modified lifting line analysis constructed are shown in Figure 4.12. It is evident that there are no considerable improvements compared to the base line analysis. Therefore, it appears that the yawed flow effects are not the primary contributors to the errors in vibratory load phase and magnitude.

4.1.4 Summary of yawed flow observations

The effects of yawed flow can be summarized as follows

1. The effects of yawed flow is small for low subsonic Mach numbers. The effects become more significant with the onset of supercritical flow. The pitching moment characteristics appear to be more sensitive to yawed flow than the lift characteristics.

2. Finite wings show more significant changes in sectional aerodynamic characteristics compared to the infinite wings. This indicates that the change in the geometry of near wake sheet caused by yawed flow is a primary contributor to the changes in aerodynamic characteristics. The non-linearities in flow field caused by yawed flow (as seen in the infinite case at high Mach numbers) is augmented by the near wake effects.

3. The yawed flow effects does not appear to be the primary contributors for the errors in the prediction of vibratory airloads. Corrections were applied to the lifting line analysis using both the steady and unsteady aerodynamic models extracted from the CFD analysis. These modifications, although found advantageous, did not show considerable improvements from the baseline model.

4.2 Inflow Effects

For the high speed forward flight condition studies, the effects of the wake modeling are relatively unimportant. The inflow is dominated by the free stream component perpendicular to the rotor disk, owing to a larger shaft tilt angle.
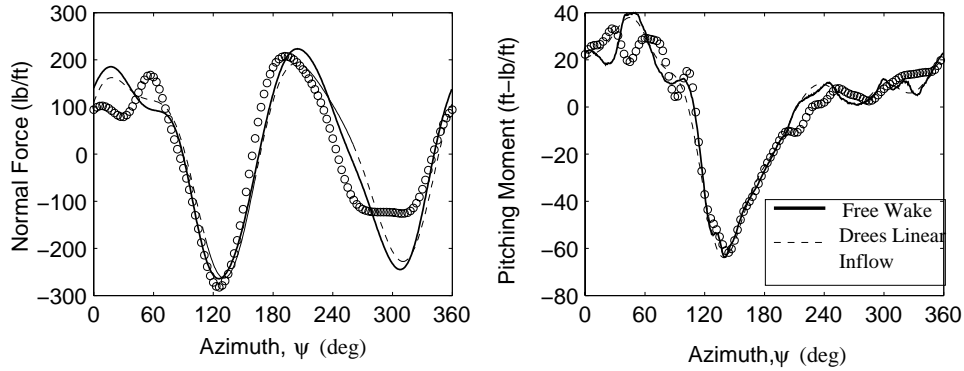
Figure 4.13: Vibratory normal force (2/rev and higher) and pitching moment (1/rev and higher) at r/R=0.865 for different inflow models

Figure 4.13 shows the oscillatory normal force and pitching moments obtained using a linear (Drees) inflow model compared with those obtained from the free wake based inflow modeling (baseline). It is evident from the plot that the induced inflow components have very little effect on both the magnitude and phase of the vibratory normal force. However, the pitching moment shows absence of some of the higher harmonics when the linear inflow model was used.

4.3 Transonic Effects

The advancing blade lift impulse (Figure 4.1) is the dominant contributor to vibratory airloads over a large portion of the span (50%R to 80%R). The studies performed here are to verify whether this phenomenon is caused by the transonic effects on the advancing side.

Moving shock waves are clearly visible in the surface pressure distributions, although they are more predominant in the outboard regions (Figure 4.14). But it suggests that transonic effects might play a key role in the production of the
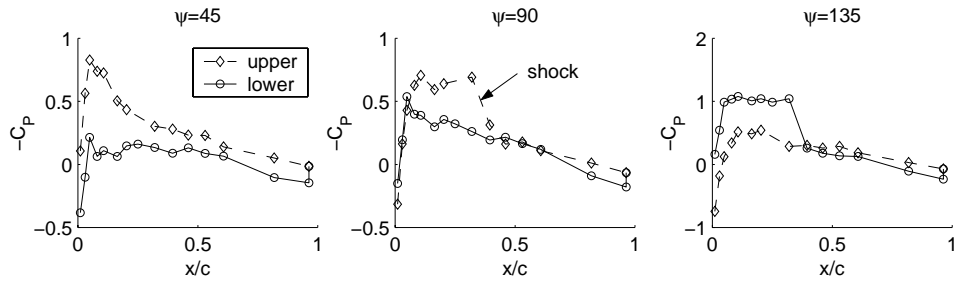
177

Figure 4.14: Surface pressure distributions at $r/R=0.965$ ($\mu=0.368$, $C_T/\sigma=0.078$)

advancing blade lift impulse. To isolate the transonic effects, simulations were conducted reducing the tip Mach number and maintaining the same advance ratio. The blade motions used are those obtained from the structural dynamic model when it is forced with the measured aerodynamic loads. The blade motions remain the same for all the cases studied.

The normal force obtained from these computations at the inboard station is shown in Fig 4.15(a). The oscillatory normal force wave form shows the presence of the up-down impulse even at the lowest tip Mach number case. Hence, it appears that the impulsive loading in the first quadrant is not a transonic effect. The pitching moment waveform (Fig 4.15(b)) on the other hand shows larger deviation from the baseline case. This is more apparent at the outboard radial station (Fig 4.16(a)). However, the oscillatory normal forces maintain the phase of the negative lift even at the lower tip Mach numbers.

Overall, the results indicate that transonic effects are the key contributors to the advancing blade pitching moment. However, it does not have any significant effect on the impulsive loading in the advancing blade lift.
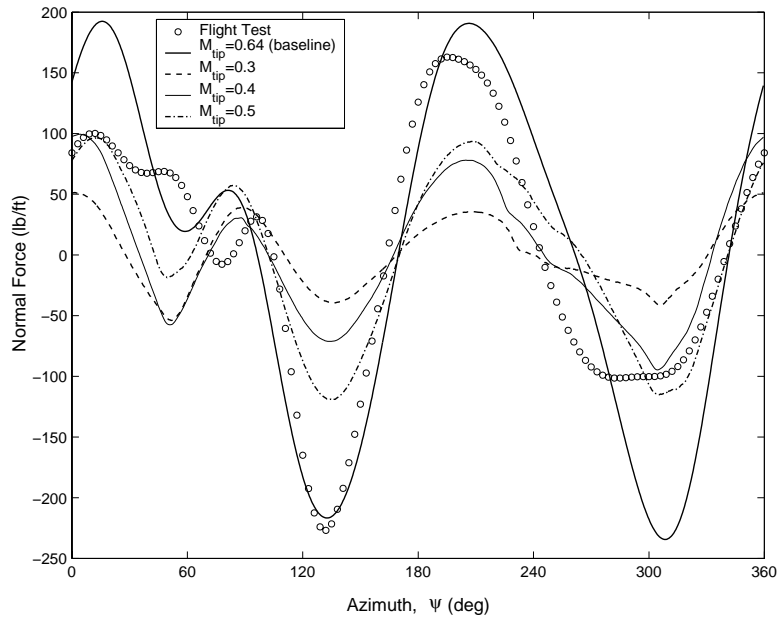
(a) Normal force (2-10/rev) predicted from CFD
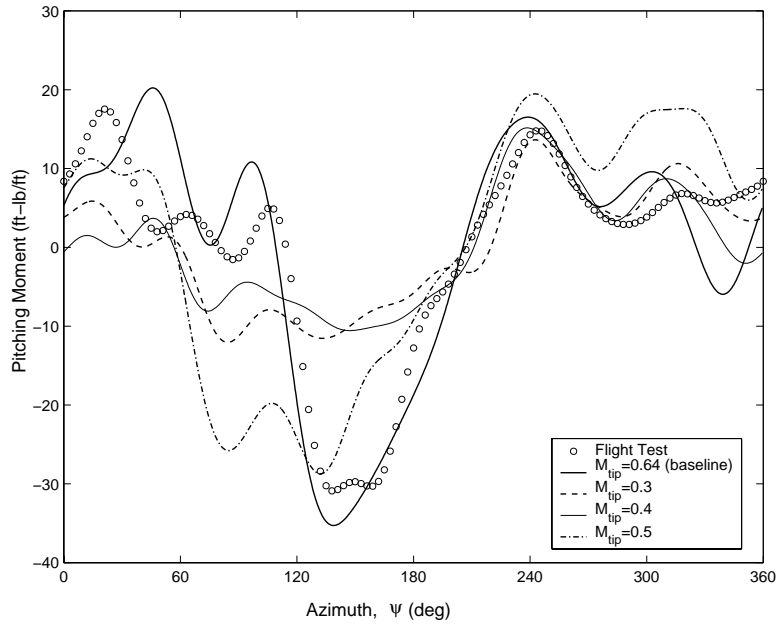
(b) Pitching Moment (1-10/rev) predicted from CFD

Figure 4.15: Effects of compressibility on vibratory airloads (r/R=0.775, μ=0.368, C_T/σ=0.078)
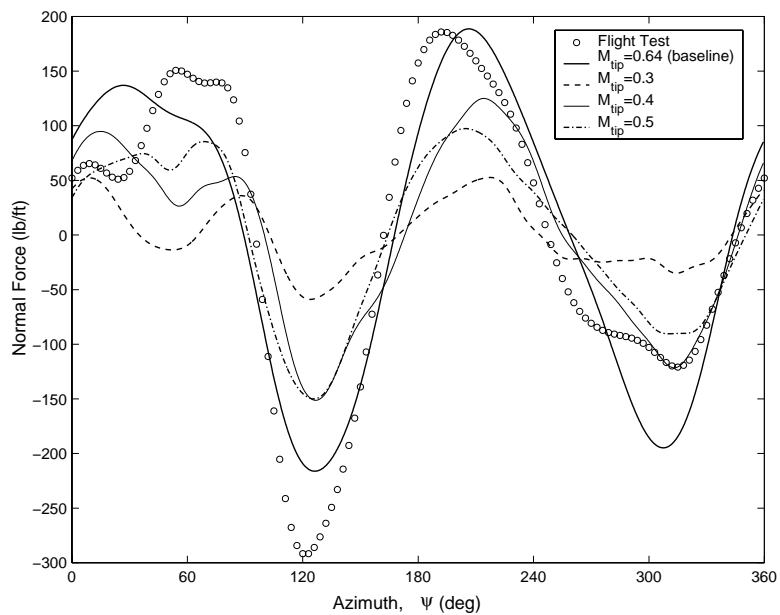
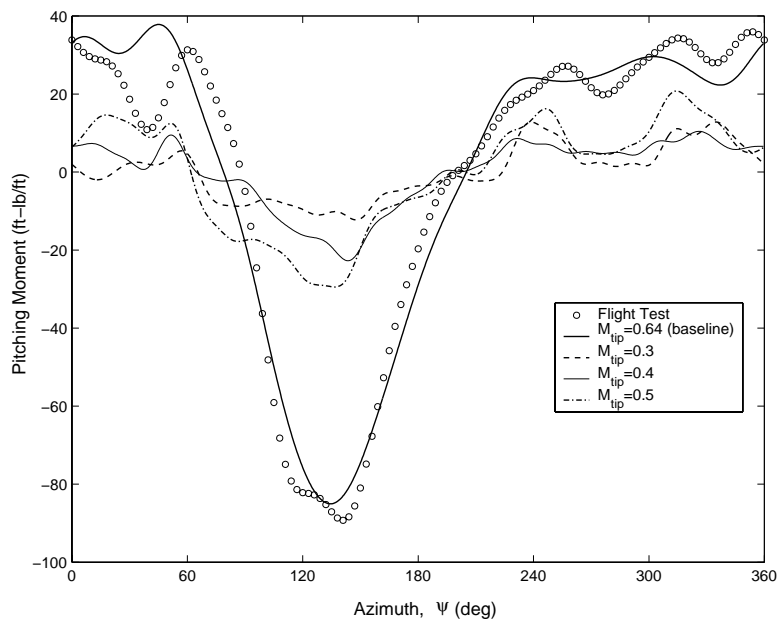(a) Normal force (2-10/rev) predicted from CFD

(b) Pitching Moment (1-10/rev) predicted from CFD

Figure 4.16: Effects of compressibility on vibratory airloads (r/R=0.965, μ=0.368, C_T/σ=0.078)

4.4   Viscous Effects

Effects of viscosity can be isolated by performing an inviscid simulation (Euler) instead of the Navier-Stokes simulations. There is no evidence of retreating blade stall at this flight condition because of the moderate blade loading (C_T/σ=0.0783). Therefore the effect of viscous forces should be small compared to the effects of the pressure forces.

Results of the Euler simulations are compared with those obtained from the Navier-Stokes simulations in Fig 4.17 and 4.18. The sectional aerodynamic loads (2/rev and higher normal force, 1/rev and higher pitching moment and 1/rev and higher chord force) are plotted for a span station of $r/R = 0.775$ and $r/R = 0.965$ respectively. It is evident that the vibratory load correlation is only degraded to a small extent (in both lift and pitching moment) when the Euler computations are used. The chord forces obtained from Euler computations show better correlation with test data compared to those obtained from the Navier-Stokes computations. The effects of viscosity is absent in the test data because the chord forces are obtained from integrating the chordwise pressure measurements. Therefore it is logical that the inviscid computations show better agreement with the test data compared to the viscous result for the chord forces.

4.5   Role of Blade Motions

The role of elastic blade motions are analyzed to understand the relative influence of flap, torsion and lag degrees of freedom. Figure 4.19 shows the first seven modes of flap, lag and torsion and their natural frequencies.

The first flap and lag modes are very close to being rigid motions. The higher
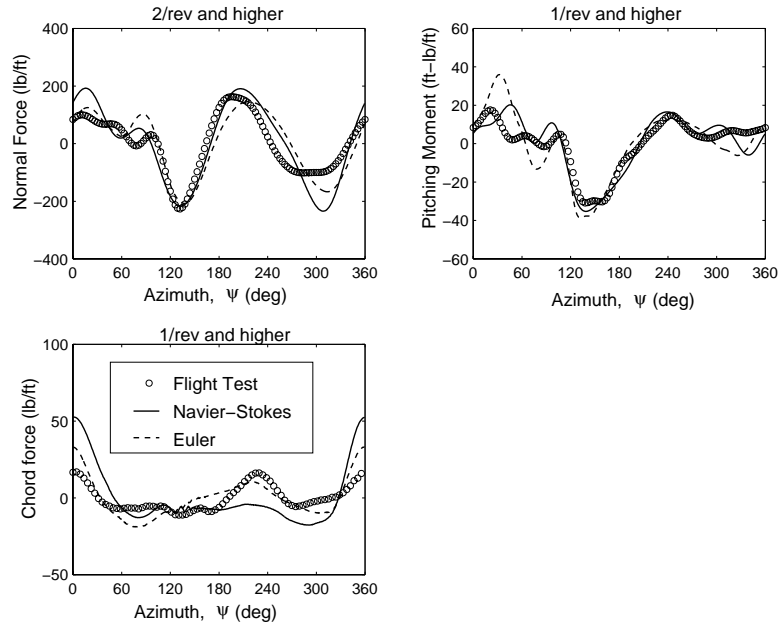
Figure 4.17: Effects of viscosity on the vibratory airloads (r/R=0.775, μ=0.368, C_T/σ=0.0783)
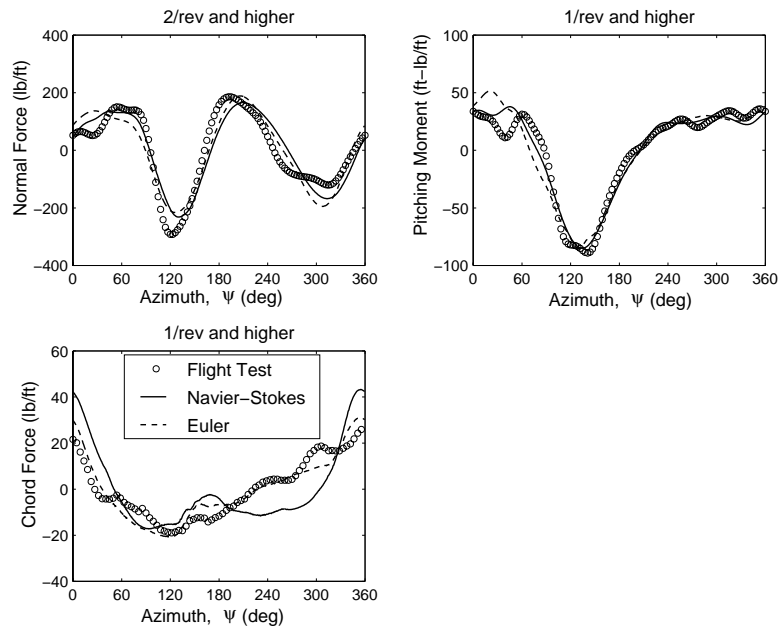

Figure 4.18: Effects of viscosity on the vibratory airloads (r/R=0.965, μ=0.368, C_T/σ=0.0783)

modes are a result of the blade elasticity. The major contributions to elastic flap motion are from the 2nd flap mode. The torsional motion is composed of the rigid motions (collective+cyclic) and the elastic torsion. The elastic torsion introduces a change of approximately -5 degrees in the advancing blade pitch angle.

The analysis is performed by eliminating one degree of freedom at a time from the given set of blade motions. The CFD calculations are conducted for the same tip Mach number and advance ratio in each case. The predictions of normal force (2/rev and higher) and pitching moment (1/rev and higher) are compared with the baseline case (all blade motions) at two span stations (r/R=0.775 and r/R=0.965).

Figure 4.20 shows the predictions obtained by eliminating the lag degree of freedom. There is very little change from the baseline in both normal force and pitching moment. Therefore, it is evident that the lag degree of freedom does not play a significant role in determining the rotor vibratory airloads.

Figure 4.21 shows the predictions obtained by eliminating the flap degree of freedom. The normal force predictions obtained show larger magnitude and inadequate resolution of the advancing blade lift impulse at the inboard station. The effect of flapping motion is to increase the effective angle of attack on the advancing side (flap down) and decrease the effective angle of attack on the retreating side (flap up). This explains the larger magnitude of the normal force predictions when the flap degree of freedom is absent. The up-down impulse appears to be an effect caused by the flap degree of freedom as it is conspicuously absent in the predictions. It is also evident that the up-down impulse plays a key role in determining the correct lift waveform on the advancing side. The
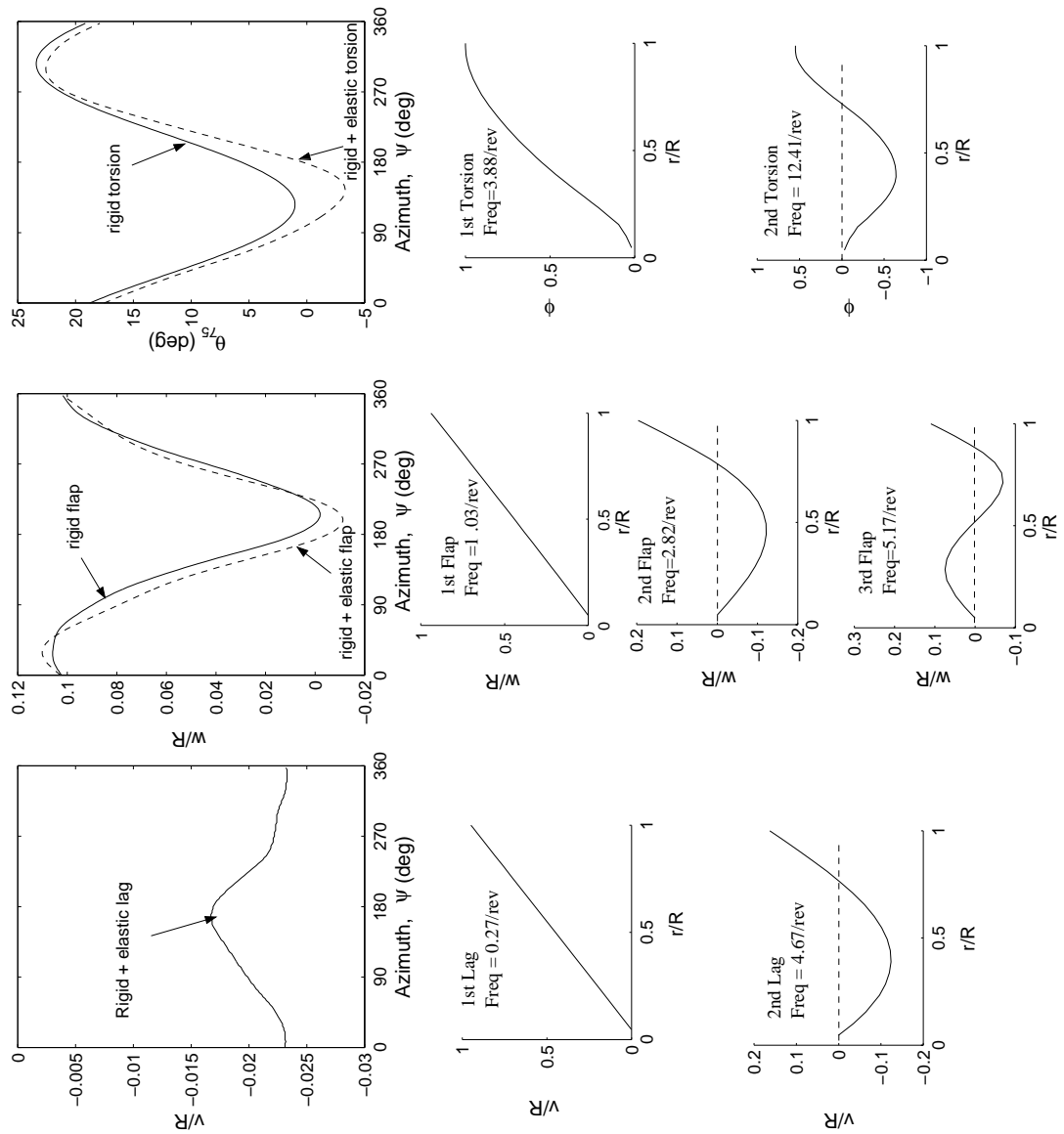
Figure 4.19: Modes, frequencies and blade motions for UH-60 A blade (μ=0.368, C_T/σ=0.0783)

Figure 4.20: Effects of eliminating lag degree of freedom on vibratory airloads (μ=0.368, C_T/σ=0.0783)

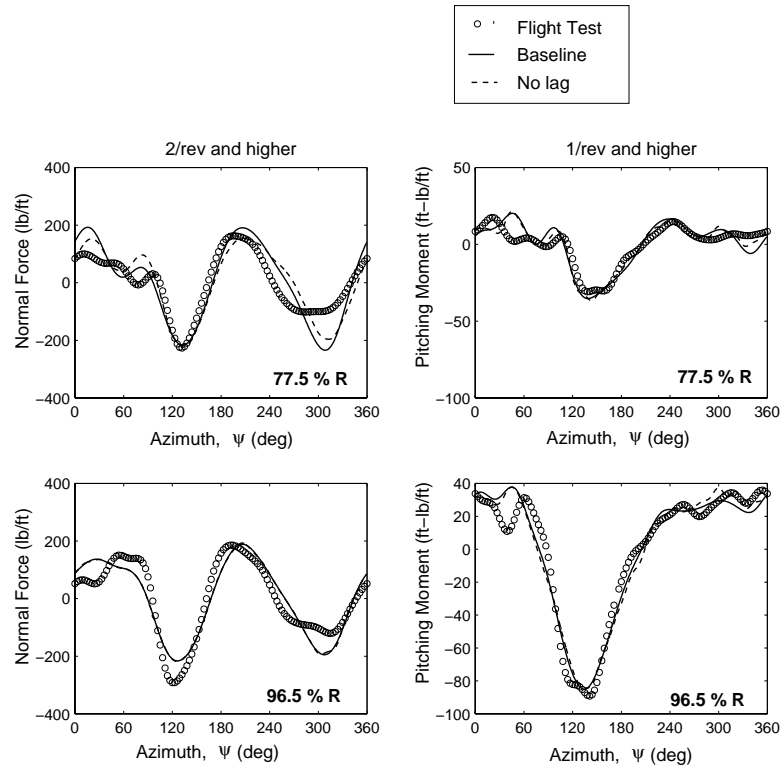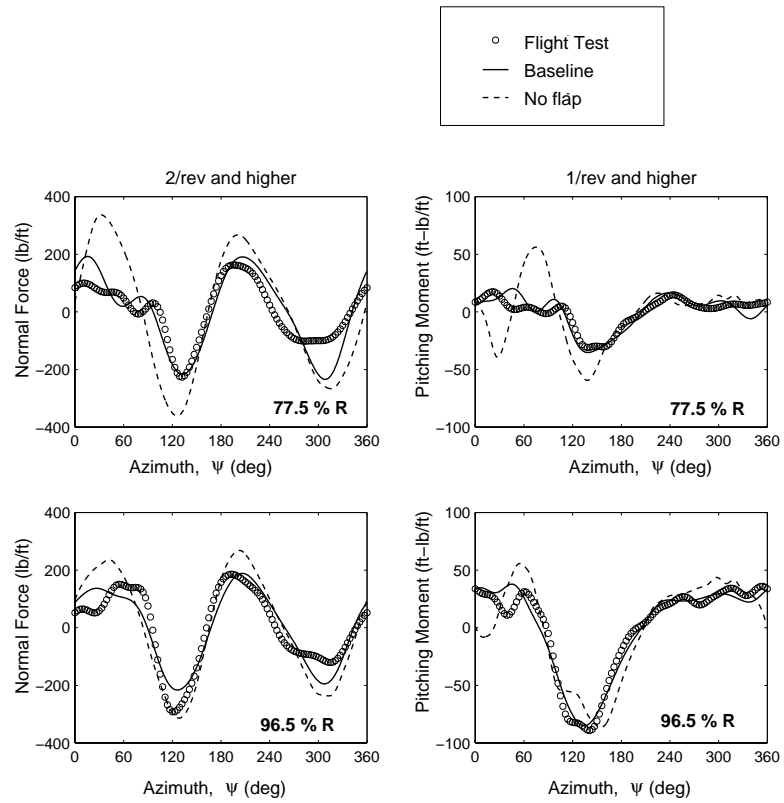Figure 4.21: Effects of eliminating flap degree of freedom on vibratory airloads (μ=0.368, C_T/σ=0.0783)
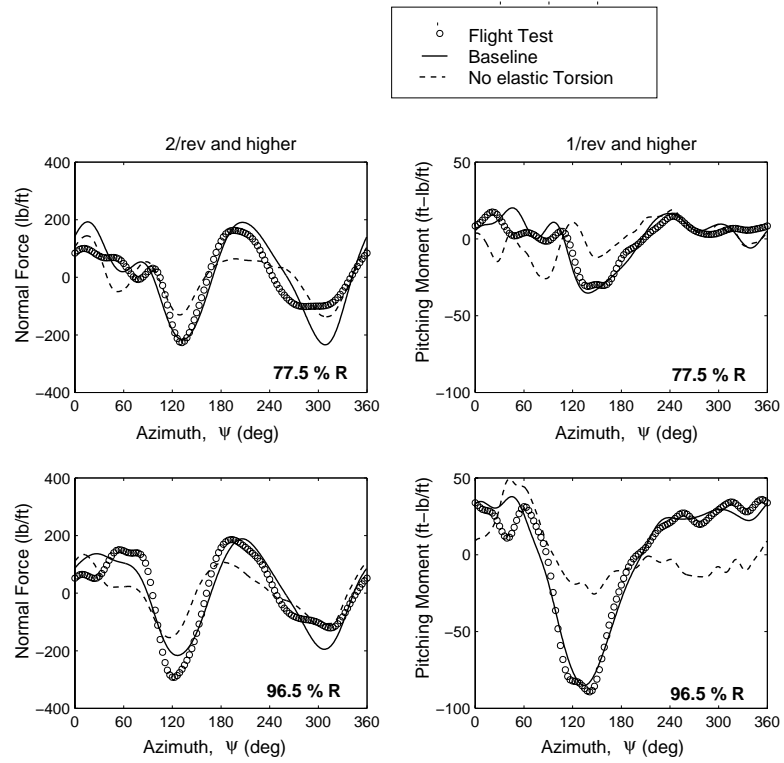
Figure 4.22: Effects of eliminating flap degree of freedom on vibratory airloads (μ=0.368, C_T/σ=0.0783)

pitching moments in the outboard station do not show large differences from the baseline. However, the pitching moments at the inboard radial station does not show the impulsive character which is present in the baseline case.

Figure 4.22 shows the predictions obtained by eliminating the elastic torsion degree of freedom. The rigid torsional motions are still preserved to maintain the approximately correct magnitude of aerodynamic loads. The normal force predictions show smaller magnitude, but the up-down impulse is still present. This further reinforces the hypothesis that the up-down impulse is produced by the flap degree of freedom. Pitching moment predictions show a large deterioration, with the correlation being worse outboard. Therefore, it is evident that the elastic torsion determines the phase and magnitude of the negative pitching moments towards the tip. The predictions at the inboard station shows the large impulsive (3/rev) nature, which is the manifestation of the flap degree of freedom. The presence of torsion appears to play an important role even at the inboard station in determining the exact magnitude and phase of the pitching moments.

Figure 4.23 summarizes the key observations and attempts to elucidate the role of the flap degree of freedom in the generation of the advancing blade lift impulse and the torsional degree of freedom in determining the correct phase and magnitude of the normal force variation at the inboard station. The results presented are the predicted vibratory normal force at the inboard radial station obtained by prescribing: (a) the rigid torsional motions (collective + cyclic) only; (b) collective + cyclic + flap (rigid and elastic); (c) collective + cyclic + elastic torsion; and (d) All the elastic and rigid motions. Prescribing only the rigid torsional motions (case (a)) clearly shows the phase error in the negative

lift phase and absence of the up-down impulse. The introduction of the flap degree of freedom shows the generation of the up-down impulse and a better phase correlation with the flight test data. However, there is a considerably less vibratory force amplitude compared to the flight test data in this case. The use of elastic torsion along with the collective and cyclic, i.e., excluding the flap degree of freedom, shows improvement in the phase correlation, but shows larger amplitude. The base line case (case (d)), which uses all the rigid and elastic motions shows good correlation of both phase and magnitude. It can be inferred that the elastic deformations (both flap and torsion) are very important for accurately capturing the vibratory load phase and magnitude.

Figure 4.24 summarizes the effects of flap and torsion degrees of freedom on the pitching moment at the outboard radial station. The results are presented for the same set of configurations as the previous figure. A negative pitching moment is produced when the rigid torsional motions (collective + cyclic) are prescribed. Inclusion of the flap degree of freedom decreases the effective angle of attack and hence decreases the magnitude of the negative pitching moment. The elastic torsional deformations which have a negative peak on the advancing side decreases the angle of attack such that the pitching moment magnitude and phase are correctly captured.

4.6 Three dimensional Effects

The 3-D flow effects are composed mainly of finiteness, yawed flow and spanwise bending curvature. The 3-D CFD calculations are now compared with 2-D CFD calculations. The 2-D CFD calculations were performed for a given section of the
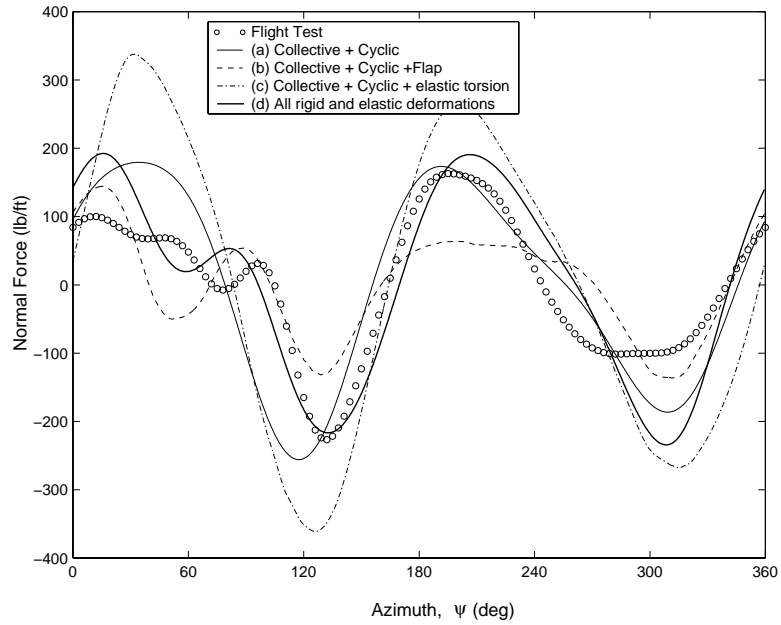
Figure 4.23: Effects of degrees of freedom on vibratory normal force (2/rev and higher) at r/R=0.775
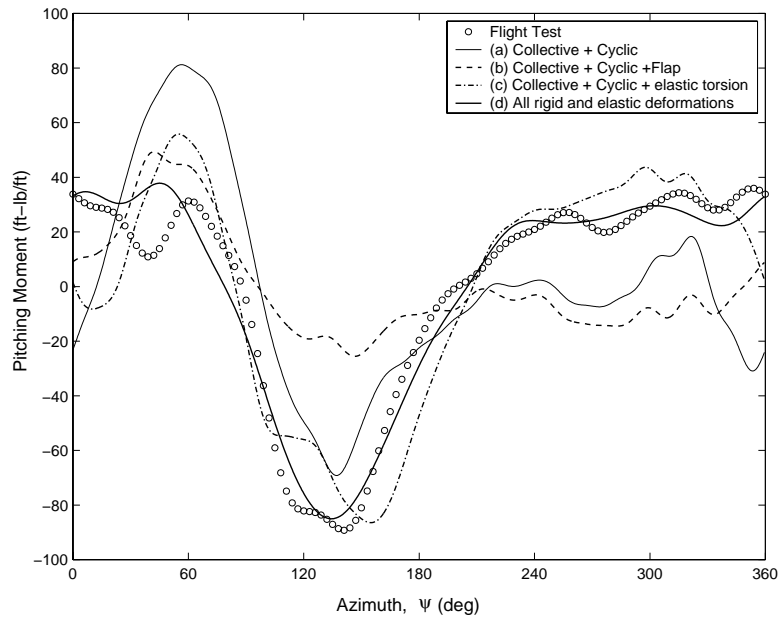
Figure 4.24: Effects of degrees of freedom on vibratory pitching moment (2/rev and higher) at r/R=0.965
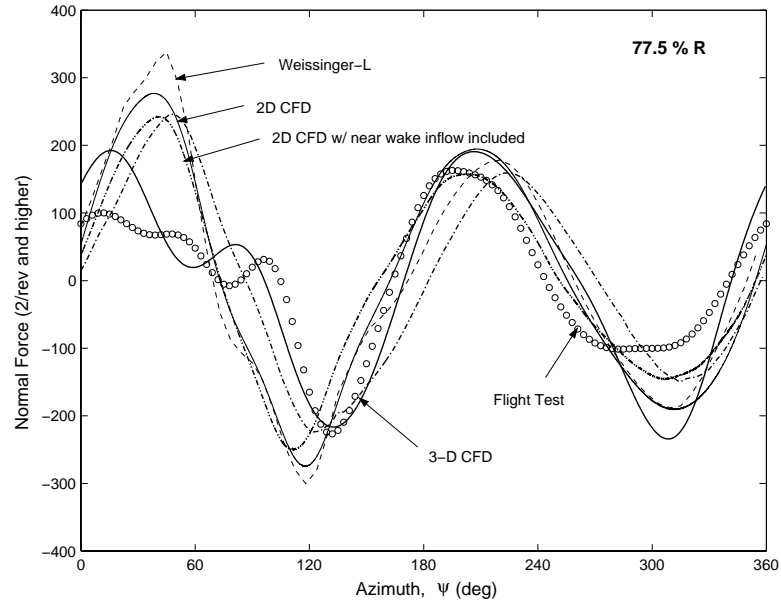
Figure 4.25: Vibratory normal force (2/rev and higher) at r/R=0.775, with and without three-dimensional effects

rotor blade by supplying the sectional deformations, inflow and the time varying chordwise velocity component. This can be considered as a 2-D strip-wise CFD calculation.

The effect of bound vortices at other sections of the blade will also be absent in such a study. A study which includes the effect of bound vortices was also conducted. The bound vortex strengths in this case were calculated using the circulation strengths obtained from 3-D CFD calculations. The strength of near wake trailers are determined using this bound vortex distributions and an induced angle of attack is calculated at the desired section for which the 2-D computations are performed. This induced angle of attack is subtracted from the pure 2-D angle of attack to get the effective 3-D angle of attack.

Figure 4.25 shows the results of vibratory normal force at the 77.5% span station. The 2-D CFD results appear to be similar to the lifting line based

analysis and shows the absence of the up down impulse and presence of the phase error in the negative lift. The use of near wake induced angle of attack correction did not improve the 2-D CFD results. Overall, it appears that the three dimensional effects are the key contributors to good correlation obtained using the 3-D CFD computations.

Figure 4.26(a) compares predicted normal force using 2-D and 3-D CFD computations. The 2-D CFD results are similar to the lifting-line results with the impulsive behavior missing on the advancing blade. In the previous section the impulse was identified as a consequence of flapping motion. It can now be concluded that it is a 3-D effect associated with the flapping motion. 2-D CFD predictions show larger peak to peak magnitudes compared to 3-D CFD predictions towards the tip. This is a consequence of the finiteness effects. This effect is accounted for in the lifting-line model.

Figure 4.26(b) compares predicted pitching moments using 2-D and 3-D CFD computations. The 2-D calculations over-predict the peak to peak moments at 77.5% R. This is again similar to the predictions obtained from the lifting line model. Therefore the phenomenon of over-prediction of inboard pitching moments is related to 3-D effects. In addition, like the normal force waveform, the 3-D pitching moments also show an impulsive behavior in the advancing blade. Towards the tip, the 2-D pitching moments shows large initial negative peak in the advancing side which is also present in the lifting line case. Further investigation revealed that the 3-D shock relief effects at the tip alleviate the initial large negative pitching moment peak. The excursion of the aerodynamic center towards the trailing edge, when the airfoil is generating positive lift is the reason for the large negative pitching moment. The shock relief effects limit

this excursion of the aerodynamic center and hence alleviate the large negative pitching moments.

Figure 4.27 elucidates the effects of shock relief. The pressure contours shown are for a finite wing. But the relief effects are similar in the rotor environment also. The pitching moment vs angle of attack curves show decay as one moves towards the tip. The lower $C_{m\alpha}$ at the tip prevents the formation of large pitching moment excursions on the advancing side. A table lookup which incorporates the tip relief effects was generated and used in the lifting line analysis. It can be observed that (Figure 4.28) the pitching moment prediction from the lifting line analysis shows considerable improvement when the shock relief effects are accounted for.

To investigate the limitations of the lifting-line model to capture the 3-D effect associated with flapping motion, the problem is further dissected. Starting from hover, for a progressively increasing set of forward speeds the prescribed flap and torsion deflections are used separately. Predictions are compared between 3-D CFD, lifting-line and 2-D CFD models. Figure 4.29 shows that for the torsion deflection both lifting-line and 3-D CFD predict similar lift. Significant discrepancy is noted for the flap deflection. This discrepancy is independent of forward speed and is therefore not a purely high-speed phenomenon. The 2-D CFD results agree well with the lifting-line predictions suggesting that the discrepancy is not a 2-D nonlinear effect but a purely 3-D phenomenon.

4.6.1 Spanwise curvature

The flap bending curvature (w'') is observed to contribute to the advancing blade lift impulse. The bending curvature changes rapidly at the inboard stations in the
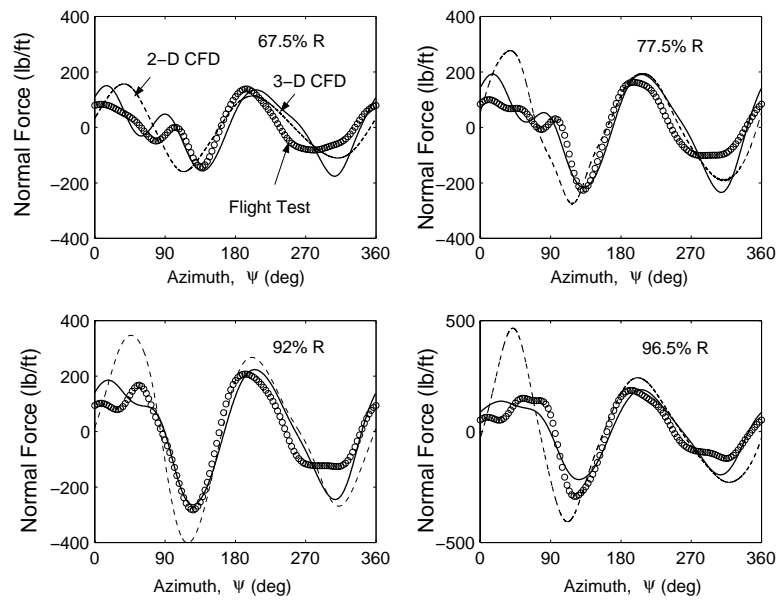
(a) Normal Force (2/rev +)
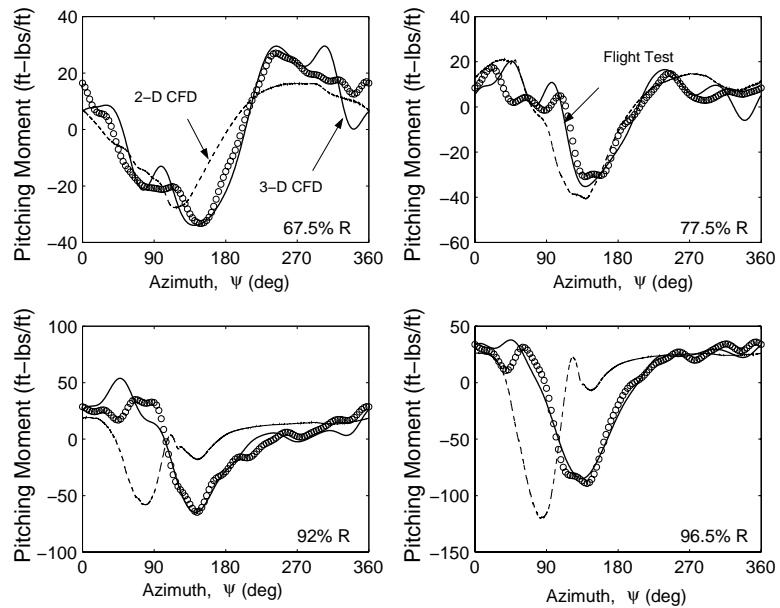
(b) Pitching Moment (1/rev +)

Figure 4.26: Effects of three dimensionality in vibratory airloads (μ=0.368, C_T/σ=0.0783)

Figure 4.27: Shock relief effects for a finite wing (AR=15.30, SC1095 cross section, M=0.8)

Figure 4.28: Pitching moments at the outboard stations from lifting line analysis with effects of shock relief included (μ=0.368, C_T/σ=0.0783)
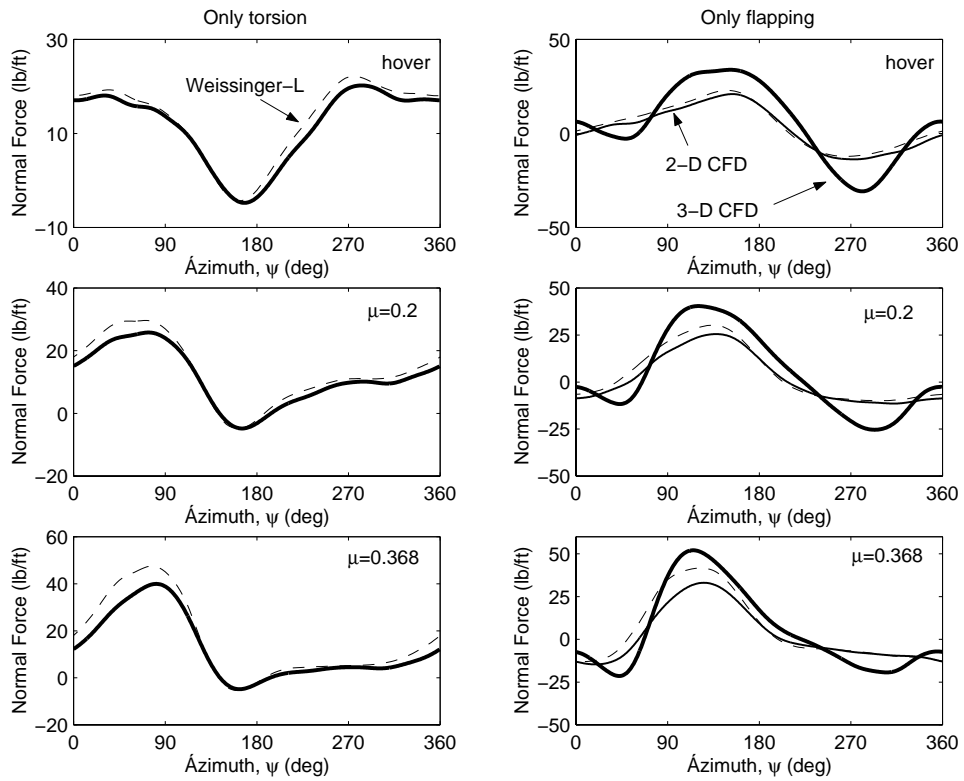
Figure 4.29: Study of advancing blade lift impulse at 77.5% R; Comparing 2-D and 3-D CFD and lifting-line predictions for specific blade motions at three flight speeds

advancing blade. This is because the blade flap response transitions from being dominated by the 1st flap mode to being dominated by the 2nd flap mode. The 2nd flap mode 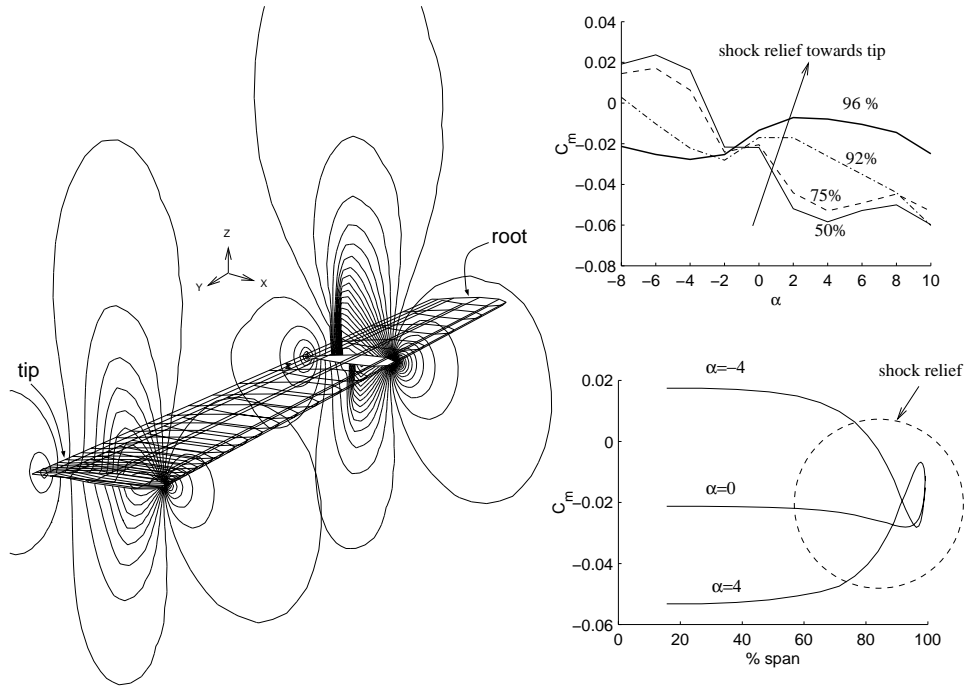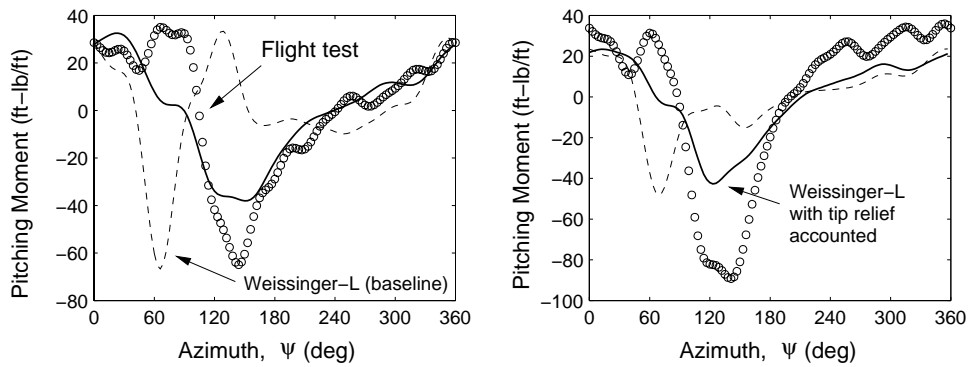has a nodal point at 78.5% R and has the largest change in slope in this region. CFD computations were performed removing the contribution of the 2nd flap mode from the flap response.

Figure 4.30 shows the normal force predictions with and without the effects of 2nd flap mode. Without the effects of curvature induced by the 2nd flap mode, 3-D CFD predictions are close to those predicted by the lifting-line model (i.e. the advancing impulse is absent). Therefore, it is clear further that the three dimensional effects of the 2nd flap mode (curvature induced effects) are the primary contributors to the advancing blade lift impulse.

The pitching moments show similar trends (Figure 4.31) in the inboard station. The impulsive character of the pitching moment is found absent when using the flap response without the 2nd flap mode contributions. However, towards the tip, there is little variation between the baseline and present case. This is true for the normal force variation also. Therefore, as expected, the curvature effects are more prominent at the inboard stations rather than at the tip.

The spanwise curvature is accounted for in the lifting-line model as the angle of attack distribution is determined relative to the deformed section. Therefore the exact aerodynamic mechanism that relates the changes in spanwise curvature to the impulsive aerodynamic loading is not clear at present. This issue is currently being investigated in detail.
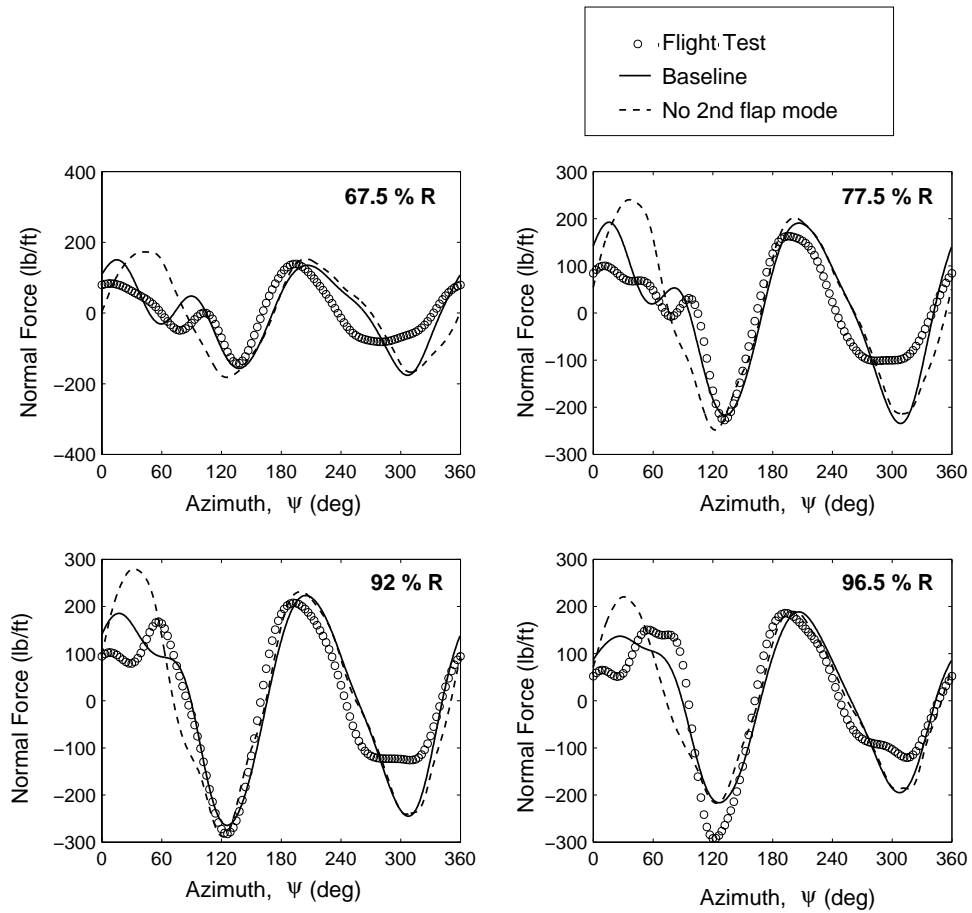
Figure 4.30: Effects of removing the 2nd flap mode contribution to the flap response on 2-10/rev normal force(μ=0.368, C_T/σ=0.0783)
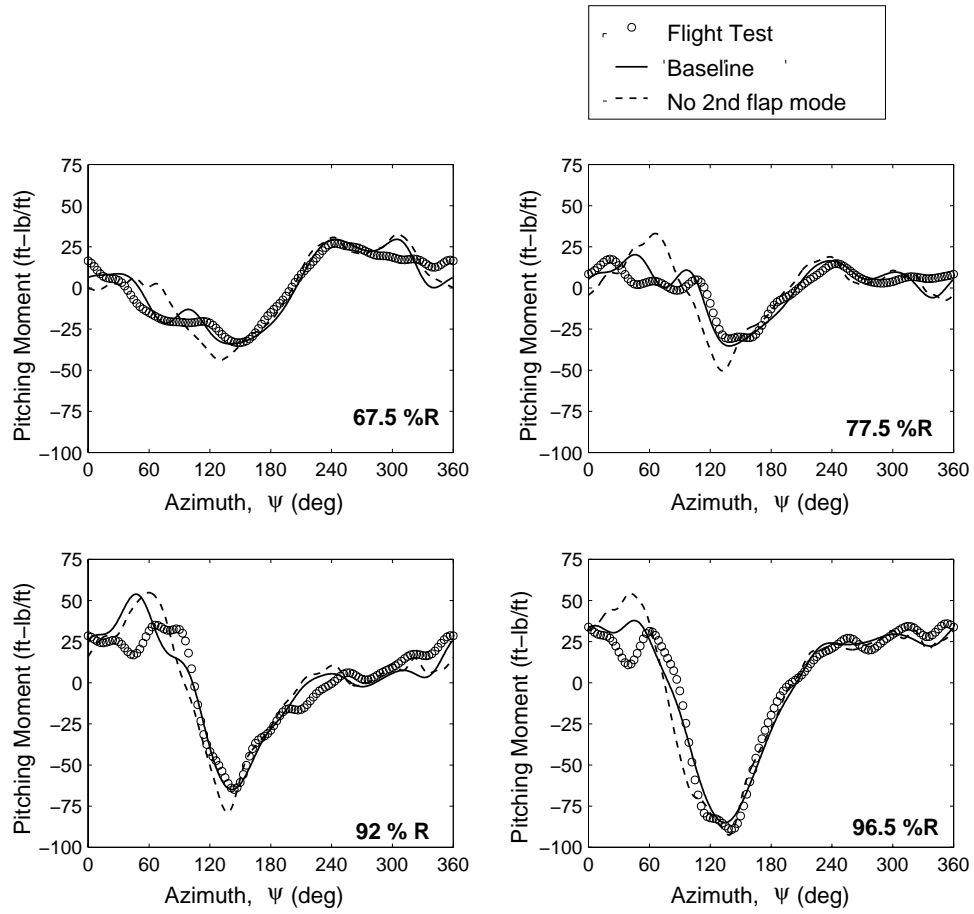
Figure 4.31: Effects of removing the 2nd flap mode contribution to the flap response on 1-10/rev pitching moments(μ=0.368, C_T/σ=0.0783)

4.7 Summary of Key Observations

1. The 3-D CFD captured advancing blade impulse in lift is not a transonic or viscous effect. This impulse is generated by 3-D aerodynamics associated with blade flapping motion. The flap bending curvature appears to play a key role.

2. The torsional degree of freedom is the key contributor to the low frequency (1/rev) component of the advancing blade pitching moment at all the stations. The high frequency components (impulsive nature) are determined by the flapping motion.

3. Near the tip, it is the 3-D transonic effects (shock relief) that play the key role in determining the peak to peak magnitude and phase of pitching moment. At the intermediate span stations (60% to 80%) the three dimensional effects associated with flap bending contribute to the phase and magnitude of the pitching moments.

Chapter 5

CFD coupling with UMARC

This chapter describes the coupling of the CFD based aerodynamic model developed with the advanced structural dynamics model. The validation of the predictions from the CFD based aerodynamic model is presented in detail in Chapter 3. Prescribed blade motions obtained by forcing the structural dynamic model with measured airloads was used for the validation purpose. It was observed that the predicted vibratory airloads showed good agreement with measured aerodynamic loads. However, the steady and 1/rev harmonics showed large deviations from the flight test data. This was because the predicted aerodynamic loads did not ensure the trim state.

In this chapter the structural dynamic model and the CFD based aerodynamic model are coupled so as to obtain a consistent blade response, trim and airload solution. In contrast to the validation study conducted using the prescribed blade motions the trim state is ensured as part of the solution in this approach. Therefore, all the harmonics of the aerodynamic loads predicted can be correlated with test data. Also, this approach does not require any input from the measured aerodynamic loads. The CFD predicted aerodynamic loads
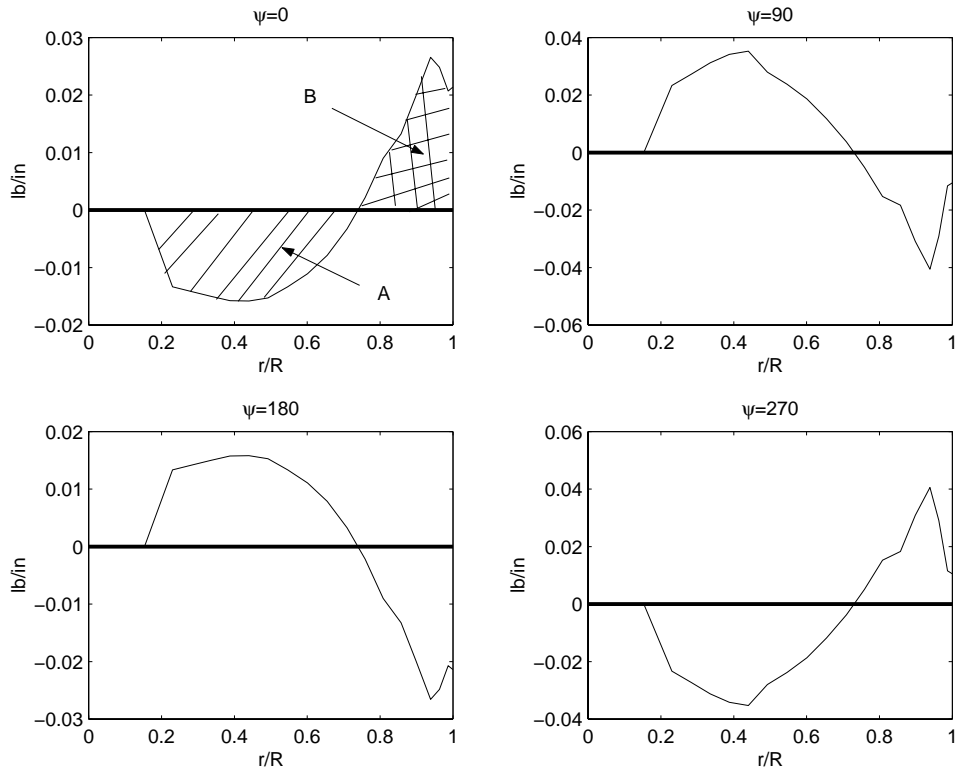
Figure 5.1: Causes of small 1/rev hinge moments: reversal of 1/rev normal force sign with radius

are used as the forcing for the structural dynamic model in every iteration of the coupling process.

5.1   Coupling Procedure

The coupling procedure used here is similar to that described in the feasibility study with a simplified structural dynamic model (Chapter 3). Briefly, the algorithm is as follows:

1. Obtain an initial guess for control angles and blade motions using UMARC comprehensive analysis solution. The sensitivity of the control angles to
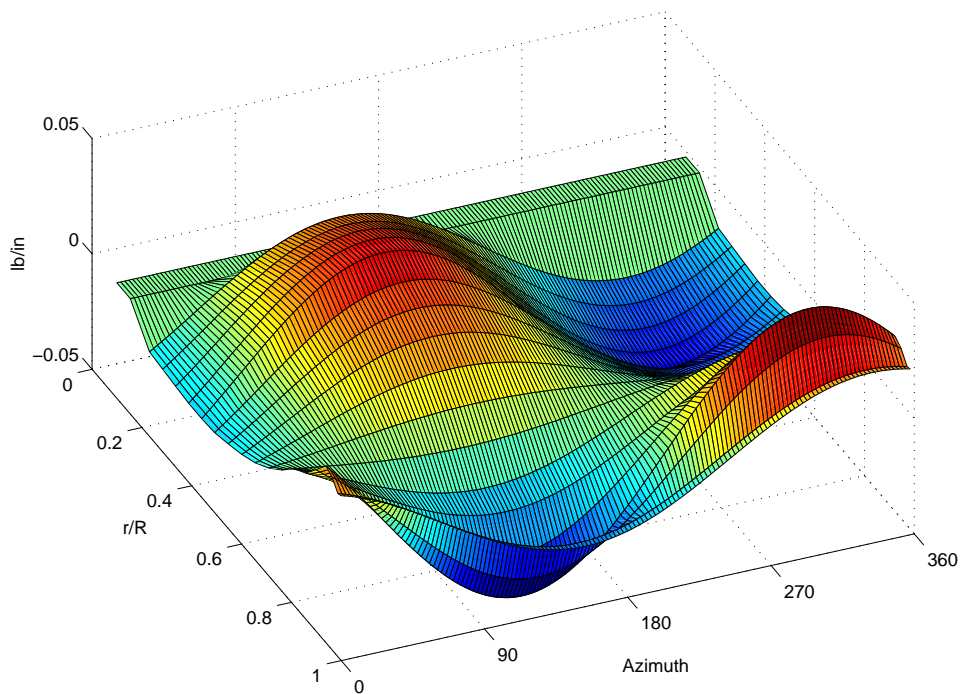
Figure 5.2: Variation of 1/rev normal forces with span and azimuth

the vehicle trim residues (trim Jacobian) is evaluated.

2. Calculate CFD airloads using the above control angles and the blade motions.

3. Calculate blade motions using the CFD airloads (normal force, pitching moment and chord force) as the forcing function.

4. Correct the control angles according to the rotor trim residues.

5. Check for blade response and trim convergence. If the convergence condition is not satisfied return to step 2.

The primary difference in the implementation of this algorithm from the feasibility study is in the modeling of aerodynamic damping terms. The predicted

CFD aerodynamic loads which form the forcing (RHS) have motion dependent components which contribute to the aerodynamic damping in the system. For the solution of the 2nd order ODE system which represents the rotor dynamics, often the motion dependent components are taken to LHS. In the feasibility study the aerodynamic damping terms were found by linearizing the motion dependent terms in the extended lifting line theory based aerodynamic model. For the coupling process described here the aerodynamic damping terms are not taken to the LHS. Therefore, the entire CFD predicted aerodynamic loads are used as the forcing.

The validation of the structural model conducted suggested that the there is some amount of structural damping present in the rotor system (4% critical) [74]. Therefore, this is the only source of damping present in this approach.

During the initial stages of the development of the coupling procedure, it was observed that the blade response diverged abruptly after showing monotonic convergence trends. This problem was traced to large 1/rev hinge moment imbalance caused by the rotor being slightly out of trim. In trimmed forward flight the 1/rev aerodynamic normal forces reverse sign as one moves radially outboard. This is because the 1/rev airloads need to be in approximate moment balance about the hub for low steady shaft moment. Therefore, in real flight the integrated 1/rev hinge moments are relatively small. Figure 5.1 explains this more clearly. The moments produced by areas (A) and (B) about the hinge line complement each other to produce a small hinge moment. Figure 5.2 shows the 3-D plot of 1/rev normal force variations with radius and azimuth. It can be observed that the trend of normal force distribution reversing its sign as one moves outboard is valid at all azimuthal locations.

In the analysis, small variations in aerodynamic loads during the trim procedure (especially when the CFD airloads are supplied back to the structural dynamics) produces large 1/rev hinge moments. In the absence of aerodynamic damping these 1/rev hinge moments diverge the flap response.

The problem was rectified by using an additional loop which adjusts the control angles iteratively to produce the same hinge moment magnitude as that produced by the first comprehensive analysis solution. This step uses the lifting line model. The lifting line analysis was found to generate similar 1/rev normal force prediction as compared to those from the CFD computations. Response convergence was obtained after the introduction of this additional correction. It is to be noted that all lift, drag and pitching moment obtained from the CFD computations are coupled to the structural analysis in this approach. Earlier loose coupling efforts have shown divergence of torsional response. This is evidently because of the discrepancy in the pitching moment predictions in previous works.

Briefly, the modified algorithm is as follows.

1. Obtain an initial guess for control angles and blade motions using UMARC comprehensive analysis solution. The sensitivity of the control angles to the vehicle trim residues (trim Jacobian) is evaluated.

2. Use the lifting line model to iteratively add corrections to the control angles (aeroelastic deformations are unchanged) to produce the same hinge moment amplitude as that obtained in step 1.

3. Calculate CFD airloads using the above control angles and the blade motions.

4. Calculate structural deformations using the CFD airloads (normal force, pitching moment and chord force) as the forcing function.

5. Correct the control angles according to the rotor trim residues.

6. Check for blade response and trim convergence. If the convergence condition is not satisfied return to step 2.

Note that step 2 was modified to add the additional corrections for the control angles in this modified approach.

5.2   Convergence of the coupling procedure

The coupling procedure converged to the prescribed numerical tolerance within 8 iterations. The convergence history of the blade response at the tip (flap and torsion) is shown in Fig 5.3. The final flap and torsion response converged to a difference of 1% between consecutive iterations. The variation of response residue

206

and the trim residue with iteration number is shown in Fig 5.4. Monotonic convergence trend can be noted from the results. However, the rate of decay of the trim residue is observed to decrease with the iteration number suggesting that the residue would tend to a constant rather than zero for a larger number of iterations.

The total normal force and pitching moment (all harmonics) at each coupling iteration are shown in Fig 5.5. The airload variation also converges to the prescribed numerical tolerance limit in 8 coupling iterations.It can be noted from the normal force variation that the changes in control angles primarily affect the lower harmonics (0-2/rev), while the higher harmonics remain relatively unaffected. This observation is illustrate more lucidly in Figure 5.6 which shows the variation of the vibratory normal force (3-10/rev). It is evident that there is little variation in the higher harmonic content with changers in control angles. Hence, it appears that good estimates of vibratory hub loads can be obtained even with just one coupling iteration.

The pitching moments show correlation with test data in both peak to peak magnitudes and phase. Also, pitching moments show a smaller variation with changes in control angles compared to the normal force. The final pitching moments obtained (after 8 iterations) capture all the trends observed in the pitching moment waveform obtained from the measurements.

The surface pressure distributions obtained at the final iteration are correlated against the available flight test data in Fig 5.7 and Fig 5.8. At the outboard (96.5%) span station an upper surface occurs at 90 degree azimuth and a lower surface surface occurs at 135 degrees azimuth. This phenomenon is well captured by the CFD predictions. Overall, the correlation of the predicted surface

pressure distributions with experimental data can be considered to be fair.
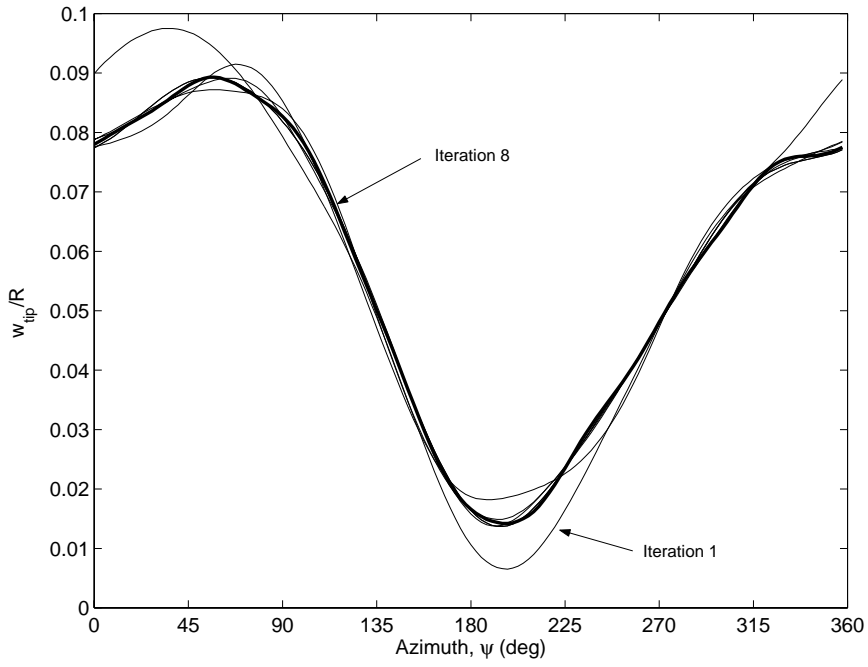
(a) Flap response at the blade tip
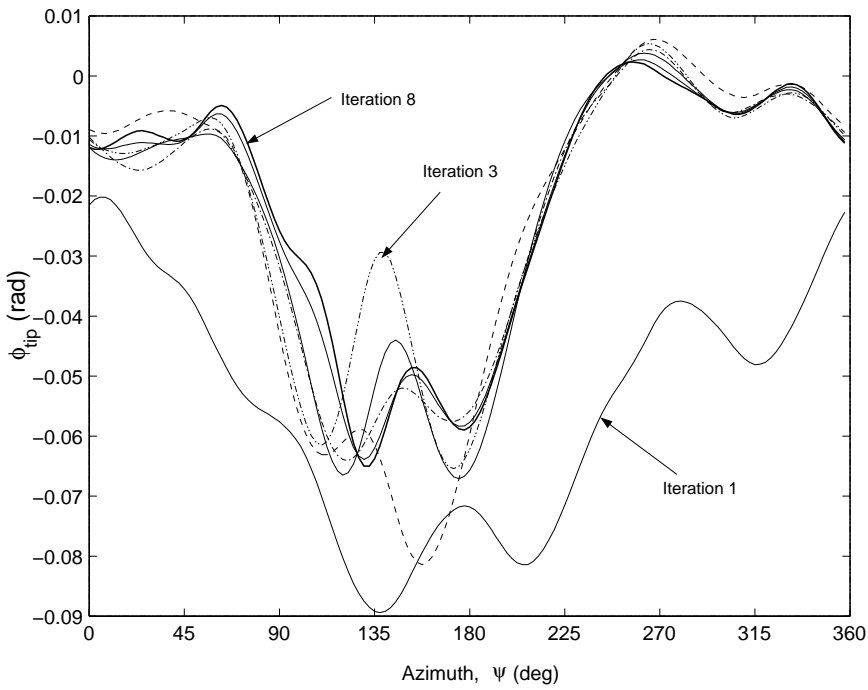
(b) Torsional response at the blade tip

Figure 5.3: Convergence of tip elastic deformations with coupling iterations
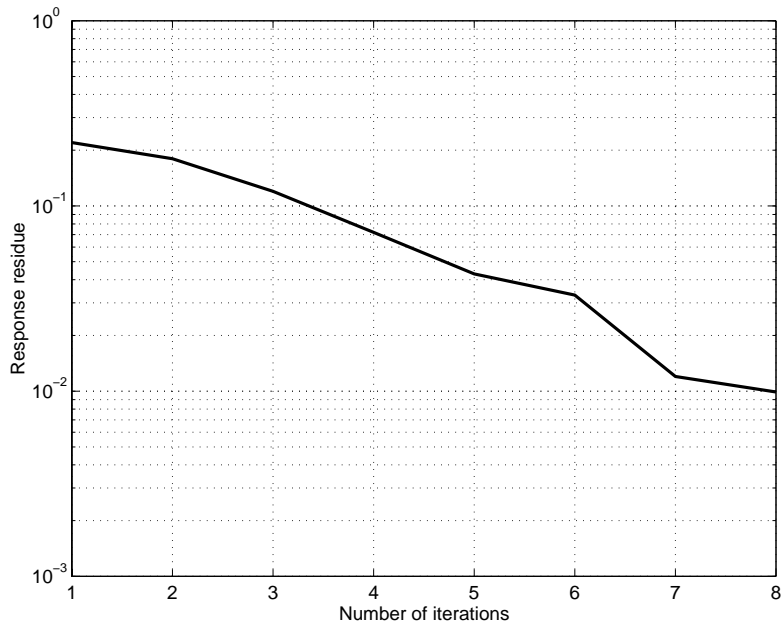
(a) Response residue (L2 norm of relative difference between consecutive iterations)
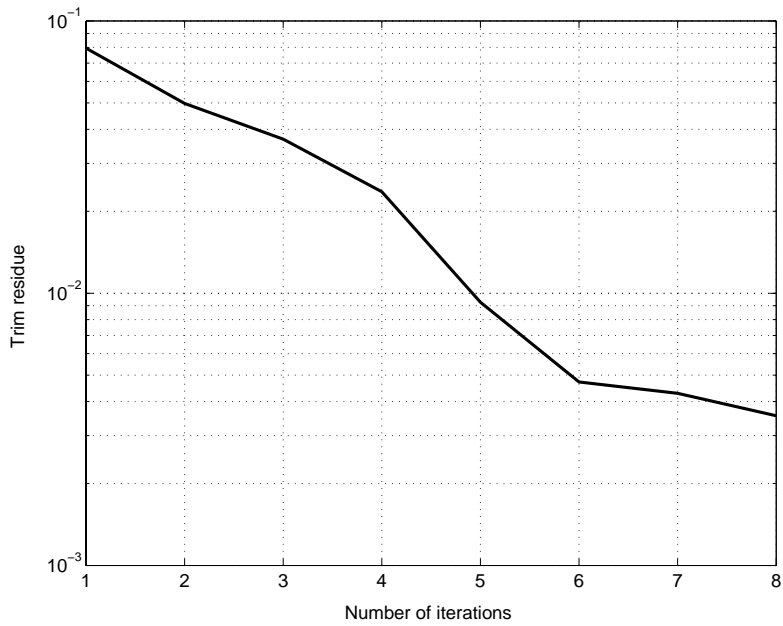
(b) Trim residue

Figure 5.4: Response and trim residue variations with coupling iterations

210
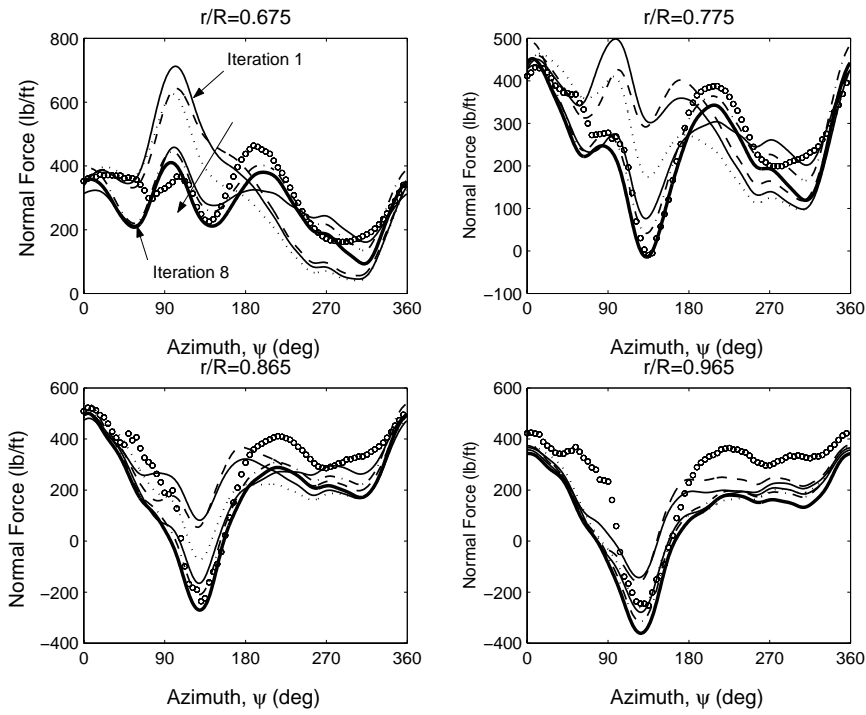
(a) Normal Force (All harmonics)
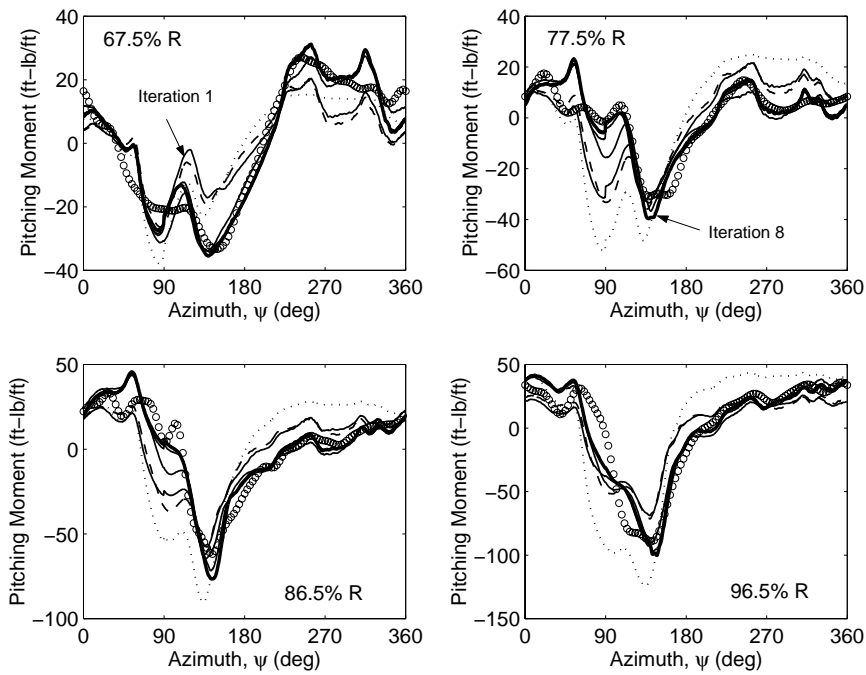
(b) Pitching Moment (1/rev and higher)

Figure 5.5: Convergence of aerodynamic loads with coupling iterations
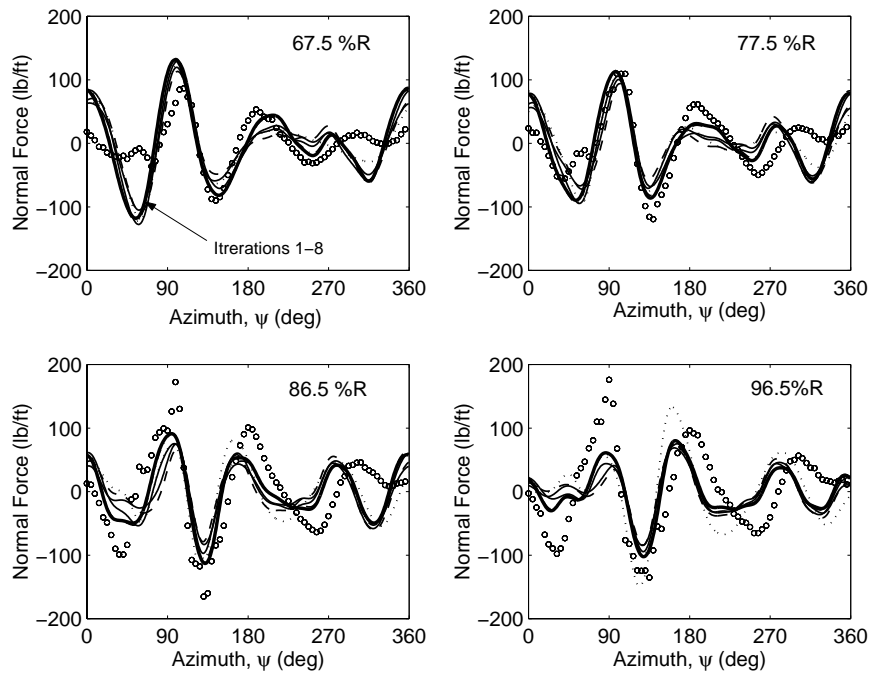
Figure 5.6: Vibratory normal force (3-10/rev) variation with coupling iterations
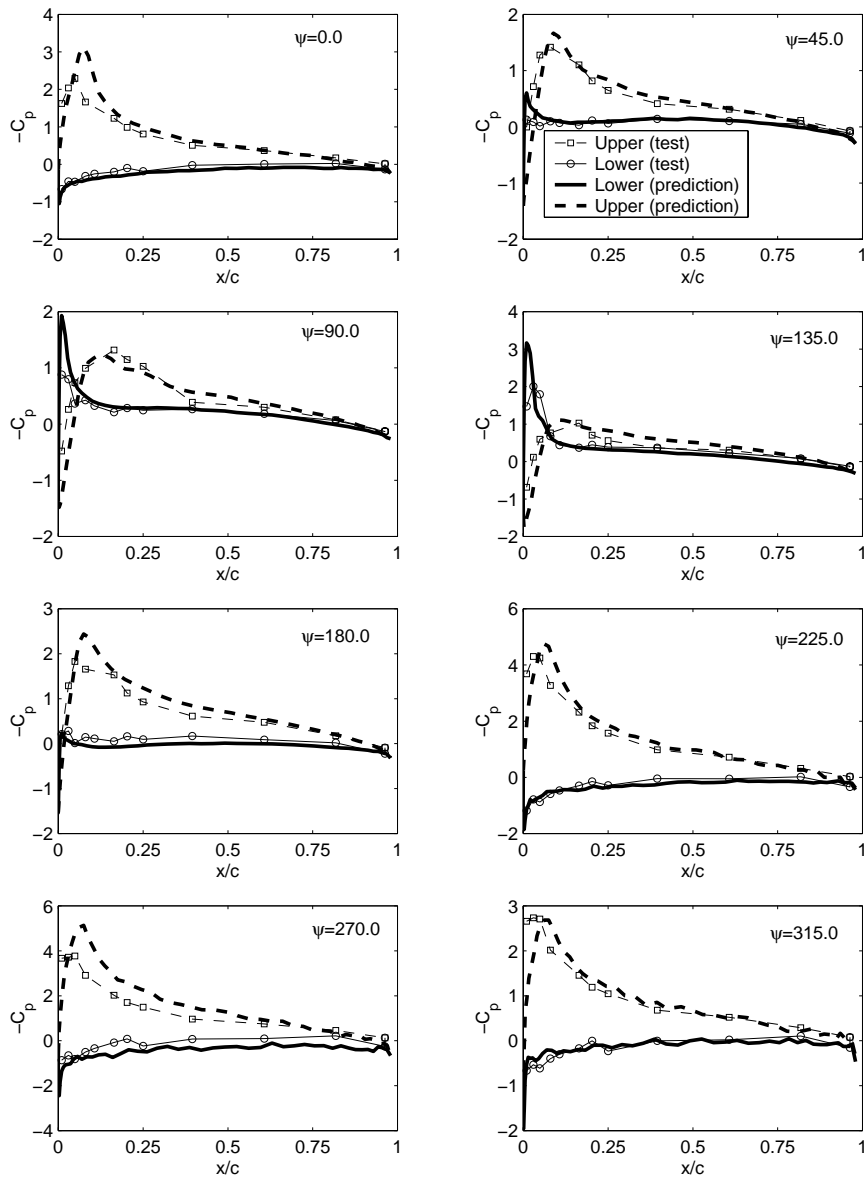
Figure 5.7: Chordwise surface pressure variation with azimuth, 77.5%R; $\mu = 0.368$, $C_T/\sigma = 0.0783$
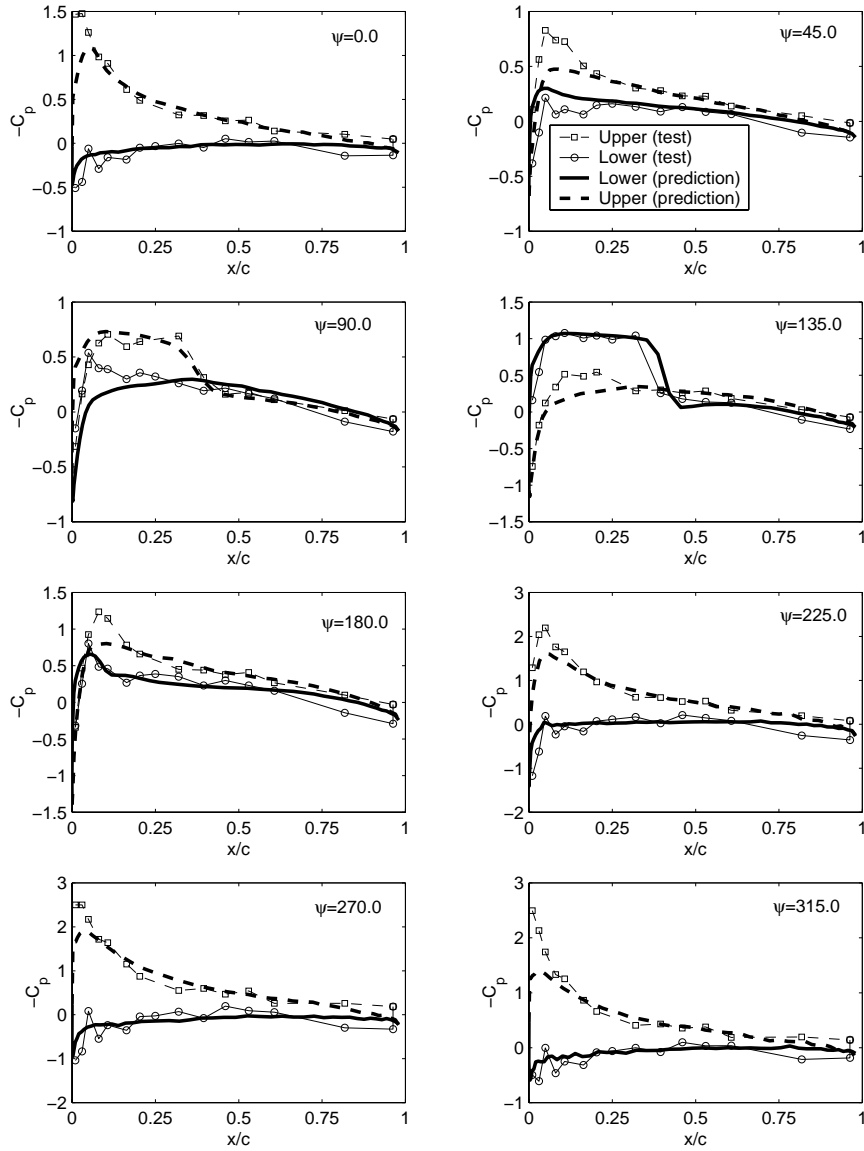
Figure 5.8: Chordwise surface pressure variation with azimuth, 96.5%R; $\mu = 0.368$, $C_T/\sigma = 0.0783$

5.3 Improvements from the Comprehensive UMARC solution

It is important to emphasize the improvements from the comprehensive UMARC brought by the use of three dimensional unsteady CFD based aerodynamics. The aerodynamic loads obtained in the final converged solution is compared with the corresponding results from the baseline UMARC in this section.

Figure 5.9 shows the total sectional normal force obtained from CFD/UMARC based calculations compared with the flight test data and baseline UMARC solutions. It is evident that the CFD calculations have definitely improved the predictions of the phase of negative lift compared to UMARC baseline case. Note that this problem as identified by Bousman [3] was one of the primary motivations for development of the coupled CFD/UMARC rotor analysis.

Figure 5.10 shows the 3/rev and higher normal forces (i.e., those which contribute directly to the hub loads). The CFD/UMARC coupled scheme gives good predictions for the peak magnitudes and phase of the vibratory loads. The impulsive loading in the advancing blade and phase of the negative lift are resolved accurately. The predictions are significantly better than those obtained from the baseline UMARC. This shows that the use of the three dimensional CFD aerodynamics does improve the state-of-the-art of vibratory airload prediction.

Figure 5.11 shows the predicted pitching moments. The CFD/UMARC predictions accurately resolve both phase and magnitude of the pitching moments at all radial stations. The push rod (pitch link) loads are directly related to the pitching moment predictions. The prediction of torsion bending moments at three spanwise stations and pitch link loads are shown in Figure 5.12. The

CFD/UMARC coupled scheme can be seen to produce much improved prediction for torsion moments at all span stations. The pitch link loads also show much better agreement with the measured data.

Better prediction of push rod loads would facilitate design more maneuverable and agile helicopters. Hence, the ability to obtain good estimates of section pitching moments is important from a designers perspective. Note that the pitching moments predicted from the baseline UMARC show large deterioration towards the tip. This was identified to be because of the deficiencies in modeling of 3-D effects and compressibility effects by the Weissinger-L based aerodynamic model (Chapter 4).

Figure 5.13 shows the control angles obtained from the CFD/UMARC coupled scheme and baseline UMARC compared with the flight test measurements. The collective and cyclic controls obtained from the coupled scheme shows fair agreement with those obtained by baseline UMARC and flight test data. However, the lateral cyclic control angle is underpredicted compared to the flight test measurement. However, the lateral cyclic obtained from the baseline UMARC also shows the similar trend as that obtained from the coupled scheme.

This study forms the proof-of-concept for the loose coupling approach. The predictions of the sectional vibratory normal force and pitching moment are significantly improved compared to the comprehensive analysis. The predicted normal force and pitching moment after full coupling show the same trends in correlation with measured aerodynamic loads as those obtained using prescribed blade motions (Chapter 4). Therefore, this study also forms the validation for both the structural and aerodynamic models used in the coupling scheme.
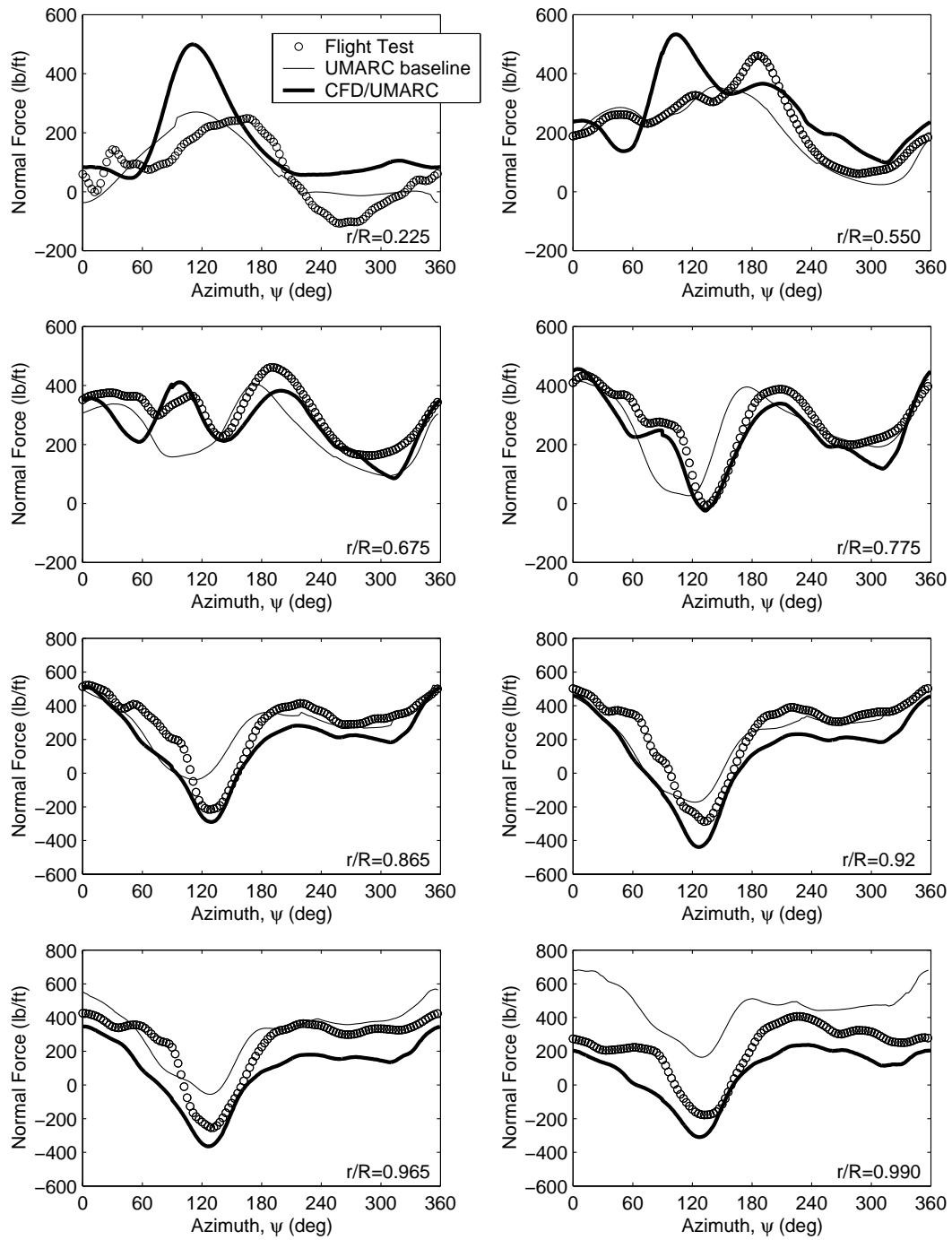
Figure 5.9: Comparison of CFD predicted normal force variations with baseline UMARC (C_T/σ=0.0783, μ=0.368)
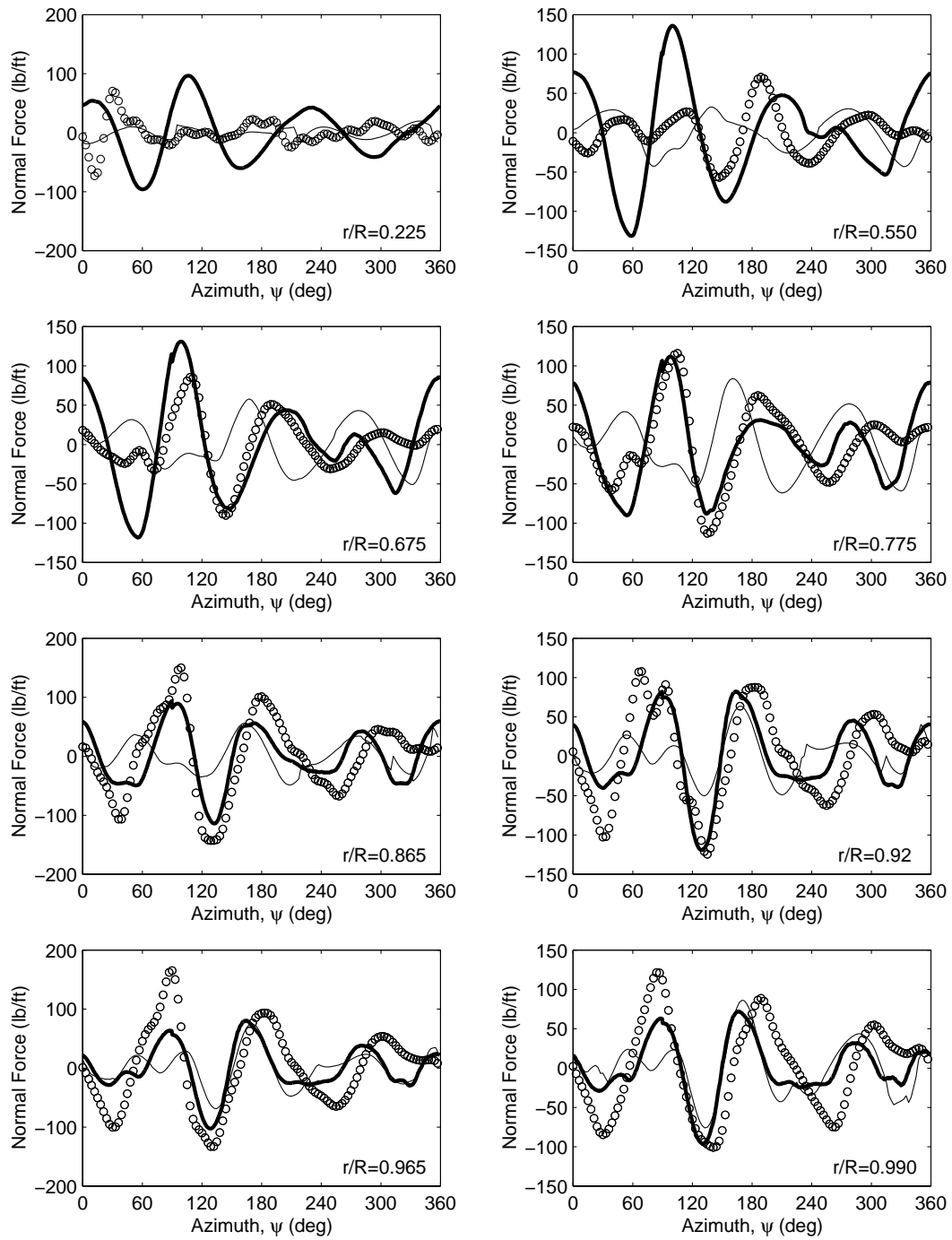
Figure 5.10: Comparison of CFD predicted vibratory normal force (3/rev and higher) variations with baseline UMARC (C_T/σ=0.0783, μ=0.368)
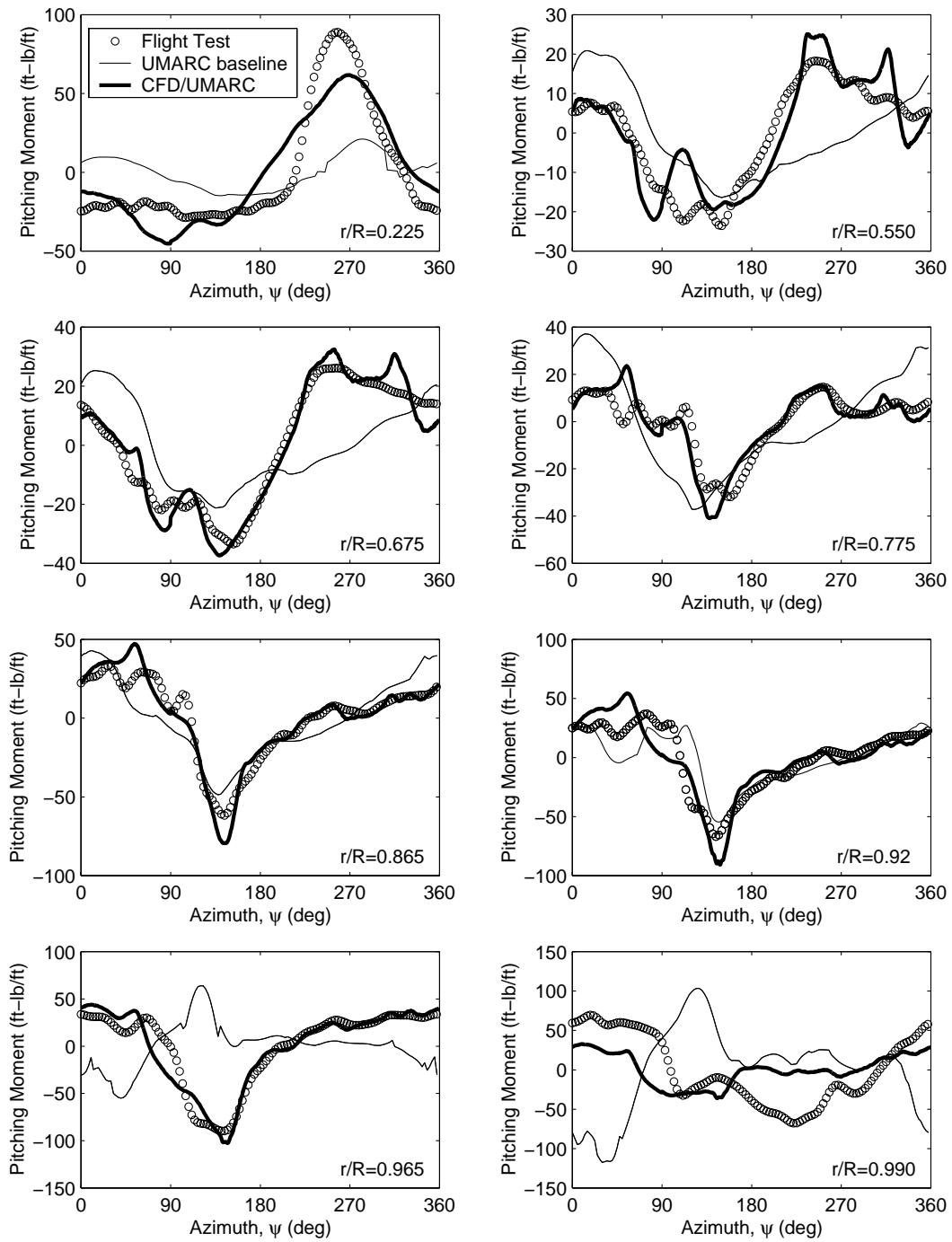
Figure 5.11: Comparison of CFD predicted pitching moment variations with baseline UMARC (C_T/σ=0.0783, μ=0.368)
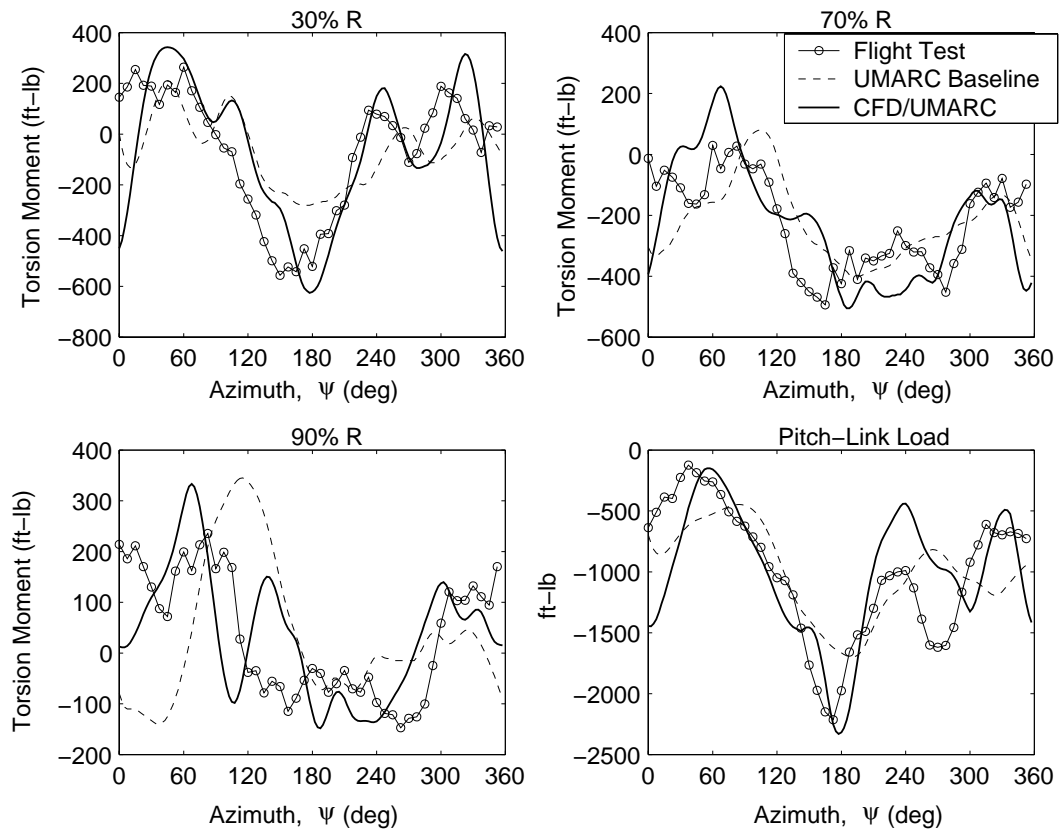
Figure 5.12: Predicted Torsion Moments from baseline UMARC and CFD/UMARC coupled scheme (C_T/σ=0.0783, μ=0.368)
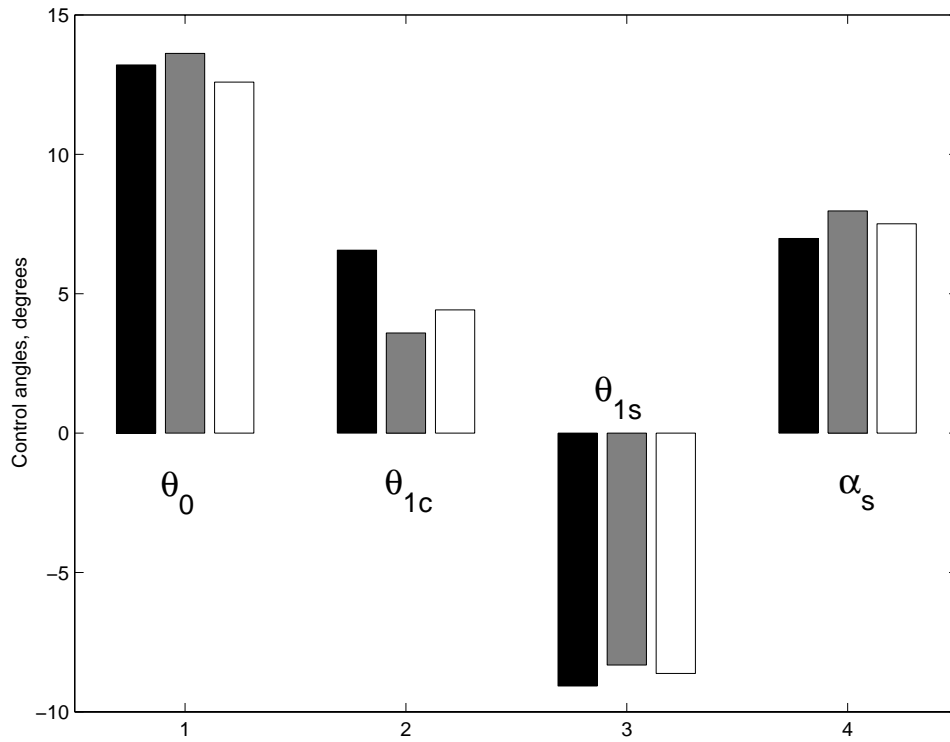
Figure 5.13: Control angles after 8 iterations of the loose coupling (C_T/σ=0.0783, μ=0.368)

5.4   Low speed forward flight case

The coupling analysis is also performed for a low speed forward flight case of the UH-60A. The flight parameters are μ=0.110 and C_T/σ=0.0783 respectively. This speed is characterized by a larger influence from the trailed vortex wake system compared to the high speed case. Therefore, the analysis conducted here is to test whether the coupling procedure developed is feasible for such a wake effect dominated case also.

Figure 5.15 shows the convergence of flap response with coupling iteration number. The flap response appears to converge faster than the high speed case. The response converges to a difference in response of 0.5% within 5 iteraions. The torsional response also shows a faster convergence trend (Figure 5.16). The normal force variation with azimuth for each iteration is shown in Figure 5.17. The rapid convergence of flap and torsional response is reflected in the convergence of the normal forces also. The normal forces converge to the final periodic steady state in only 5 coupling iterations. As observed for the high speed case, the vibratory normal forces (3/rev and higher) show little variation with coupling iterations for this case too (Figure 5.18). The changes in trim controls during the coupling iterations affect the steady and 1/rev harmonics to a large extent and the 2/rev harmonic to a moderate extent. But the vibratory harmonics (3/rev and higher) are relatively unaffected by changes in trim.

The final converged solution obtained after CFD coupling is contrasted with the baseline comprehensive analysis solution in Figures 5.19 and 5.21 respectively. From the normal force variations one can observe that the CFD predictions better capture the impulsive loadings in the advancing (60 degrees) and retreating blade phase (250 degrees) compared to the baseline comprehensive

222

analysis. Also, the baseline comprehensive analysis shows a a large steady offset at the outboard station (99%). The CFD predictions capture the normal force magnitude and phase accurately even at this span station.

The CFD predicted vibratory normal force (3-10/rev) variation shows good agreement with the flight test data. The impulsive loadings at $\psi=60$ deg and $\psi=300$ deg dominate the phase and magnitude of the vibratory normal forces. These impulsive loadings are primarily generated by the interaction of the rotor blade with the trailed vortex wake. Therefore, it is evident that the inclusion of the vortex wake modeling is important for obtaining accurate vibratory load prediction at this flight speed. The vibratory loads obtained from the baseline comprehensive analysis also shows fair agreement with the flight test data. However, the coupled scheme gives better predictions for the phase and peak-to-peak magnitudes of the impulsive loadings.

The pitching moment waveform at the inboard stations are characterized by the presence high frequency components (Fig 5.18). The baseline comprehensive analysis does not resolve any of these high frequency components. The CFD predictions do show presence of these higher frequency components in the pitching moment waveform at the inboard stations. However, the correlation with test data is not as good as the high speed case. However, the pitching moment predictions from CFD towards the tip show better correlation with test data than at the inboard stations. The baseline comprehensive analysis on the other hand tends to overpredict the pitching moments right near the tip.

The control angles obtained by the coupled scheme is shown in Fig 5.22. The collective control shows good agreement with the flight test data. All the other control angles show only a fair agreement with the flight test data. The

control angles obtained after a baseline UMARC computation also shows the same trends in agreement as those obtained by the coupled scheme.

It should be noted that for a test case such as this there might be improvements possible even in the baseline comprehensive analysis if a finer temporal discretization was used. The higher frequencies may have been aliased to the lower ones because of the coarse temporal discretization in the baseline comprehensive analysis.
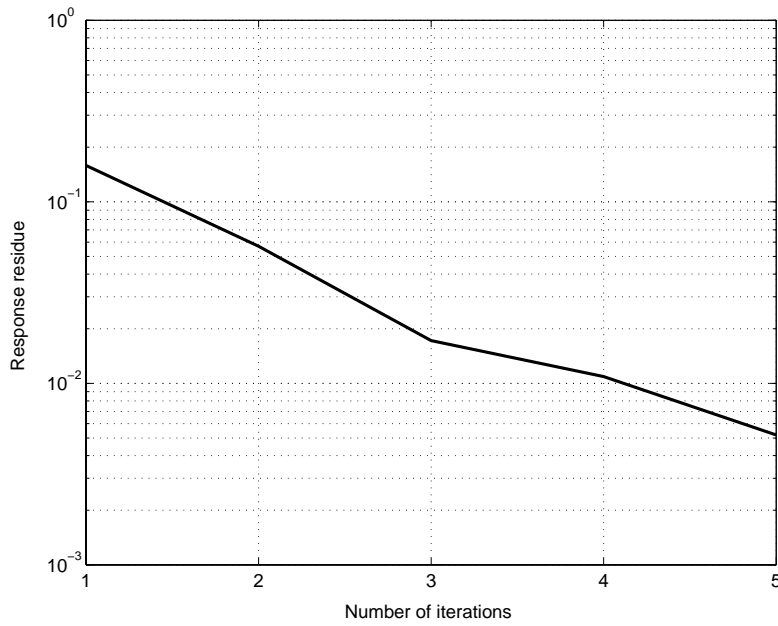
(a) Response residue (L2 norm of relative difference between consecutive iterations)
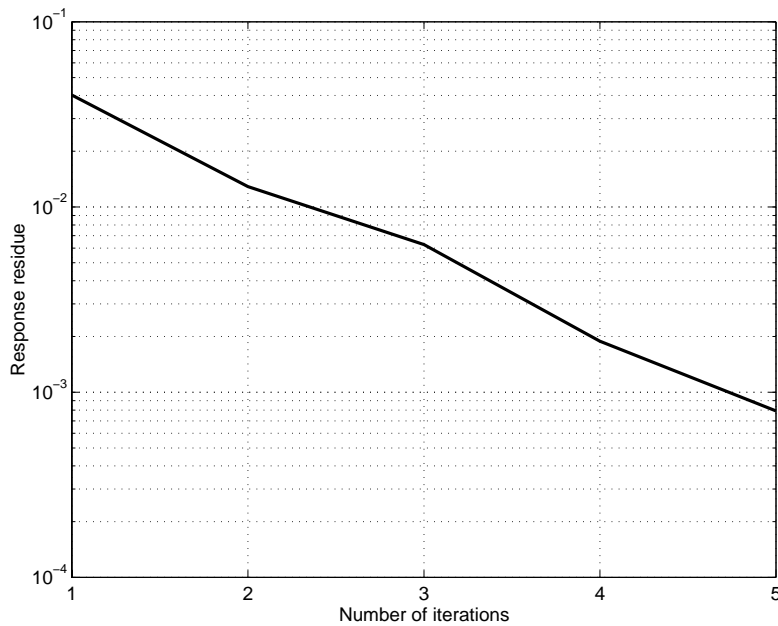
(b) Trim residue

Figure 5.14: Response and trim residue variations with coupling iterations $(C_T/\sigma=0.0783, \mu=0.110)$

225
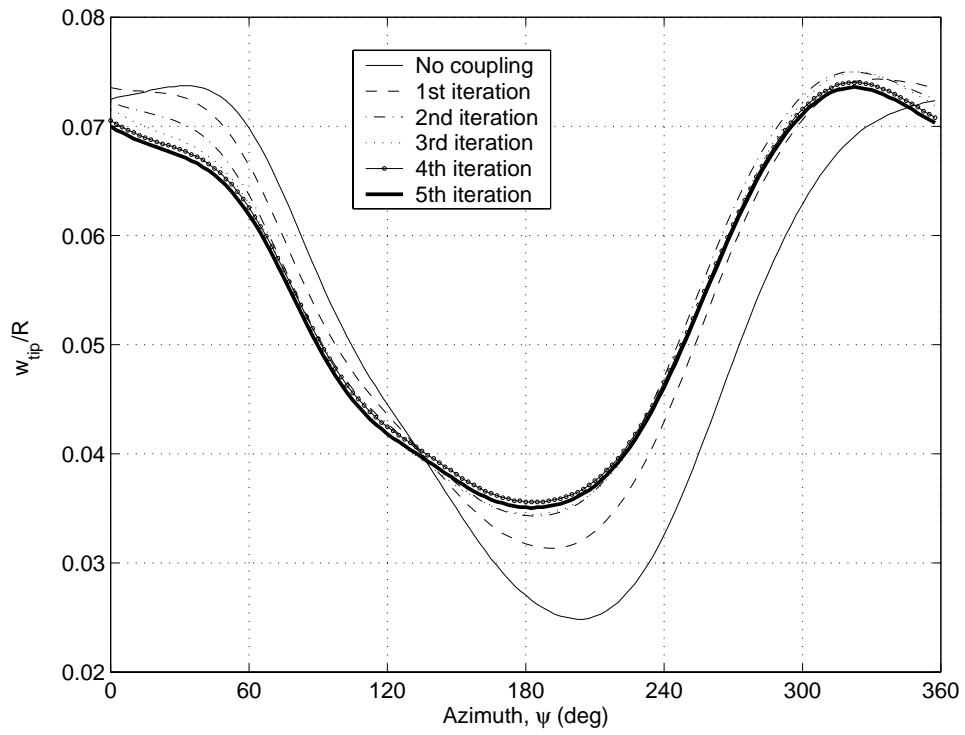
Figure 5.15: Variation of the flap response at the tip with coupling iterations (C_T/σ=0.0783, μ=0.110)
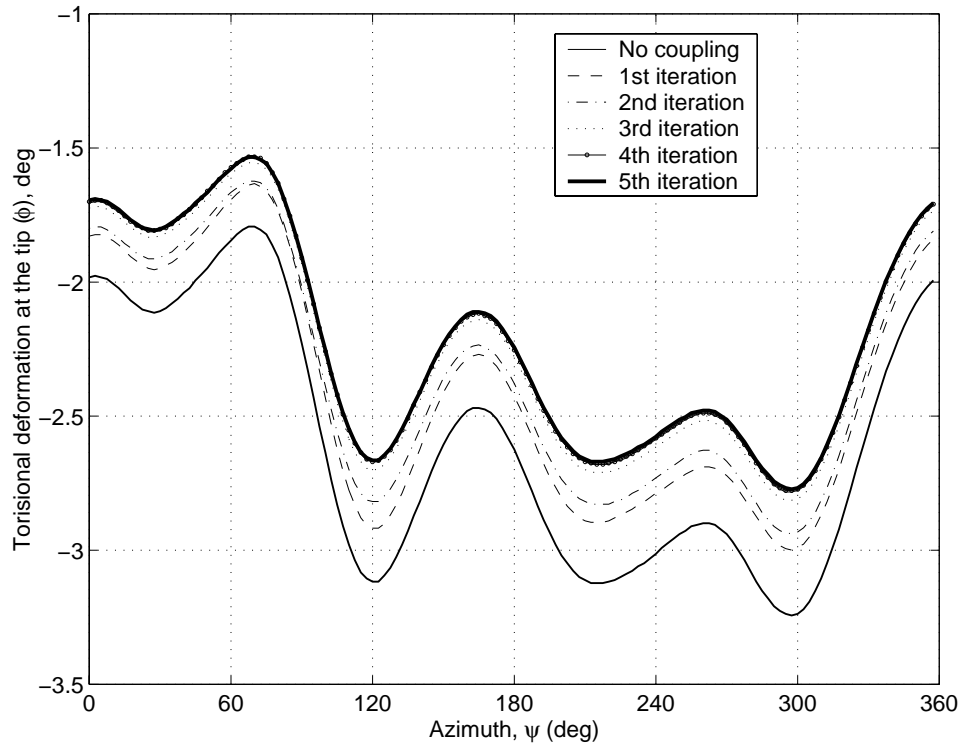
Figure 5.16: Variation of the torsional response at the tip with coupling iterations $(C_T/\sigma=0.0783, \mu=0.110)$
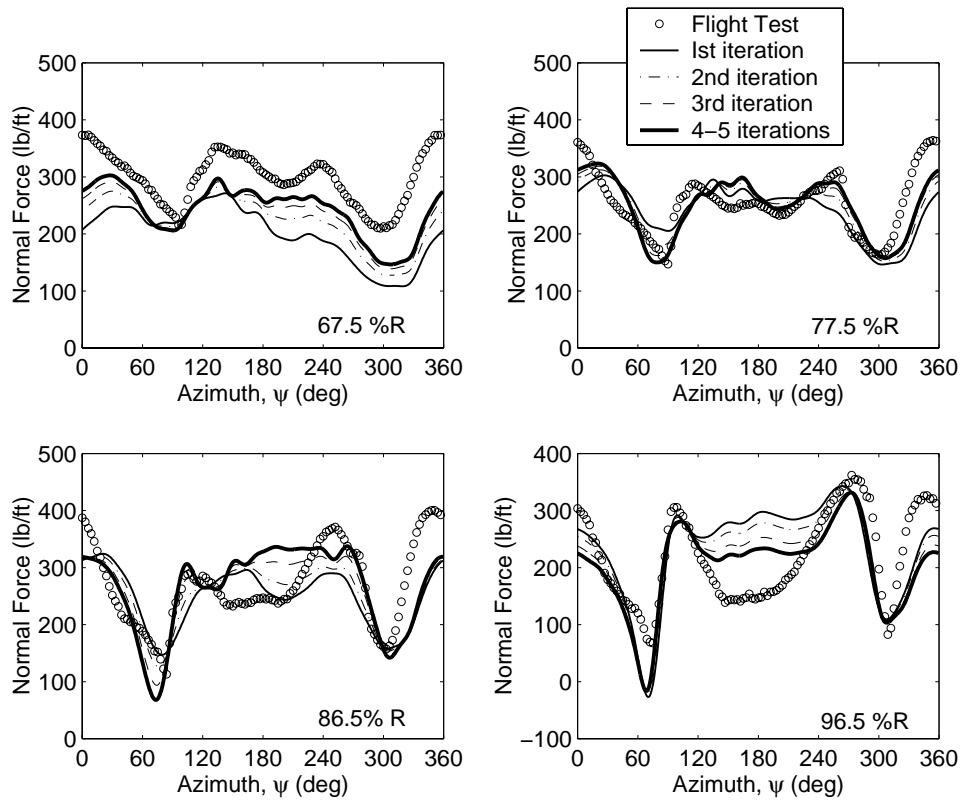
Figure 5.17: Normal force variation with coupling iterations (C_T/σ=0.0783, μ=0.110)
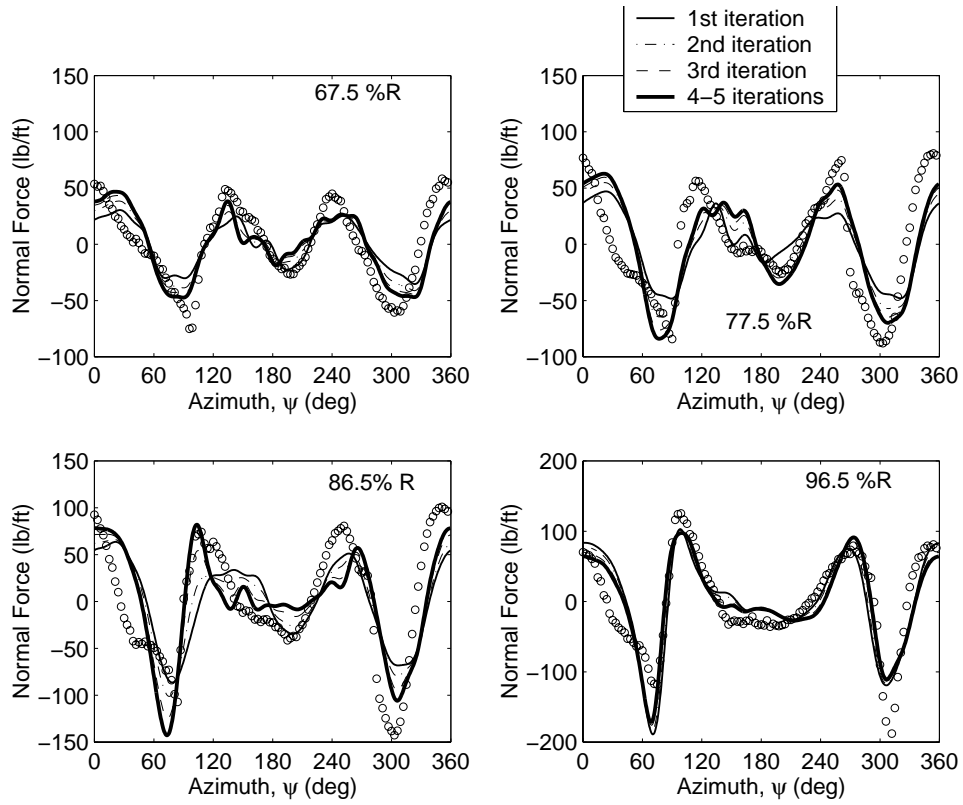
Figure 5.18: Vibratory normal force (3-10/rev) variation with coupling iterations
(C_T/σ=0.0783, μ=0.110)
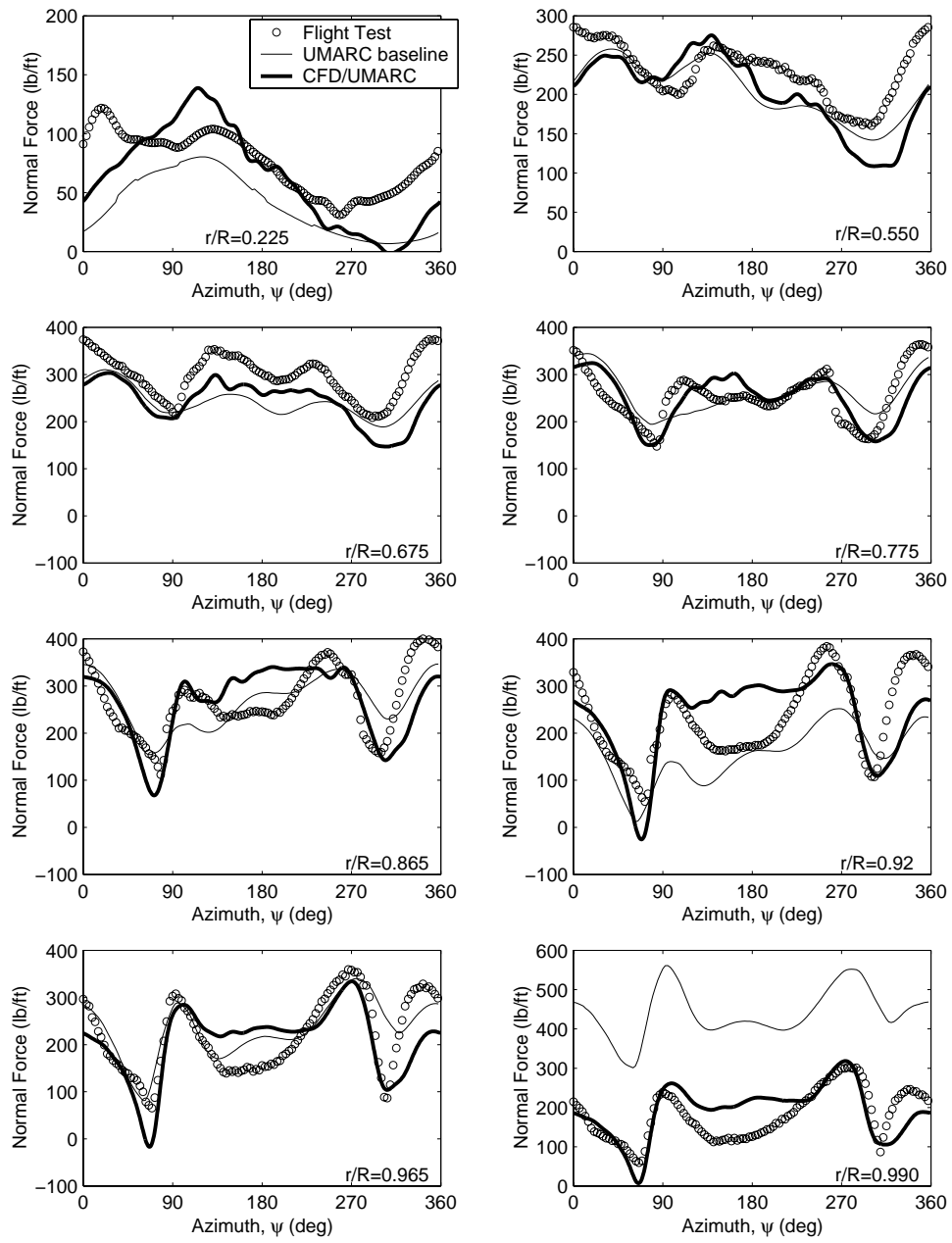
Figure 5.19: Comparison of CFD predicted normal force variations with baseline UMARC (μ=0.110)
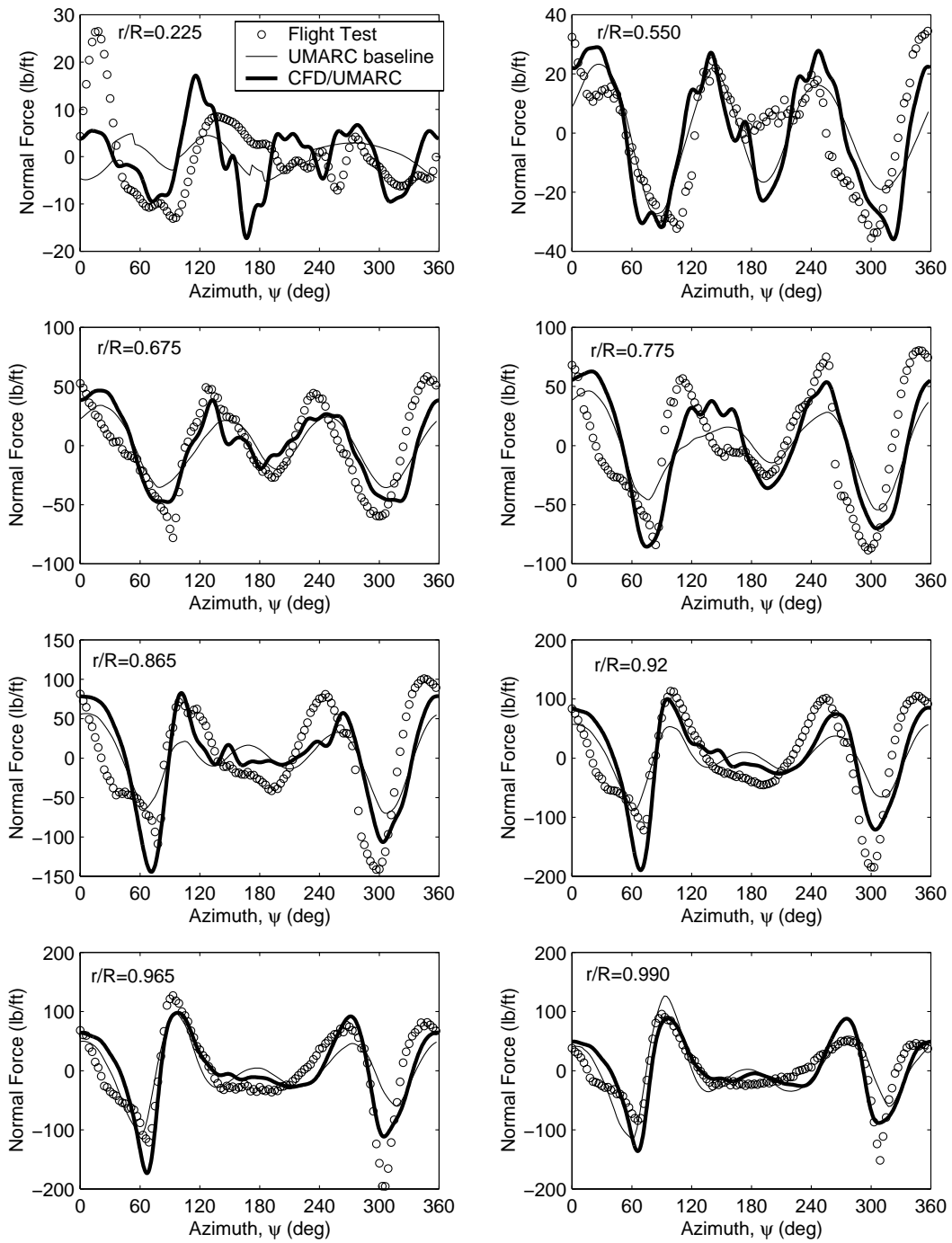
Figure 5.20: Comparison of CFD predicted vibratory normal force (3/rev and higher) variations with baseline UMARC (C_T/σ=0.0783, μ=0.110)
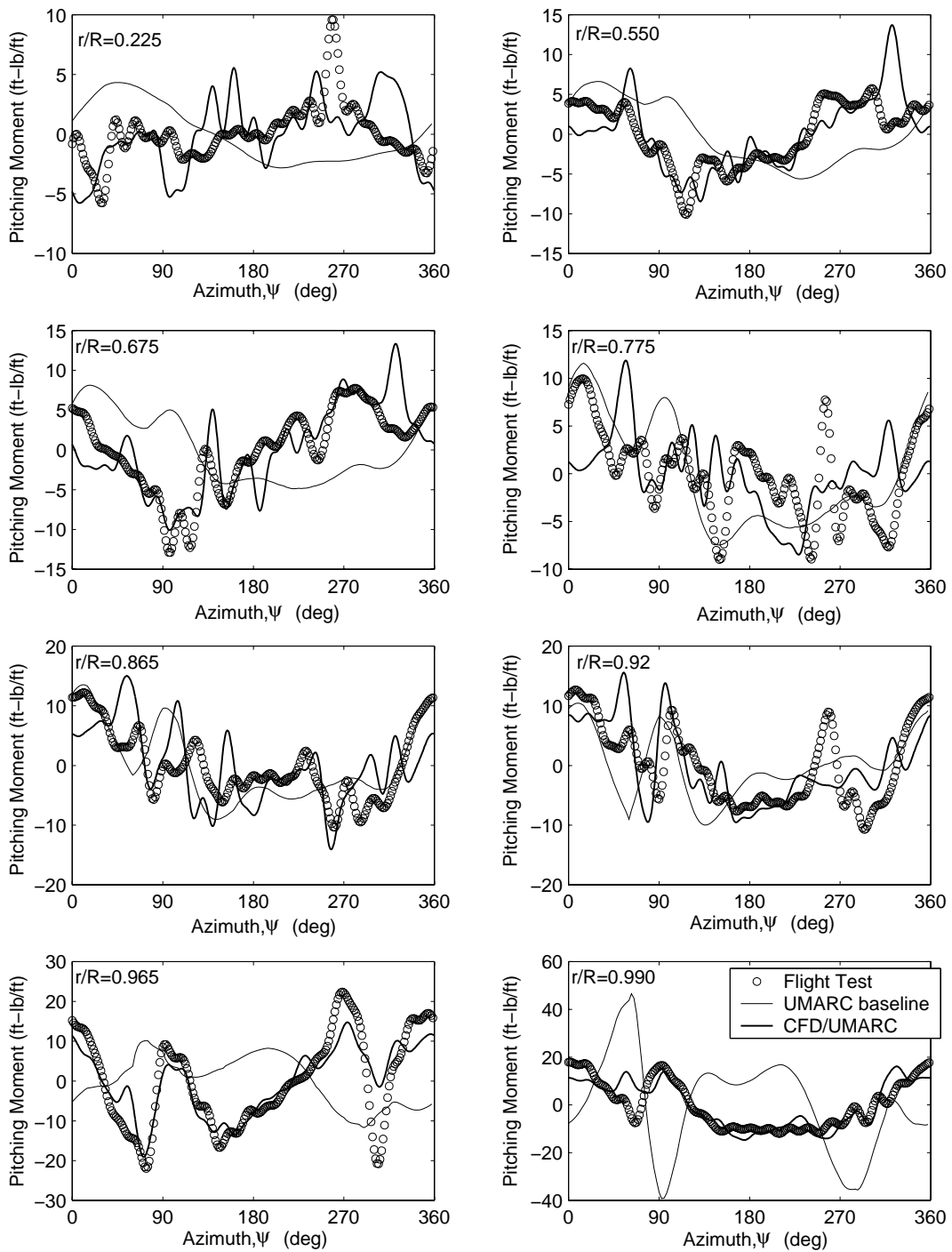
Figure 5.21: Comparison of CFD predicted pitching moment variations with baseline UMARC (μ=0.110)
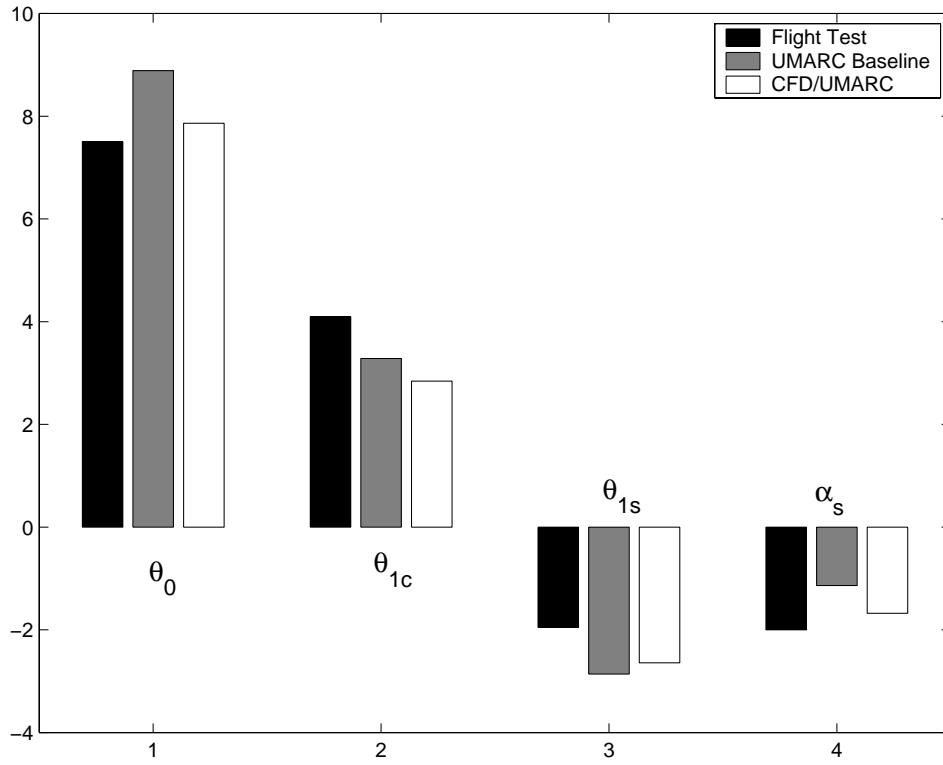
Figure 5.22: Control angles after 8 iterations of the loose coupling (C_T/σ=0.0783, μ=0.110)

5.5 Alternate coupling methodology

An alternate coupling methodology (termed Δ method) is investigated for the low speed flight case. This methodology follows that adopted by Carradona et al. [54]. The approach is can be briefly described as follows.

The difference between the airloads computed by the CFD solver and those predicted by the comprehensive analysis is evaluated every iteration. This difference is provided as a constant forcing to the structural model of the comprehensive analysis. This is in addition to the aerodynamic loading produced by the lifting line model internal to the comprehensive analysis. Therefore, the aerodynamic damping terms are evaluated using the lifting line analysis and the 3-D aerodynamics predicted by the CFD is provided as an additional correction. The comprehensive analysis performs the trim computations in this approach in contrast to the previous approach where the trim computations were conducted by an external module. As the coupling iterations progress, the differences between the CFD computed airloads and the lifting line analysis tends to a constant at every azimuthal station.

The major differences in this approach compared to previous approach is the presence of aerodynamic damping. Also, the trim iterations are performed internally by the comprehensive analysis. Therefore, as mentioned earlier, an external function for evaluating the trim residues and changes in control angle is not required in this case. Also, this method has the advantage that every coupling iteration inherently produces a trimmed solution. The coupling approach is illustrated schematically in Figure 5.23.

The convergence of the blade response using the alternate coupling scheme is shown in Figures 5.24 and 5.25 respectively. The response shows a very rapid

convergence trend compared to the previous coupling scheme for both the high speed and low speed cases. The response converges to 0.5% of its original value in about 3 iterations for the low speed case and 4 iterations for the high speed case. It should be noted that for the high speed case the first harmonic component of ΔC_l had to be underrelaxed to obtain an accurate solution. Otherwise, the converged solution obtained showed large deviation in shaft tilt angle and blade flapping, even when both trim and response residues are converged. Multiple solutions are possible for the non-linear coupled trim/blade response convergence problem. Therefore, it is possible that the phase change introduced in the blade flapping can produce a different trim solution. It is to be noted that the phase change in blade flapping is primarily produced by changes in the modeling of the aerodynamic damping terms.

The normal force variations also reflect the same convergence trend as the blade response itself (Figure 5.26). Again, the high speed case required one more iteration compared to the low speed case for the normal force variation to converge to within a plotting accuracy. The results also show satisfactory agreement with the flight test data, capturing the major trends such as the impulsive nature at the advancing and retreating azimuths.

The results obtained for the two coupling schemes are contrasted in Figures 5.27. The normal force variation shows small phase differences. This is because of the phase difference present in the torsional elastic response. The phase differences in the normal forces appear as a phase difference in the flap response also. For the high speed case there is a steady difference between the flap response obtained from the both the coupling methods. As mentioned earlier, the differences in the modeling of aerodynamic damping in system is the major

reason for this steady offset. The torsional response shows a much smoother variation compared to that obtained using the previous coupling method. This is again because of the aerodynamic damping present in this approach, while it was absent in the first method.

The normal force and pitching moment variations show good agreement in both the coupling methods indicating that the steady offsets in flapping is countered by the change in the shaft angle so as to produce a similar aerodynamic environment for the blades. Overall predictions from both the methods show good correlation with each other reinforcing the fidelity of both the coupling approaches.

The second coupling approach is preferable for routine applications compared to the first one for its obvious robustness qualities. The trim solution to a prescribed tolerance is assured as it is performed at each step by the comprehensive analysis in this case, compared to the requirement for simultaneous convergence in the previous analysis. Also, this method shows faster convergence compared to the first method. There was no aerodynamic damping present in the first method which caused generation of some instabilities. Aerodynamic damping is inherently present in the second method as the aerodynamic model internal to the comprehensive analysis is active during coupling. This helps to stabilize the response and prevent divergence. However, for the high speed case, it was noted that the second method bifurcated to a different trim and response solution if the first harmonic component of ΔC_l is not underrelaxed.
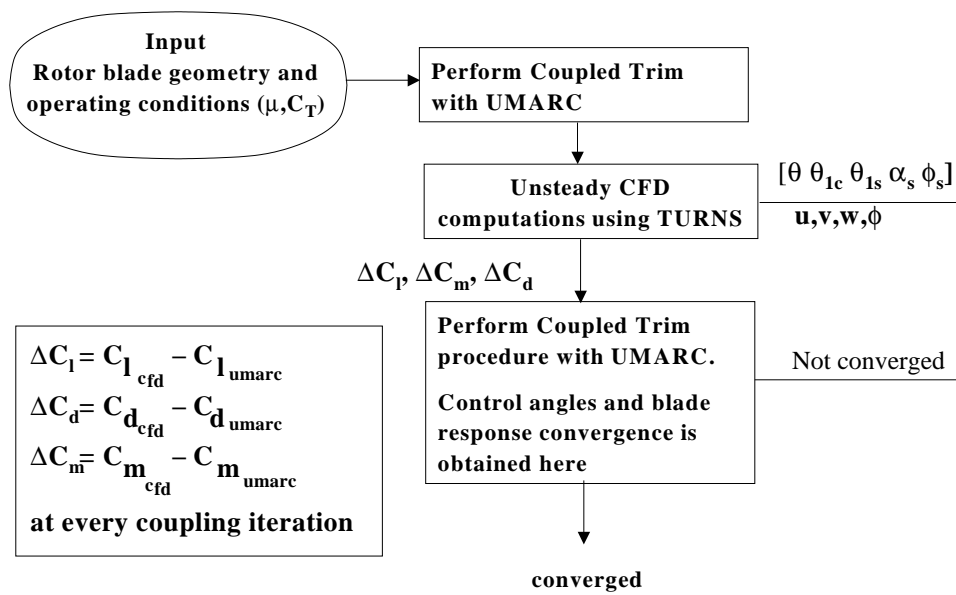
Figure 5.23: Alternate loose coupling scheme
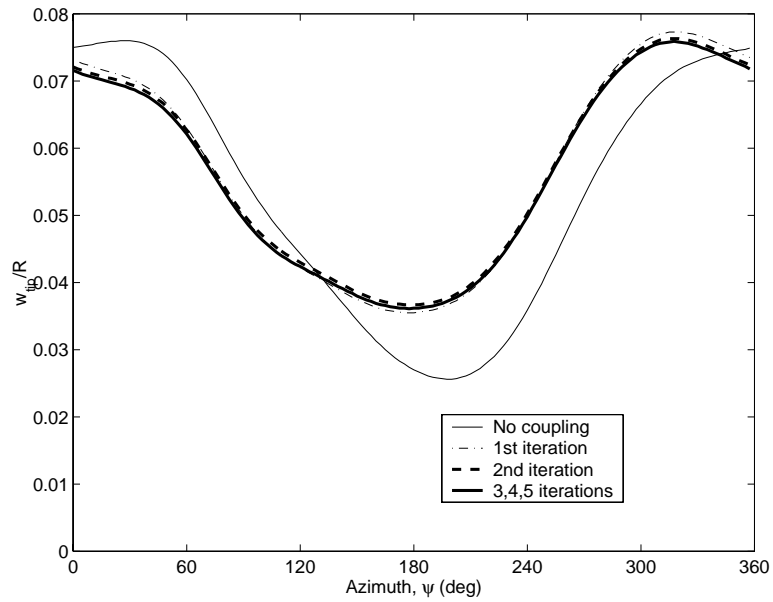
(a) Low speed case $\mu=0.110$

(b) High speed case $\mu=0.368$

Figure 5.24: Variation of the flap response at the tip with coupling iterations $(C_T/\sigma=0.0783)$

(a) Low speed case μ=0.110

(b) High speed case μ=0.368

Figure 5.25: Variation of the torsional response at the tip with coupling iterations (C_T/σ=0.0783)

(a) Low speed case μ=0.110

(b) High speed case μ=0.368

Figure 5.26: Normal force variation with coupling iterations (C_T/σ=0.0783

(a) Low speed case μ=0.110

(b) High speed case μ=0.368

Figure 5.27: Comparison of results between the two coupling approaches investigated (C_T/σ=0.0783)

Chapter 6

Closure

6.1 Summary

This thesis has investigated the use of the CFD based aerodynamic modeling for application to rotorcraft aeroelastic analysis. The primary requirement for coupling with an aeroelastic analysis is a deforming mesh capability. This is because the mesh has to conform to the geometry of the deformed blade. Another equally important requirement is to account for the effects of the trailed vortex wake because it plays an important role in determining the sectional aerodynamic loads.

An existing CFD solver (TURNS) was modified such that it could be coupled with comprehensive helicopter rotor analysis codes. A mesh deformation algorithm was implemented to account for the aeroelastic deformations of the rotor blade. The numerical scheme was formulated to be strictly conservative, even for deforming meshes. A finite volume approach for calculating the space and time metrics was constructed such that the Geometric Conservation Law (GCL) was always satisfied. The simulations were conducted for a single rotor blade to re-

duce the computational complexity of the problem. The trailed vortex wake was accounted for using the field velocity approach. The field velocity approach is a way of including the effects of a external field via apparent grid movement. This approach requires evaluation of the induced velocities at all the mesh points. This is a very computationally expensive operation. Therefore, a fast hierarchical algorithm that uses adaptive space partitioning was implemented to enhance the computational speed of the induced velocity calculations. The trailed vortex wake geometry was computed using a free vortex wake analysis.

The CFD solver developed was validated systematically before coupling to the structural analysis models. The validations were performed on an incremental basis, starting from validations of 2-D rotor airfoil characteristics, to complete validations for rotors in forward flight cases. The methodologies implemented were also validated independently. For example, the field velocity approach was validated for a range of 2-D unsteady model problems that have exact analytical solutions. Predictions were also compared with results obtained from alternate methods. The performance enhancement techniques for induced velocity evaluation were found to give sufficiently accurate results, with large improvements in run times.

A high speed forward flight problem for the UH-60 helicopter was studied next. This flight regime is characterized by moderately large aeroelastic blade deformations. The blade deformations were obtained by prescribing measured aerodynamic loads on to the structural model. These blade deformations were prescribed as inputs then in to the CFD method, and sectional airloads were predicted. The vibratory loads predicted showed good correlations with the measured test data. *There was remarkable improvement in the phase of the*

normal force at the advancing blade and peak-to-peak magnitude of the predicted pitching moments.

The CFD solver was then coupled with a simplified structural analysis model to study the feasibility of the so called "loose" coupling approach. In the loose coupling approach there is an exchange of information between the CFD analysis and structural methodologies every rotor revolution. This study was necessary to gain understanding of the numerical robustness problems before resorting to coupling with an advanced structural model. Studies were conducted for both articulated and hingeless rotor systems, and also for different flight regimes. The results indicated the success of the loose coupling approach *even when both the lift and pitching moments obtained from the CFD model were included into the aeroelastic analysis.* Previous researchers had identified torsional response divergence problems when the pitching moments were included. However, this was attributed to the inaccurate prediction of magnitude of the pitching moment. The present CFD methodology provides accurate prediction for section pitching moments, and hence did not show any response convergence problems.

The validated CFD solver was then used as a diagnostic tool to identify the aerodynamic mechanisms that lead to helicopter rotor vibrations. The different mechanisms investigated include the effects of yawed flow, transonic flow, viscous flow, blade elastic deformations and three dimensional effects. Elastic torsion and the 2nd elastic flap mode were found to be the significant contributors to the vibratory aerodynamic load phase and magnitude in the inboard radial stations. At the outboard radial stations, the elastic torsion alone dictated the phase and magnitude of the vibratory aerodynamic loads. Corrections were attempted to improve the prediction capabilities of the lifting line analysis based on the

insights gained from this study.

Finally, the CFD methodology was coupled to an advanced structural dynamic model (UMARC). The problems with loose coupling methodology were identified for the high-speed forward flight case, and methods to guarantee convergence of the aerodynamic loads and the blade response were proposed. The coupling calculations were also performed for a low speed forward flight case, i.e. where the measured test data was available. An alternate coupling methodology was also investigated. The convergence trends and the final results obtained from the two coupling methodologies were also compared. Overall, the loose coupling methodology was found to be *successful for all the flight cases studied.* Also, significant improvements were noted in the prediction of both vibratory normal force and pitching moments.

6.2 Conclusions

The major conclusion of this dissertation is that the inclusion of CFD based aerodynamic modeling in to a rotor aeroelastic analysis framework considerably improved the prediction of vibratory aerodynamic loads, especially the pitching moments. Also it was demonstrated that simultaneous convergence of trim and blade response could be obtained even when lift and pitching moments from the CFD computations were included into the rotor aeroelastic analysis. Therefore, this study formed the "proof of concept" for the coupling of a Navier-Stokes based CFD analysis to a comprehensive rotor aeroelastic analysis model. Specific conclusions and observations noted during the development, validation and application of the analysis developed are now summarized in this section.

The accuracy of the CFD solver was investigated in Chapter 3. The predictions for rotor airfoil characteristics were compared with experimental data (available as C81 tables) for a range of Mach numbers and angle of attacks. The predictions obtained for the 2-D indicial response problems were compared with the exact analytical solutions. Furthermore, the vibratory airloads predicted at the high speed forward flight were compared with flight test data. Prescribed blade motions were used in this case. These blade motions were obtained by forcing the strcutural dynamic model with measured aerodynamic loads. Following are the key conclusions noted in this chapter:

1. The CFD methodology showed good prediction capabilities for 2-D airfoil characteristics in the pre-stall regime.

   - Accurate prediction of both upper and lower surface pressure distributions were obtained for the case (RAE2822 airfoil) studied. The shock location on the upper surface was resolved accurately.

   - 2-D validation with measurements for two rotor airfoils (SC1095 and SC1095R8), showed very good correlation with the test data in the pre-stall regime. However, the predictions deteriorated at higher Mach numbers ($M >0.7$).

   - In the post stall regime, use of the Spalart-Allmaras turbulence model gave better predictions compared to the Baldwin-Lomax model. The predictions in the pre-stall regime were identical for both these turbulence models.

2. The field velocity approach showed good correlation with exact analytical results for the 2-D unsteady model problems studied. For the model

problem of airfoil vortex interaction, the results obtained from the present method (using field velocity approach), showed good agreement with those predicted using alternate approaches.

3. The hierarchical algorithms for fast evaluation of the induced velocities were found to give sufficiently accurate results (within 0.5% of the baseline approach) with a large gain in the run time performance (80% less CPU time).

4. The CFD predictions gave good predictions of vibratory airloads when the prescribed aeroelastic deformations are used.

   - The phase of the advancing blade lift was resolved accurately (within 2 degrees).

   - The up-down characteristic (advancing blade lift impulse) in the normal force waveform at advancing blade azimuthal locations was captured.

   - The peak-to-peak magnitudes of the pitching moment variations were predicted accurately at all span stations. The phase of the negative pitching moments and the impulsive nature of the wave form present in the inboard stations were also captured.

5. The CFD analysis was tested with differing meshes and varying spatial and temporal discretizations for the same set of blade motions. The results are found to be fairly grid independent. All the major trends seem to be resolved even with the coarsest mesh.

6. Satisfying the Geometric Conservation Law (GCL) was found to be a necessity for accurately resolving the phase and magnitude of section pitching moments. The normal forces appear to be less sensitive to an absence of the GCL.

The aerodynamic mechanisms generating the vibratory airloads were investigated in Chapter 4. The Weissinger-L based aerodynamic analysis was found to give inaccurate predictions for the phase of advancing blade lift, the impulsive loading in the advancing blade phase and the phase and magnitude of the pitching moments compared to the CFD calculations for identical set of blade motions. Therefore, the investigations used the CFD analysis as a diagnostic tool to isolate the physical phenomenon that are better modeled by the CFD, thus leading to a better correlation. The following are the major observations noted from the study:

1. The absence of yawed flow modeling is not the primary contributor to the inaccurate prediction of vibratory airloads by the Weissinger-L analysis. Yawed flow effects are more prominent for a finite wing than an infinite wing. For the infinite wing the effects of yawed flow are absent (independence principle) until the advent of supercritical flow. For the finite wing yawed flow effects are caused predominantly by the differences in the near wake field. Yawed flow for finite wings causes larger changes in the final steady state value than changes in the unsteady aerodynamic response.

2. The onset of transonic flow is not a key contributor to the advancing blade lift impulse. However, it plays a key role in the determination of the section pitching moments. The effects are especially apparent at the outboard span

stations.

3. Viscous effects play a minor role in determination of the vibratory airloads. All the major trends were captured with an inviscid simulation.

4. Blade elastic torsion plays the key role in determining the phase of the advancing blade lift. Accurate 1/rev elastic torsional response prediction is a requirement for accurate prediction of the 2/rev advancing blade lift. The prediction of accurate 1/rev elastic torsion requires good predictions of the 1/rev pitching moment.

5. Blade flapping response plays the key role in generating the advancing blade lift impulse at the inboard blade stations. The advancing blade lift impulse is the source of all 3/rev and higher vibratory airloads. It also affects the phasing of the advancing blade lift. The flap degree of freedom also contributes to the impulsive nature in the section pitching moments at the advancing blade.

6. Furthermore, the effects of spanwise curvature because of the elastic flapping (that caused by the 2nd flap mode) appear to play a key role in determining the advancing blade lift impulse. The impulse is not captured with a Weissinger-L blade analysis or a 2-D CFD simulation.

7. Shock relief effects contribute to the accurate prediction of vibratory pitching moment towards the tip. The lifting line analysis obtains better predictions of the pitching moments when the shock relief effects are accounted for through modified lookup tables (C81 format).

A feasibility study of the loose coupling approach was conducted and is docu-

249

mented in Chapter 3. A simplified structural analysis with only flap and torsion degrees of freedom was used for this case. The loose coupling approach was further examined in Chapter 5, whereby the simplified structural analysis was replaced with an advanced structural model (UMARC). The CFD calculated airloads replaced the UMARC aerodynamic modeling completely in this case. Therefore, the aerodynamic damping terms were not modeled by the structural model. An alternate coupling method that allows the aerodynamic modeling in UMARC to become active was also investigated. In this approach, the differences between the CFD computed airloads and UMARC computed airloads were provided as forcing to the structural model. Therefore, the aerodynamic damping terms, which are evaluated by linearizing the aerodynamic forcing, were retained in the structural dynamic model. Following are the conclusions noted from this investigation:

1. The loose coupling approach was found to give simultaneous convergence of both trim and blade response, even when the lift and pitching moment obtained from the CFD computations were included in to the structural analysis.

2. For the first coupling algorithm, the trim and blade response were closely tied in the high speed forward flight regime. Small errors in the trim solution produced large 1/rev hinge moments that caused the divergence of the blade flapping response. Therefore, additional trim corrections that bound the 1/rev hinge moment magnitude was required for ensuring the convergence of the coupling process.

3. The second coupling approach (which allows the aerodynamic modeling

in UMARC to be active) showed rapid convergence trends for the low speed forward flight case. The final blade response and aerodynamic loads obtained in this approach showed good agreement with those predicted by the former coupling approach. However, for the high speed case, the 1/rev component of the difference in normal force was underrelaxed to obtain an accurate and converged solution.

4. In general, the lack of consistency between the CFD methods and the aerodynamic modeling used in the comprehensive analysis, especially in the prediction of 1/rev normal forces, is what causes divergence of the simultaneous trim and blade response solution. The divergence manifests itself in the flap response solution. This inconsistency is more prevalent at the higher forward flight speed than the lower speeds. Therefore, at the higher speed case, modifications that affect the coupling of the 1/rev normal force (discussed in (2) and (3)) from CFD were required in both the coupling approaches to obtain a converged solution.

6.3   Recommendations for Future Work

Although the present scheme provides good prediction of aerodynamic loads, it is still impractical for routine rotor design. The run times for a complete coupling is of the order of 5 days. Therefore, the first suggested work is the investigation of the feasibility of a reduced order model that would give sufficiently accurate vibratory load predictions. The reduced order model may be the Weissinger-L analysis with a set of corrections based on the insights obtained from the CFD analysis. Alternatively, one could investigate eigen mode decomposition based

aerodynamic modeling (which has matured for fixed-wing analysis) for rotor problems. The CFD solver developed can be used both as an investigative tool and as the test bed for validating the predictions of reduced order models.

The validation of the methodology developed needs to be extended for a larger range of test cases to further evaluate the robustness and accuracy of the approach. This is the first effort in this direction. The technology needs to be comprehensively validated before it is mature enough to be used for routine analysis. The following improvements to CFD methodologies are suggested:

1. Investigation higher order space discretizations of the governing equation (e.g., 5th order). The present method use a 3rd order accurate solution.

2. Improvement of modeling of the inboard boundary conditions. Also the mesh topology can be improved to form a smoother definition to the root blade geometry.

3. Inclusion of a refined tip vortex mesh using the chimera approach. This would help to better estimate the exact roll up location of the tip vortex and also its circulation strength. This would improve the coupling between the CFD and free wake analysis. Currently, the analysis developed assumes the wake to roll up in 30 degrees of azimuth, and, therefore neglects the first 30 degrees of the tip vortex geometry predicted by the free vortex wake. Also, the circulation strength of the tip vortex is determined using bound circulation strengths calculated using the sectional aerodynamic loads predicted by CFD.

4. Modeling of the effect of fuselage on the rotor wakes and fuselage induced downwash at the rotor disk. In the low speed cases, the inflow at the

rotor disc is influenced by the presence of fuselage. Therefore modeling the fuselage effects will improve the fidelity of the approach.

5. Further validation BVI dominated conditions and coupling to acoustic codes for estimating perceived noise levels. This problem is more challenging than the steady flight conditions investigated in this dissertation. Therefore, such a study would help further evaluate the prediction capabilities and identify the potential modeling deficiencies in the present approach.

6. The loose coupling approach assumes the periodicity of the aerodynamic loads with rotor frequency. During maneuvering flight conditions the aerodynamic loads are often aperiodic. Therefore, a tight coupling methodology (i.e., one which integrates the structural and aerodynamic equations simultaneously every time step) needs to be developed for such flight conditions. The present method can be used for validating the results for the tight coupling methodology for steady flight cases.

Appendix A

Fast Evaluation Methods For Evaluating Vortex Induced Velocity Fields

The aerodynamic flow field around a helicopter rotor blade in forward flight is characterized by interacting tip vortices trailed by the rotor blades. Computational Fluid Dynamic modeling of this problem has the limitation in that the tip vortices trailed by the rotor blades are diffused faster than their physical diffusion rate because of the inherent numerical dissipation. So, often one needs a high resolution grid and a higher order numerical scheme with lower numerical dissipation to model the problem. But resorting to complete wake capturing using high resolution grids and modeling all the rotor blades is still prohibitive from a designers point of view. Hence, often only one rotor blade is modeled and the effects of the trailed vortex wake from the other rotor blades are included from a separate free wake analysis, such as using a unique methodology called the field velocity approach [42].

In the field velocity approach the effect of the trailed wake is simulated by

254

superposing a velocity field equivalent to that induced by the wake over the free stream conditions. This is accomplished by changing grid velocities at every grid point by an amount equal to that induced by the vortex wake. In other words, this is a way of modeling an unsteady velocity field by apparent grid movement. Numerical schemes which are strictly conservative have been developed to facilitate efficient use of this approach [45].

The vortex wake geometry, which is usually represented as a set of vortex filaments oriented in a particular way in space and time, is externally computed from the principle of vorticity transport. The solution is performed in a Lagrangian frame of reference. This requires that one evaluates the mutually induced velocities of vortex filaments at each time step and convect the filaments with these induced velocities. Therefore, this computation requires an $O(N^2)$ calculation per time step, where N is the number of vortex filaments.

The field velocity approach requires the computation of wake induced velocities at all the grid points in the mesh. This is an $O(M*N)$ computation where M is the number of grid points and N is the number of vortex filaments. Here, M is of the order 10^6 and N is of the order 10^3. The velocity induced at a point by a vortex filament is given by the Biot-Savart law. So a fast methodology for computation of the Biot-Savart law could tremendously improve the performance of both the wake geometry computation, and the inclusion of this wake geometry in to the CFD computations by field velocity approach. This is the main motivation for developing and testing methodologies for fast evaluation of Biot-Savart kernels.

A.1 The Biot-Savart Kernel

The velocity induced by a vortex filament of length l with a circulation strength Γ, located at $\vec{y}$ at a point with position vector $\vec{x}$ is given by

$$V(x) = \frac{1}{4\pi} \int_0^l \Gamma(\vec{y}) \times \frac{(x-y)}{|x-y|^3} dy \tag{A.1}$$

For points sufficiently in the far-field, i.e. when $|x - y|$ is large computed to l the integral can be approximated by considering $\Gamma(y) = \Gamma \hat{n}$ and $x - y = x - y_{\frac{1}{2}}$. Here, $\hat{n}$ is unit vector in the direction of the vortex filament and $y_{\frac{1}{2}}$ is the position vector of the mid point of the vortex filament. Then the integral in the Eq. A.1 can be reduced to:

$$V(x) = \frac{1}{4\pi} \vec{\omega} \times \frac{(x-y)}{|x-y|^3} \tag{A.2}$$

$$\text{where } \vec{\omega} = (\Gamma l)\hat{n}.$$

Now, if we define $\nabla = \frac{\partial}{\partial x}$, it follows that

$$\frac{(x-y)}{|x-y|^3} = \nabla \frac{1}{|x-y|}$$

Then, expression Eq. A.2 could be rewritten as:

$$V(\vec{x}) = \frac{1}{4\pi} \vec{\omega} \times \nabla \frac{1}{|x-y|}$$

As, $\vec{\omega}$ is not a function of $\vec{x}$, this equation is further rewritten in a convenient form as

$$V(\vec{x}) = \frac{1}{4\pi} \nabla \times \frac{\vec{\omega}}{|x-y|}$$

Hence, one could define a vector potential $\vec{\phi}(x)$ analogous to that in magnetic field [124], as $\vec{\phi}(x) = \frac{\vec{\omega}}{|x-y|}$ and write the velocity field induced by the vortex filaments as $V(x) = \nabla \times \vec{\phi}(x)$. Now, the velocity induced at $\vec{x}$ by a group of N vortex filaments located at $\vec{y_i}(i{=}1,N)$ is given by:

$$V(\vec{x}) = \frac{1}{4\pi} \nabla \times \sum_{i=1}^{N} \frac{\vec{\omega_i}}{|x - y_i|} \tag{A.3}$$

From Eq A.3, it is clear that the primary task in devising a fast evaluation methodology is to find local and far-field series expansions to the vector potential $\vec{\phi}(x)$.

A.2   Far-field expansion of $\vec{\phi}(x)$

The Far-field expansion (termed as S-expansion from now on) is the series expansion of the far-field vector potential around a chosen basis target location(origin for now) due to a vortex filament located in the immediate neighborhood of the basis location.

We need to find a series expansion vector potential $\vec{\phi}(x) = \frac{\vec{\omega}}{|x-y|}$. Let us define $x = (r, \theta, \phi)$ and $y = (\rho, \alpha, \beta)$ in spherical coordinates. Let γ be the angle between vectors x and y. Then from the law of cosines we have:

$$|x - y| = r^2 + \rho^2 - 2r\rho\cos(\gamma)$$

with

$$\cos(\gamma) = \cos(\theta)\cos(\alpha) + \sin(\theta)\sin(\alpha)\cos(\phi - \beta)$$

Thus,

$$\frac{\vec{w}}{r} = \frac{\vec{w}}{r\sqrt{1 - 2\frac{\rho}{r}cos(\gamma) + \frac{\rho^2}{r^2}}} = \frac{\vec{w}}{r\sqrt{1 - 2u\mu + \mu^2}} \tag{A.4}$$

having set

$$\mu = \frac{\rho}{r} \quad \text{and} \quad u = \cos(\gamma)$$

For $\mu < 1$, which is evident from the definition of S-expansion, we may expand the inverse square root in powers of μ, resulting in the series form:

$$\frac{1}{\sqrt{1 - 2u\mu + \mu^2}} = \sum_{n=0}^{\infty} P_n(u)\mu^n$$

and, in general, $P_n(u)$ is the Legendre polynomial of degree n. Our expression for the vector field now takes the form:

$$\frac{\vec{w}}{|x - y|} = \left(\sum_{n=0}^{\infty} P_n(u)\frac{\rho^n}{r^{n+1}} \right) \vec{w} \tag{A.5}$$

But, the formula Eq A.5, unfortunately does not meet our needs. The parameter u depends on both the source and the target locations. We cannot use it to expand the field due to a large number of vortex filaments. A more general representation will require the introduction of spherical harmonics.

For this, we write the Laplace equation in spherical coordinates:

$$\frac{1}{r^2}\frac{\partial}{\partial r}\left(r^2\frac{\partial \Phi}{\partial r}\right) + \frac{1}{r^2 \sin(\theta)}\frac{\partial}{\partial \theta}\left(\sin(\theta)\frac{\partial \Phi}{\partial \theta}\right) + \frac{1}{r^2 \sin^2(\theta)}\frac{\partial^2}{\partial \Phi^2} = 0 \tag{A.6}$$

The standard solution of this equation by separation of variables results in an expression for the field as a series, the terms of which are known as spherical harmonics:

$$\Phi = \sum_{n=0}^{\infty} \sum_{m=-n}^{n} \left(L_n^m r^n + \frac{M_n^m}{r^{n+1}} \right) Y_n^m(\theta, \phi)$$

The terms $Y_n^m(\theta, \phi)r^n$ are referred to as spherical harmonics of degree n, the terms $Y_n^m(\theta, \phi)/r^{n+1}$ are called spherical harmonics of degree $-(n+1)$, and the coefficients L_n^m and M_n^m are known as the moments of the expansion.

The spherical harmonics can be expressed in terms of partial derivatives of $1/r$, but one can also use the simple expression given by the relation

$$Y_n^m(\theta, \phi) = \sqrt{\frac{(n-|m|)!}{(n+|m|)!}} P_n^{|m|} cos(\theta) e^{im\phi}$$

omitting a normalization factor of $\sqrt{\frac{(2n+1)}{4\pi}}$. The special functions P_n^m are called associated Legendre functions and can be defined by the Rodrigues' formula.

$$P_n^m(x) = (-1)^m (1-x^2)^{m/2} (1-x^2)^{m/2} \frac{d^m}{dx^m} P_n(x) \tag{A.7}$$

Now, we use the addition theorem for Legendre polynomials known from the theory of spherical harmonics, to separate the source and target locations in Eq A.5. The addition theorem for spherical harmonics is given by [125]:

$$P_n(\cos(\gamma)) = \sum_{m=-n}^{m=n} Y_n^{-m}(\alpha, \beta) . Y_n^m(\theta, \phi) \tag{A.8}$$

Now, suppose that N vortex filaments of circulation strengths $\omega_i, \ i = 1, .., N$ are located at points $y_i = (\rho_i, \alpha_i, \beta_i)$, with $|\rho_i| < a$. Then for any point $x = (r, \theta, \phi)$ with $r > a$, the vector potential $\vec{\phi}(x)$ is given by:

$$\vec{\phi}(x) = \sum_{n=0}^{\infty} \sum_{m=-n}^{n} \frac{\vec{M}_n^m}{r^{n+1}} . Y_n^m(\theta, \phi) \tag{A.9}$$

259

where

$$\vec{M}_n^m = \sum_{i=1}^{N} \vec{\omega}_i \left(\rho_i^n . Y_n^{-m}(\alpha_i, \beta_i) \right) \tag{A.10}$$

The expansion can be truncated to p^2 (truncation number) terms by making the limits of the outer sum finite (from $n = 0$ to p).

A.3 Local expansion of $\vec{\phi}(x)$

The local expansion (termed R-expansion from now on) is the expansion of the vector potential in the immediate neighborhood of a specified target location due to a vortex filament located in the far-field. The derivation of such an expansion can follow the same steps as one followed for the S-expansion. But, in this case $r < \rho$, or μ should be redefined as $\mu = \frac{r}{\rho}$. Then Eq A.5 can be modified as

$$\frac{\vec{r}}{|x - y|} = \left(\sum_{n=0}^{\infty} P_n(u) \frac{r^n}{\rho^{n+1}} \right) \vec{w} \tag{A.11}$$

Replacing the Legendre polynomial terms in Eq A.5 appropriately as in the derivation of Eq A.9, one could arrive at the expression for R-expansion. Now, the vector potential at $x = (r, \theta, \phi)$ with $r < a$ caused by N vortex filaments of circulation strengths located inside sphere of radius D_Q of radius a with center $Q = (\rho, \alpha, \beta)$ which satisfies $\rho > (c + 1)a$ and $c > 1$ is given by:

$$\vec{\phi}(x) = \sum_{n=0}^{\infty} \sum_{m=-n}^{n} \vec{L}_n^m r^n . Y_n^m(\theta, \phi) \tag{A.12}$$

where

$$\vec{L}_n^m = \sum_{i=1}^{N} \vec{w}_i \frac{Y_n^{-m}(\alpha_i, \beta_i)}{\rho^{n+1}} \tag{A.13}$$

It is to be reiterated that the coefficients $\vec{L}_n^m$ in Eq A.12 and $\vec{M}_n^m$ in Eq A.9 are invariant with spatial coordinates of the evaluation point. Hence the curl of the vector potential can be evaluated analytically by taking appropriate derivatives of the expansion equations. In this work the authors perform it by evaluating the derivatives in spherical coordinates and then transforming them to the Cartesian domain.

A.4   Translation Operators

The far-field expansion (Eq. A.9 and A.10) is sufficient to construct an $O(N \log(N))$ scheme using a divide and conquer approach [112]. But, for the construction of an $O(N)$ scheme one requires operators which would facilitate re-expansion of both the far-field and local expansion over a shifted basis. These were originally derived for scalar potentials by Greengard [93] and can be trivially extended to the vector potential case presented above.

A.4.1   S-S translation operator

Suppose that N vortex filaments of circulation strengths $\vec{w}_i$ and position vectors $\vec{\rho}_i$ are located inside the sphere D of radius a with center at $x_1^* = (\rho_1^*, \alpha_1^*, \beta_1^*)$, then the potential due to these charges for points $x = (r, \theta, \phi)$ is given by the S-expansion (truncated to p^2 terms)

$$\vec{\phi}(x - x_1^*) = \sum_{n=0}^{p} \sum_{m=-n}^{n} \frac{\vec{O}_n^m}{r'^{n+1}} . Y_n^m(\theta', \phi') \tag{A.14}$$

where $(r', \theta', \phi') = x - x_1^*$ and $r' > |\rho_i - x_1^*|$

This S-expansion can be reexpanded on a shifted basis $x_2^* = (\rho_2^*, \alpha_2^*, \beta_2^*)$ with $T = x_1^* - x_2^* = (t, \nu, \xi)$. The reexpansion is given by

$$\vec{\phi}(x - x_2^*) = \sum_{j=0}^{p} \sum_{k=-j}^{j} \frac{\vec{M}_j^k}{r_1^{j+1}} . Y_j^k(\theta_1, \phi_1) \tag{A.15}$$

where $(r_1, \theta_1, \phi_1) = x - x_2^*$ the translation operator $\vec{M}_j^k$ is defined as

$$M_j^k = \sum_{n=0}^{j} \sum_{m=-n}^{m} \frac{\vec{O}_{j-n}^{k-m} . i^{|k|-|m|-|k-m|} . A_n^m . A_{j-n}^{k-m} . t^n . Y_n^{-m}(\nu, \xi)}{A_j^k} \tag{A.16}$$

with A_n^m defined by

$$A_n^m = \frac{(-1)^n}{\sqrt{(n-m)!(n+m)!}} \tag{A.17}$$

A.4.2 S-R translation operator

Suppose that N vortex filaments of circulation strengths $\vec{w}_i$ and position vectors $\vec{\rho}_i$ are located inside the sphere D of radius a with center at $x_1^* = (\rho_1^*, \alpha_1^*, \beta_1^*)$, the S-expansion of vector field about the basis x_1^* is given Eq. A.14. Then the corresponding local expansion around a shifted basis $x_2^* = (\rho_2^*, \alpha_2^*, \beta_2^*)$ truncated to p^2 terms, provided $t = (\rho_1^* - \rho_2^*) > (c+1)a$ with $c > 1$ is given by:

$$\vec{\phi}(x - x_2^*) = \sum_{j=0}^{p} \sum_{k=-j}^{j} L_j^k . Y_j^k(\theta_1, \phi_1) . r_1^j \tag{A.18}$$

where $(r_1, \theta_1, \phi_1) = x - x_2^*$ the translation operator $\vec{L}_j^k$ is defined as

$$L_j^k = \sum_{n=0}^{p} \sum_{m=-n}^{n} \frac{\vec{O}_n^m . i^{|k-m|-|k|-|m|} . A_n^m . A_j^k . Y_{j+n}^{m-k}(\nu, \xi)}{(-1)^n A_{j+n}^{m-k} . t^{j+n+1}} \tag{A.19}$$

where $T = x_1^* - x_2^* = (t, \nu, \xi)$ and A_r^s is defined by Eq A.17

A.4.3 R-R translation operator

Let $x_1^* = (\rho_1^*, \alpha_1^*, \beta_1^*)$ be the origin of the local expansion (truncated to p^2 terms)

$$\vec{\phi}(x - x_1^*) = \sum_{n=0}^{p} \sum_{m=-n}^{n} \vec{O}_n^m . Y_n^m(\theta', \phi') . r'^n \tag{A.20}$$

where $(r', \theta', \phi') = x - x_1^*$ and $r' < |\rho_i - x_1^*|$

Then, the local expansion around a shifted basis $x_2^* = (\rho_2^*, \alpha_2^*, \beta_2^*)$ is given by

$$\vec{\phi}(x - x_2^*) = \sum_{j=0}^{p} \sum_{k=-j}^{j} L_j^k . Y_j^k(\theta_1, \phi_1) . r_1^j \tag{A.21}$$

where $(r_1, \theta_1, \phi_1) = x - x_2^*$ and the translation operator L_j^k is given as:

$$\vec{L}_j^k = \sum_{n=j}^{p} \sum_{m=-n}^{n} \frac{\vec{O}_n^m . i^{|m|-|m-k|-|k|} . A_{n-j}^{m-k} . A_j^k . Y_{n-j}^{m-k}(\nu, \xi) . t^{n-j}}{(-1)^{n+j} . A_n^m} \tag{A.22}$$

where $T = x_1^* - x_2^* = (t, \nu, \xi)$ and A_r^s is defined by Eq A.17.

A.5 Algorithms for Fast Evaluation

There are two algorithms proposed for the fast evaluation. The first approach follows the divide and conquer strategy. This scheme has been implemented and tested with the field velocity approach for a realistic blade vortex interaction case. The $O(N)$ scheme has been tested for a sample geometry of randomly distributed vortex and evaluation points inside a unit cube. More realistic geometries require use of adaptive FMM techniques as the limits of enclosures in the different coordinate directions are non-equal.

A.5.1   Divide and Conquer Scheme

The approach is summarized in Figure A.1. A box that encloses the grid is devised (level 0). This box is recursively subdivided in to smaller boxes (finer and finer levels). The algorithm is as follows.

Local expansion: The R-expansion of all the vortex filaments about the center of the level 0 box due to all the vortex filaments which lie outside the limits of the level 0 box is evaluated

Far-field expansion: The number of vortices in each box are identified and the S-expansion for all boxes in all levels are evaluated.

For EveryGridPoint:

1. The box in the finest level that contains the current gridpoint is found.

2. The Biot-Savart kernal is evaluated for all the vortex filaments in the particular box and its nearest neighbors.

3. The velocity due to the far-field potential is evaluated using S-expansions of boxes at coarser levels. Larger boxes are used as the distance between the evaluation points and vortex increases. In other words, vortex filaments are grouped together as one multipole expansion. The larger the distance, the larger the volume that can be grouped as a single multipole expansion.

Figure A.2 shows the lift time history obtained for the BVI problem shown in Figure A.3. Here, the vortex wake geometry was obtained from a Lagrangian free vortex wake analysis [94] and included in the CFD solver [80] using the field velocity approach. The grid sizes and CPU time taken for the baseline and fast simulations are shown in Table A.1. It is evident from these results that the algorithm presents a very efficient approach with little loss in accuracy.
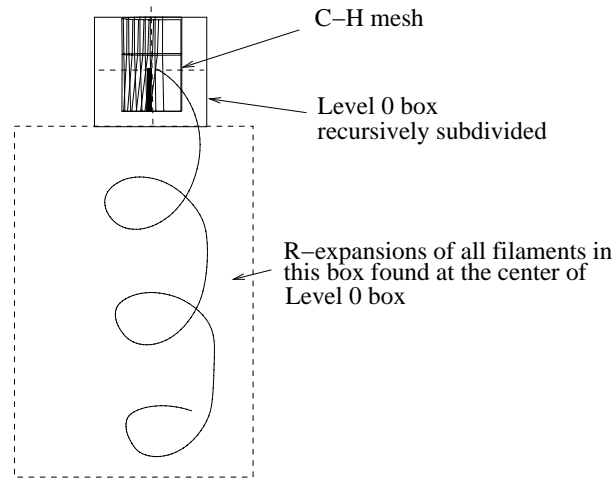
Figure A.1: Schematic of the divide and conquer approach
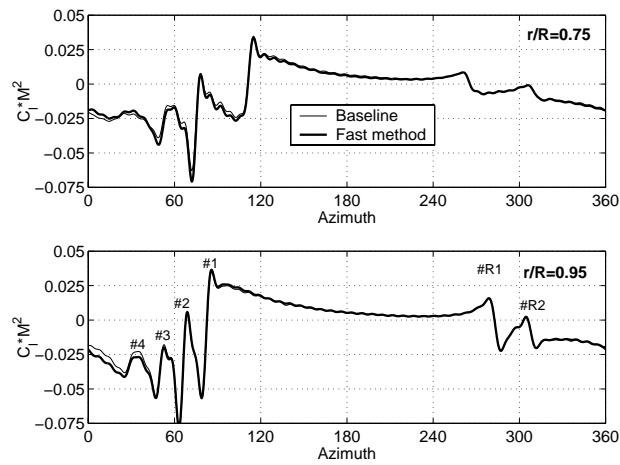
Figure A.2: Computed lift vs azimuth for a BVI problem for the OLS rotor test case [113]
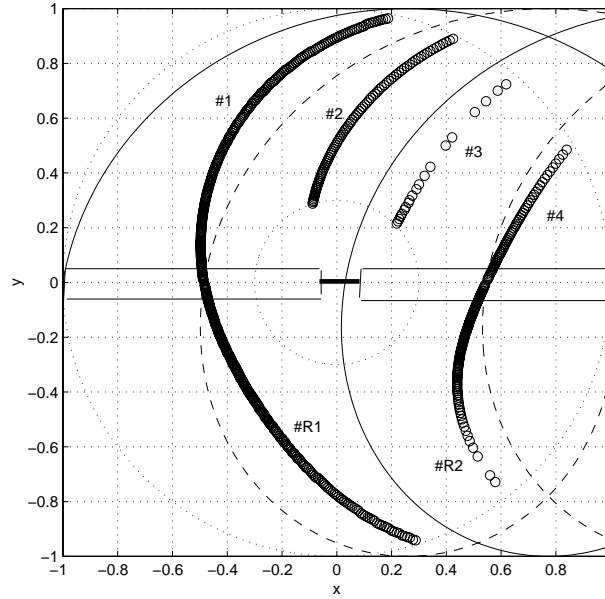
Figure A.3: BVI locations at μ=0.164 for the OLS rotor

Approach	M	N	Wall clock time
Baseline	940,000	900	84h
Fast	940,000	900	12h

Table A.1: Wall clock times for Fast method compared with baseline for one revolution of the rotor $(d\psi = 0.25^o)$, M=number of mesh points, N=number of vortex filaments

A.5.2 Multilevel Fast Multipole Algorithm

An octree based algorithm was developed to perform the fast multipole calculations. The method implements all the analytical machinery developed in the previous sections of Appendix A. Also calculation are performed in a multi level hierarchical manner to further accelerate the computations. A brief description of the algorithm is shown below:

Initialization : Choose level of refinement $n \leq log_8 N$, the precision parameter ϵ, and set truncation number (number of terms in the expansions) p

Upward Pass :

1. Form S-expansions at the center of each box at the finest level. (Eq A.10)

2. For all levels up to the coarsest, starting from the parent level of the finest level, find the S-expansions of all boxes at that particular level by S-S translating the S-expansions of their children (Eq A.13).

Downward Pass:

1. For all boxes in level 2 to the finest level, compute the R-expansions at the box centers by S-R translating (Eq A.19)the S-expansions of boxes in its *interaction list*. The interaction list of any box is a set of all boxes which are children of the nearest neighbors of the parent of the present box, but are not its own nearest neighbors(See Fig. A.4).

2. Aggregate the R-expansions of the box with expansions obtained by R-R translating (Eq A.22) of the parent box.

3. For all the evaluation points, find the box at the finest level containing the evaluation point. Compute direct influences of all sources in this box and
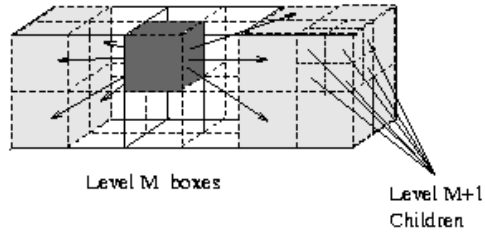
Figure A.4: Interaction List (Greengard [93])

    its immediate neighbors. Compute the R-expansion (Eq A.12) with the center of the box as the basis. Aggregate the two potentials thus obtained to get the full potential.

A performance comparison is conducted between the direct and Multi-level Fast Multipole Method (MLFMM). Equal number of source and evaluation points randomly distributed in a unit cube is chosen as input. The cpu time taken by each approach was measured and plotted against number of sources in Figure A.5. It can be seen that the fast multipole code breaks even with the direct simulation at approximately $N = 10^3$. The performance of the multipole code asymptotes to $O(N)$ while that of the direct simulation asymptotes to $O(N^2)$.

The variation of the maximum absolute error (L1 norm of error) between the fast method and direct method is plotted against the truncation number p in Figure A.6. It is seen that desirable accuracy can be achieved even with a truncation number as low as $p = 3$.

This method is still under the implementation stage for the free vortex wake solver. An adaptive geometrical partitioning strategy is needed in this case to avoid redundant performance degrading computations.
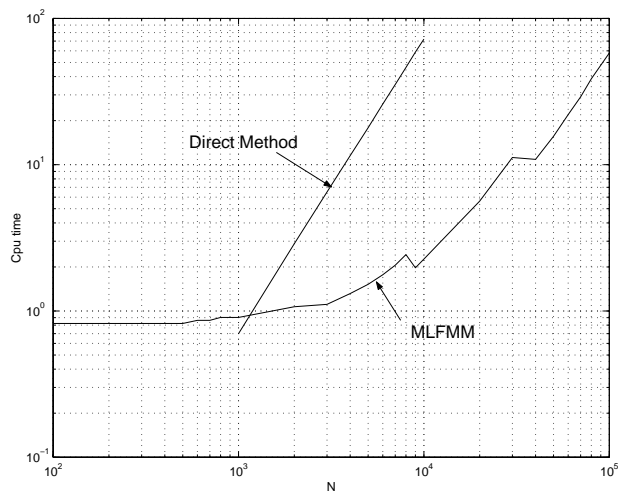
Figure A.5: CPU time comparison for the direct and fast methods for $(N = M)$
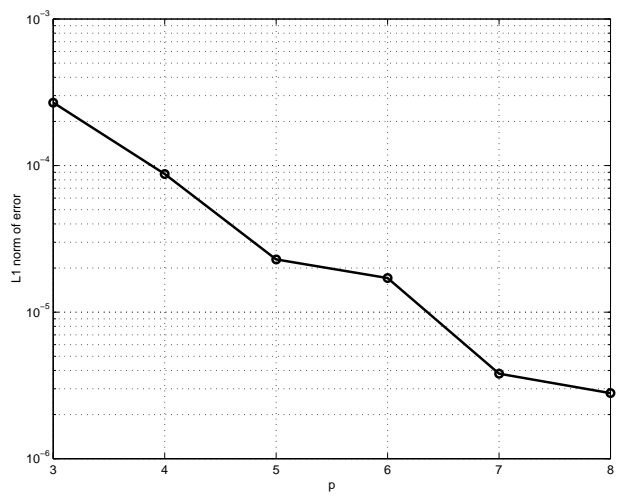
Figure A.6: Variation of maximum absolute error with truncation number

A.6 Summary

The analytic machinery required for the fast multipole method, namely the series expansions and the translation operators for the Biot-Savart kernel, are obtained. A divide and conquer methodology and a multi level fast multipole method are developed and effectively implemented. The divide and conquer methodology is validated for a realistic test problem and found to give good results.

Performance comparisons are conducted for both random and uniform source and evaluation point distributions for the multilevel FMM algorithm. Significant improvement in the performance is observed when the Fast multipole methods are used. Also, use of the truncation number of $p = 3$ is found to give the required accuracy. The module developed is in a form for easy integration with any analysis requiring evaluation of vortex induced velocity fields.

Appendix B

Computation of Cell Volumes

The cell volumes are hexahedra in shape and are in general bounded by faces which are ruled surfaces (i.e. all the four vertices do not lie on a plane). Therefore, an algorithm needs to be devised such that computation of the cell volume is consistent with that of the neighboring cell. This is required to prevent the formation of spurious gaps or overlaps when computing adjacent volumes. There are two methods proposed, they are:

1. Evaluating the individual contribution of each bounding face to the total volume. The contribution would be added to one volume and will be subtracted from the adjacent volume which shares the same bounding face.

2. Splitting each bounding face in to two triangles so as to split the hexahedron in to 6 tetrahedra whose volumes can be easily evaluated.

B.1   Method 1

The first method requires the mapping of the given tetrahedra to a computational domain as shown in Fig B.1. This mapping provides a iso-parametric
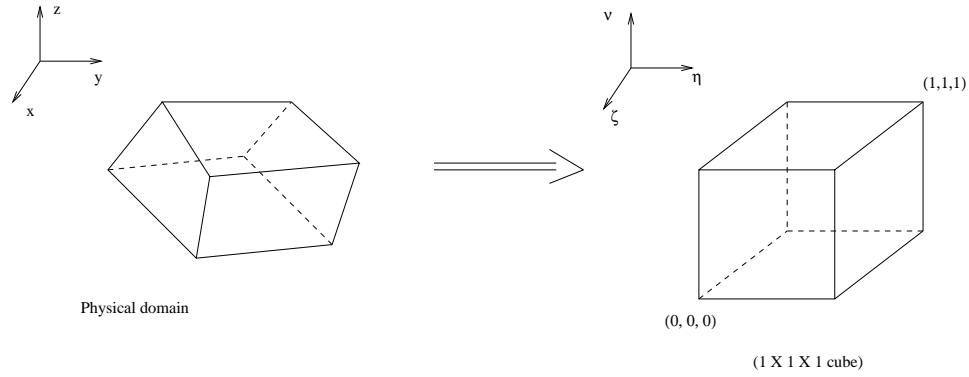
Figure B.1: Mapping of a hexahedron to a unit cube

transformation which can be used to define any position vector inside the cell volume as a convex combination of the position vectors of the vertices. Let r be any position vector inside the volume, r is given by

$$r = \sum_{i=1}^{8} H_i r_i \tag{B.1}$$

Here r_i are the position vectors of the vertices and H_i are trilinear interpolants given by:

$$
\begin{aligned}
H_1 &= (1 - \zeta) * (1 - \eta) * (1 - \nu) \\
H_2 &= \zeta * (1 - \eta) * (1 - \nu) \\
H_3 &= \zeta * (1 - \eta) * \nu \\
H_4 &= (1 - \zeta) * (1 - \eta) * \nu \\
H_5 &= (1 - \zeta) * \eta * (1 - \nu) \\
H_6 &= \zeta * \eta * (1 - \nu) \\
H_7 &= \zeta * \eta * \nu \\
H_8 &= (1 - \zeta) * \eta * \nu
\end{aligned}
\tag{B.2}
$$

Now, the volume in the cartesian domain can be represented as

$$V = \int \int \int dV \tag{B.3}$$

This can be further written as

$$V = \frac{1}{3} \int \int \int \nabla . r dV \tag{B.4}$$

where $r = (x, y, z)$ is the position vector of the small volume dV. Eq B.4 uses the identity $\nabla . r = 3$. Applying Gauss divergence theorem to Eq B.4 gives:

$$
\begin{aligned}
V &= \frac{1}{3} \int \int r.n dS \\
&= \frac{1}{3} \sum_{i=1}^{nfaces} \int \int r_i.n_i dS \\
&= \frac{1}{3} \sum_{i=1}^{nfaces} S_i
\end{aligned}
\tag{B.5}
$$

Now the volume contribution S_i can be evaluated as

$$
\begin{aligned}
S_i &= \int \int r.n_i dA \\
&= \int_0^1 \int_0^1 r.[\frac{\partial r}{\partial \zeta} \times \frac{\partial r}{\partial \eta}] d\zeta d\eta
\end{aligned}
\tag{B.6}
$$

Using Eq A.22 and substituting the analytical expressions for r, $\frac{\partial r}{\partial \zeta}$ and $\frac{\partial r}{\partial \eta}$ one can obtain the closed form solution to the integral in Eq B.6 as

$$
\begin{aligned}
S_i &= \frac{1}{4} \sum_{ijk} r_i.(r_j \times r_k) \\
ijk &\in 123, 124, 134, 234
\end{aligned}
\tag{B.7}
$$

Here r_1, r_2, r_3 and r_4 represent the vertices of the bounding face. The contribution S_i to the volume of a particular cell is algebraically added to the inside cell (i.e one which has the normal pointing outwards from the phase) and subtracted for an outside cell (normal of the face pointing inwards). This process provides a way of maintaining the consistency in evaluating volumes. Also, this

TETRAHEDRA

No	Vertex order
1.	1 6 2 3
2.	1 5 6 3
3.	1 4 5 3
4.	4 8 5 7
5.	7 4 3 5
6.	7 3 6 5
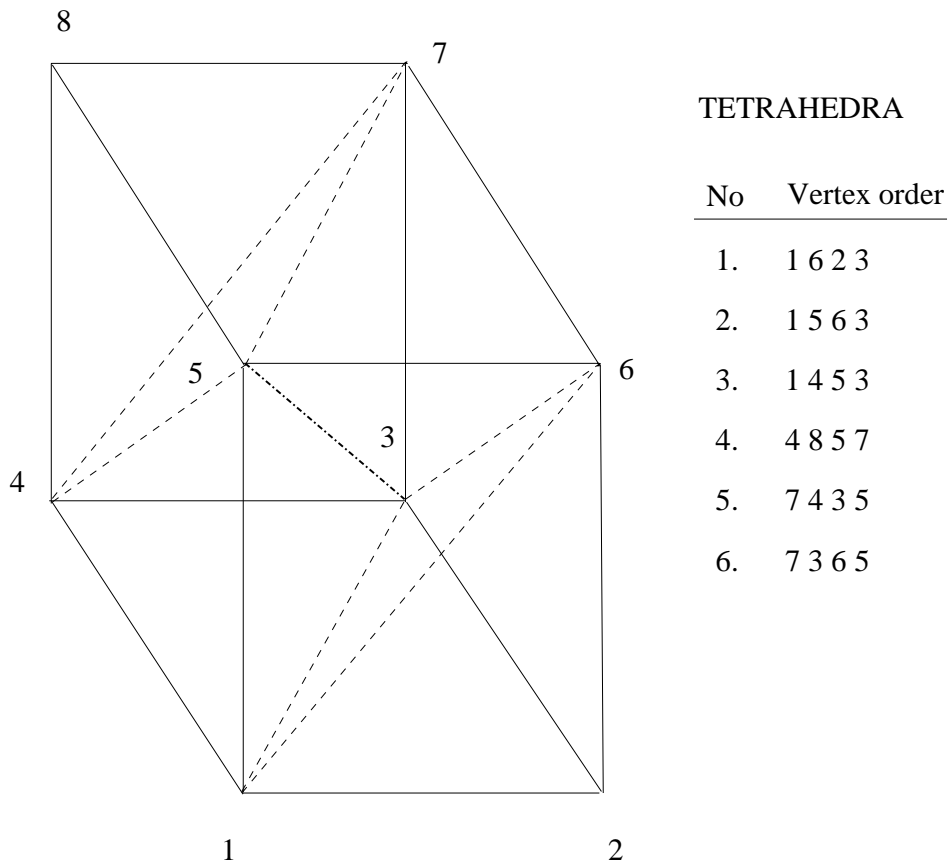
Figure B.2: Division of a Hexahedron in to 6 tetrahedra

method is generic and can be extended to polyhedra with multiple (more than 6) bounding surfaces.

B.2   Method 2

The second method uses splitting of the hexahedron in to 6 tetrahedra (See Fig B.2). The minimum number of tetrahedra a hexahedron can be split to occupy the same volume is 5. But in the present case it had to be split in to 6 tetrahedra to make the opposite faces be split in to triangles in the same way (i.e. the diagonals have similar orientation relative to the face edges). The
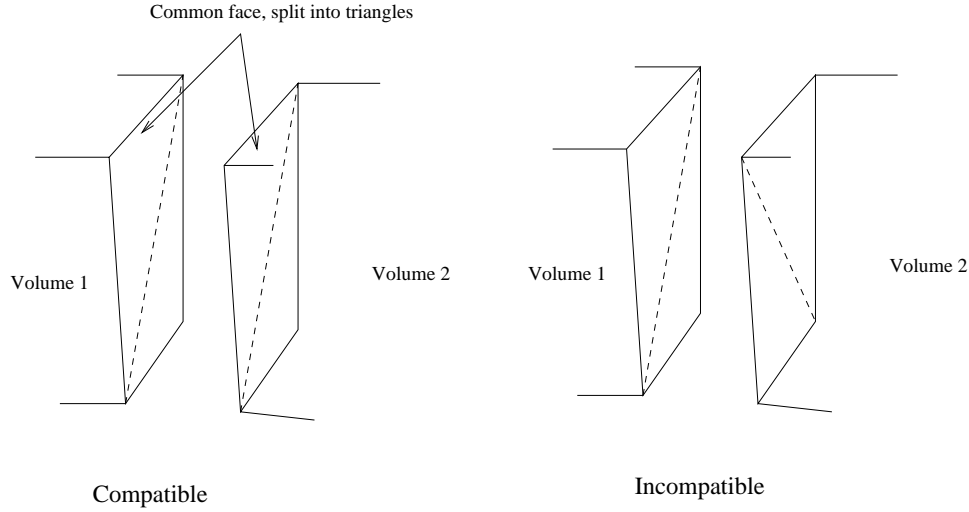
Figure B.3: Compatibility of opposite faces of neighboring hexahedra

opposite faces have to split in the same fashion to maintain consistency of volume evaluation between neighboring volumes. If the diagonals on the opposite faces are reversed, one can generate spurious gaps (See Fig B.3).

The volume of a tetrahedron with sides represented by vectors $\vec{a}$, $\vec{b}$ and $\vec{c}$ is given by

$$V_i = \frac{1}{6}\vec{a}.(\vec{b} \times \vec{c}) \tag{B.8}$$

The volume of the hexahedron can be evaluated as the sum of the volumes of the 6 tetrahedra it was split into. It was found that this method provides a robust approach for computing volumes. The previous method although more accurate and mathematically rigorous poses some robustness problems for highly skewed tetrahedra. This is because the definition of the faces by the trilinear interpolation can cause bounding faces to intersect and create negative volumes. Therefore, the second method is preferable for routine computations because of its robustness.

Appendix C

C-O mesh generation

The C-O grid generation techniques are used to generate meshes which provide a better tip definition. A C-O mesh has stacked C-type meshes along the span until the very tip. Near the tip the C-type meshes are folded such that they conform to a body of revolution type geometry at the tip (Figure C.1).

The method used here uses a C-H mesh topology as input and modifies it to a C-O mesh topology. In the C-H mesh topology the C-meshes are stacked in spanwise direction. At the tip the solid boundary reduces to a zero thickness (straight line) creating a bevel type geometry. Following are the definitions of
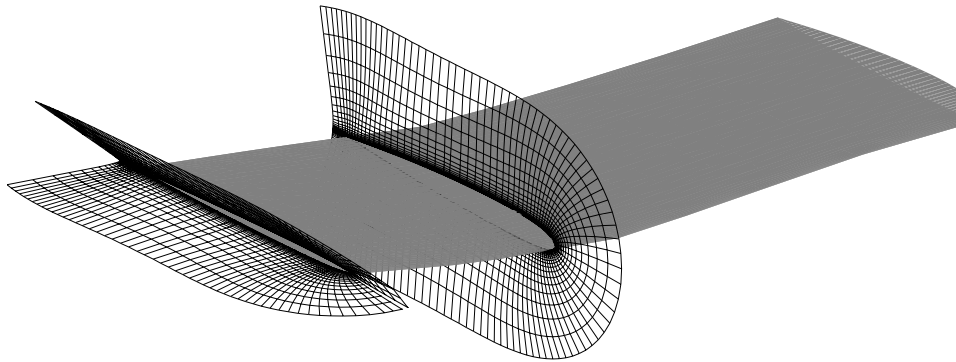
Figure C.1: C-O mesh topology

j	wrap around direction
k	spanwise direction
l	normal direction
jle	leading edge j coordinate
jtail1	trailing edge j coordinate on bottom surface
jtail2	trailing edge j coordinate on upper surface
ktip	k-plane after which the body of revolution starts
jmax	final j-plane
kmax	final k-plane
lmax	final l-plane

the grid parameters.

C.1 Step 1

The first step is to rotate the k=ktip plane by prescribed amounts about the chord axis. This would give initial definition of the all the k-planes with ($ktip \leq k \leq kmax$). The rotation is achieved using quarternions. Quarternions provide the ease of rotating a given point about a chosen center of rotation around an arbitrarily aligned axis by the specified rotation angle. They also are devoid of so called "gimbal locks" which are present when using conventional tranformation matrices. A rotation about unit vector $\hat{n}$ by an angle θ can be computed using the quarternion :

$$q = (s, v) = (cos(\frac{1}{2}\theta), \hat{n}sin(\frac{1}{2}\theta)) \tag{C.1}$$

The components of this quarternion are called Euler parameters. After rotation a point $p = (0, p)$ is then given by

$$p' = qpq^{-1} = qp\bar{q} \qquad (C.2)$$

Here the formula follows the multiplication and conjugation identities of the quarternion formulation [126].

The vector $\hat{n}$ chosen is the unit vector in the direction of the chord line at the k=ktip plane. The centers of rotation for any point is found as the average of the (j,ktip,l) and (jmax-j+1,ktip,l) position vectors (Figure C.2). The following pseudo code describes the algorithm.

Algorithm Rotate:

1: stretching factor $\leftarrow \lambda$

2: number of planes(n) $\leftarrow kmax - ktip$

3: determine $d\theta$ (using $d\theta * (1 + \lambda.. + \lambda^n) = \pi/2$)

4: **for all** $\vec{r}(j, k, l), j \in [1, jmax], k \in [ktip + 1, kmax], l \in [1, lmax])$ **do**

5:

6:     **if** $j \neq jle$ **then**

7:       $\theta(k) = d\theta * \sum_{i=1}^{k} \lambda^{i-1}$

8:       $\vec{r}(j, k, l) \leftarrow rotate(\vec{r}(j, ktip, l), \hat{n}, \theta(k), \vec{r}_c)$

9:     **else**

10:       $\vec{r}(j, k, l) \leftarrow \vec{r}(j, ktip, l)$

11:     **end if**

12: **end for**

The mesh topology obtained after step 1 is shown in Figure C.3. There are singularities in this mesh topologies as the j=jle line and the l=1 line are
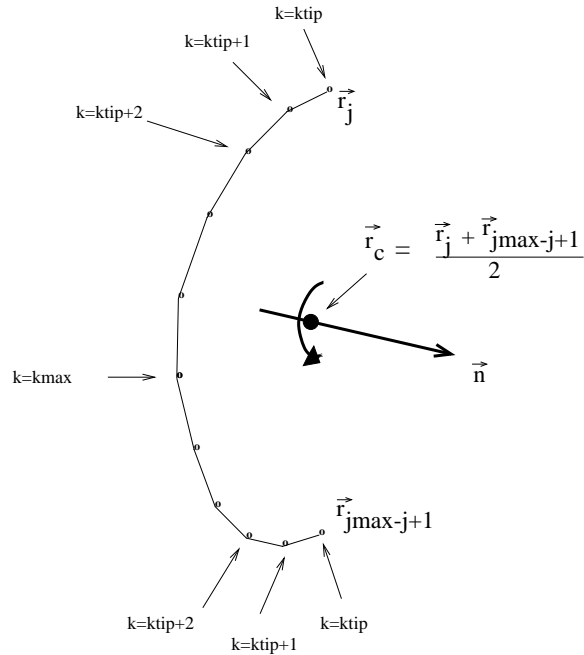
Figure C.2: Rotation vector and point of rotaion

the same for all k-planes with $k \leq ktip$. Such a mesh would cause numerical problems in the solver because of the presence of zero volumes. Step 2 looks in to rectifying this problem by redistributing points at the leading and trailing edges.

C.2 Step 2

Fixing the trailing edge: The points are redistributed such that on and k=constant ($ktip \leq k \leq kmax$) and l=1 line, all the points in the wrap around direction located behind (in the streamwise direction) the point of maximum thickness, is given the y-coordinate value as that of the point of maximum thickness.

Algortihm Trailing:

j= jtail1, jtail2
of l=1 plane

trailing edge

leading edge

k=ktip

j=jle of l=1 plane

k=kmax

j
l
k
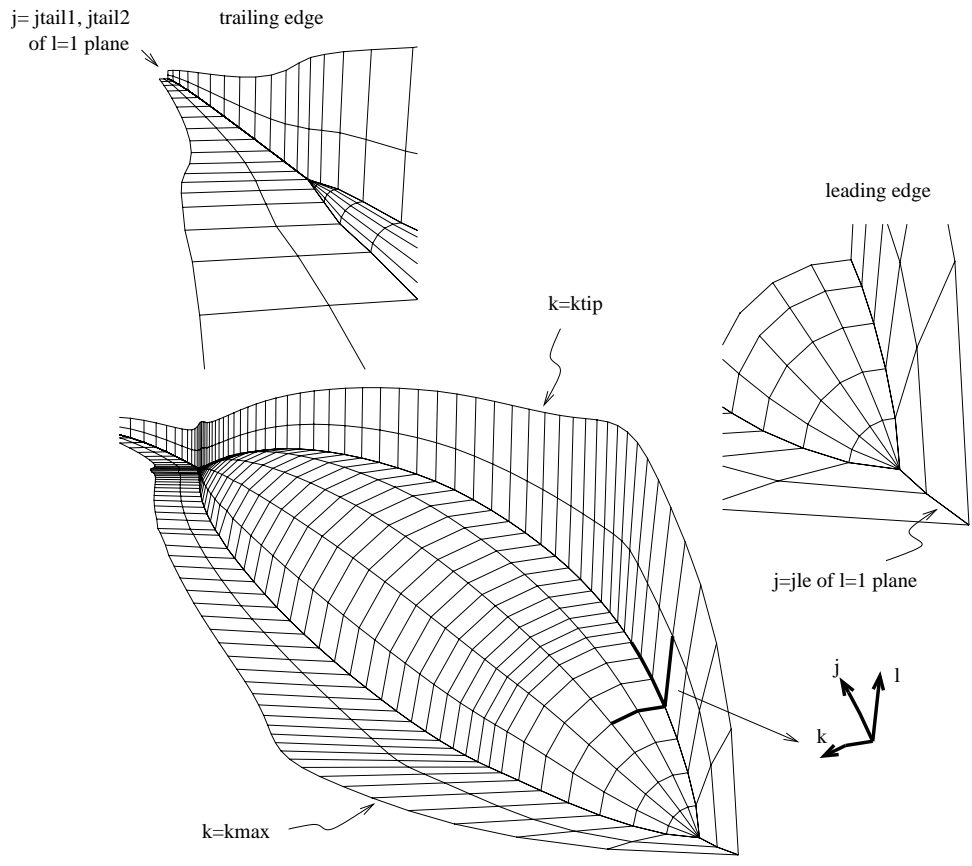
Figure C.3: Mesh topology obtained after Step 1

1: **for all** $k \in [ktip + 1, kmax]$ **do**

2:     determine j_t (point of maximum thickness)

3:     $ymax \leftarrow y(j_t, k, 1)$

4:     **for all** $\vec{r}(j, k, l) j \in [1, j_t - 1] \cup [jmax - j_t + 2, jmax], l \in [1, lmax]$ **do**

5:         $y(j, k, l) \leftarrow y(j, k, l) + (ymax - y(j, k, 1))$

6:     **end for**

7: **end for**

Fixing the leading edge: The leading edge singularity is removed simply by redistributing the points between the k=ktip and k=kmax planes. The following pseudocode explains the algrorithm.

Algorithm Leading:

1: **for all** $\vec{r}(j, k, l), j = jle, k \in [ktip + 1, kmax], l \in [1, lmax]$ **do**

2:     $\vec{r}(j, k, l) \leftarrow interp(\vec{r}(jle, ktip, l), \vec{r}(jle - 1, kmax, l), k)$

3: **end for**

The resulting mesh obtained is shown in Figure C.4. It can be observed that the singularities at the leading and trailing edge are removed.

C.3 Summary

An algorithm for modifying a given C-H mesh topology to a C-O mesh topology is devised. The mesh obtained has a smoother tip definition and is devoid of any geometrical singularities. The CFD methods can incorporate the mesh obtained without any numerical robustness problems.

trailing edge

leading edge

k=ktip

k=kmax
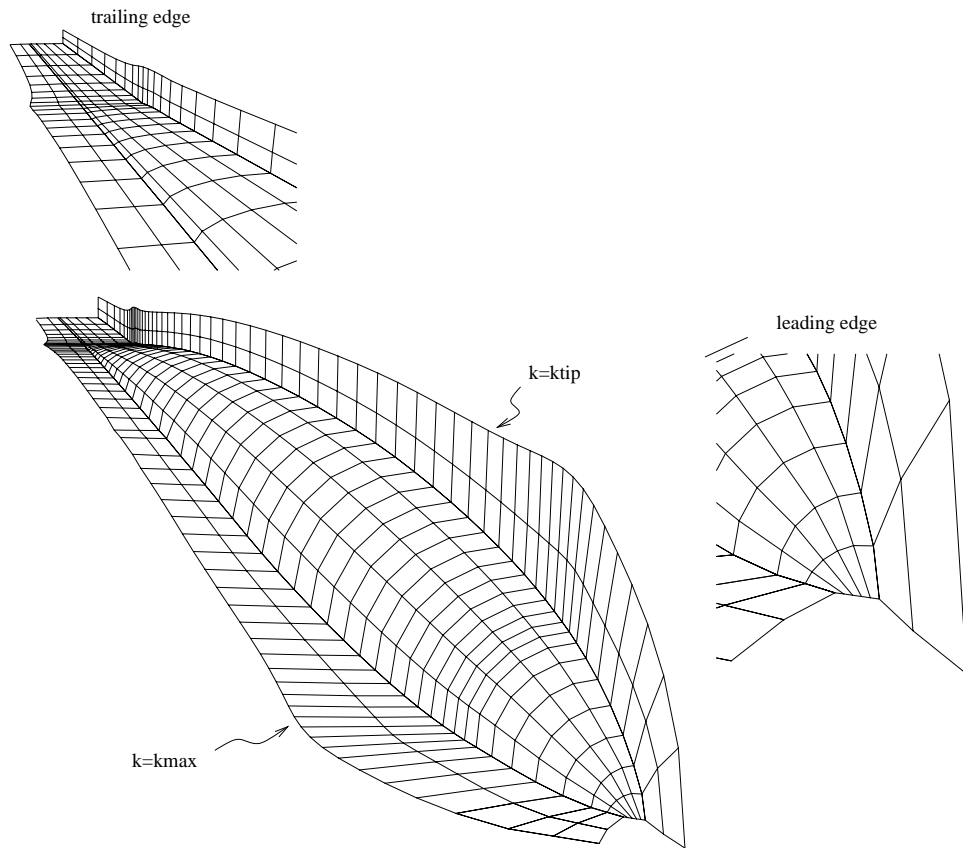
Figure C.4: Mesh topology obtained after the leading and trailing edge redistributions

Appendix D

Validation of the Field Velocity Approach

This appendix presents the results of the computational investigations conducted for two indicial response problems, namely (1) Step change in angle of attack and (2) Interaction with a traveling vertical gust. The field velocity approach (Section 3.13) is used to model the indicial changes in flow conditions.

D.1   Step change in angle of attack

Computations are performed to obtain responses of various airfoils to a step change in angle of attack using the field velocity approach. The indicial response is a combination of noncirculatory (wave propagation) and circulatory effects. For compressible flow, the noncirculatory component exponentially decays and the circulatory component grows to a final asymptotic value. A schematic of the problem is illustrated in Fig D.1(a). Figure D.1(b) shows the lift and pitching moment responses obtained from the CFD computations. The responses obtained from the CFD computations clearly show the physical trend of the

compressible flow. It is possible to obtain closed form analytical solutions to both the normal force and pitching moment responses for small times for a flat plate in linearized compressible flow [102]. The expressions of normal force and pitching moment coefficients are given by:

$$\frac{C_n(s)}{\alpha} = \frac{4}{M}\left[1 - \frac{1-M}{2M}s\right] \tag{D.1}$$

$$\frac{C_m(s)}{\alpha} = \frac{1}{M}\left[1 - \frac{1-M}{2M}s + \left(1 - \frac{M}{2}\right)\frac{s^2}{2M}\right]$$
$$0 \le s \le \frac{2M}{1+M} \tag{D.2}$$

In these equations the quantity s represents the non-dimensional time, which is defined as the distance traveled by the airfoil in semi-chords. Figures D.2(a) and D.2(b) shows the comparison of the CFD results with the exact analytical solution for 4 different airfoils for the small non-dimensional times (i.e. in the region the exact solution is valid). The results show good correlation with the exact solution for both lift and pitching moment. The correlation seems to degrade slightly with increasing thickness and camber. The NACA0006 airfoil, which is the closest to a flat plate approximation, shows excellent correlation. However, the NACA0015 airfoil shows the largest differences with the exact linear solution, especially at the higher Mach numbers where the flow becomes non-linear.

A more detailed description and results of this approach for extracting indicial responses to build both linear and non-linear kernels for reduced order aerodynamics models are documented in previous research efforts [43, 104, 106].
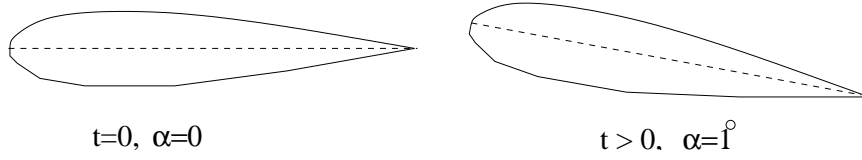
(a) Illustration of step change in angle of attack
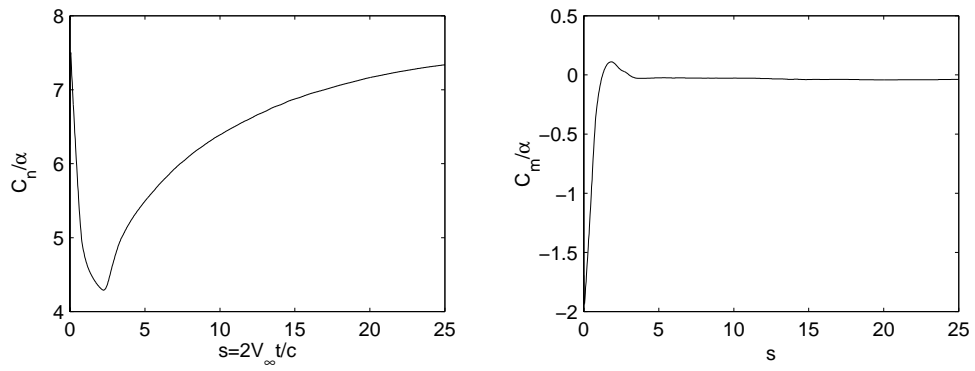
(b) Normal force and pitching moment responses for SC1095 airfoil (M=0.5)

Figure D.1: Response to step change in angle of attack using field velocity approach

(a) CFD vs exact analytical (Normal force)

(b) CFD vs exact analytical (Pitching moment)

Figure D.2: Correlation between computed and exact analytical results for step change in angle of attack

D.2 Interaction of an airfoil with a traveling gust
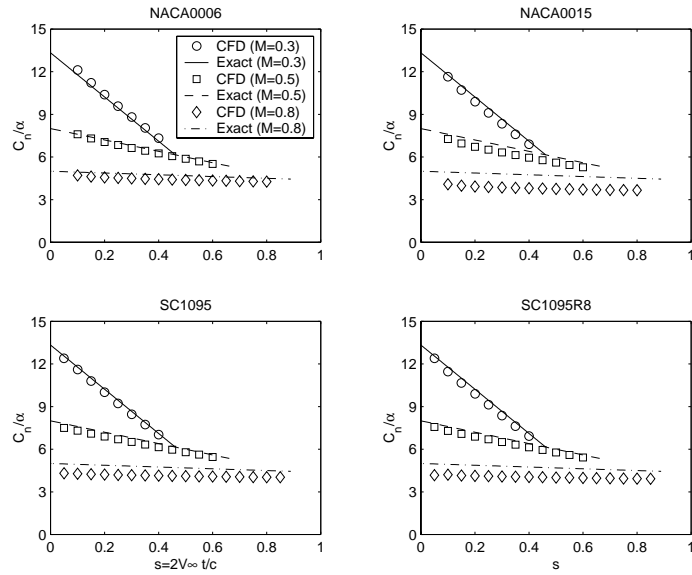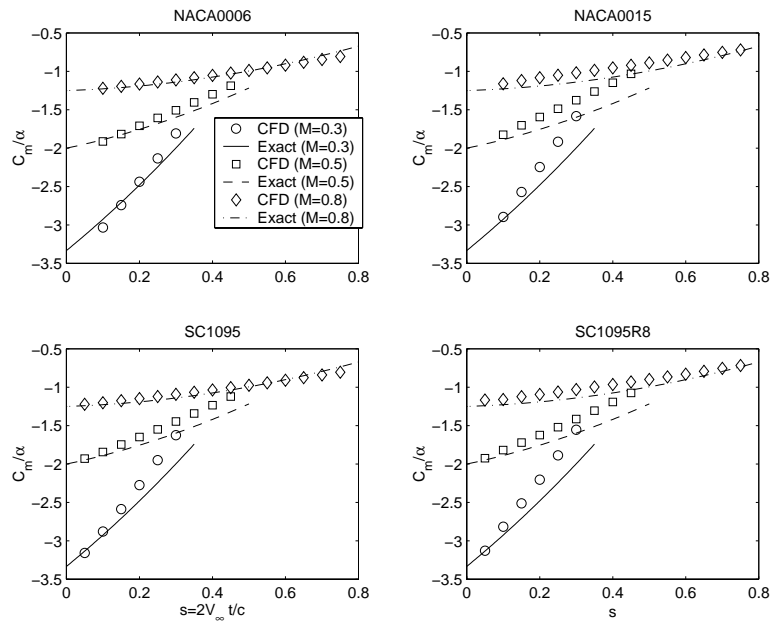
The next unsteady flow problem studied is the aerodynamic response of an airfoil penetrating through a traveling vertical gust. The schematic of the problem is illustrated in Fig D.3(a). The parameter that quantifies the relative convection speed of the gust is termed the gust speed ratio ($\lambda = \frac{V}{V+V_g}$, V=free stream velocity, V_g=gust convection speed).

The exact analytical solution for the response to a traveling vertical gust in compressible flow for small periods of time $0 \leq s \leq \frac{2M}{1+M}$ was developed using Evvard's [107] theorem and verified against Leishman's [108] results from the reverse flow theorem by Singh [109]. The exact analytical solutions are as follows:

$$C_l(s) = \frac{2s}{\sqrt{M\lambda^3}} \left[\frac{\lambda}{\lambda + (1-\lambda)M} \right]^{\frac{1}{2}} \tag{D.3}$$

$$C_{m_{le}}(s) = \frac{-s^2}{4\sqrt{M^3\lambda^2}} \left[\frac{\sqrt{2M + (1-M)\lambda}}{\lambda + (1-\lambda)M} \right] \tag{D.4}$$

Figure D.3(b) shows the numerical prediction of the aerodynamic responses of a NACA 0012 airfoil to a traveling vertical gust. The field velocity approach which was described earlier is used to implement the unsteady flow conditions for predicting the gust response. The effect of the gust is simulated by suitably modifying the field velocities in the vertical direction. At any instant of time the gust front can be calculated from the gust speed ratio. Thus, the field velocity values at all grid points behind the gust front are modified to be equal to the gust magnitude to simulate a propagating gust.
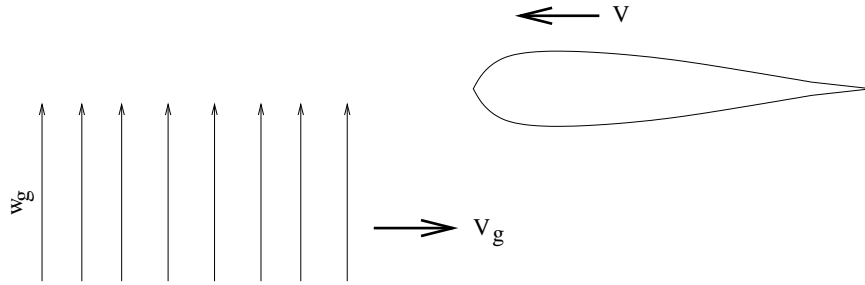
(a) Schematic of interaction with a vertical gust
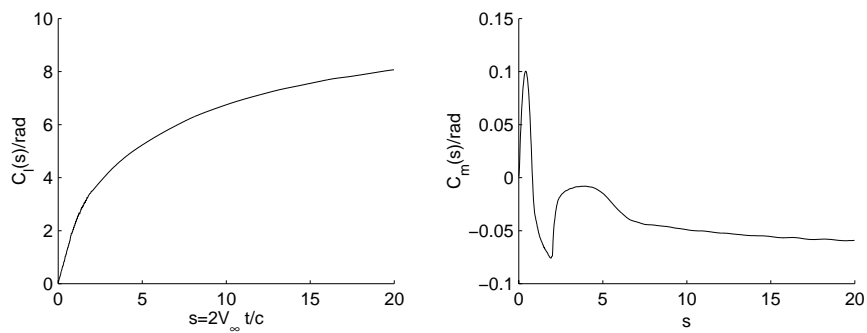
(b) Aerodynamic response to a vertical gust

Figure D.3: Response to a traveling vertical gust using field velocity approach

The initial flow conditions for the unsteady simulation is generated by obtaining a steady state flow solution around the airfoil. Once the initial steady state is obtained, the gust is initiated 15 chords upstream of the airfoil and made to convect at the desired speed representing the gust speed ratio $(V_g = V(\lambda^{-1} - 1))$. The instant of time $s = 0$ corresponds to the instant where the gust front meets the airfoil leading edge.

For moving gusts the rate of increase of the normal force is larger for the faster moving gusts. This is because of the acceleration effects associated with the
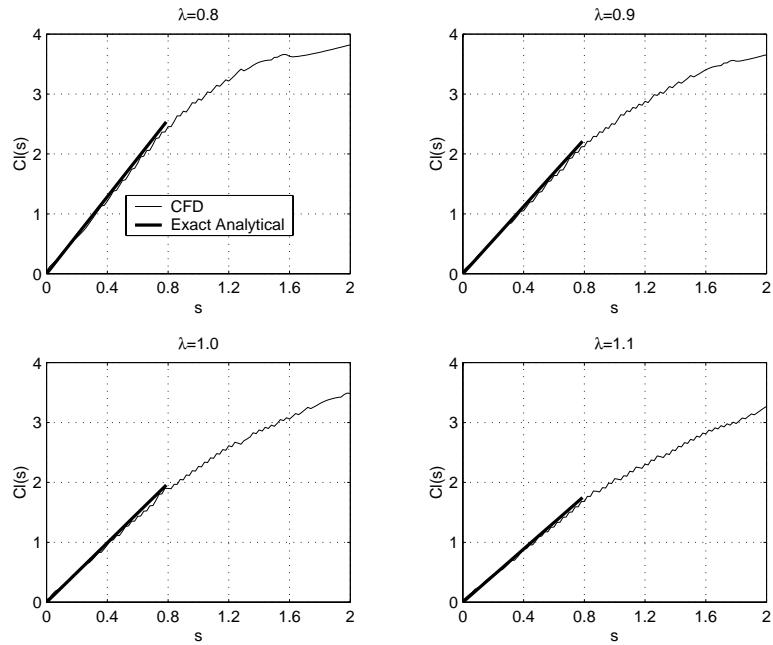
(a) lift coefficient
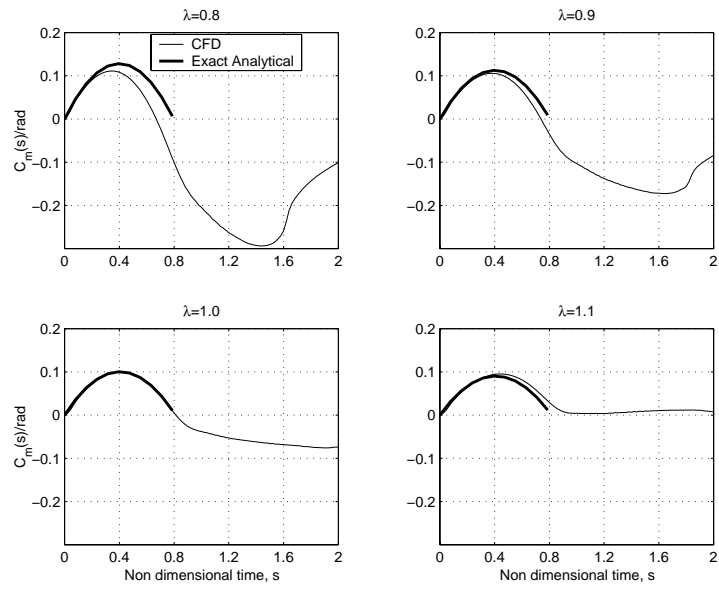
(b) pitching moment

Figure D.4: Correlation between computed and exact analytical results for interaction of an airfoil with a traveling gust (M=0.6)

289

impulsive change in the velocity field over a portion of the airfoil. This additional lift, which is the non-circulatory lift, decays rapidly and thereafter the total circulatory lift builds up slowly towards the steady state. The steady state magnitude is the same for all cases and is determined by the effective angle of attack caused by the vertical gust velocity. In the limiting case of infinite gust propagation speeds, the lift response corresponds to an indicial change in the angle of attack of equivalent magnitude (Wagner [96] problem). The case of zero gust speed or penetration of the airfoil in to a stationary vertical gust is called the Küssner [110] problem.

The comparison of numerical solutions for a NACA 0012 and exact solutions for a flat plate for four different gust speeds are presented in Figures D.4(a) and D.4(b). The numerical solutions show excellent correlation with the exact analytical results especially for the stationary gust case ($\lambda=1$); for the faster and slower convecting gust cases there are some deviations from the exact solution. Lower order aerodynamic models can be constructed for this problem by extracting the indicial responses for aerodynamic load time history obtained from the CFD calculations [43, 45].

Bibliography

[1] Weissinger, J., "The Lift Distribution on Swept-Back Wings," NACA TM 1120, March 1947.

[2] Hansford, E.R. and Vorwald, J., "Dynamics Workshop On Rotor Vibratory Loads," Presented at the American Helicopter Society 52nd Annual Forum, Washington, DC, June 4-6, 1996.

[3] Bousman, W. G., "Putting the Aero Back Into Aeroelasticity," Presented at the 8th ARO Workshop on Aeroelasticity of Rotorcraft Systems, University Park, PA, October 18-20, 1999.

[4] Magnus, R. and Yosihara, H., "Unsteady Transonic Flows Over and Airfoil," *AIAA Journal*, Vol. 13, No.1, 1975, pp. 1622-1628.

[5] VanDyke, M., *Perturbation Methods in Fluid Mechanics*, Academic Press, New York, 1964.

[6] Ballhaus, W.F. and Goorjian, P.M., "Implicit Finite Difference Computations of Unsteady Transonic Flows about Airfoils," *AIAA Journal*, Vol. 15, No. 12, 1977, pp. 1728-1735. 1977.

[7] Ballhaus, W.F. and Goorjian, P.M., "Computation of Unsteady Transonic Flows by the Indicial Method," *AIAA Journal*, Vol. 16, No. 2, 1978, pp. 117-124.

[8] Guruswamy, P.G. and Yang, T.Y., "Aeroelastic Time-Response Analysis of Thin Airfoils by Transonic code LTRAN2," *Computers and Fluids*, Vol. 9, No. 4, 1980, pp. 409-425.

[9] Guruswamy, P.G., "Unsteady Aerodynamic and Aeroelastic Calculations for Wings Using Euler Equations," *AIAA Journal*, Vol. 28, No. 3, 1990, pp. 461-469.

[10] Guruswamy, P.G., "Unsteady Transonic Aerodynamics and Aeroelastic Calculations at Low-Supersonic Freestreams," *Journal of Aircraft*, Vol. 25, No. 10, 1988, pp. 955-961.

[11] Guruswamy, P.G., "User's Guide for ENSAERO- A Multidisciplinary Program for Fluid/Structural/Control Interaction Studies of Aircraft," NASA TM 108853, Oct. 1994.

[12] Robinson, B.A., Batina, J.T. and Yang, H.T.Y., "Aeroelastic Analysis of Wings Using the Euler Equations with a Deformed Mesh," *Journal of Aircraft*, Vol. 28, No. 11, 1991, pp. 781-788.

[13] Cunningham, H.J., Batina, J.T. and Bennet, R.M., "Modern Wing Flutter Analysis by Computational Fluid Dynamics Methods," *Journal of Aircraft*, Vol. 25, No. 10, 1988, pp. 962-968.

[14] Lee-Rausch, E.M. and Batina, J.T., "Wing Flutter Computations Using an Aerodynamic Model Based on the Navier-Stokes Equations," *Journal of Aircraft*, Vol. 33, No. 6, 1996, pp. 1139-1147.

[15] Crouse G.L.Jr. and Leishman, J.G., "Transonic Aeroelasticity Analysis Using State-Space Unsteady Aerodynamic Modeling," *Journal of Aircraft*, Vol. 29, No. 1, 1992, pp. 153-160.

[16] Mazelsky, B., "On the Noncirculatory Flow About a Two-Dimensional Airfoil at Subsonic Speeds," *Journal of the Aeronautical Sciences*, Vol. 19, No. 12, 1952, pp. 848-849.

[17] Edwards, J.W., Bennett, R.M., Whitlow, W.Jr., and Seidel, D.A., "Time-Marching Transonic Flutter Solutions Including Angle of Attack Effects," *Journal of Aircraft*, Vol. 20, No. 11, 1983, pp. 899-906.

[18] Wagner, H., "Uber die Entstehung des dynamischen Auftriesbes von Tragflugeln," *Zeitschrift fur angewandte Mathematik un Mechanick*, Vol. 5, No . 1, 1925, pp. 17-35.

[19] Mahajan, A., Dowell, E., and Bliss, D., "Eigenvalue Calculation Procedure for and Euler/Navier-Stokes Solver with Application to Flows over Airfoils," *Journal of Computational Physics*, Vol. 97, 1991, pp. 398-413.

[20] Romanowski, M. and Dowell, E., "Using Eigenmodes to Form an Efficient Euler Based Unsteady Aerodynamics Analysis," Proceedings of the Special Symposium on Aeroelasticity and Fluid/Structure Interaction Problems, ASME International Mechanical Engineering Congress and Exposition, AD-Vol. 44, pp. 147-160, 1994.

[21] Hall, K., "Eigen Analysis of Unsteady Flows about Airfoils, Cascades and Wings," *AIAA Journal*, Vol. 32, No.12, 1994, pp. 2426-2432.

[22] Hall, K.C., Thomas, J.P., and Dowell, E.H., "Reduced Order Modeling of Unsteady Small-Disturbance Flows Using a Frequency-Domain Proper Orthogonal Decomposition Technique," AIAA Paper 99-0655, 1999.

[23] Wilcox, K. and Peraire, J., "Balanced Model Reduction Via The Proper Orthogonal Decomposition," AIAA Paper 2001-2611, 2001.

[24] Wilcox, K., Paduano, J.D. and Peraire, J., "Low Order Aerodynamic Models For Aeroelastic Control of Turbomachines," AIAA 99-1467, 1999.

[25] Roberts, T.W. and Murman, E.M., "Solution Method for a Hovering Helicopter Rotor Using Euler Equations," AIAA Paper 85-0436, Jan. 1985.

[26] Kramer, E., Hertel, J. and Wagner, S., "Computation of Subsonic and Transonic Helicopter Rotor Flow Using Euler Equations," *Vertica*, Vol.12, No. 3, 1988, pp. 279-291.

[27] Chen, C.-L. and McCroskey, W.J., "Numerical Simulation of Helicopter Multi-Bladed Rotor Flow," AIAA Paper 88-0046.

[28] Srinivasan, G.R., Baeder, J.D., Obayashi, S. and McCroskey, W.J., "Flowfield of a Lifting Rotor in Hover: A Navier-Stokes Simulation," *AIAA Journal*, Vol. 30, No. 10, 1992, pp. 2371-2378.

[29] Caradonna, F.X. and Tung, C., "Experimental and Analytical Studies of a Model Helicopter Rotor in Hover," NASA TM 81232, Sept 1981.

[30] Wake, B.E. and Baeder, J.D., "Evaluation of a Navier-Stokes Analysis Method for Hover Performance Prediction," *Journal of American Helicopter Society*, Vol. 41, No. 1, 1992, pp. 7-17.

[31] Tang, L. and Baeder, J.D., "Recent Rotor CFD Development for Capturing Vortex," AHS Technical Specialist Meeting for Rotorcraft Acoustics and Aerodynamics, Williams burg, VA, October 1997.

[32] Duque, E.P.N. and Srinivasan, G. R., "Numerical Simulation of a Hovering Rotor Using Embedded Grids," American Helicopter Society, 48th Annual Forum, Washington, DC, June 3-5, 1992.

[33] Strawn, R.C., Duque, E.P.N. and Ahmad, J., "Rotorcraft Aeroacoustics Computations with Overset-Grid CFD Methods," American Helicopter Society, 54th Annual Forum, Washington D.C, May 20-22, 1998.

Journal of American Helicoter Society, Vol. 44, No. 2, April, 1999.

[34] Ahmad, J.U. and Strawn, R.C., "Hovering Rotor and Wake Calculations with an Overset-Grid Navier-Stokes Solver," Presented at the American Helicopter Society 55th Annual Forum, Montreal, Canada, May 25-27, 1999.

[35] Pomin, H. and Wagner, S., "Navier-Stokes Analysis of Helicopter Rotor Aerodynamics in Hover and Forward Flight," AIAA 2001-0998, Reno, NV Jan 2001.

[36] Bagai, A., "Contributions to the Mathematical Modeling of Rotor-Flow-Fields Using Pseudo-Implicit Free Wake Analysis," *PhD dissertation*, University of Maryland at College Park, MD, 1995.

[37] Bhawat, M., "Mathematical Modeling Of The Transient Dynamics Of Helicopter Rotor Wakes Using A Time-Accurate Free-Vortex Method," *PhD dissertaion*, University of Maryland at College Park, MD, 2001.

[38] Srinivasan, G., R. and McCroskey, W., J., "Numerical Simulations of Unsteady Airfoil Vortex Interactions," *Vertica*, Vol. 11, No. 12, 1987.

[39] Tang, L., "Improved Euler Simulation of Helicopter Vortical Flows," *PhD Dissertation*, University of Maryland at College Park, MD, 1998.

[40] Ramachandran, K., Tung, C. and Caradonna, F.X., "Rotor Hover Performance Prediction Using a Free-wake, Computational Fluid Dynamics Method," *Journal of Aircraft*, Vol. 26, No. 12, 1989, pp. 1105-1110.

[41] Caradonna, F.X. and Tung, C.,"A Review of Current Finite Difference Rotor Flow Methods," Proceedings of 42nd Annual Forum of the American Helicopter Society, Washington D.C., Jun 1985.

[42] Paramesvaran, V. and Baeder, J.D., "Indicial Aerodynamics in Compressible Flow - Direct Computational Fluid Dynamic Calculations," *Journal of Aircraft*, Vol. 34, No. 1, 1997, pp. 131-133.

[43] Singh, R. and Baeder, J.D., "The Direct calculation of Indicial Lift Response of a Wing Using Computational Fluid Dynamics," *Journal of Aircraft*, Vol. 35, No. 4, 1997, pp. 465-471.

[44] Khanna, H. and Baeder, J. D., "Coupled Free-Wake/CFD Solutions For Rotors in Hover Using A Field Velocity Approach," Presented at the 52nd Annual Forum of the American Helicopter Society, Washington D.C. June 4-6, 1996.

[45] Sitaraman, J. and Baeder, J. D., "Linearized Unsteady Aerodynamic Models for Simulating Blade Wake Interaction," AIAA 2001-0995, Reno, NV, Jan 2001.

[46] Boisard, R., "Linear Acoustic Analysis of Blade Vortex Interaction of a Rotor," *Masters Thesis*, University of Maryland at College Park, MD, 2001.

[47] Steinhoff, J. and Suryanarayana, K., "The Treatment of Vortex Sheets in Compressible Potential Flow," Proceedings of Computational Fluid Dynamics Conference, AIAA, New York, July 1983.

[48] Steinhoff, J., "A Vortex Embedding Method for Free-Wake Analysis of Helicopter Rotors Blades in Hover," Paper 2-11, 13th European Rotorcraft Forum, Arles, France, 1987.

[49] Steinhoff, J. and Ramachandran, K., "Free-Wake Analysis of Compressible Rotor Flows," *AIAA Journal*, Vol. 28, No. 3, 1990, pp. 427-431.

[50] Bridgeman, J.O., Prichard, D. and Caradonna, F.X., "The Development of a CFD Potential Method for the Analysis of Tilt-Rotors," presented at the AHS Technical Specialist Meeting on Rotorcraft Acoustics and Fluid Dynamics, Philadelphia, PA, October 15-17, 1991.

[51] Strawn, R.C., and Caradonna, F.X., "Conservative Full Potential Model for Unsteady Transoncic Rotor Flows," *AIAA Journal*, Vol. 25, No.2, 1987, pp. 193-198.

[52] Lee, C.S., Saberi, H. and Ormiston, R.A., "Aerodynamic and Numerical Issues for Coupling CFD into Comprehensive Rotorcraft Analysis," pre-

sented at the 53rd forum of American Helicopter Society, Virginia Beach, VA, April 29-May 1, 1997.

[53] Bridgeman, J.O. and Dietz, W.E., "Vorticity Confinement Modeling of Dynamic Stall With Tight Structural Coupling," Presented at the American Helicopter Society Aerodynamics, Acoustics and Test and Evaluation Specialists Meeting, San Francisco, CA, Jan 23-25, 2002.

[54] Tung, C., Caradonna, F., X. and Johnson, W., "The Prediction of Transonic Flows on an Advancing Rotor," *Journal of American Helicopter Society*, Vol. 32, No. 7, 1986, pp. 4-9.

[55] Johnson, W., "Development of Comprehensive Analysis for Rotorcraft - I : Rotor Model and Wake Analysis : II: Aircraft Model, Solution Procedure and Applications," *Vertica*, Vol. 5, 1981, pp 99-130 and pp 185-216.

[56] Strawn, R.C. and Tung, C., "Prediction of Unsteady Transonic Rotor Loads with a Full-Potential Rotor Code," American Helicopter Society, 43rd Annual Forum, St. Louis, MO, May 18-20, 1987.

[57] Strawn, R.C. and Tung, C., "The Prediction of Transonic Loading on Advancing Helicopter Rotors," NASA TM-88238, 1986.

[58] Strawn, R.C., Desopper, A., Miller, J. and Jones, A., "Correlation of Puma Airloads - Evaluation of CFD Prediction Methods," Paper No. 14, 15th European Rotorcraft Forum, Sept 1989.

[59] Strawn, R.C., Bridgemen, 0., "An Improved Three Dimensional Aerodynamic Model for Helicopter Airloads Predictions," Presented at the 29th Aeropace Sciences Meeting, Reno, NV, Jan 7-10, 1991.

[60] Yamauchi, G.K., Heffernan, R.M., and Gaubert, M., "Correlation of SA349/2 Helicopter Flight Test Data with a Comprehensive Rotorcraft Model," *Journal of American Helicopter Society*, Vol. 33, No. 2, 1988, pp. 31-42.

[61] Kim, K. C., Desopper, A. and Chopra, I.,"Blade Response Calculations Using Three-Dimensional Aerodynamic Modeling,"*Journal of American Helicopter Society*, Vol .36, No. 1, 1991, pp. 68-77.

[62] Bauchau, O.A. and Ahmad, J.U., " Advanced CFD and CSD Methods for Multidisciplinary Applications of Rotorcraft Problems," AIAA 6th Symposium on Multidisciplinary Analysis and Optimization, Seattle, WA, Sept. 1996.

[63] Buning, P.G, Chan, K.J., Renze D.L., Sondak, I.-T. and Slotnick, J.P., "OVERFLOW User's Manual," Version 1.6ab, 26 January 1993, NASA Ames Research Center, Moffett Field, CA, Jan. 1993.

[64] Bauchau, A. O., "DYMORE: A Finite Element Based Tool for the Analysis of Nonlinear Flexible Multibody Systems," Georgia Institute of Technology Report, 2001.

[65] Rutkowski, M., J., Ruzicka, G., C., Ormiston, R., A., Saberi, H., Yoon, J., "Comprehensive Aeromechanics Analysis of Complex Rotorcraft Using 2GCHAS," Journal of the American Helicopter Society, Vol. 40, No. 4, October, 1995, pp 3-15.

[66] Buchtala, B., Wehr, D. and Wagner, S., "Coupling of Aerodynamic and Dynamic Methods for Calculation of Helicopter Rotors in Forward Flight,"

Proceedings of 23rd European Rotorcraft Forum, pp. 5.1-5.12, Dresden, Germany, September 1997.

[67] Beaumier, P., Pahlke, K. and Celli, E., "Navier-Stokes Prediction of Helicopter Rotor Performance in Hover Including Aero-Elastic Effects", Presented at the American Helicopter Society 56th Annual Forum, Virginia Beach/Virginia, May 2-4, 2000.

[68] Altmikus, A., Wagner, S., Hablowetz, T. and Well, K., "On the Accuracy of Modular Aeroelastic Methods Applied to Fixed and Rotary Wings," AIAA 2000-4224, Denver, Colorado, August 2000.

[69] Berkman, E. M., Sankar, L. N., Berezin, C. R. and Torok, M. S., "A Navier-Stokes/Full Potential/Free Wake Method For Advancing Multi-Bladed Rotors," Presented at the American Helicopter Society 53rd Annual Forum, Virginia Beach, Apr 29-May 1, 1997.

[70] Yang, Z., Smith, M. J., Bauchau, O. and Sankar, L. N., "A Hybrid Flow Analysis for Rotors in Forward Flight," Presented at the American Helicopter Society Aeromechanics Specialists Meeting, Atlanta, Georgia, November 13-14, 2000.

[71] Bousman, W.G., Young, C., Toulmay, F., Gilbert, N.E., Strawn, R.C., Miller, J.V., Maier, T.H., Costes, M. and Beumier, P., "A Comparison of Lifting-Line and CFD methods with Flight Test Data from a Research Puma Helicopter," NASA TM 110421, October 1996.

[72] Lim, J.W., Anastassiades, T., "Correlation of 2GCHAS Analysis with Experimental Data," *Journal of American Helicopter Society*, Vol. 40, No. 4, 1995, pp. 18-33.

[73] Bousman, W.G., "A Note on Torsional Dynamic Scaling," *Journal of American Helicopter Society*, Vol. 43, No. 2, 1998, pp. 172-175.

[74] Datta, A. and Chopra, I., "Validation and Understanding of UH-60A Vibratory Loads in Steady Level Flight," 58th Annual Forum of the American Helicopter Society, Montreal, Canada, June 2001.

[75] Torok, M. S., Goodman and Kufeld, R., "Analysis of Rotor Blade Dynamics using Experimental UH-60A airloads obtained at the DNW," *Journal of the American Helicopter Society*, Vol. 39, No. 1, 1994, pp. 63-69.

[76] Lorber, P.F., "Aerodynamic Results of Pressure Instrumented Model Rotor Test at the DNW," *Journal of the American Helicopter Society*, Vol. 36, No. 4, 1991, pp. 66-76.

[77] Torok, M.S. and Berezin, C., "Aerodynamic and Wake Methodology Evaluation Using Model UH-60A Experimental Data," *Journal of the American Helicopter Society*, Vol. 39, No. 2, 1994, pp. 21-29.

[78] Leishman, J. G., "Subsonic Unsteady Aerodynamics Caused by Gusts Using the Indicial Method," *Journal of Aircraft*, Vol. 33, No. 5, 1996, pp. 869-879.

[79] Pulliam, T. and Steger, J., "Implicit Finite Difference Simulations of Three Dimensional Compressible Flow," *AIAA Journal*, Vol. 18, No. 2, 1980, pp. 159-167.

[80] Srinivasan, G.R. and Baeder, J.D., "TURNS: A Free Wake Euler/ Navier-Stokes Numerical Method for Helicopter Rotors," *AIAA Journal*, Vol. 31 No. 5, 1993, pp. 959-962.

[81] Baeder, J.D. and Srinivasan, G. R., "Computational Aeroacoustics Study of Isolated Blade-Vortex Interaction Noise," Presented at the American Helicopter Society Aeromechanics Specialists Conference, San Francisco, CA, Jan. 1994.

[82] Roe, P.L., "Approximate Riemann Solvers, Parametric Vectors, and Difference Schemes," *Journal of Computational Physics*, Vol. 43, No. 3, 1981, pp. 357-372.

[83] Vatsa, V.N., Thomas, J.L., and Wedan, B.W., "Navier-Stokes Computations of Prolate Spheroids at Angle of Attack," AIAA Paper 87-2627, Aug. 1987.

[84] Van Leer, B., "Towards the Ultimate Conservative Difference Scheme V, A Second-Order Sequel to Godunov's method," *Journal of Computational Physics*, Vol. 32, 1979, pp.101-135.

[85] Koren, B., "A robust upwind discretisation method for advection, diffusion and source terms," *Numerical Methods for Advection-Diffusion Problems*, Vieweg, Braunschweig, p117, 1993.

[86] Jameson, A., and Yoon, S., "Lower-Upper Implicit Schemes with Multiple Grids for the Euler Equations," *AIAA Journal*, Vol. 25, No. 7, 1987, pp. 929-935.

[87] Yoon, S. and Jameson, A., "An LU-SSOR Scheme for the Euler and Navier Stokes Equations," AIAA Paper, Vol. 87-0600, 1987.

[88] Suresh, A. and Huynh, H. T., "Accurate Monotonicity- Preserving Schemes with Runge-Kutta Time Stepping," *Journal of Computational Physics*, Vol. 136, 1997, pp. 83-99.

[89] Huynh, H., T., "Accurate Monotone Cubic Interpolation," *SIAM Journal on Numerical Analysis*, Vol. 30, No. 1, 1993, pp.57-100.

[90] Thomas, P.D., and Lombard, C.K., "Geometric Conservation Law and its Application to Flow Computations on Moving Grids," *AIAA Journal*, Vol. 17, No. 10, 1979, pp.1030-1037.

[91] Vinokur, M., "An Analysis of Finite-Difference and Finite-Volume Formulations for Conservation Laws," *Journal of Computational Physics*, Vol. 81, No.2, 1989, pp. 1-52.

[92] Barth, T. J., Puliam, T. H. and Buning P. G., "Navier-Stokes Computations for Exotic Airfoils," AIAA Paper 85-0109, 1985.

[93] Greengard, L. and Rokhlin, V., "A Fast Algorithm for Particle Simulations," *Journal of Computational Physics* Vol. 73, 1987, pp. 324-345.

[94] Bagai, A. and Leishman, J.G., "The Maryland Free-Wake Analysis - Theory, Implementation and User's Manual," University of Maryland, Department of Aerospace Engineering, Technical Report Prepared for NASA Langley Research Center, Aeroacousitics Branch, Fluid Mechanics and Acoustics Division, Contract No. 015-2685, December 1995.

[95] Bir, G. and Chopra, I., "University of Maryland Advanced Rotorcraft Code (UMARC) Manual," University of Maryland, College Park, 1995.

[96] Leishman, J. G., *Principles of Helicopter Aerodynamics*, Cambridge University Press, 2000.

[97] Totah, J., "A Critical Assessment of UH-60 Main Rotor Airfoil Data," AIAA paper 93-3413, Aug 1993.

[98] McCroskey, J., "Critical Assessment of Wind Tunnel Results for the NACA 0012 Airfoil," NASA TM 100019, October 1987.

[99] Yeo, H., "Inverstigation of SC1095 and SC1095R8 Airfoil Characteristics," 3rd NRTC/RITA Rotorcraft Airloads Workshop, University of Maryland, College Park, Aug 27-28, 2002.

[100] Leishman, J.G., "Validation of Approximate Indicial Aerodynamics Functions for Two-Dimensional Subsonic Flow," *AIAA Journal*, Vol. 25, No. 10, Oct. 1993, pp. 914-922.

[101] Bisplinghoff, R.L., Ashley H. and Halfman, R.L., *Aeroelasticity*, Addison-Wesley Publishing Co., Reading, MA, 1995.

[102] Lomax, H., "Indicial Aerodynamics," *AGARD Manual of Aeroelasticity*, Pt. II, Nov. 1968, Chap. 6.

[103] Sitaraman, J., "Computational Fluid Dynamics based Enhanced Indicial Aerodynamic Models," *Masters Thesis*, University of Maryland at College Park, MD, 2000.

[104] Dongwook, L., Leishman, J.G. and Baeder J. D., "Non-linear Indicial Method for Calculation of Unsteady Airloads," Presented at the 59th Forum of American Helicopter Society, Phoenix, Arizona, May 2003.

[105] Cook, P.H., McDonald, M.A. and Firmin, M.C.P, "Aerofoil RAE 2822 - Pr essure Distributions, and Boundary Layer and Wake Measurements," Experimental Data Base for Computer Program Assessment, AGARD Report 138, 1979.

[106] Sitaraman, J., "Computational Fluid Dynamics Based Enhanced Indicial Aerodynamic Models," *Master's thesis*, University of Maryland, College Park, 2002.

[107] Evvard, J.C., "Use of Source Distribution for Evaluating Theoretical Aerodynamics of Thin Finite Wings at Supersonic Speeds," NACA Report 951, 1950.

[108] Leishman, J. G., "Unsteady Aerodynamics of Airfoils Encountering Traveling Gusts and Vortices," *Journal of Aircraft*, Vol. 34, No. 6, 1997, pp. 719-729.

[109] Singh, R., "Transonic Effects on Aerodynamics and Acoustics of Blade-Vortex Interaction," *PhD dissertation*, University of Maryland at College Park, MD, 1999.

[110] Küssner, H. G., "General Airfoil Theory," NASA TM 979, 1941.

[111] Beddoes, T.S., "A Wake Model for High Resolution Airloads" International Conference on Rotorcraft Basic Research, February 1985.

[112] Barnes, J.E. and Hut, P., "A Hierarchical Force Calculation Algorithm," *Nature*, Vol. 324, 1986, pp. 446-449.

[113] Splettsttoesser, W.R., Schultz, K.J., Boxwell, D.A., and Schmitz, F.H., "Helicopter Model Rotor-Blade Vortex Interaction Impulsive Noise: Scalability and Parametric Variations," Presented at the 10th European Rotorcraft Forum, the Hague, Netherlands, Aug 28-31, 1984.

[114] Brentner, K.S., "Prediction of Helicopter Rotor Noise - A Computer Program Incorporating Realistic Blade Motions and Advanced Formulation," NASA TM 87721, 1986.

[115] FFowcs Williams, J.E. and Hawkings, D.L., "Sound Generation by Turbulence and Surface in Arbitrary Motion," *Philosophical Transactions of the Royal Society*, London, Series A. Vol. 264, No. 1151, May 1969, pp. 321-342.

[116] Bousman, G. and Kufeld, R.M., Balough, D., Cross, J.L., Studebaker, K.F. and Jennison, C.D., "Flight Testing the UH-60A Airloads Aircraft", 50th Annual Forum of the American Helicopter Society, Washington, D.C., May, 1994.

[117] Ormiston, R.A., "UH-60 Rotor Blade Structural Dynamic Response to Measured Loads, Updates, Interpetations and Spec/Data Issues," 4th NRTC/RITA Rotorcraft Airloads Workshop, Phoenix, Arizona, Feb 27-28, 2003.

[118] Bousman, W.G., "UH-60A Database," 4th NRTC/RITA Rotorcraft Airloads Workshop, Phoenix, Arizona, Feb 27-28, 2003.

[119] Bousman, W.G., "UH-60A Repeat points," 4th NRTC/RITA Rotorcraft Airloads Workshop, Phoenix, Arizona, Feb 27-28, 2003.

[120] Purser, P.E., and Spearman, M.L., "Wind-Tunnel Tests at Low Speed of Swept and Yawed Wings Having Various Plan Forms, NACA Technical Note 2445, December 1951.

[121] Harris, F. D., "Preliminary Study of Radial Flow Effects on Rotor Blades," Boeing Vertol Report, Morton, Pennsylvania, 1966.

[122] Jones, R. T., "Wing Planforms For High Speed Flight," NACA report 863, 1947.

[123] Datta, A., and Chopra, I., "Validation of Structural and Aerodynamic Modeling Using UH-60A Flight Test Data," Presented at the 59th Annual Forum of American Helicopter Society, Phoenix, AZ, May 6-8, 2003.

[124] Jackson, J.D., *Classical Electrodynamics*, Wiley, New York (1975).

[125] Arfken, G., "The Addition Theorem for Spherical Harmonics," Section 12.8 in *Mathematical Methods for Physicists*, Academic Press, pp. 693-695, 1985.

[126] Altmann, S. L., *Rotations, Quaternions, and Double groups Oxford*, England, Clarendon Press, 1986.